UNIVERSITY OF SOUTHAMPTON

Development and Application of Theoretical Models for High Frequency Vibration of Railway Track

by

Tianxing Wu

Submitted for the degree of

Doctor of Philosophy

INSTITUTE OF SOUND AND VIBRATION RESEARCH

FACULTY OF ENGINEERING AND APPLIED SCIENCE

APRIL 2000

UNIVERSITY OF SOUTHAMPTON

ABSTRACT

FACULTY OF ENGINEERING AND APPLIED SCIENCE

INSTITUTE OF SOUND AND VIBRATION RESEARCH

Doctor of Philosophy

Development and Application of Theoretical Models for High Frequency Vibration of Railway Track

by Tianxing Wu

Railway track vibration caused by the rolling of the wheel on the rail is a significant source of noise. A theoretical study of track dynamics is carried out by developing new rail models and investigating the effects on track vibration of various factors which might arise in practice.

New analytical models for high frequency rail vibration are developed and both vertical and lateral vibrations are studied using these models. Comparisons with FE models and measurement data are made to validate the newly developed models.

The non-linearity of the track foundation is taken into account in the track model in accordance with the static loads in the track foundation caused by the train weight. Their influences on track vibration are explored.

The concept of the random sleeper spacing and ballast stiffness is introduced into the track model because both are found to be irregular in practice even for a newly built railway track. The influence on track vibration of random sleeper spacing and ballast stiffness is investigated from a statistical point of view.

The effects on track vibration of multiple wheel/rail interactions are studied. Predictions are made for track vibration and noise radiation by taking account of both original and passive wheel/rail interactions, which are caused by roughnesses and rail vibration respectively, and the non-linearity of the track foundation. Results from different models are compared and discussed in terms of the receptance of the track vibration, wheel/rail excitation and noise radiation.

This study show that when a train runs on a track, both the wheel static load and the presence of wheels on the rail affect the track vibration. The static load due to the train weight in the track foundation is local. Thus the pads and ballast near the wheel loads are preloaded and become stiffer. Due to the stiffened pad and ballast the point receptance at low frequencies is reduced and the vibration decay rate in the frequency range up to the first pinned-pinned resonance is enhanced.

The wheel/rail interaction due to the wave in the rail is weak at low frequencies. Because of the presence of the wave reflections the point receptance of the track with wheels on it fluctuates from higher frequency. The first pinned-pinned resonance peak experiences a cancellation due to the wave reflection from other wheels when a wheel/rail excitation acts at mid-span. The vibration decay is enhanced in the wheel/rail interaction areas.

The wheel/rail excitation force is related to the roughness spectrum and the point receptance sum of the wheel, contact spring and rail. For the same roughness level, the wheel/rail excitation force is determined by the wheel and rail receptances at low frequencies, whereas at high frequencies it is determined by the receptance of the contact spring. In the middle frequency region it fluctuates strongly due to the presence of the wave reflection from other wheels, with a low receptance of the rail corresponding to a high excitation force and vice versa.

The influences of the preloads and wave reflections from wheels on noise radiation from the track are limited. This is because the variations in the rail vibration receptance and in the wheel/rail excitation are opposite. Their effects cancel each other to a large extent.

Statistical results reveal the effect of the random sleeper spacing and ballast stiffness on the track vibration. The point receptance and the vibration decay rate are distributed in a certain area instead of having a fixed value due to the variations in the sleeper spacing and ballast stiffness. Due to the random sleeper spacing the pinned-pinned resonance phenomenon is much less sharp than in the uniform sleeper spacing case and in some cases is completely suppressed.

In terms of railway rolling noise, the randomness of the track foundation leads to only small effects and no significant increase or decrease in the track noise.

ACKNOWLEDGEMENTS

I wish to express my gratitude in particular to my supervisor, Dr. David Thompson, for his valuable encouragement, guidance and advice throughout the work.

I also wish to thank Dr. Mike Brennan and Dr. Chris Jones for their valuable suggestions on carrying out this research.

My grateful acknowledgements also go to Mr. Keith Sims, technician of ISVR, for his help during the measurements at Chilworth, especially with moving the bogie to the middle of the track and jacking it up.

Special thanks must be given to the Faculty of Engineering and Applied Science, ISVR and Dr. David Thompson who sponsored my PhD research at ISVR.

Finally, I would like to thank my wife, Jianhua, and my son, Kaiyu, for their continuous understanding and supporting my pursuit of the PhD degree.

Contents

List of symbols

A	Cross-sectional area of rail
$\mathbf{A}$	System matrix in state space
A_f	Cross-sectional area of rail foot
A_h	Cross-sectional area of rail head
A_w	Cross-sectional area of rail web
d	Sleeper separation distance
E	Young's modulus
f	Frequency
F	Wheel/rail excitation force
g	Green's function
G	Shear modulus
g_{ij}	Green's function
h_f	Height of rail foot
h_h	Height of rail head
h_w	Height of rail web
i	$\sqrt{-1}$
I	Area moment of rail cross-section
I_f	Area moment of rail foot cross-section
I_h	Area moment of rail head cross-section
I_{pf}	Polar moment of rail foot cross-section
I_{ph}	Polar moment of rail head cross-section
I_w	Area moment of rail web for web bending
J_f	Torsional moment of rail foot cross-section
J_h	Torsional moment of rail head cross-section

J_w	Torsional moment of rail web cross-section
k	wave-number
K_b	Ballast stiffness
k_b	Ballast stiffness per unit length of track
k_f	Equivalent stiffness for rail-foot flapping
K_H	Wheel/rail contact stiffness
K_M	Modal stiffness of wheel
K_p	Pad stiffness
k_p	Pad stiffness per unit length of track
K_{pr}	Pad rotational stiffness
k_{pr}	Pad rotational stiffness per unit length of track
M_s	Sleeper mass
m_s	Sleeper mass per unit length of track
M_w	Wheel mass (including all unsprung mass)
P	Wheel/rail interaction force induced by rail vibration
$\mathbf{Q}$	Amplitude of displacement vector of rail
$\mathbf{q}$	Displacement vector of rail
r	Combined roughness on wheel tread and rail-head surface
u	Vertical motion of rail
u_f	Vertical motion of rail foot
u_h	Vertical motion of rail head
v	Vertical velocity of rail vibration
v_f	Lateral motion of rail foot
v_h	Lateral motion of rail head
$\mathbf{X}$	State variable
Z_{ij}	Dynamic stiffness of track support (double Timoshenko beam model)
Z_r	Rotational dynamic stiffness of track support for lateral vibration
Z_s	Dynamic stiffness of track support (single Timoshenko beam model)
Z_t	Translational dynamic stiffness of track support for lateral vibration
Z_w	Dynamic stiffness of wheel (including contact spring)

α^C	Point receptance of wheel/rail contact spring
α^R	Point receptance of rail
α^{RT}	Transfer receptance of rail
α^W	Point receptance of wheel
α_w^R	Point receptance of rail with multiple wheel interactions
α_w^{RT}	Transfer receptance of rail with multiple wheel interactions
Δ	Wave propagation decay rate (dB/m)
η_b	Loss factor of ballast
η_p	Loss factor of pad
η_r	Loss factor of rail
θ_f	Torsional motion of rail foot
θ_h	Torsional motion of rail head
κ	Shear coefficient of rail
κ_f	Shear coefficient of rail foot
κ_h	Shear coefficient of rail head
λ_r	Roughness wavelength
ρ	Density
Φ	Rotation of rail cross-section for vertical vibration
Φ_f	Rotation of rail foot cross-section for vertical vibration
Φ_h	Rotation of rail head cross-section for vertical vibration
ψ_f	Rotation of rail foot cross-section for lateral vibration
ψ_h	Rotation of rail head cross-section for lateral vibration
ω	Circular frequency

CHAPTER 1

Introduction

1.1. Railway rolling noise and track vibration

Railways are usually seen as an environmentally friendly option for transport because the energy consumption is much less for railways compared with roads for the same transport capacity, so is the air pollution. This has recently led to considerable interest in their role in the movement of freight, in long-distance high-speed passenger travel, and in solving road congestion. For example the French TGV Est project, a 504 km line linking Paris and Strasbourg, has been under way since 1998 as an expansion of the existed TGV system. In east China construction of a long-distance high-speed railway linking Beijing and Shanghai will be soon launched as the existing Beijing-Shanghai line is getting more and more congested. At the turn of the millennium it is indicated by a survey conducted by BBC (Panorama "The Great Train Jam", On BBC One, 29 November, 1999) that £41bn is required to increase the capacity of the national railway network to an acceptable level due to the increase in the demand for passenger journeys in the first ten years of the twenty-first century.

Unfortunately, the environmental noise and vibration works against the promotion of rail. Noise pollution in the vicinity of railways is increasing, partly as a result of rail network expansion and because of increasing use of existing infrastructure. The development of high-speed rail is an issue of particular concern as far as future railway noise is concerned and noise is the main subject of complaint from the public, when new lines are under discussion. At the same time, European legislation is expected to set tight noise emission limits. For example, the EU Green Paper on Future Noise Policy has targeted railway noise as a prime area for legislation [5]. The basic approach to reducing railway environmental noise exposure is to place tall barriers to limit the noise transmission. However, this approach costs a lot of money, for example in Switzerland it has been estimated that 220 km of barriers averaging 5 m in height costing SFR 1.4 billion (£600M) are required for the 550 km transit lines of Basel-Brugg-Gotthard-Chiasso and Schaffhausen-Brugg to comply with the noise legislation [55]. Other measures include route changes and lowering rail alignments into cuttings or even into tunnels. Such measures are of course very expensive. Therefore, the most effective way to reduce railway noise is to reduce noise at its source.

Amongst the other sources, rolling noise is an important issue which forms the principal source of noise from railway operations. It is caused by vibrations of both the rail and the wheel, which are generated by the combination of small scale undulations (roughnesses) on the wheel tread and railhead, see Figure 1.1. When a train runs along the track, these roughnesses produce dynamic interaction forces between the wheel and rail at the frequencies corresponding to the passage speed of the wheel/rail contact over the particular roughness wavelength so that the wheel and rail are excited, vibrate and radiate noise. Typically, on both surfaces, there are undulations with amplitudes from less than 1 μm up to tens of μm [83]. The undulations of importance for noise have wavelengths of several centimetres. For an irregularity of wavelength λ, this causes vibration with a frequency f given by

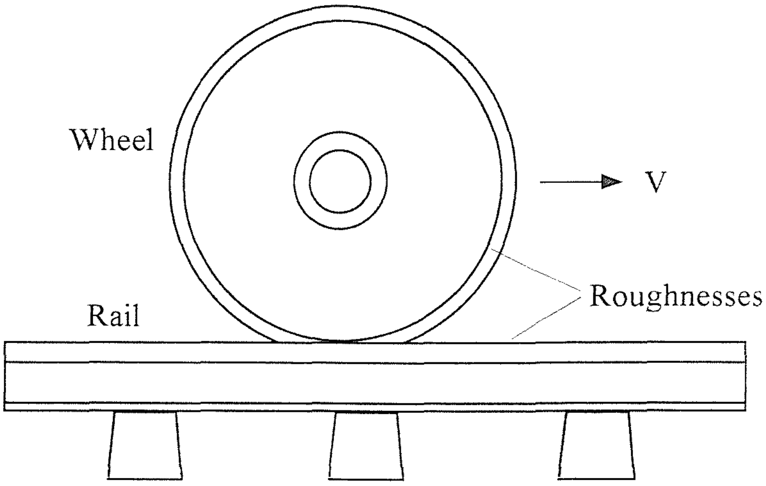

Figure 1.1. Rolling noise generation.

$$f = v/\lambda$$

where v is the speed of a train. Wavelengths which are short in comparison with the contact patch are attenuated in their excitation of the system. The rolling noise generation process can be summarised in the flow diagram of Figure 1.2. It is found empirically that the rolling noise increases by approximately 9 dB per doubling of speed [90].

In order to determine the wheel/rail interaction forces, to predict the wheel and rail vibrations and to estimate the noise radiated by the wheel and rail, a knowledge

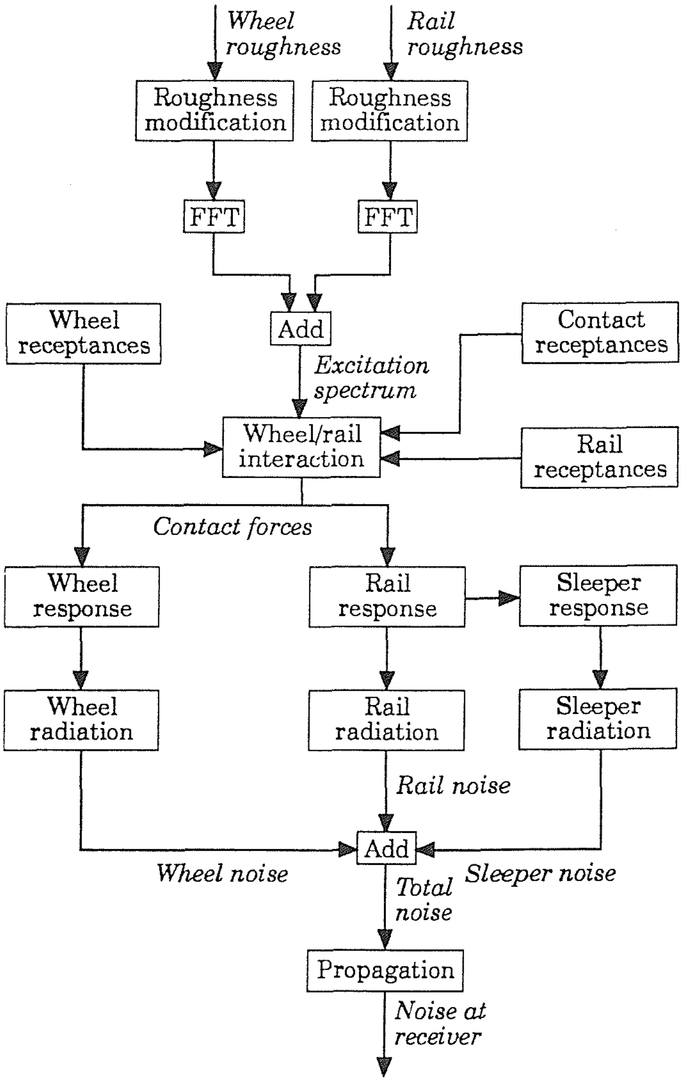

Figure 1.2. Rolling noise generation process model (from [86]).

of dynamic properties (receptances, defined as displacement divided by force, or impedances) of the wheel and rail is essential. The rail vibration is a significant source of noise in a fairly broad frequency range 50–5000 Hz, with the highest levels occurring in the range 800–2500 Hz [76]. Compared with wheel vibration, rail vibration is a more complex topic because the railway track is effectively infinite and contains pronounced non-linear components such as the railpad and ballast. Rail vibration is also affected by multiple wheel/rail interactions. Moreover, account should be taken of the cross-sectional deformations of the rail for high frequency vibration. Furthermore, the sleeper spacing and the ballast stiffness are irregular rather than uniform. Their random variations affect the track vibration.

Different models have been developed to investigate the dynamic behaviour of the railway track over the years. For simplicity, however, some of these important factors are neglected in the usual track vibration models. For example, the pad stiffness and the ballast stiffness are usually regarded as constant along the whole railway track or assigned the same value at each support although these parameters vary with load and frequency and have significant effects on the track vibration. The rail vibration response is generally calculated without taking any account of other wheel/rail interactions apart from at the single wheel/rail contact where excitation takes place. It is then assumed that the average response of the rail to multiple wheels can be obtained from the response to a series of single wheels, whereas in practice there may be interaction between the different wheel on a rail. In order to obtain a better understanding of the railway track vibration, track models are needed that take account of these various effects.

1.2. Literature review

Perhaps it could be said that the research on railway track dynamics is one of the most historical and fruitful topics in engineering. For example, the term Winkler foundation is well known in civil engineering as referring to a beam on a continuous, uniform, elastic foundation. This was in fact a preliminary model of railway track developed by Winkler [97, 98] more than a century ago. Strength problems of railway track were one of Timoshenko's main research interests [91, 92, 93] eighty years ago. This early work on railway track mainly concentrated on static problems. Indeed, until the late 1960s there were rather few papers in which dynamic models of track were used to solve particular problems. This might be because dynamic models need extensive calculations whereas digital computers were not well developed before that time.

In the last 30 years there has been very much greater interest in applying dynamic models to understand and solve practical problems in railway track and vehicle/track interaction. The state of the art paper by Knothe and Grassie [40] summarises a lot of work in this area. Comprehensive work was carried out by Grassie et al. [16, 17, 18, 19], in which the dynamic behaviour of railway track and wheelsets was extensively studied in the frequency range 50–1500 Hz.

In terms of the railway rolling noise Remington's work [60, 61, 62, 63] was regarded as the most comprehensive single model as it covers the whole noise generation process. However, this has been achieved at the expense of using over-simplified models of the various constituent parts and thus the deficiencies in Remington's model should be improved by the inclusion of further work. Within the framework of Remington's model (see Figure 1.2) Thompson [76 ,77, 78, 79, 80, 81] developed much improved models for wheel and rail response predictions, including using the finite element method (FEM), along with the more generalised wheel/rail interaction model corresponding to the FE models of the wheel and rail. Based on these advanced models and the framework of Remington's model, a software package named TWINS has been developed by Thompson [84, 86, 87] for railway rolling noise predictions.

Aspects of the problem, in particular related to track vibration, are reviewed in the following, sorted into different topics.

1.2.1. *Excitation—wheel/rail interaction*

A review of different models for wheel/rail interaction was presented in by Knothe and Grassie [40]. These models were divided into a stationary load, a moving load, a moving irregularity between a stationary wheel and rail, and a wheel rolling over irregularities on the track. Perhaps, the most realistic model of vertical excitation arising in wheel/rail contact is that of a wheel rolling over irregularities on the rail which was presented by Sibaei [71]. However, this model is also the most difficult to use, and simpler models are more preferable in particular circumstances. The stationary load model is appropriate for calculating the receptance of a track and for comparing the calculated and measured response of the track to the excitation. The moving load model is used in most of the theoretical investigations which will be reviewed in section 1.2.4. below.

The moving irregularity model can be regarded physically as a model in which the wheelset remains in a fixed position on the rail, and a strip combining the roughness on the wheel tread and railhead is effectively pulled at a steady speed between wheel and rail. The combined roughness forms a relative displacement input between the wheel and rail, and thus the wheel/rail interaction force depends on the receptances of the wheel and rail (including contact zone) at the contact position. At wavelengths of the roughness which are short in relation to the contact patch length, the effectiveness of this roughness is reduced. This effect was modelled by Remington using a wavenumber filter [62]. The moving irregularity model has been much used to investigate problems of wheel/rail interaction and rolling noise by Frýba [14], Grassie et al. [16, 23], Meinke et al. [46], Patil [57], Sato et al. [67] and Thompson [76].

The local elasticity or Hertzian contact between the wheel and rail is actually non-linear, but linearization is acceptable if the dynamic displacements are small. For larger vibration amplitudes, however, the non-linearity in the contact spring becomes important, leading eventually to loss of contact, see O. R. E. [56] and Ripke [65]. The non-linear relation of the Hertzian contact has been included by Clark et al. [4] and Ripke [65] in a time-stepping model.

In the moving irregularity model the wheel and rail are static, thus only the receptances of a static wheel and rail are used. Ferguson [11] has studied the effects of rolling on the wheel theoretically, by examining the vibration of a rolling disc excited by various types of force and moment at its contact with a plane. This was extended to the case of a random input by Thompson [81].

The tangential contact problem is more difficult. Much work on rolling contact theory has been done by Kalker [35, 36], and this has been successfully applied to the quasi-static behaviour of a railway vehicle. The creep force in normal rolling has been modelled by Ferguson [11] as a damper coupling the wheel with the rail. The dependence of creep coefficients on frequency has been studied by Knothe and Gross-Thebing [39]. A comprehensive model for wheel/rail contact in six degrees of freedom has been developed by Thompson [80], which includes the effects of the (linearised) Hertzian contact spring and Kalker's creep force formulation using frequency-dependent creep coefficients.

1.2.2. *Track modelling*

Track models are used to calculate the rail vibration and to determine the wheel/rail interaction force using the moving irregularity model. The most common track models can be divided into two categories according to their support type: (a) an infinite rail continuously supported by damped resilient and mass layers (railpads, sleepers and ballast); (b) a rail discretely supported by pad, sleeper and ballast. Track models can also be categorised according to whether the cross-sectional deformations of a rail are included in the models. If the cross-sectional deformations can be included in the models, they are referred to here as advanced models, otherwise they are simple models. In the simple models the rail is represented by a beam and thus they are also called simple beam models.

A simple beam model with continuous supports was used by Timoshenko [91, 92, 93] and Sato [66], in which the rail was represented by an Euler-Bernoulli beam. A model in which the rail was represented by a Timoshenko beam, i.e. including shear deformation and rotational inertia, on a continuous layer composed of the pad, sleeper and ballast was developed by Grassie et al. [16, 20] and used later by Tassilly and Vincent [74]. Simple beam models are found to be very useful to find parameters for the stiffness and damping of the railpad and ballast by fitting calculated values of the rail receptance to those measured. The continuously supported Timoshenko beam model has also been included in the software package TWINS [84, 85].

The advantage of a simple beam model with discrete supports is that using such a model the pinned-pinned resonance can be observed, in which the track receptance has a maximum when the excitation acts between sleepers and a minimum when the excitation acts at a sleeper. This occurs because the sleeper spacing is equal to half the wavelength of the flexural waves at this frequency. The discretely supported simple beam model has been used by Grassie [16], Heckl [26, 27, 28], Nordborg [52] and Thompson [84, 85]. The calculation of the receptance for the infinite track with periodic supports is much more difficult compared to the continuous model. There are two main ways to solve the problem. One way is to make use of Floquet's theory (see Nafeh's book [100]) and the other is to use the Green's function and the superposition principle. The former was used by Grassie [16], Munjal and Heckl [47], Nordborg [52] and Ripke and Knothe [64]. The latter was used by Heckl [28] and Kurze [42].

At high frequencies the cross-sectional deformations of a rail (web bending and foot flapping) become significant and simple beam models cannot represent these deformations. Thus advanced rail models are needed for vertical vibration above about 2000 Hz and for lateral vibration above about 1200 Hz. Knothe et al. [41] has introduced three types of advanced rail models, which are referred to as one-dimensional, two-dimensional and three-dimensional, according to whether their constituent elements are beam, plate or solid respectively. Advanced models based on the finite element method or a derivative have been developed by Gavric [15], Gry [25], Ripke and Knothe [64], Strzyzakowski and Ziemanski [73] and Thompson [79] for analysing high frequency rail vibration. Some theoretical models were also developed by Scholl [68, 69, 70] for the analysis of dispersion relations in a free rail. An experimental study for identifying various propagating waves in railway tracks has been carried out by Thompson [82].

Response calculations for the advanced track models with discrete supports are fairly time consuming because a large number of degrees of freedom have to be included. Indeed, there are only a few advanced models available to deal with high frequency vibrations of a track with discrete supports. Ripke and Knothe [64] have developed a beam-plate finite element model for a rail with discrete supports and investigated both the vertical and the lateral vibration behaviour up to 2000 Hz. Gry [25] has developed a method called "span wave co-ordinates method" to predict vertical and lateral vibration behaviour of a discretely supported rail up to 5000 Hz.

1.2.3. *Track foundation components*

The track foundation components such as the pad, sleeper and ballast have significant effects on the track vibration. The effect of track parameter changes on vertical rail vibration has been examined by Dalenbring [7] through numerical calculations and measurements. It was claimed in [7] that a proper choice of track parameters can give a 20 dB reduction of rail vibration level in some cases.

A great difficulty in practice is to find appropriate values to represent actual railpads which are conventionally represented by two parameters, stiffness and damping. Many tests have been undertaken in the laboratory and in track by Dalenbring [7], Fenander [10], Grassie [22], Kanamori [37] and Thompson et al. [88, 89] to determine the dynamic properties of a railpad. It has been found that the railpad is effectively non-linear and its dynamic stiffness is strongly load dependent and mildly frequency dependent [89]. The pad dynamic stiffness increases with load and is greater than or equal to the tangent stiffness found from the static load/deflection curves [22]. The ratio of the dynamic stiffness to the tangent static stiffness mainly depends on the pad material.

The effect of different railpads (soft, medium and stiff) on track vibration has been studied experimentally by de France [8] in terms of receptance and vibration attenuation. As for rolling noise control, it has been found by Vincent et al. [96] that by reducing pad stiffness the noise radiation from the sleepers is reduced but the radiation from the rail is increased, and vice versa. The optimum pad stiffness is found when the rail and sleeper components are equal, for which the track radiation is minimum.

The model of damping used for the track, especially the railpad, has a significant effect on the decay rate of vibration in the track and hence on the noise, see Thompson et al. [86]. Railpad can be modelled using viscous damping (e.g. Grassie [16]) or constant loss factor damping (e.g. Thompson et al. [85, 95]). The latter is found to give better agreement with laboratory measurements by Thompson et al. [88, 89].

A problem arise at high frequencies where the decay rate is often under-predicted. A way of compensating for this is to add damping to the rail in the form of a loss factor by de France [8] and Thompson et al. [88, 89]. Although this does not correspond to the physical mechanism of damping, it provides a simple means of preventing over-prediction of the noise at high frequencies.

In a continuously supported track model the sleeper is treated as a mass layer, whereas in a discretely supported track model it is modelled as either a mass block or a flexible component. The most complete sleeper model is a Timoshenko beam of non-uniform widths and thickness, which can readily be analysed using a finite element model (FEM). This approach has been used by Dahlberg and Nielsen [6, 50]. Another approach is to use an equivalent uniform beam to approximate the non-uniform sleepers. This approach has been used by Grassie [24]. The influence of the sleepers' resonant behaviour not only on the sleepers themselves but also on the track responses has been presented by Clark et al. [4], Grassie et al. [20, 21] and Janssens and Thompson [33].

In track modelling the ballast seems to be the element to which least attention has been paid up to now. Less data and references are available for the ballast stiffness. An experimental investigation carried out by Frémion et al. [12] has shown that the ballast stiffness is influenced by a static preload and increases significantly with the frequency. It has been suggested that the ballast stiffness may be approximated by the Hertz law. Moreover, measurement results from de France [8] and Igeland and Oscarsson [30] have shown that the measured values of the ballast stiffness vary significantly even for the ballast at adjacent sleepers. Further experimental work is essential to investigate the dynamic properties of the ballast.

1.2.4. *Moving load on track*

The problem of a moving load on a beam with an elastic foundation arises directly from the practice of a train running on the track. Much work has been carried out from either theoretical or application aspects for more than seventy years. The earliest work by Timoshenko [92] showed that for a beam on a massless Winkler foundation subjected to a moving steady load, resonance occurs when the load's speed equals a critical speed. This critical speed is typically much greater than operational speeds of a train.

A comprehensive theory of the effect of moving loads on structures can be found in Frýba's book [13]. The response to a moving harmonic load of an infinite Timoshenko beam on a Winkler foundation has been investigated by Chonan [3] and Bogacz et al. [1]. To include the effect of the pinned-pinned resonance in a solution to the problem of a moving load it is necessary to use a track model with a discretely supported rail. There are two general techniques to treat this problem, which have been summarised by Müller et al. [48]. One of these is a wave-type solution which utilises Floquet's theorem. Mead's papers [43, 44, 45] appear to be the first in this field. Smith and Wormley [72] applied this method to calculate the response to a moving load of a periodically supported guideway. A second approach is based on the assumption that the response to a moving load of a periodically supported beam is given by the following infinite series:

$$w(r,t) = \sum_{n=-\infty}^{\infty} A_n(r) e^{i2\pi n(r+vt)/L} e^{i\omega t}$$

where r is in a moving co-ordinate system having the same speed v as the load, L is the span length and ω is the circular frequency of the load. This approach was proposed first by Jezequel [34] and used later by Kisilowski et al. [38], Ilias and Knothe [32], Sibaei [71] and Nordborg [53]. It has been found in [32] that in the speed range of practical interest (up to 100 m/s), the moving load influences the response significantly only around the frequency of the pinned-pinned resonance. The pinned-pinned resonance (vertical point receptance) splits into two peaks as the speed of the load increases. The increment of frequency between the two peaks is $\Delta f = vL$.

The track response to a moving vibration mass has been studied by Duffy [9], Kisilowski et al. [37], Sibaei [71] and Nordborg [53, 54]. In [53, 54] the parametric excitation to the wheel/track system has been investigated using a model of a moving mass on a discretely supported beam. The parametric excitation occurs at low frequencies (50 – 100 Hz) due to the periodic variation of the track stiffness. It has been found by Nordborg that when the sleeper-passing frequency coincides with the wheel-ballast resonance, the vertical vibration reaches a maximum.

1.3. Research topics to be carried out

Amongst the existing models of railway track vibration, the following problems have yet to be satisfactorily solved or to be considered, and the research in this thesis are therefore focused on these problems.

(1) *Discretely supported track models for high frequency vibration.* The cross-sectional deformations of a rail become dominant at high frequencies and thus advanced rail models are needed to allow these deformations. Commonly used advanced models are usually FE models. It is inconvenient to calculate responses of the rail to external excitation using such models, because a large number of degrees of freedom on the boundaries have to be dealt with. This forms the main barrier to calculate a discretely supported track at high frequencies. Some simplified yet reliable analytical models, with which the cross-sectional deformations can be represented, should be developed.

(2) *Non-linearity of the track foundation and its effect on track vibration.* The resilient components in the track foundation such as the pad and ballast have pronounced non-linearity and thus the pad and ballast stiffness depends on the preload in them. For example, a train's weight causes local preload in the track foundation, and the preload increases the pad and ballast stiffness in the loaded region, hence modifying the rail vibration. What is more, the track foundation is loaded only in a local area around the wheel so that the pad and ballast stiffness has different values along the rail. The load dependence of the resilient components should be taken account of in the track models.

(3) *Multiple wheel/rail interactions.* When a rail is excited at the wheel/rail contact point due to the roughnesses on the contact surfaces of the wheel and rail, a wave propagates along the rail and interacts with other wheels. This leads to the generation of an interaction force between the wheel and rail at the contact position (different from the original excitation). Thus the vibration of the rail is a combination of the wave caused by the original excitations and the wave caused by the generated wheel/rail interaction forces. Therefore a multiple wheel/rail interaction model should be set up.

(4) *Irregularities of sleeper spacing and ballast stiffness.* In practice the sleeper spacing is irregular along the track rather than uniform. This occurs due to limited precision during track installation, and is further increased by movement in service and maintenance operations. As mentioned before, the ballast stiffness is also found to be irregular at different sleepers. This is because the ballast stiffness is related to the contact state of the sleeper with the ballast and the contact state is not uniform at each support. In order to examine the effects on track vibration of the irregular sleeper spacing and ballast stiffness, statistical analysis is essential using a track model in which these parameters are taken as random variables.

In chapter 2 a double Timoshenko beam model is developed for vertical vibration analysis at high frequencies. This model includes the essential cross-sectional deformation of a rail in the vertical vibration at high frequencies. Based on this model, the dispersion relation of propagating waves in an unsupported and a continuously supported rail is studied and vertical vibration receptances of the rail are calculated.

In chapter 3 an interconnected beam model is presented for studying the lateral vibration behaviour of railway track. All essential cross-sectional deformations of the rail can be included in this model. Detailed investigation of the lateral vibration for both continuously and discretely supported rail has been carried out efficiently using this model.

Non-linearity of the track foundation is considered in chapter 4. In this chapter the preloads in the pad and ballast caused by a single wheel load are studied by considering the non-linear properties of the foundation. The preloaded pad and ballast stiffnesses are determined and then they are included in the track model. Using such a model its vertical vibration behaviour under the influence of the local wheel load is investigated.

Chapter 5 deals with random parameters of the track foundation. The concept of the random sleeper spacing and ballast stiffness is introduced into the track model and their distributions are assumed. The effects on the track vibration of these random parameters is investigated from a statistical point of view.

In chapter 6 the effects on the rail vibration of multiple wheel/rail interactions are explored. Firstly the receptance of a rail with a single additional wheel on it is studied to acquire a physical insight into the effects of wheels on a rail. Then more complicated models are developed and used to investigate the effects of multiple wheels on a rail. Useful conclusions are obtained through calculations and through comparison and analysis of the rail vibration with and without consideration of additional wheel/rail interactions. Some measurement results of the multiple wheel/rail interactions are also presented.

In chapter 7 the influences on track vibration of multiple wheel loads combined with multiple wheel/rail interactions are studied based on the investigations in chapter 4 and chapter 6.

An application example for vertical track vibration is presented in chapter 8. In this example the double Timoshenko beam model developed in chapter 2 is employed. Other factors such as the non-linearity of the pad and ballast, multiple wheel loads and wheel/rail interactions are included in the model. The vibration and noise radiation of the railway track are predicted based on the whole train/track interactions. Results from different track models are compared.

Ultimately one could attempt to combine the various models and effects studied into an ever more complex model of wheel/rail interaction and noise. However, the purpose is not to introduce complexity for its own sake, but to study the necessity of including each effect, and to quantify the error which would be introduced by its omission. The thesis concludes with an assessment of these factors.

In the last chapter, chapter 9, the conclusions in the corresponding chapters are summarised to show the more important among them.

CHAPTER 2

Double Timoshenko Beam Model for Vertical Vibration

In this chapter a double Timoshenko beam model is developed for vertical vibration analysis of a rail at high frequencies. Although simple, this model includes the essential cross-sectional deformation of a rail in the vertical vibration for frequencies up to at least 6 kHz. Based on this model, the dispersion relation of propagating waves in a free and a continuously supported rail is studied. Vertical vibration receptances of the rail are calculated using both continuously and discretely supported models. The results show good agreement with an FE model and measurement data in terms of frequency-wavenumber curves, point receptance and vibration decay rate.

2.1. Introduction

Models of the dynamic behaviour of track are required, amongst other things, for predicting the noise emitted as a train passes. For such applications, frequencies up to at least 5 kHz have to be considered [76]. It is more difficult to study the dynamic behaviour of railway track at high frequencies than at low frequencies because the cross-sectional deformation of the rail appears in high frequency vibration. Simple beam models used by Grassie [16] and Heckl [26] can not represent the cross-sectional deformation and thus are not appropriate to investigate high frequency vibration of railway track. Therefore, more comprehensive models that allow the rail cross-sectional deformation are needed. Such models in the literature are usually based on the finite element method (FEM) and thus need to be treated numerically.

Among these models there are three typical ways to deal with an infinite rail. The first method is to consider a piece of rail up to about one metre long and mesh this length of rail with different elements (beam and plate elements or solid elements), applying symmetric and/or antisymmetric boundary conditions at both ends in order to simulate the waves in an infinite rail. Thompson [79] obtained the dispersion relation of the waves in an infinite rail using this method. The second method is also to deal with a length of meshed rail based on periodic structure theory (PST, see Mead [43, 44, 45]) which allows an infinite structure of constant cross-section, such as the rail, to be considered as a periodic structure of arbitrary period. Knothe et al. [41] obtained the wavenumber-frequency relation of a free rail through this method, with different element meshing models. Thompson [79] predicted wavenumbers and receptances in a continuously supported rail using a PST model. The third method is by meshing only the cross-sectional area of the rail instead of meshing the whole rail in three dimensions, while along the rail the wave propagation factor $e^{i(\omega t-kz)}$ is introduced. The nodal displacements on the cross-sectional area can be either 2D (only displacements in plane) or 3D (including cross-sectional warping and longitudinal displacement). Gavric [15] and Gry [25] calculated the frequency-wavenumber relation and cross-sectional deformation wave shapes (including cross-sectional warping) using this third method. Furthermore, Gry introduced a span wave co-ordinates method to calculate the point accelerance of the discretely supported rail. Apart from the three typical ways there is also a model from the finite strip method (FSM) which was developed by Strzyzakowski and Ziemanski [73]. In another approach some theoretical models were developed by Scholl [68, 69, 70] to investigate dispersion relations in the rail and allow consideration of rail foot and rail web deformations. Ripke and Knothe [64] developed a beam-plate finite element model for a rail with discrete supports and investigated both the vertical and the lateral vibration behaviour up to 2000 Hz. Nielsen [51] developed a track model composed of two rails which are connected through flexible sleepers. Some finite element track models of finite length were used by Clark [4], Nielsen [51] and Ripke [65].

Most of the models cited above are based on the FEM / FSM or a derivation of the FEM (the third method). They are complicated models and thus numerical treatment is essential. For identifying the wavenumber-frequency relation in a free rail these models are straightforward. However, it is inconvenient to calculate responses of the rail to external excitation using such models, especially when the discrete supports of the rail are taken into account, because a large number of degrees of freedom on the boundaries have to be included. As a result a lot of computation time is required to calculate responses.

This may be improved by using some simplified rail models if such models can properly represent the corresponding cross-sectional deformations. As the vertical and lateral vibration behaviour of a rail are effectively uncoupled from each other due to symmetry and are affected by different properties of the cross-section, it is reasonable to study separately vertical and lateral vibration of a rail by different simplified models. Note however that 'lateral' vibration in this context includes vertical motion of the foot which is antisymmetrical with respect to the centreline. Moreover some coupling of vertical and lateral motions will occur in practice via the sleeper, but this is not considered here, see also Thompson [79]. In this chapter only vertical vibration is taken into account. The lateral vibration of a rail is studied in the next chapter. In principle, a simplified rail model for high frequency vertical vibration should allow the rail foot deformation of the cross-section. Based on this, a double Timoshenko beam model is developed, with one beam representing the rail head and web and another beam representing the rail foot. They are connected by an elastic component. At low frequencies the two beams vibrate together in the same way as a single Timoshenko beam, whereas at high frequencies a relative motion between the two beams appears, which represents the cross-sectional deformation between the rail head (and web) and foot.

Several aspects of the vertical vibration behaviour of railway track are investigated using the double beam model. Firstly, the dispersion relation of waves in a free and a continuously supported rail is explored, and then the point receptances of a continuously supported rail are studied. Lastly, the corresponding analysis of the point receptances is carried out but for a discretely supported rail. Comparison with an FE model shows good agreement in terms of the frequency-wavenumber relation. Compared with measurement data good agreement is reached in terms of both point receptance and vibration decay.

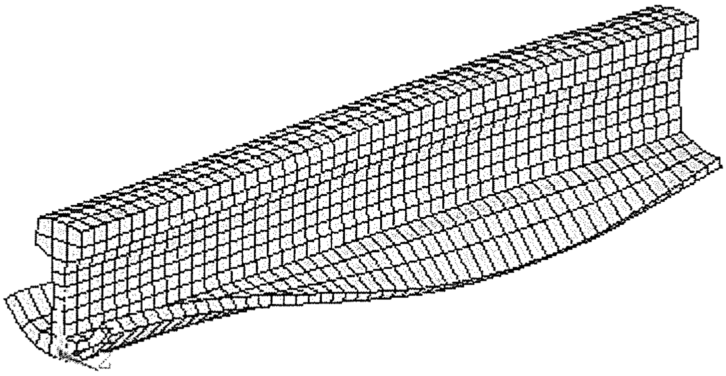

Figure 2.1. Deformation of UIC 60 rail vertical vibration at 5125 Hz (boundary conditions imply this is part of an infinite rail).

2.2. Double beam model of rail

The essential cross-sectional deformation of vertical vibration of a rail at high frequencies consists of foot flapping [79] (foot bending as a cantilever), see Figure 2.1. A simplified rail model for high frequency vertical vibration should allow this type of cross-sectional deformation. The double beam model is schematically shown in Figure 2.2. The rail is divided into two parts: the upper part representing the head (and web), the lower part representing the foot. Although the foot has two branches, they may be combined together due to symmetry. Both the head and the foot are represented by infinite Timoshenko beams in the rail axis direction. These two beams are connected by continuously distributed springs to allow relative

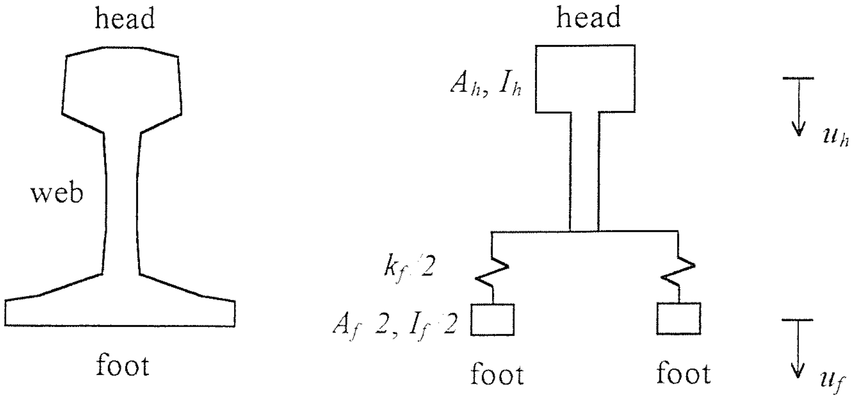

Figure 2.2. Cross-section of the double beam model of rail.

motion between them, which represents the foot flapping. In fact the rail foot cross-section may be regarded as a cantilever beam. If considering the first order vibration mode only, this cantilever beam can be simplified to a single degree of freedom (SDOF) system. The cross-section of the double beam model is just an SDOF system (rigid body motion excluded), thus the cross-sectional deformation—foot flapping can be represented by this model. It remains to be shown whether appropriate parameters can be found which allow this model to represent a rail across the required frequency range.

The material properties of the model are represented by E, the Young's modulus, G, the shear modulus and ρ, the density. The geometric properties of each cross-section are characterised by A, the cross-sectional area, I, the area moment of inertia and κ, the shear coefficient. The subscripts h and f are used to represent the rail head and foot respectively. k_f represents the equivalent stiffness (per unit length) for foot flapping. Applying Newton's second law of motion to the upper Timoshenko beam (the rail head and web) gives

$$\rho A_h \ddot{u}_h + GA_h \kappa_h (\Phi_h' - u_h'') + k_f (u_h - u_f) = 0 \tag{2.1}$$

$$\rho I_h \ddot{\Phi}_h + GA_h \kappa_h (\Phi_h - u_h') - EI_h \Phi_h'' = 0 \tag{2.2}$$

where u represents the transverse (vertical) motion of the beams, Φ the rotation of the cross-sections and $'$ indicates the derivative with respect to z. Similar equations can be written for the lower Timoshenko beam (the rail foot). Combining these equations gives

$$\mathbf{M}\ddot{\mathbf{q}} - \mathbf{D}\mathbf{q}'' - \mathbf{G}\mathbf{q}' + \mathbf{K}_{\mathrm{R}}\mathbf{q} = \mathbf{0} \tag{2.3}$$

where

$$\mathbf{M} = \rho \begin{bmatrix} A_h & & & \\ & I_h & & \\ & & A_f & \\ & & & I_f \end{bmatrix} \tag{2.4}$$

$$\mathbf{D} = \begin{bmatrix} GA_h\kappa_h & & & \\ & EI_h & & \\ & & GA_f\kappa_f & \\ & & & EI_f \end{bmatrix} \tag{2.5}$$

$$\mathbf{G}=\begin{bmatrix} 0 & -GA_h\kappa_h & & \\ GA_h\kappa_h & 0 & & \\ & & 0 & -GA_f\kappa_f \\ & & GA_f\kappa_f & 0 \end{bmatrix} \tag{2.6}$$

$$\mathbf{K}_{\mathrm{R}}=\begin{bmatrix} k_f & 0 & -k_f & 0 \\ 0 & GA_h\kappa_h & 0 & 0 \\ -k_f & 0 & k_f & 0 \\ 0 & 0 & 0 & GA_f\kappa_f \end{bmatrix} \tag{2.7}$$

$$\mathbf{q}=\begin{pmatrix} q_1 & q_2 & q_3 & q_4 \end{pmatrix}^T=\begin{pmatrix} u_h & \Phi_h & u_f & \Phi_f \end{pmatrix}^T \tag{2.8}$$

To use the double beam model an important aspect is to determine the cross-sectional parameters. The foot area, A_f, is an equivalent value related to the first order frequency of foot flapping (cantilever beam bending, from the view of the cross-section). The equivalent mass of a uniform cantilever beam at its free end in its first bending mode of vibration is equal to $(33/140)m$, which can be obtained by making the kinetic energy of the equivalent mass equal to the vibration energy of the cantilever beam, assuming the static deflection of the beam as its first vibration mode. Here m is the mass of whole cantilever beam. The rail foot corresponds to approximately one third of the rail cross-sectional area. Thus A_f is roughly equal to $0.08A_r$, where A_r represents the rail cross-section area. The equivalent stiffness k_f is determined according to the foot flapping cut-on frequency. This frequency can be found by using a two-dimensional FE model of the cross-section. This is much

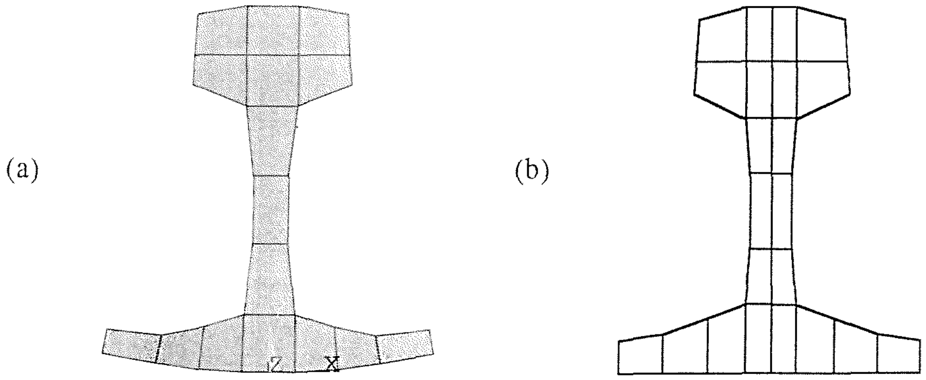

Figure 2.3. (a) 2-D FE model of rail cross-section and the mode at foot flapping cut-on frequency 5562 Hz, (b) FE mesh of cross-section of UIC 60 rail (3-D FE model).

simpler than the FE models for the whole rail considered in [15, 25, 41, 64, 73, 79]. The 2-D FE model for UIC 60 rail cross-section and the mode at the foot flapping cut-on frequency are shown in Figure 2.3(a). This frequency can also be determined by an experimental approach. The foot area moment of inertia, I_f, is taken with respect to the local neutral axis of the foot cross-section, so it is small and thus the head area moment of inertia, I_h, is approximately equal to that of the whole rail cross-sectional area. The head area, A_h, is equal to $A_r - A_f$. UIC 60 rail is chosen as an example. According to the principles listed above, the following parameters have been derived for use in calculations:

$E = 2.1\times10^{11}$ N/m^2 $\quad G = 0.77\times10^{11}$ N/m^2 $\quad \rho = 7850$ kg/m^3

$A_h = 7.09\times10^{-3}$ m^2 $\quad I_h = 30.40\times10^{-6}$ m^4 $\quad \kappa_h = 0.45$

$A_f = 0.60\times10^{-3}$ m^2 $\quad I_f = 0.118\times10^{-6}$ m^4 $\quad \kappa_f = 0.85$

$k_f = 5.33\times 10^9$ N/m^2

A_f and k_f correspond to a foot flapping cut-on frequency of about 5600 Hz.

2.3. Propagating waves in free rail

2.3.1. *Equation of dispersion relation*

Assuming the displacement vector **q** has the form of

$$\mathbf{q} = \mathbf{q}(z)e^{i\omega t}, \quad \text{where } \mathbf{q}(z) = \begin{pmatrix} u_h(z) & \Phi_h(z) & u_f(z) & \Phi_f(z) \end{pmatrix}^T \qquad (2.9, 2.10)$$

and substituting (2.9) into equation (2.3) and taking derivatives with respect to time only, results in

$$\mathbf{D}\mathbf{q}''(z) + \mathbf{G}\mathbf{q}'(z) + (\omega^2\mathbf{M} - \mathbf{K}_\mathrm{R})\mathbf{q}(z) = \mathbf{0} \qquad (2.11)$$

Taking $\mathbf{q}(z) = \mathbf{Q}e^{-ikz}$ (**Q** is the amplitude vector) and substituting it into (2.11) gives

$$[-k^2\mathbf{D} - ik\mathbf{G} + (\omega^2\mathbf{M} - \mathbf{K}_\mathrm{R})]\mathbf{Q} = 0 \qquad (2.12)$$

This is a quadratic eigenvalue problem. Since the matrices are of dimension 4 × 4, there are eight solutions for k at each frequency ω, four of which apply to each direction. The solutions for wavenumber k at a given frequency ω are usually complex and have the form of $k = \pm(a \pm ib)$, where a and b are positive real. They appear in opposite pairs when k is purely real or purely imaginary or in double pairs when k is complex. The imaginary part b represents the wave decay. When $b = 0$, the wave is propagating. The eigenvector $\mathbf{Q}$ represents the wave shapes and it is also complex. When $k = 0$, equation (2.12) becomes

$$(\omega^2\mathbf{M} - \mathbf{K}_R)\mathbf{Q} = \mathbf{0} \tag{2.13}$$

Then the cut-on frequencies can be obtained from (2.13). At a cut-on frequency each cross-section in the rail vibrates in phase over the whole length.

To solve the quadratic eigenvalue problem, it is appropriate to convert equation (2.11) into the state space form. Taking

$$\mathbf{X} = \begin{bmatrix} \mathbf{q}(z) \\ \mathbf{q}'(z) \end{bmatrix}, \quad \mathbf{A} = \begin{bmatrix} \mathbf{0} & \mathbf{I} \\ -\mathbf{D}^{-1}(\omega^2\mathbf{M} - \mathbf{K}_R) & -\mathbf{D}^{-1}\mathbf{G} \end{bmatrix} \tag{2.14, 2.15}$$

equation (2.11) can be written in the state space form:

$$\mathbf{X}' = \mathbf{A}\mathbf{X} \tag{2.16}$$

This leads to a normal eigenvalue problem

$$\det(\lambda\mathbf{I} - \mathbf{A}) = 0 \tag{2.17}$$

where $\lambda = -ik$. From equation (2.17) the dispersion relation of propagating waves in the rail can be determined.

2.3.2. *Waves in a free rail*

To validate the double beam model a 3-D FE model representing UIC 60 rail is used. The FE mesh of the rail cross-section is shown in Figure 2.3(b). It is a short length of rail (1 m) with symmetric or antisymmetric boundary conditions at the ends to simulate the waves in an infinite rail. Calculations are carried out using ANSYS with 3-D linear solid elements. The results from the double beam model and FE model are shown in Figure 2.4. Two waves are extracted from the FE model for comparison, whereas three propagating waves are predicted by the simplified model in the frequency region studied. In fact there are four waves in each direction according to equation (2.12), but one of them, the cross-sectional rotation of the first beam, only becomes propagating at very high frequencies (above 32 kHz). Wave I represents vertical bending at low wavenumbers, but also involves foot flapping at high wavenumbers. Wave II is characterised by foot flapping. In the double beam model this wave starts at a lower frequency and initially features cross-

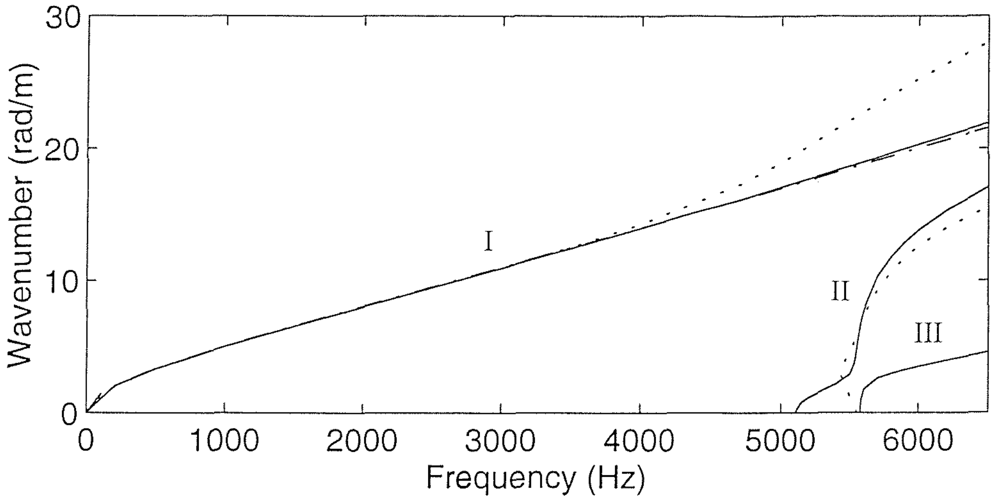

Figure 2.4. Dispersion relation of waves in a free rail for vertical vibration. — from the double beam model, ······ from the 3-D FE model, -·-·- from the single Timoshenko beam model.

sectional rotation of the second Timoshenko beam representing the foot. Wave III starts as foot flapping and then transfers to the cross-sectional rotation of the second beam. A significant deviation for wave I between the simplified model and FE model can be seen starting at about 5000 Hz. This is not critical, however, because the foot flapping characteristic wave becomes dominant in the response of the rail above this frequency. Thus the simplified model is expected to give satisfactory results in later calculations. For comparison, the result from a single Timoshenko beam model is also included in Figure 2.4. The wavenumber in the single Timoshenko beam can be seen to be very close to the wave I of the double beam model, but in the single Timoshenko beam model the whole cross-section of a rail vibrates in the same way and there is no cross-sectional deformation at all.

2.4. Continuously supported rail model

Although a realistic rail is discretely supported by pads and sleepers, a continuously supported rail model can be used to explore the basic dynamic properties of a railway track without involving the complication of the periodic support. In this section a continuously supported rail model is employed to calculate the dispersion relation of waves in the rail and the receptances of the rail. The pad, sleeper and the ballast are represented by equivalent continuous layers of mass and stiffness. The parameters of these layers and the rail are the same as in the previous sections.

2.4.1. *Waves in continuously supported rail*

The continuously supported rail model is schematically shown in Figure 2.5, where the pad stiffness k_p is split into two components: $k_p = k_{p1} + k_{p2}$, with k_{p1} acting beneath the centre of the rail and k_{p2} beneath the foot, and taking $k_{p1} = k_{p2}$. The rotational stiffness of the pad is omitted because its effects on track vibration are very limited, see Appendix A. m_s and k_b represent sleeper mass and ballast stiffness respectively. In the rest of the chapter, it will be assumed that forces and responses are harmonic, so the $e^{i\omega t}$ term will usually be omitted. The equation of motion for the continuously supported rail is

$$-\mathbf{D}\mathbf{q}''(z) - \mathbf{G}\mathbf{q}'(z) - (\omega^2\mathbf{M} - \mathbf{K}_\mathrm{R})\mathbf{q}(z) = \begin{pmatrix}-k_{p1}(u_h - u_s) & 0 & -k_{p2}(u_f - u_s) & 0\end{pmatrix}^T \tag{2.18a}$$

and for the sleeper

$$-m_s\omega^2 u_s = -k_{p1}(u_s - u_h) - k_{p2}(u_s - u_f) - k_b u_s \tag{2.18b}$$

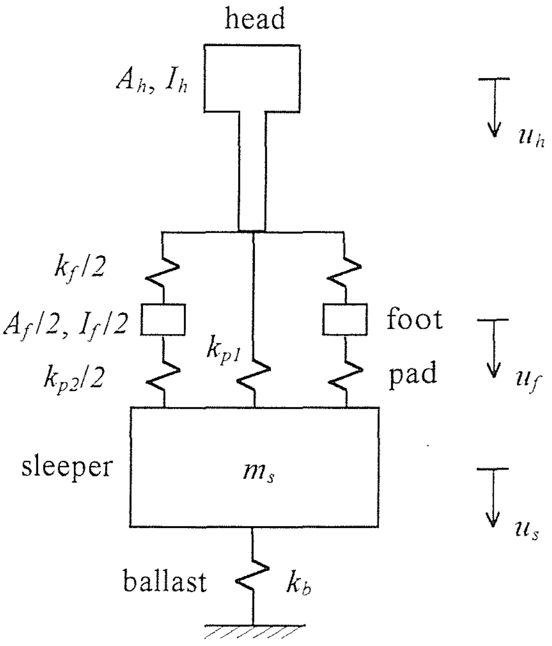

Figure 2.5. Cross-section of continuously supported rail.

From (2.18b) u_s can be written as follows:

$$u_s = \frac{k_{p1}u_h + k_{p2}u_f}{k_p + k_b - m_s\omega^2} \tag{2.19}$$

Substituting (2.19) into (2.18a) gives

$$-\mathbf{D}\mathbf{q}''(z) - \mathbf{G}\mathbf{q}'(z) - (\omega^2\mathbf{M} - \mathbf{K}_{\mathrm{R}})\mathbf{q}(z) = \begin{pmatrix}-Z_{11}u_h - Z_{13}u_f & 0 & -Z_{31}u_h - Z_{33}u_f & 0\end{pmatrix}^T \tag{2.20}$$

where Z_{11}, Z_{13}, Z_{31} and Z_{33} are the dynamic stiffnesses of the continuous foundation:

$$Z_{11} = \frac{k_{p1}(k_{p2} + k_b - m_s\omega^2)}{k_p + k_b - m_s\omega^2} \tag{2.21a}$$

$$Z_{33} = \frac{k_{p2}(k_{p1} + k_b - m_s\omega^2)}{k_p + k_b - m_s\omega^2} \tag{2.21b}$$

$$Z_{13} = Z_{31} = -\frac{k_{p1}k_{p2}}{k_p + k_b - m_s\omega^2} \tag{2.21c}$$

Thus equation (2.18) can be simplified to

$$\mathbf{D}\mathbf{q}''(z) + \mathbf{G}\mathbf{q}'(z) + (\omega^2\mathbf{M} - \mathbf{K})\mathbf{q}(z) = \mathbf{0} \tag{2.22}$$

where

$$\mathbf{K} = \mathbf{K}_{\mathrm{R}} + \begin{bmatrix} Z_{11} & 0 & Z_{13} & 0 \\ 0 & 0 & 0 & 0 \\ Z_{31} & 0 & Z_{33} & 0 \\ 0 & 0 & 0 & 0 \end{bmatrix} \tag{2.23}$$

To calculate the frequency-wavenumber relation in a supported rail, the following parameters of the track foundation are used which are based on values from [95] for track C (a monobloc concrete sleepered track with 'medium' stiffness pads):

$k_p = 583.3$ MN/m^2 $k_b = 83.3$ MN/m^2 $m_s = 270$ kg/m

The frequency-wavenumber relation in the supported rail can be seen from Figure 2.6 to be almost the same as in the free rail except wave I at low frequencies. There is a branch for this vertical bending wave I at about 80 – 250 Hz. In this frequency region the rail vibration is coupled with the foundation mass. In the higher frequency region the wavenumber-frequency relation of waves I, II and III are the same as in the free rail.

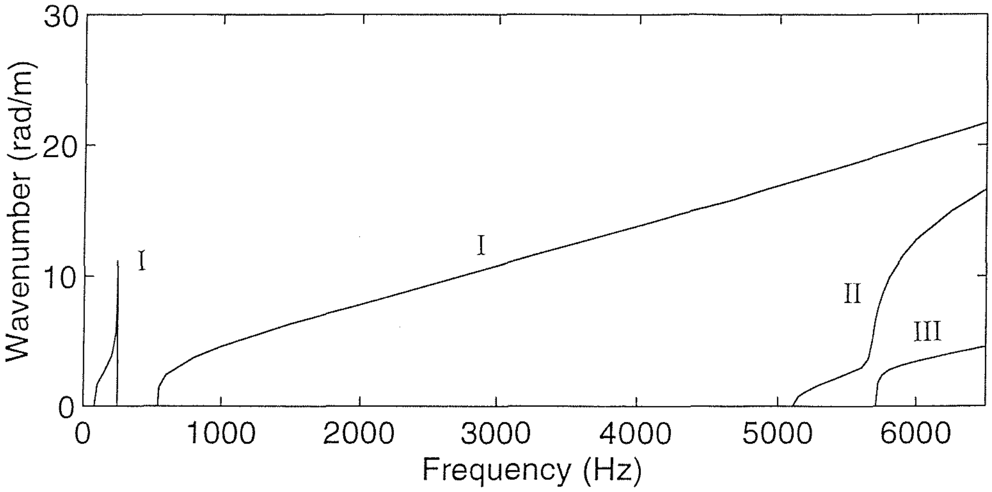

Figure 2.6. Dispersion relation of waves in a continuously supported rail without damping for vertical vibration.

For a realistic railway track, damping should be taken into consideration. It can be added by means of a loss factor to the pad and ballast stiffnesses to make them complex in the form of $K(1+i\eta)$. This approach is used by Thompson et al. [85, 95] and found to give good agreement with measurement data [88, 89]. Here $\eta_p = 0.25$ and $\eta_b = 1.0$ are taken for the pad and ballast respectively as in [95]. No damping is added to the rail at this stage. Damping will make the wavenumber k always complex with the form of $k = \pm(a \pm ib)$, and thus waves with exponential decay. The decay rate Δ (in dB/m) of various waves is determined by their imaginary part of k and can be calculated using

$$\Delta = 20\log_{10}(e^{b}) = 8.686b \tag{2.24}$$

The frequency-wavenumber relation in a supported rail with damping is shown in Figure 2.7 where the solid lines represent the real part of the wavenumber and the dotted lines the imaginary part. The curves of the real part can be seen to be similar to the case of no damping, apart from near the cut-on frequencies. The wave of cross-sectional rotation of the foot forms a single curve in Figure 2.7, whereas in Figure 2.6 this wave is separated in waves II and III. The imaginary parts can be seen to be higher near the cut-on frequencies and much lower thereafter. The decay rates of various waves in Figure 2.8 show this more noticeably. They can be seen to decrease dramatically after the cut-on frequencies.

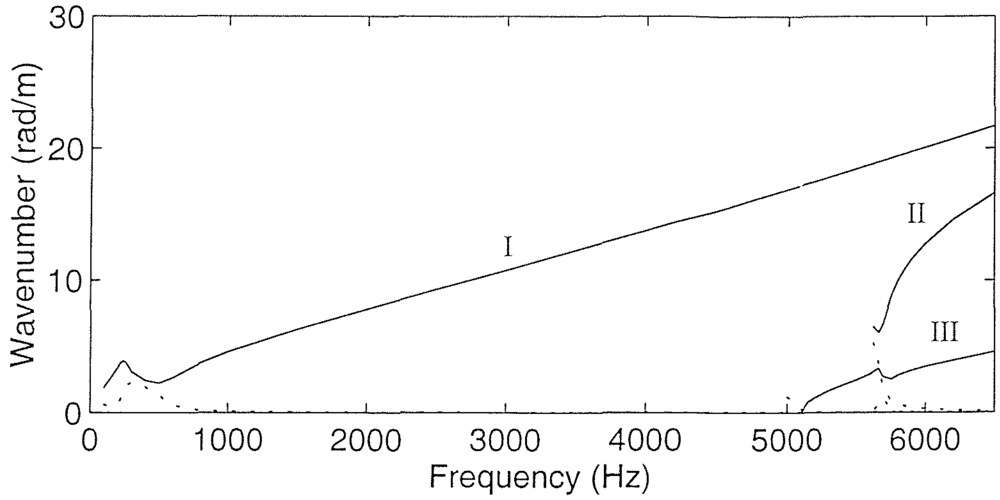

Figure 2.7. Dispersion relation of waves in a continuously supported rail with damping for vertical vibration. — real part of the wavenumber, ······ imaginary part of the wavenumber.

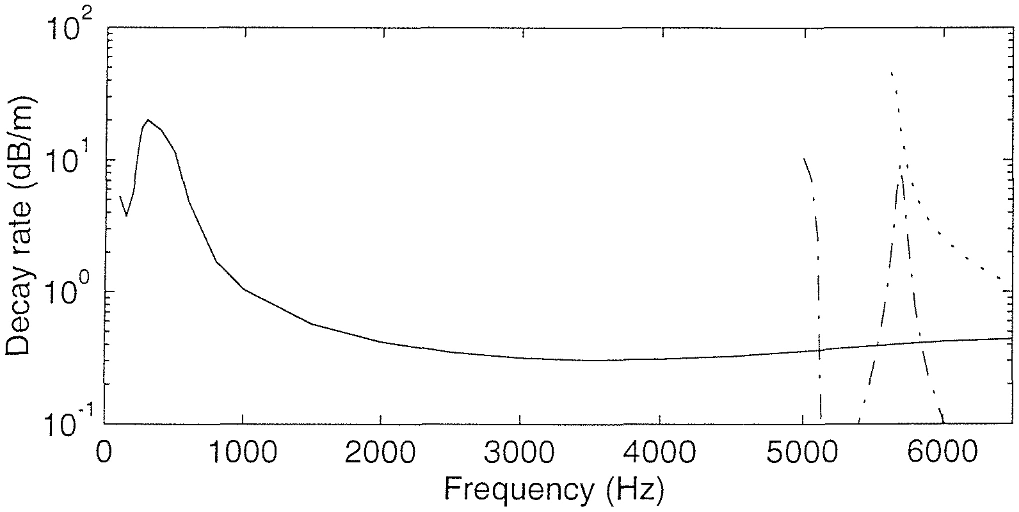

Figure 2.8. Decay rates of different waves in a continuously supported rail. — wave I, ······ wave II, -·-·- wave III.

2.4.2. *Receptances*

Supposing a harmonic external force $Fe^{i\omega t}$ acting on the rail head at z = 0, the equation of motion is given as follows:

$$-\mathbf{D}\mathbf{q}''(z)-\mathbf{G}\mathbf{q}'(z)-(\omega^2\mathbf{M}-\mathbf{K})\mathbf{q}(z)=\begin{pmatrix}F\delta(z) & 0 & 0 & 0\end{pmatrix}^T \tag{2.25}$$

Equation (2.25) can be written in the state space form:

$$\mathbf{X}'=\mathbf{A}\mathbf{X}+\mathbf{P}\delta(z) \tag{2.26}$$

where **A** has the same form as in equation (2.15) but $\mathbf{K}_R$ is replaced by **K** which is the sum of rail stiffness matrix $\mathbf{K}_R$ and foundation dynamic stiffness matrix, see equation (2.23), and

$$\mathbf{P} = [\ \mathbf{0}\ \ -\mathbf{D}^{-1}\mathbf{F}]^{\mathrm{T}} \tag{2.27a}$$

$$\mathbf{F} = \begin{pmatrix} F & 0 & 0 & 0 \end{pmatrix}^{\mathrm{T}} \tag{2.27b}$$

Taking the Laplace transform of equation (2.26) gives

$$(s\mathbf{I} - \mathbf{A})\mathbf{X}(s) = \mathbf{P} \tag{2.28}$$

According to Cramer's rule the Laplace transform of the rail head and foot displacements, respectively, has the form of

$$U_h(s) = \frac{\Delta_1(s)}{\Delta(s)}, \qquad U_f(s) = \frac{\Delta_3(s)}{\Delta(s)} \tag{2.29, 2.30}$$

where, $\Delta(s)$ is the determinant of matrix $s\mathbf{I} - \mathbf{A}$. $\Delta_1(s)$ and $\Delta_3(s)$ are the determinants of the matrices which are obtained from $s\mathbf{I} - \mathbf{A}$ by replacing its first column and third column by **P** respectively. The vertical responses of the rail head and foot are found by performing the Laplace inverse transform using contour integration:

$$u_h(z) = \frac{1}{2\pi i}\int_{\gamma - i\infty}^{\gamma + i\infty} U_h(s)e^{sz}ds = \sum_{\substack{k \text{ with } \mathrm{Re}(s_k)<0 \text{ or} \\ \mathrm{Im}(s_k)<0 \text{ if } \mathrm{Re}(s_k)=0}} \mathrm{Res}[\mathrm{U}_h(s_k)e^{s_k z}] \qquad z > 0 \tag{2.31}$$

$$u_f(z) = \frac{1}{2\pi i}\int_{\gamma - i\infty}^{\gamma + i\infty} U_f(s)e^{sz}ds = \sum_{\substack{k \text{ with } \mathrm{Re}(s_k)<0 \text{ or} \\ \mathrm{Im}(s_k)<0 \text{ if } \mathrm{Re}(s_k)=0}} \mathrm{Res}[\mathrm{U}_f(s_k)e^{s_k z}] \qquad z > 0 \tag{2.32}$$

where the residues at the poles s_k are given by

$$\mathrm{Res}[\mathrm{U}_h(s_k)e^{s_k z}] = \frac{\Delta_1(s_k)}{\Delta'(s_k)}e^{s_k z} \tag{2.33}$$

$$\mathrm{Res}[\mathrm{U}_f(s_k)e^{s_k z}] = \frac{\Delta_3(s_k)}{\Delta'(s_k)}e^{s_k z} \tag{2.34}$$

The responses of the rail head and foot at $z = 0$ to a unit harmonic excitation at the same point are shown in Figure 2.9 in terms of amplitude and phase. Three resonance peaks can be seen at about 80 Hz, 520 Hz and 5600 Hz. At 80 Hz the whole track bounces on the vertical stiffness of the ballast, while at 520 Hz the rail vibrates on the pad stiffness. These two peaks can be regarded as the cut-on of the

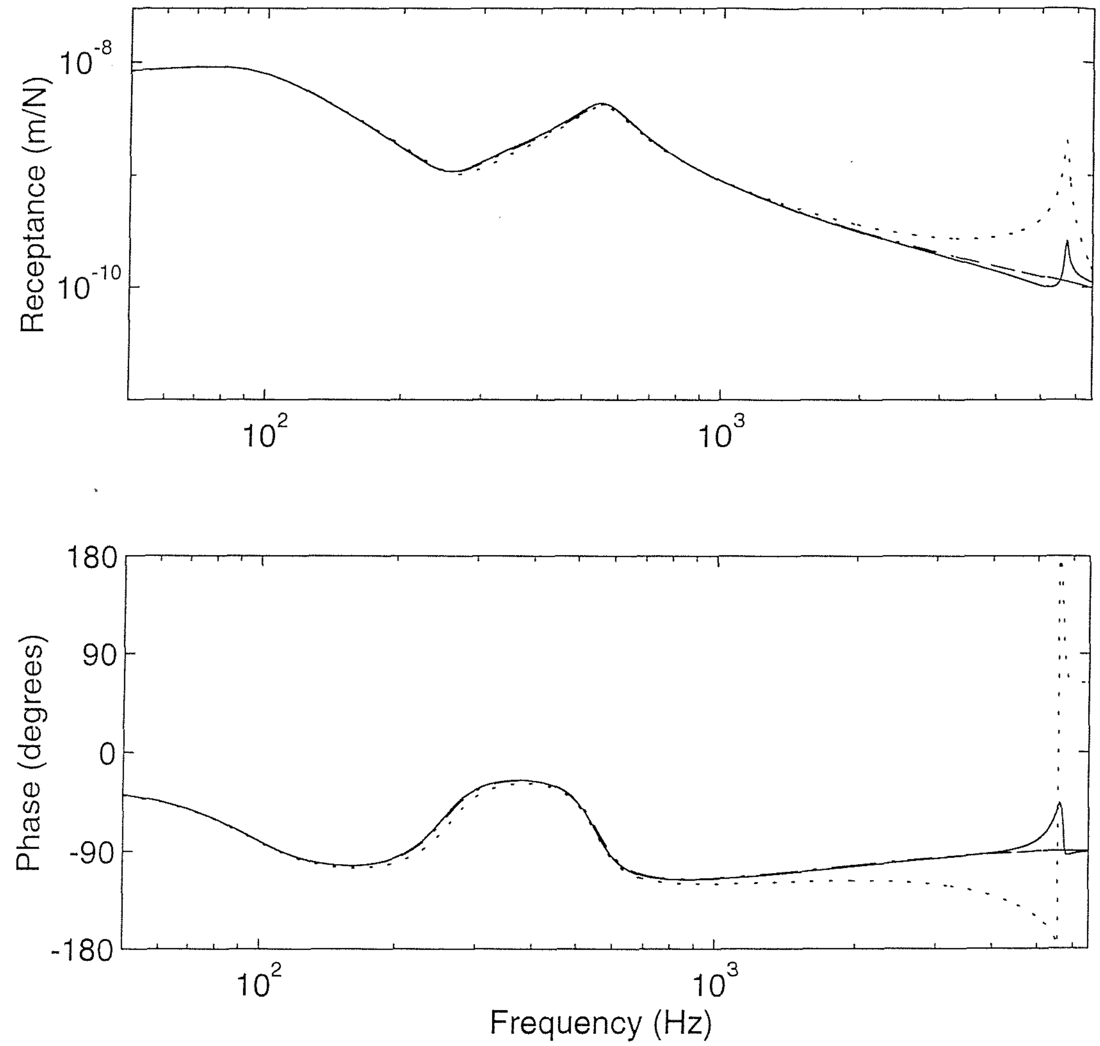

Figure 2.9. Amplitude and phase of the point receptance (head response) and foot response of the continuously supported rail for vertical vibration. — head response, ······ foot response, ----- point receptance of the single Timoshenko beam model.

vertical bending wave (two branches, see Figure 2.6), and the peak at 5600 Hz is due to the cut-on of the foot flapping. The foot response can be observed to be very similar to the head response below 2000 Hz, whereas at high frequencies it is much higher than the head response, up to a factor 10. At the peak area near the foot flapping cut-on frequency the foot response can be seen to be very sharp and out of phase with the head. Comparing all these results with those in [79], which are redrawn in Figure 2.10 and show the same trends from a more complex model but with different parameters, one can see that the vertical vibration properties of a rail at high frequencies are very well predicted using the double Timoshenko beam

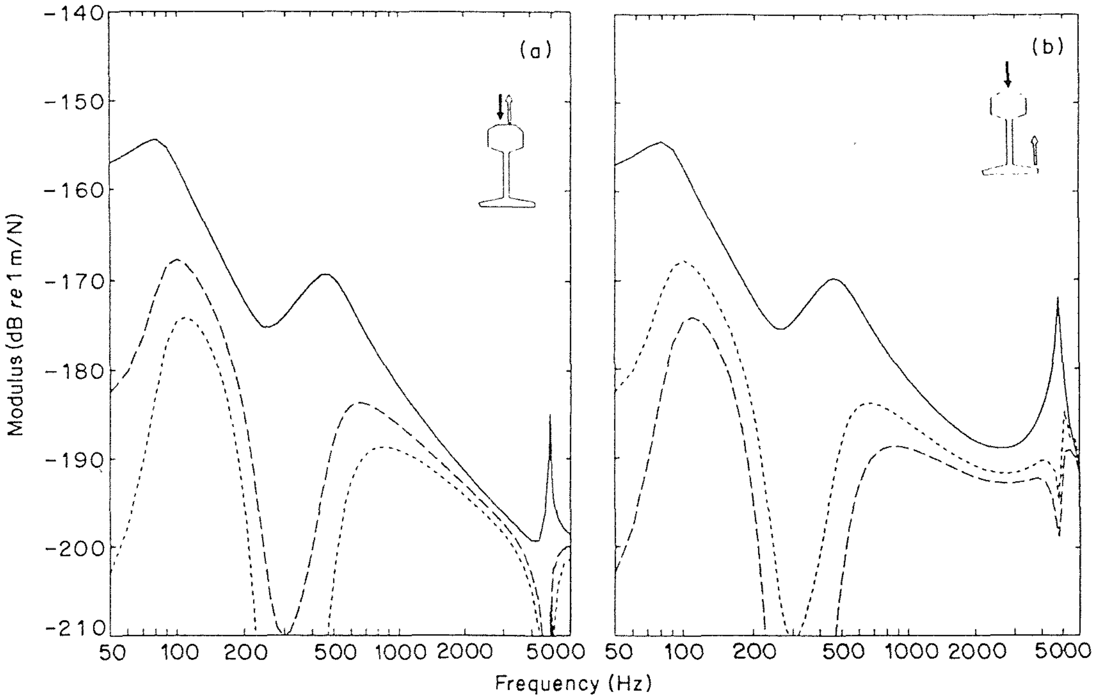

Figure 2.10. Predicted vertical responses (receptances, from [79]) of continuously supported rail, (a) at rail head, (b) at rail foot. — (a) at excitation point, (b) at opposite excitation point, ····· (a) at 4.8 m, (b) at 2.4 m, - - - (a) at 2.4 m, (b) at 4.8 m.

model. The result from a single Timoshenko beam model is also shown in Figure 2.9. The point receptance of the single beam model can be seen to be almost the same as the head response of the double beam model except for the peak at the foot flapping cut-on frequency. Therefore, a conventional beam model may be used for vertical vibration very well up to about 2000 Hz, but above this up to about 5000 Hz such a model may only be used for predicting the head response because at high frequencies the deviation between the head and foot response becomes more and more significant. Moreover, the decay rate of the vertical bending wave can be seen in Figure 2.8 to stabilise around 0.4 dB/m whereas the result for a single Timoshenko beam continues to fall at high frequencies (refer to Figure 2.15). The higher decay rate found with the double beam model, which corresponds qualitatively to that found in [79], is due to the higher amplitudes of vibration on the foot acting on the rail pad.

2.5. Discretely supported rail model

A more realistic model for railway track should be an infinite rail with periodic supports. Such a model will introduce the complication of the periodic support nature and thus difficulties in dealing with it, but some important characteristics, for example, pinned-pinned resonances can only be obtained using a discretely supported model. In this section the complication of the discretely supported model is addressed using Green's function and the superposition principle.

2.5.1. *Equation of motion*

An infinite periodically supported rail model is shown in Figure 2.11. The supports are characterised by pad stiffnesses, K_{pn}, sleeper mass, M_s and ballast stiffness, K_{bn}. The pad stiffness K_{pn} is also split into two components as in the continuously supported model: $K_{pn} = K_{pn1} + K_{pn2}$, with K_{pn1} acting beneath the centre of the rail and K_{pn2} beneath the foot, and taking $K_{pn1} = K_{pn2}$. Damping is considered by introducing loss factors η_r into the Young's modulus E and shear modulus G of the rail and the equivalent stiffness k_f of foot flapping, η_p into the pad stiffnesses K_{pn}, η_b into the ballast stiffness K_{bn}, and making E, G, k_f, K_{pn}, and K_{bn} complex with the appropriate factor $(1+i\eta)$. In fact the rail damping is very small, usually less than 0.0001. The main reason for adding extra damping to the rail is to suppress the pinned-pinned resonance peaks on which the track foundation damping has very little effect. In reality, the pinned-pinned resonance peaks are not as sharp as in theoretical analysis because of the variable sleeper spacing as shown in chapter 5 and the distributed contact between the rail and pads. In the theoretical model here,

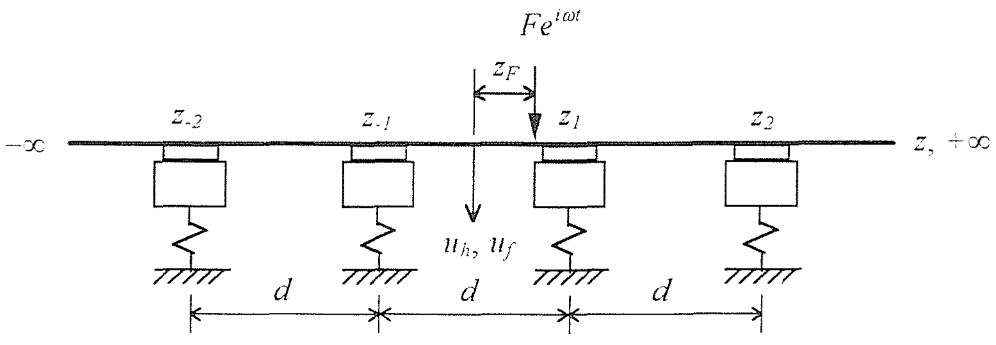

Figure 2.11. Discretely supported rail model.

however, the sleeper spacing is chosen as constant and the rail is assumed as ideally point-supported. Assuming the n-th support is at the position $z = z_n$ and a single external harmonic force $Fe^{i\omega t}$ acts on the rail head at $z = z_F$, the equation of motion of the discretely supported rail is given as

$$-\mathbf{D}\mathbf{q}''(z) - \mathbf{G}\mathbf{q}'(z) - (\omega^2\mathbf{M} - \mathbf{K}_\mathrm{R})\mathbf{q}(z) = \begin{pmatrix} F\delta(z - z_F) + F_1 & 0 & F_3 & 0 \end{pmatrix}^T \tag{2.35}$$

where

$$F_1 = -\sum_{\substack{n=-\infty \\ n\neq 0}}^{\infty}[Z_{11n}u_h(z_n) + Z_{13n}u_f(z_n)]\delta(z - z_n) \tag{2.36a}$$

$$F_3 = -\sum_{\substack{n=-\infty \\ n\neq 0}}^{\infty}[Z_{31n}u_h(z_n) + Z_{33n}u_f(z_n)]\delta(z - z_n) \tag{2.36b}$$

where Z_{11n}, Z_{13n}, Z_{31n} and Z_{33n} are the dynamic stiffnesses at n-th support:

$$Z_{11n} = \frac{K_{p1n}(K_{p2n} + K_{bn} - M_s\omega^2)}{K_{pn} + K_{bn} - M_s\omega^2} \tag{2.37a}$$

$$Z_{33n} = \frac{K_{p2n}(K_{p1n} + K_{bn} - M_s\omega^2)}{K_{pn} + K_{bn} - M_s\omega^2} \tag{2.37b}$$

$$Z_{13n} = Z_{31n} = -\frac{K_{p1n}K_{p2n}}{K_{pn} + K_{bn} - M_s\omega^2} \tag{2.37c}$$

2.5.2. *Response of the discretely supported rail*

The discretely supported track model can be treated in various ways. One approach is developed by Heckl [28]. In this approach, the discrete rail supports are replaced by corresponding external forces, and thus the railway track can be simply considered as an infinite beam with many point forces acting on it. Based on the Green's function (which is identical to a transfer receptance) and the superposition principle the stationary response of the rail to the harmonic excitation can be obtained. In addition the infinite beam is modelled with a finite number of supports, the number being chosen large enough to guarantee a reliable approximate solution. This approach is also employed here, but now, for the double beam model, Green's function matrices have to be used instead of a single Green's function. Moreover the symmetry of the railway track about the forcing point for excitation above a sleeper or at mid-span is taken into account to increase the efficiency of the calculation.

The Green's function $g_{ij}(z,z')$ is defined as the response at z of the i-th component of the displacement vector $\mathbf{q}(z)$ caused by a unit harmonic force at z' which is the j-th component of the excitation vector $\mathbf{F}$. It can be obtained by applying a similar method as used in section 2.4.2., but now to a free rail instead of the continuously supported rail and with the force and response positions at different values of z.

Using the superposition principle the displacements of the rail head and foot are given by

$$u_h(z) = -\sum_{\substack{n=-N \\ n\neq 0}}^{N} \{[Z_{11n}u_h(z_n) + Z_{13n}u_f(z_n)]g_{11}(z,z_n) + [Z_{31n}u_h(z_n) + Z_{33n}u_f(z_n)]g_{13}(z,z_n)\} + Fg_{11}(z,z_F) \tag{2.38a}$$

$$u_f(z) = -\sum_{\substack{n=-N \\ n\neq 0}}^{N} \{[Z_{11n}u_h(z_n) + Z_{13n}u_f(z_n)]g_{31}(z,z_n) + [Z_{31n}u_h(z_n) + Z_{33n}u_f(z_n)]g_{33}(z,z_n)\} + Fg_{31}(z,z_F) \tag{2.38b}$$

or in matrix form

$$\begin{pmatrix} u_h(z) \\ u_f(z) \end{pmatrix} = -\sum_{\substack{n=-N \\ n\neq 0}}^{N} \begin{bmatrix} Z_{11n}g_{11}(z,z_n) + Z_{31n}g_{13}(z,z_n) & Z_{13n}g_{11}(z,z_n) + Z_{33n}g_{13}(z,z_n) \\ Z_{11n}g_{31}(z,z_n) + Z_{31n}g_{33}(z,z_n) & Z_{13n}g_{31}(z,z_n) + Z_{33n}g_{33}(z,z_n) \end{bmatrix} \begin{pmatrix} u_h(z_n) \\ u_f(z_n) \end{pmatrix} + F\begin{pmatrix} g_{11}(z,z_F) \\ g_{31}(z,z_F) \end{pmatrix} \tag{2.39}$$

Equation (2.39) can be presented in a compact form:

$$\mathbf{u}(z) = -\sum_{\substack{n=-N \\ n\neq 0}}^{N} \mathbf{G}_u(z,z_n)\mathbf{u}(z_n) + F\mathbf{G}_F(z,z_F) \tag{2.40}$$

If $Fe^{i\omega t}$ acts at mid-span ($z = 0$), the following symmetric relationship holds:

$$\mathbf{u}(z) = \mathbf{u}(-z) \tag{2.41a}$$

$$Z_{ijn} = Z_{ij(-n)} \tag{2.41b}$$

$$g_{ij}(z,z') = g_{ij}(-z,-z') \tag{2.41c}$$

Equation (2.40) can be simplified to

$$\mathbf{u}(z) = -\sum_{n=1}^{N}[\mathbf{G}_u(z,z_n) + \mathbf{G}_u(z,-z_n)]\mathbf{u}(z_n) + F\mathbf{G}_F(z,0) \tag{2.42}$$

At each support point $z = z_m$ the displacements of the rail head and foot can be written as follows:

$$\mathbf{u}(z_m) = -\sum_{n=1}^{N}[\mathbf{G}_u(z_m,z_n) + \mathbf{G}_u(z_m,-z_n)]\mathbf{u}(z_n) + F\mathbf{G}_F(z_m,0) \quad m = 1, 2, \cdots, N \tag{2.43}$$

By taking the sum to the left-hand side equation (2.43) can be combined as

$$\mathbf{GU} = \mathbf{F} \tag{2.44}$$

where

$$\mathbf{G} = \begin{bmatrix} \mathbf{G}_{11} & \mathbf{G}_{12} & \cdots & \mathbf{G}_{1N} \\ \mathbf{G}_{21} & \mathbf{G}_{22} & \cdots & \mathbf{G}_{2N} \\ \vdots & & & \\ \mathbf{G}_{N1} & \mathbf{G}_{N2} & \cdots & \mathbf{G}_{NN} \end{bmatrix} + \mathbf{I} \tag{2.45a}$$

where **I** is an identity matrix and

$$\mathbf{G}_{ij} = \mathbf{G}_u(z_i,z_j) + \mathbf{G}_u(z_i,-z_j) \qquad i,j = 1, 2, \ldots, N \tag{2.45b}$$

$$\mathbf{U} = \left(\mathbf{u}^T(z_1) \quad \cdots \quad \mathbf{u}^T(z_N)\right)^T \tag{2.45c}$$

$$\mathbf{F} = F\left(\mathbf{G}_F^T(z_1,0) \quad \cdots \quad \mathbf{G}_F^T(z_N,0)\right)^T \tag{2.45d}$$

From equation (2.44) the displacements of the rail head and foot at each support point can be solved. Substituting them into equation (2.42), displacements of the rail head and foot at any point can be obtained.

For $Fe^{i\omega t}$ acting above a sleeper (this sleeper is now chosen as $n = 0$ and also $z = 0$) the similar equations for the displacements of the rail head and foot can be given as follows:

$$\mathbf{u}(z) = -\mathbf{G}_u(z,0)\mathbf{u}(0) - \sum_{n=1}^{N}[\mathbf{G}_u(z,z_n) + \mathbf{G}_u(z,-z_n)]\mathbf{u}(z_n) + F\mathbf{G}_F(z,0) \tag{2.46}$$

$$\mathbf{u}(z_m) = -\mathbf{G}_u(z_m,0)\mathbf{u}(0) - \sum_{n=1}^{N}[\mathbf{G}_u(z_m,z_n) + \mathbf{G}_u(z_m,-z_n)]\mathbf{u}(z_n) + F\mathbf{G}_F(z_m,0)$$

$$m = 0, 1, 2, \cdots, N \tag{2.47}$$

In a similar way the displacements of the rail head and foot at each support point can be solved from equation (2.47). Substituting them into equation (2.46), displacements of the rail head and foot at any point can be obtained.

2.5.3. *Numerical results*

The point receptance and the foot response at the forcing point are calculated in the frequency range 50 – 6500 Hz for a unit vertical excitation acting at the rail head either above a sleeper or at mid-span. Parameters for each support are identical and chosen as follows (to correspond to those used earlier for the continuous support):

$$K_p = 350 \text{ MN/m} \qquad K_b = 50 \text{ MN/m} \qquad M_s = 162 \text{ kg/m}$$

Other parameters such as loss factors are the same as used in the previous sections. In addition damping is added to the rail with loss factor $\eta_r = 0.01$. As will be seen later this has a beneficial effect on the agreement with measured decay rates. This technique was used by Thompson [85]. The span length (the distance between two sleepers) is chosen as d = 0.6 m, and the number of supports $2N$ = 80 for the excitation acting at mid-span, $2N + 1$ = 81 for the excitation acting above a sleeper.

The amplitude and phase of the point receptance are shown in Figure 2.12, and the corresponding amplitude of the foot response is shown in Figure 2.13. Some characteristic peaks or troughs are marked with numbers from 1 to 9 in Figures 2.12 and 2.13. In general the response at low frequencies up to about 800 Hz can be seen to be similar for the excitation either acting at mid-span or above a sleeper. At low frequencies the responses of the rail head are similar to those of the foot, but at high frequencies the foot responses are higher than the head responses. This observation has also been obtained from the continuously supported model (Figure 2.9). Two peaks at about 80 Hz and 520 Hz marked with 1 and 2 can be identified as the cut-on of the vertical bending wave (including its branch). Another peak at about 5600 Hz marked with 6 is the cut-on of the foot flapping. These three peaks are the same as those from the continuously supported model.

The main pinned-pinned resonance marked with 3 appears at about 1050 Hz. Here the vertical bending wavelength is equal to twice the span length and this corresponds to a wavenumber of 5.2 rad/m in Figure 2.6. The third pinned-pinned resonance marked with 5 appears at about 4600 Hz when the vertical bending wavelength is equal to two thirds of the span length (corresponding to a wavenumber of 15.7 rad/m in Figure 2.6). The pinned-pinned resonances due to the

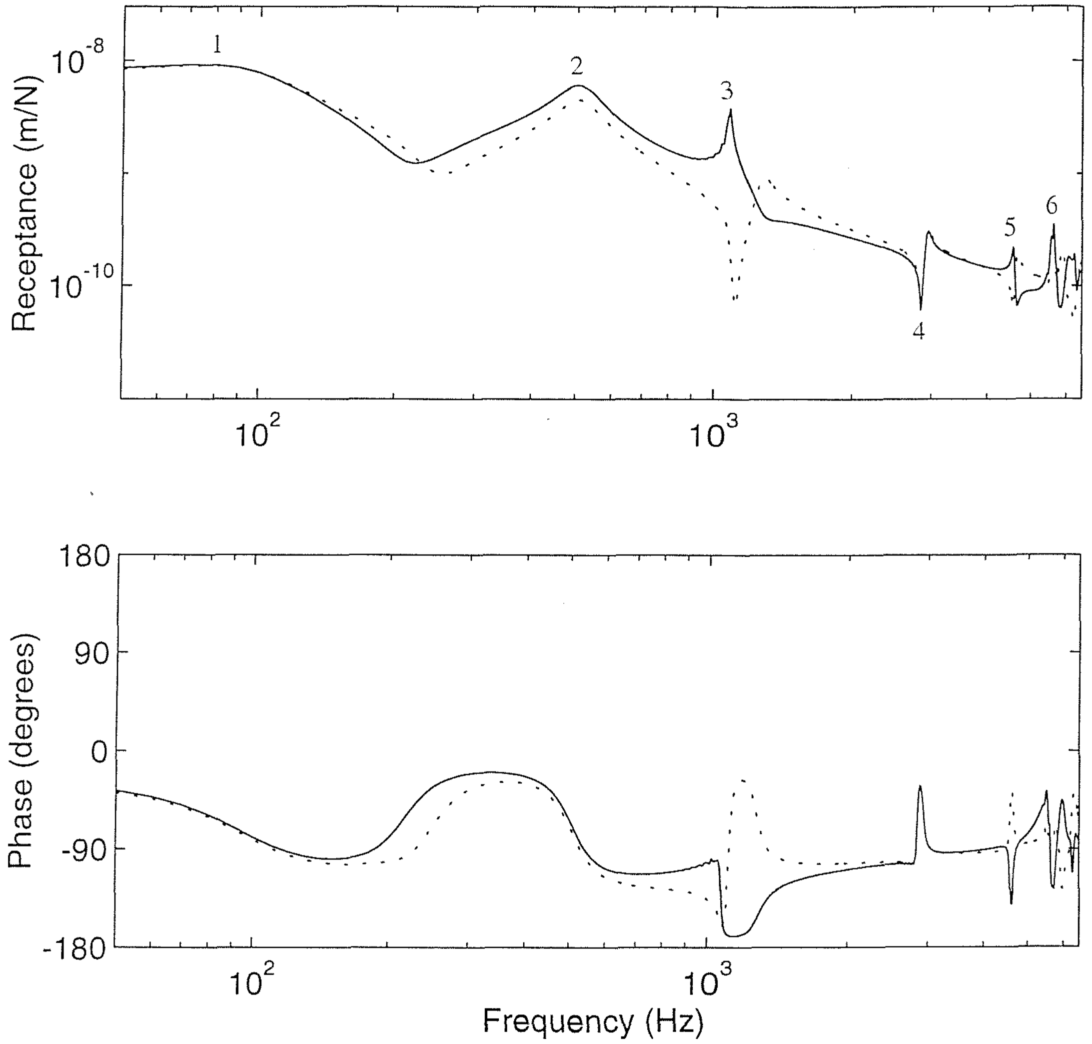

Figure 2.12. Amplitude and phase of the point receptance of the discretely supported rail for vertical vibration. — for excitation acting at mid-span, ······ for excitation acting above a sleeper (for meaning of numbers see text).

foot flapping wave appear at much higher frequencies. They may be observed from the foot response in Figure 2.13, being marked with 7 and 9. When the wavelength is equal to the span length (corresponding to a wavenumber of 10.4 rad/m in Figure 2.6), the second pinned-pinned resonance occurs. However, for excitation at either mid-span or above a sleeper both the point receptances and the foot responses at the forcing point should be minimum. For the vertical bending wave the frequency corresponding to this minimum response is about 2800 Hz, whereas for the foot flapping it is about 5700 Hz. These two troughs are marked with 4 and 8 in Figures 2.12 and 2.13. All these properties related to the span length can only be observed

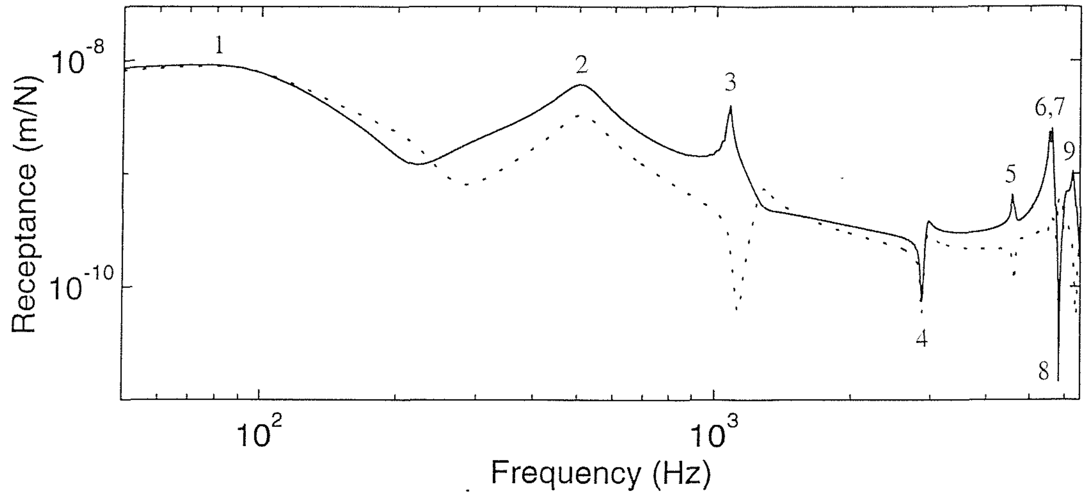

Figure 2.13. Vertical vibration amplitude of the foot response at forcing point. — for excitation acting at mid-span, ······ for excitation acting above a sleeper (for meaning of numbers see text).

using a discretely supported rail model and were not seen in Figure 2.9.

2.5.4. *Comparison with measurement data*

Some experimental results are available in [95] and comparisons are made here with results from one track, track C, which had UIC 60 rail with concrete monobloc sleepers. The measurements were carried out on unloaded tracks by means of impact excitation using an instrumented hammer. For vertical vibration the excitation acted in the centre of the rail head and the response was obtained from the sum of two acceleration signals on either side of the head. The measured and predicted vertical accelerances are compared in Figures 2.14(a) and 2.14(b) which are for the excitation acting at mid-span and above a sleeper respectively. The input parameters for the track are as in previous sections. A good agreement can be seen from Figure 2.14 in the whole frequency region, and especially in the region of 600 – 4000 Hz which is of most importance for noise radiation. The main deviations can be seen to occur near 500 Hz and in the region of 4000 – 5000 Hz for excitation at mid-span, and in the low frequency region up to about 500 Hz for excitation above a sleeper. The deviations in the low frequency region may be improved by considering the effect of sleeper vibration modes on the dynamic stiffness at the support point [20, 33].

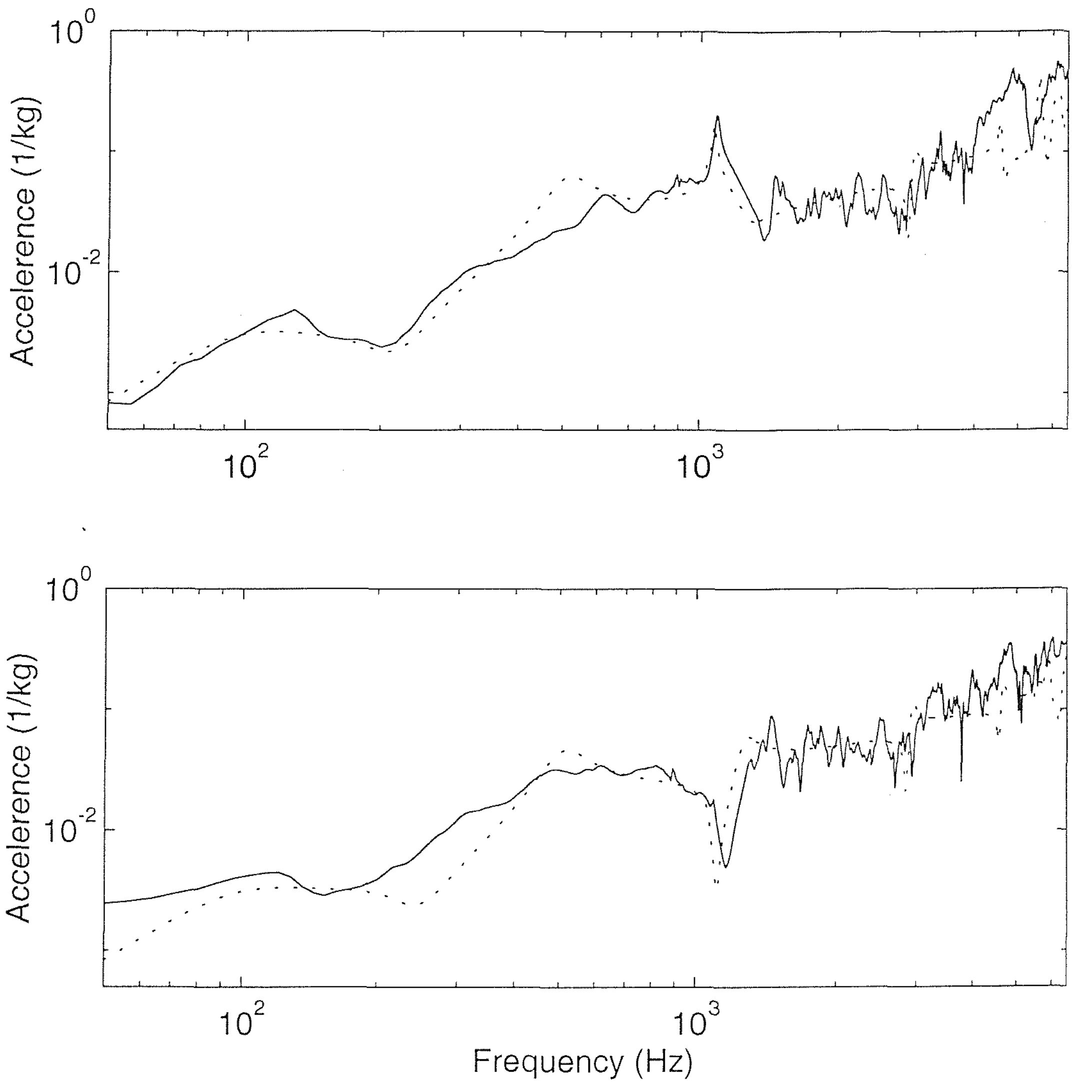

Figure 2.14. Comparison of predictions from the discretely supported double beam model and measurements. Point accelerance on railhead (a) excitation acting at mid-span, (b) excitation acting above a sleeper. — from measurements [95], ······ from predictions.

The decay rates of the vertical vibration along the rail from the continuous and periodic models are also compared with measurement data. For the continuous model the decay rate is represented by the imaginary part of the vertical bending wavenumber and calculated by equation (2.24). For the periodic model it is calculated from the attenuation in vibration level over a 25 span length from the excitation point divided by this distance (15 m). The measured decay rate is the average decay rate from the measurement in 1/3 octave bands. The comparison is shown in Figure 2.15. It can be seen that the tendency of the decay rates from the theoretical models is consistent with the measurement, that is, the vertical vibration

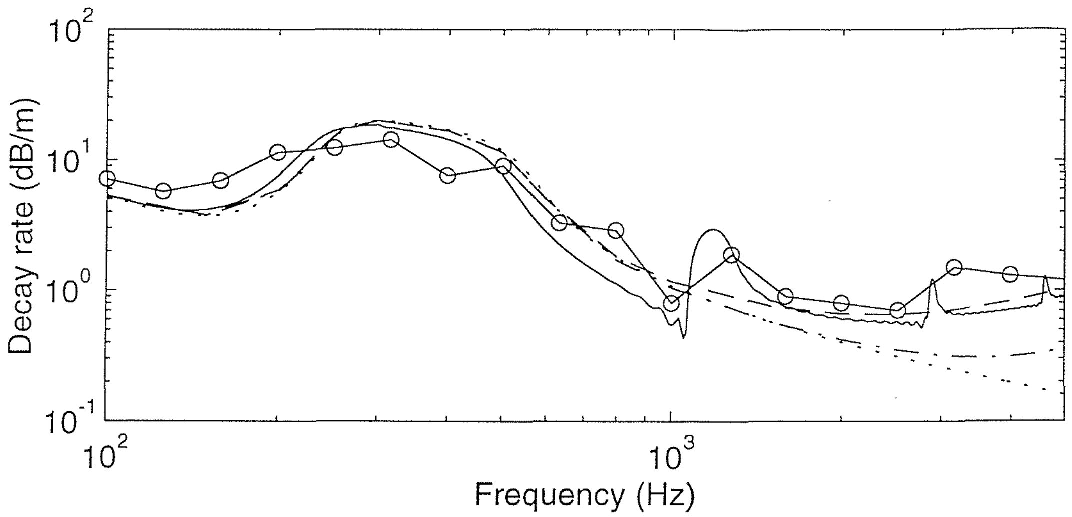

Figure 2.15. Decay rates of vertical vibration along the rail. o—o measured from [95], — from the discretely supported double beam model, - - - from the continuously supported double beam model with rail damping ($\eta_r = 0.01$), -·-·- from the continuously supported double beam model without rail damping ······ from the continuously supported single Timoshenko beam model without rail damping.

decay is generally higher at low frequencies and lower at high frequencies. The periodic model gives a better result in the decay rate throughout the whole frequency region from 100 Hz to 5000 Hz, whereas the decay rate from the continuous model without rail damping is underestimated at high frequencies but better than that of the single Timoshenko beam model. This is because the double beam model allows the foot flapping at high frequencies which results in more energy being dissipated through the damping in the track foundation. The decay rate in the periodic model and continuous model with rail damping is further enhanced by the assignment of a loss factor (0.01) to the rail, although it should be realised that this does not correspond to material damping of the rail, but some other feature of the support not incorporated in the model in this chapter.

2.6. Conclusions

A double beam model has been developed for analysing the vertical vibration behaviour of railway track at high frequencies. This model is much simpler than the commonly used FE or FE-based models and allows the essential cross-sectional deformation for the vertical vibration up to at least 6500 Hz to be included. The dispersion relation of propagating waves in a free and a continuously supported rail has been studied. Vertical vibration receptances of the rail have been calculated using both continuously and discretely supported rail models. Comparison with an FE model has shown good agreement in terms of frequency-wavenumber relation. Good agreement with measurement data has also been reached in terms of point receptance and vibration decay rate along the rail.

The results show that the conventional Timoshenko beam model may be used only up to about 2000 Hz because the rail foot flapping occurs at high frequencies which leads to the foot response being considerably larger than that of the head at high frequencies, up to a factor 10 at about 5600 Hz. Compared with the continuously supported rail model, the predictions from the discretely supported rail model show that the track support has significant effects on the vertical vibration from about 1000 Hz to 6500 Hz. Many peaks or troughs of the receptance appear in this frequency region. Since these peaks reach relatively high levels, neglecting them may cause significant errors. Thus the discretely supported rail model is more appropriate than the continuously supported model for vertical vibration.

CHAPTER 3

Multiple Beam Model for Lateral Vibration

In this chapter a new model for studying the lateral vibration behaviour of railway track is developed. It is a simple model consisting of two infinite Timoshenko beams connected by an array of finite beams. Detailed investigation of the lateral vibration has been carried out using this model to represent a free rail, a continuously supported rail and a discretely supported rail. The free wave dispersion relation calculated using this model have been shown to be in good agreement with an FE model. Good agreement between the predictions and the measurement data has also been reached in terms of accelerances.

3.1. Introduction

The lateral vibration of railway track is a more difficult research topic, compared with the vertical vibration, because the rail exhibits complicated cross-sectional deformations and thus multiple waves are present. The most important cross-sectional deformations include bending and torsion of the rail head and foot and relative motion between the head and foot, for example, bending of the web. Therefore, more comprehensive models that allow these cross-sectional deformations are needed. As mentioned in the last chapter, such models used for lateral vibration are usually based on the finite element method (FEM) or a derivation of the FEM and it is inconvenient to calculate responses of the rail to external excitation using such models, especially when the discrete supports of the rail are taken into account.

In spite of the complication of these models Gry [25] developed a method called "span wave co-ordinates method" to predict lateral vibration behaviour of a discretely supported rail, but the comparison with measurement data did not show a good agreement for lateral vibration in the frequency region above 2000 Hz. Ripke and Knothe [64] investigated both the vertical and the lateral vibration behaviour using their beam-plate model for a rail with discrete supports, but the frequency region in the investigation was only up to 2000 Hz.

In this chapter a new model for studying the lateral vibration behaviour of railway track is developed. This model consists of two infinite Timoshenko beams, which represent the rail head and foot, and their connections — an array of many finite beams, which represent the web of rail. Although simple, this model includes all the essential cross-sectional deformations up to at least 5 kHz such as bending and torsion of the rail head and foot and web bending. Although the twisting stiffness of the web in the axis of the rail is omitted in this model, its effects may be compensated by adjusting some parameters of the model. The predictions from this model are shown to have a good agreement with measurements in the frequency region 50 – 5000 Hz. Since it is simple, some more detailed investigation of the lateral vibration properties of railway track can be achieved using this model.

This chapter is divided into seven sections. After the introduction, the multiple beam model is introduced. In section three the frequency-wavenumber relation in the rail is obtained and it is compared to that from a finite element model. In sections four and five the receptances are calculated for continuously and discretely supported rails respectively, by using Green's function and the superposition principle. Section six deals with wave propagation and decay along the rail. Before the conclusion section the predictions from this model are compared with measurements and a good agreement can be seen.

3.2. Modelling of the rail

For the lateral vibration of a rail at high frequencies the essential cross-sectional deformation types are rail head bending and torsion, rail foot bending and torsion and the relative motion between the rail head and foot, web bending, see Figure 3.1. A model for studying the lateral vibration of a rail should allow all these kinds of deformation.

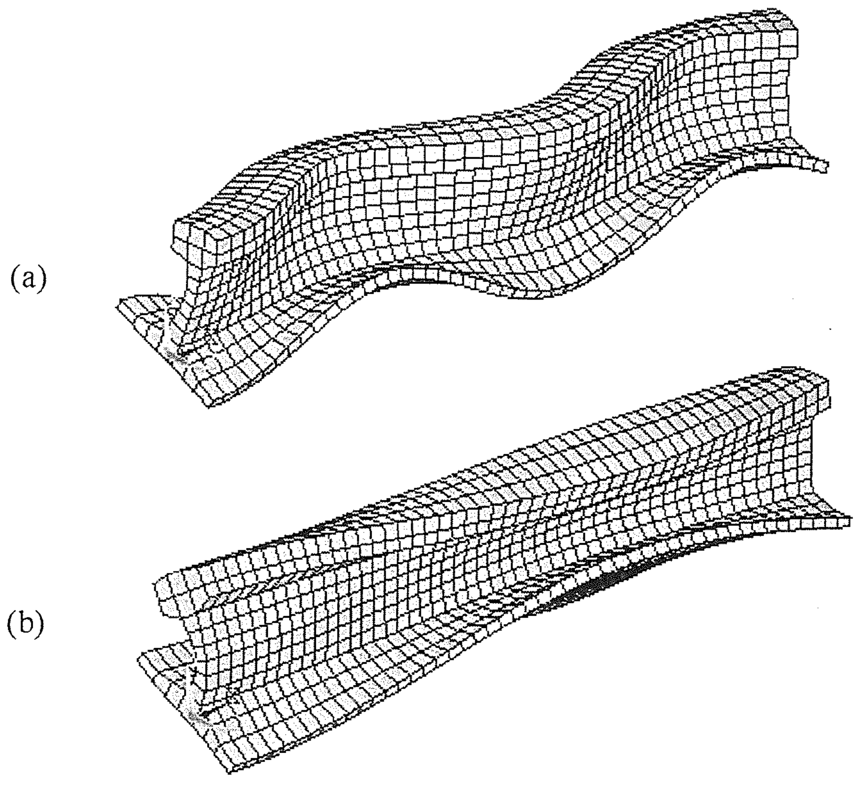

Figure 3.1. Deformations of UIC 60 rail lateral vibration at high frequencies. (a) Lateral bending combined with torsion at 1757 Hz, (b) web bending combined with torsion at 1800 Hz. Boundary conditions imply this is part of an infinite rail.

3.2.1. *Multiple beam model*

The cross-section of the multiple beam model is shown in Figure 3.2(a). In this model the whole rail is divided into three parts: the head and the foot are represented by two infinite Timoshenko beams which can be subjected to both bending and torsion and the web is replaced by numerous beams along the rail which connect the head and foot. In this simplified model the twisting stiffness and the bending stiffness of the web in the direction of the rail axis vanish. The effects of the web twisting stiffness can be compensated by adjusting the head and foot torsional stiffnesses. Ignoring the bending stiffness of the web in the rail axis direction will cause no problem because it is much smaller than the lateral bending stiffnesses of the rail head and foot. As this model consists of only beams, it is analytical rather than numerical and thus the calculation is relatively simple and some detailed study

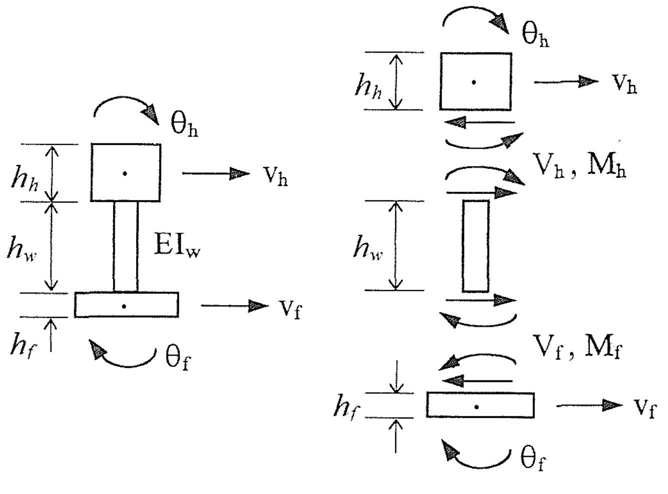

(a) (b)

Figure 3.2. Multiple beam model for lateral vibration.

for the lateral vibration behaviour should be possible.

3.2.2. *Equations of motion for free rail*

The material properties of the model are represented by E, the Young's modulus, G, the shear modulus and ρ, the density. The geometric properties of each cross-section are characterised by A, the cross-sectional area, I, the area moment of inertia, J, the torsional moment of inertia, I_p, the polar moment of inertia and κ, the shear coefficient of the rectangle. The subscripts h, f and w are applied to represent the rail head, foot and web respectively. The isolated diagrams for the rail head, foot and web are shown in Figure 3.2(b), where v_h and θ_h represent the head lateral displacement and rotation about the rail axis respectively, v_f and θ_f the foot lateral displacement and rotation about the rail axis, and their positive direction is pointed out in Figure 3.2. In Figure 3.2(b) V_h and M_h represent the force and moment per unit length between the head and web, V_f and M_f the force and moment per unit length between the web and foot. They appear in pairs.

Applying Newton's second law of motion to the rail head gives

$$\rho A_h \ddot{v}_h + G A_h \kappa_h (\psi_h' - v_h'') = -V_h \tag{3.1a}$$

$$\rho I_h \ddot{\psi}_h + G A_h \kappa_h (\psi_h - v_h') - E I_h \psi_h'' = 0 \tag{3.1b}$$

$$\rho I_{ph}\ddot{\theta}_h - GJ_h\theta_h'' = -M_h + V_h\frac{h_h}{2} \tag{3.1c}$$

Similarly for the foot

$$\rho A_f\ddot{v}_f + GA_f\kappa_f(\psi_f' - v_f'') = -V_f \tag{3.2a}$$

$$\rho I_f\ddot{\psi}_f + GA_f\kappa_f(\psi_f - v_f') - EI_f\psi_f'' = 0 \tag{3.2b}$$

$$\rho I_{pf}\ddot{\theta}_f - GJ_f\theta_f'' = -M_f - V_f\frac{h_f}{2} \tag{3.2c}$$

and for the web

$$\mathbf{M}_w\begin{pmatrix} \ddot{v}_h - \dfrac{h_h\ddot{\theta}_h}{2} \\ 0 \\ \ddot{\theta}_h \\ \ddot{v}_f + \dfrac{h_f\ddot{\theta}_f}{2} \\ 0 \\ \ddot{\theta}_f \end{pmatrix} + \mathbf{K}_w\begin{pmatrix} v_h - \dfrac{h_h\theta_h}{2} \\ 0 \\ \theta_h \\ v_f + \dfrac{h_f\theta_f}{2} \\ 0 \\ \theta_f \end{pmatrix} = \begin{pmatrix} V_h \\ 0 \\ M_h \\ V_f \\ 0 \\ M_f \end{pmatrix} \tag{3.3}$$

where ψ_h and ψ_f represent the cross-sactional rotation due to lateral bending of the rail head and foot respectively and $'$ indicates the derivative with respect to z, the co-ordinate along the axis of the rail. $\mathbf{M}_w$ and $\mathbf{K}_w$ are the mass and stiffness matrices respectively (given in Appendix B) of the web (beam, per unit length of rail).

Equations (3.1), (3.2) and (3.3) can be combined to give a compact formula as follows:

$$\mathbf{M}\ddot{\mathbf{q}} - \mathbf{D}\mathbf{q}'' - \mathbf{G}\mathbf{q}' + \mathbf{K}_R\mathbf{q} = \mathbf{0} \tag{3.4}$$

here **M**, **D**, **G** and $\mathbf{K}_R$ are also given in Appendix B, and

$$\mathbf{q} = \begin{pmatrix} v_h & \psi_h & \theta_h & v_f & \psi_f & \theta_f \end{pmatrix}^T \tag{3.5}$$

3.2.3. *Equations of motion for a continuously supported rail*

The isolated diagram of a continuously supported rail is shown in Figure 3.3, where V_F and M_F are the reaction force and moment per unit length from the railway track foundation respectively. If Z_t and Z_r represent the translational and rotational dynamic stiffnesses per unit length of the foundation respectively, the equation of motion for the continuously supported rail can be given as follows:

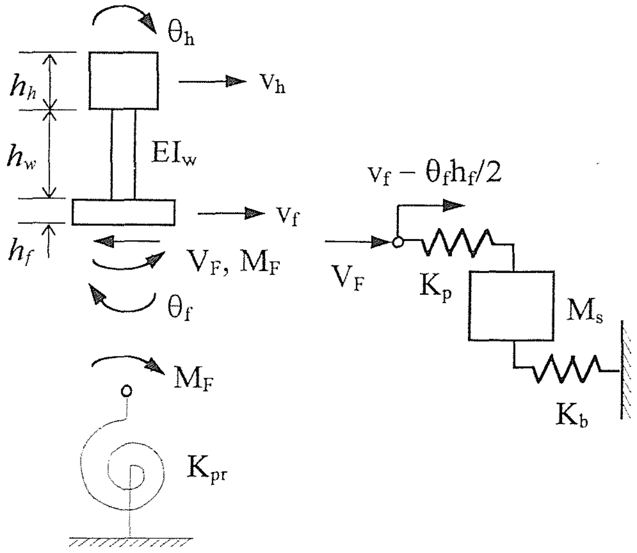

Figure 3.3. Isolated diagram of continuously supported rail.

$$\mathbf{M}\ddot{\mathbf{q}} - \mathbf{D}\mathbf{q}'' - \mathbf{G}\mathbf{q}' + \mathbf{K}_R\mathbf{q} = -\begin{pmatrix} 0 & 0 & 0 & Z_t(v_f - \frac{h_f\theta_f}{2}) & 0 & Z_r\theta_f - Z_t(v_f - \frac{h_f\theta_f}{2})\frac{h_f}{2} \end{pmatrix}^T \tag{3.6}$$

Z_t and Z_r are given by

$$Z_t = \frac{k_p(k_b - m_s\omega^2)}{k_p + k_b - m_s\omega^2} \tag{3.7a}$$

$$Z_r = k_{pr} \tag{3.7b}$$

where k_p and k_b are the lateral stiffnesses per unit length of the pad and ballast respectively, k_{pr} is the rotational stiffness per unit length of the pad and m_s the sleeper mass per unit length. In equation (3.7b) the rotational inertia of the sleeper and the rotational stiffness of the ballast are not taken into account because they are much larger than the rotational inertia of the rail cross-section and the rotational stiffness of the pad respectively, so that the underside of the pad is effectively blocked in the rotational degree of freedom. Equation (3.6) can be simplified to

$$\mathbf{M}\ddot{\mathbf{q}} - \mathbf{D}\mathbf{q}'' - \mathbf{G}\mathbf{q}' + \mathbf{K}\mathbf{q} = \mathbf{0} \tag{3.8}$$

where

$$\mathbf{K} = \mathbf{K}_R + \mathbf{K}_F \tag{3.9}$$

and

$$\mathbf{K}_F = \begin{bmatrix} 0 & 0 & 0 & 0 & 0 & 0 \\ 0 & 0 & 0 & 0 & 0 & 0 \\ 0 & 0 & 0 & 0 & 0 & 0 \\ 0 & 0 & 0 & Z_t & 0 & -\dfrac{Z_t h_f}{2} \\ 0 & 0 & 0 & 0 & 0 & 0 \\ 0 & 0 & 0 & -\dfrac{Z_t h_f}{2} & 0 & Z_r + \dfrac{Z_t h_f^2}{4} \end{bmatrix} \tag{3.10}$$

3.2.4. *Cross-sectional parameter determination*

The cross-sectional data (from [70]) of a simplified version of UIC 60 rail are shown in Figure 3.4. In the multiple beam model developed in this section there are two infinite beams representing the rail head and foot and an array of finite beams representing the web. The characteristic data for these beams can be calculated from the data given in Figure 3.4. Since the twisting stiffness of the web vanishes in the model, the torsional stiffness of the whole cross-section of the rail has become softer. To overcome this drawback, the torsional moment of inertia of the web cross-section is added to the rail head and foot. One third of the torsional moment of inertia of the web is added to the rail head, whereas two thirds are added to the rail foot. This is because the rail head is already much stiffer than the rail foot in terms of torsional stiffness. Thus the total torsional stiffness of the rail cross-section remains unchanged. In addition, I_w, the web area moment of inertia per unit length about the rail axis, is increased by ten percent in order to offset the difference between the beam model and a plate model for the web. This results in an increase in the cut-on frequencies of web bending. The cut-on frequencies of an actual rail

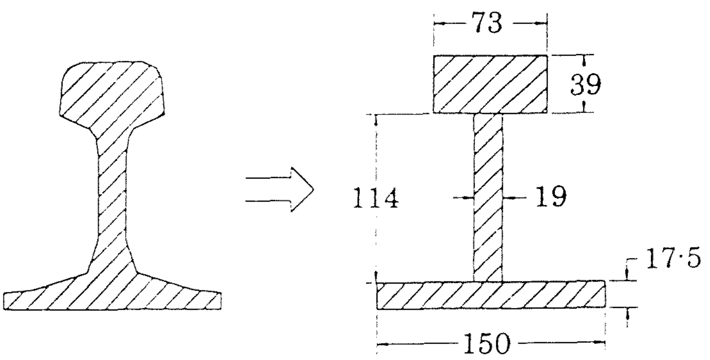

Figure 3.4. Simplified cross-section for UIC 60 rail (from [70]).

section can be found from measurements or by using a two-dimensional FE model of the cross-section. Such a model is much simpler than the FE models for the whole rail and need only be performed once for a given type of rail. By the adjustments described above the results from the simpler multiple beam model are found to become much closer to those from an FE model.

The following parameters are used in the multiple beam model:

$E = 2.1\times10^{11}$ N/m^2	$G = 0.77\times10^{11}$ N/m^2	$\rho = 7850$ kg/m^3
$A_h = 2.847\times10^{-3}$ m^2	$\kappa_h = 0.85$	
$I_h = 1.264\times10^{-6}$ m^4	$I_{ph} = 1.625\times10^{-6}$ m^4	$J_h = 0.9549\times10^{-6}$ m^4
$A_f = 2.625\times10^{-3}$ m^2	$\kappa_f = 0.85$	
$I_f = 4.921\times10^{-6}$ m^4	$I_{pf} = 4.988\times10^{-6}$ m^4	$J_f = 0.2471\times10^{-6}$ m^4
$A_w = 2.166\times10^{-3}$ m^2	$I_w = 0.5716\times10^{-6}$ m^4	$J_w = 0.2338\times10^{-6}$ m^4

The cut-on frequencies from the multiple beam model and from the FE model are shown in Table 3.1. The FE model is used in section 3.3.2 and shown in Figure 3.5 later on.

3.3. Propagating waves in the rail

In this section the dispersion relation of the waves in the rail are explored. Firstly, the waves in a free rail are calculated and the results from the multiple beam model are compared with those from an FE model. Then the waves in a continuously supported rail without damping are calculated. Lastly, the dispersion relation of propagating waves and their decay rate in a damped rail with a damped continuous foundation are studied.

Table 3.1

Web bending cut-on frequencies from the FE model and multiple beam model

Model	FE	Multiple beam I	Multiple beam II
Web bending I	1300 Hz	1299 Hz	1237 Hz
Web bending II	3623 Hz	3632 Hz	3460 Hz

Multiple beam I: I_w is increased by ten percent. Multiple beam II: I_w without increase.

3.3.1. *Equation of dispersion relation*

To identify the wave dispersion relation from the equation of motion, the same procedure is used here as in the last chapter for vertical vibration. Assuming the displacement vector **q** has the form of

$$\mathbf{q} = \mathbf{q}(z)e^{i\omega t} \tag{3.11}$$

where

$$\mathbf{q}(z) = \begin{bmatrix} v_h(z) & \psi_h(z) & \theta_h(z) & v_f(z) & \psi_f(z) & \theta_f(z) \end{bmatrix}^T \tag{3.12}$$

and substituting (3.11) into equation (3.4) and taking derivatives with respect to time only gives

$$\mathbf{D}\mathbf{q}''(z) + \mathbf{G}\mathbf{q}'(z) + (\omega^2\mathbf{M} - \mathbf{K}_R)\mathbf{q}(z) = \mathbf{0} \tag{3.13}$$

Substituting $\mathbf{q}(z) = \mathbf{Q}e^{-ikz}$ into (3.13) gives

$$[-k^2\mathbf{D} - ik\mathbf{G} + (\omega^2\mathbf{M} - \mathbf{K}_R)]\mathbf{Q} = \mathbf{0} \tag{3.14}$$

When the wavenumber $k = 0$, equation (3.14) becomes

$$(\omega^2\mathbf{M} - \mathbf{K}_R)\mathbf{Q} = \mathbf{0} \tag{3.15}$$

Then the cut-on frequencies can be obtained from (3.15). At cut-on frequencies no wave is produced.

3.3.2. *Waves in a free rail*

From equation (3.14) the dispersion relation of propagating waves in the rail can be determined. For comparison, an FE model representing the idealised UIC 60 rail of Figure 3.4 is also used. The FE model is shown in Figure 3.5. It is a short length of rail (1m) with symmetry or antisymmetry boundary conditions at the ends to

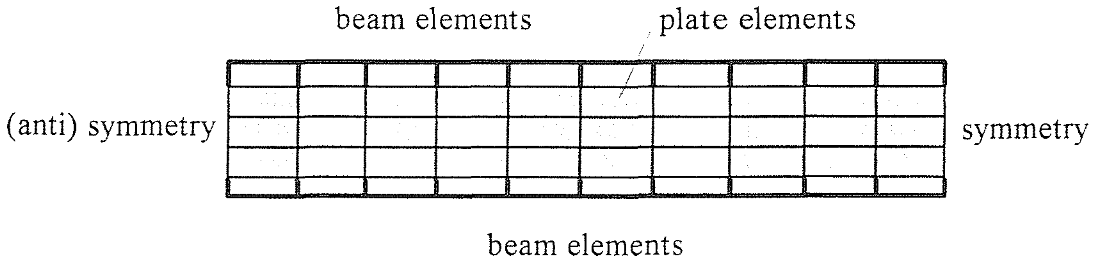

Figure 3.5. Schematic representation of the finite element idealisation of a 1m length of rail (web is actually 6 × 30 elements).

simulate the waves in an infinite rail. The rail head and foot are each represented by 30 Timoshenko beam elements and the web is meshed with 6 × 30 plate elements (the full number of elements is not shown in Figure 3.5). To consider the distances from the rail head axis to the web and from the rail foot axis to the web, two sets of 31 short stiff and massless beam elements are placed between the head and the web and between the foot and the web. These beams are used for transmitting force and moment only and almost no elastic deformations occur on them.

The results from the multiple beam model and from the FE model are shown in Figure 3.6. As conventional [79], the first wave (I) and the second wave (II) are called lateral bending wave and torsional wave respectively though at high frequencies these two waves have a compound deformed shape. The third wave (III) involves the web bending and torsion of both the head and the foot out of phase with each other. The fourth wave (IV) involves a double bending of the web, so that the head and foot are again each in torsion, but in phase with each other. Further features of these waves can be found in references [15, 25, 41, 79]. The important thing to be emphasised here is that the results from the simpler model have a very good agreement with those from the FE model. The agreement in terms of the dispersion relation of waves in the rail is crucial, especially for those near the cut-on frequencies, because rail vibration can be regarded as the superposition of different

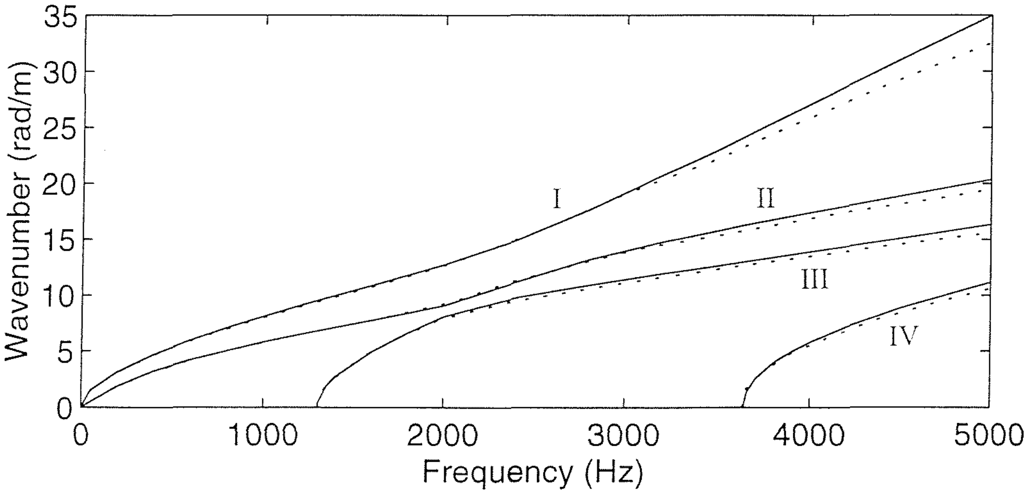

Figure 3.6. Dispersion relation of waves in a free rail for lateral vibration. — from the multiple beam model, ······ from the FE model.

waves in the rail.

3.3.3. *Waves in a continuously supported rail*

To calculate the frequency-wavenumber relation in a supported rail, the dynamic stiffness of the foundation is employed and it is added to the system stiffness matrix, see equations (3.9) and (3.10). The parameters of the railway track foundation

$k_p = 83.3$ MN/m^2 $\quad k_{pr} = 1.09$ MN $\quad k_b = 133.3$ MN/m^2 $\quad m_s = 270$ kg/m

are derived from the values of track C from [95] and initially have no damping.

The results are shown in Figure 3.7. Compared with the case of the free rail, the cut-on frequencies of waves I, II, and III are increased because of the foundation dynamic stiffness, but for wave IV it is almost unchanged. In addition the first wave, the lateral bending wave, has a branch at about 100 – 150 Hz. In this frequency region the rail vibration is coupled with the foundation mass. Apart from the regions close to cut-on frequencies, the dispersion relation curves in the supported rail are close to those for the free rail at higher frequencies. This implies that the railway track foundation mainly affects the low frequency vibration of the rail, apart from the effects of damping.

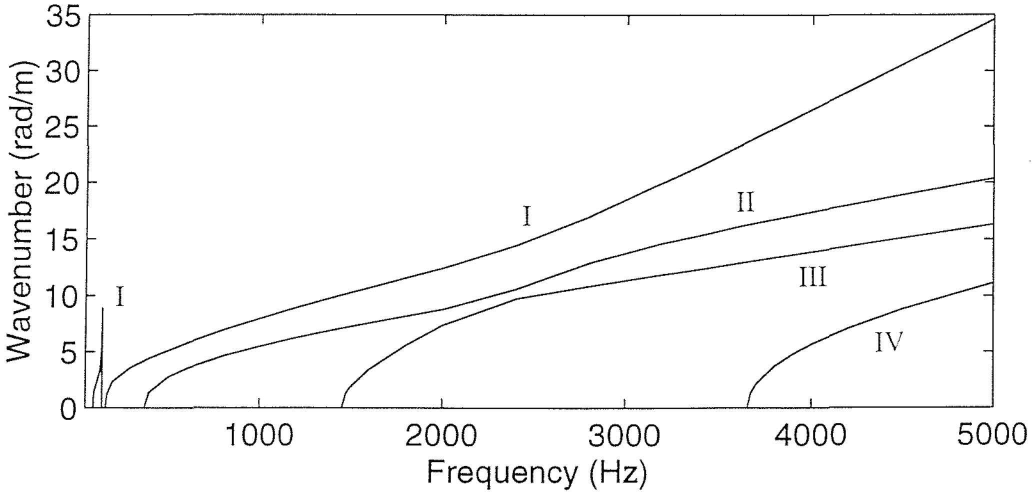

Figure 3.7. Dispersion relation of waves in a continuously supported rail without damping for lateral vibration.

If damping is introduced into both the rail and the foundation, the wavenumber k is always complex and has the form of $k = \pm (a - ib)$ which represent two waves propagating in two opposite directions with exponential decay. The decay rate Δ (in dB/m) of various waves is determined by their imaginary part of k and can be calculated using equation (2.24) in the last chapter. Damping is added through loss factors: $\eta_r = 0.01$ for the rail, $\eta_p = 0.25$ for the pad and $\eta_b = 0.6$ for the ballast.

The frequency-wavenumber relation in the supported rail with damping is shown in Figure 3.8, where the solid lines represent the real part of the wavenumber and the dotted lines the imaginary part. The curves of the real parts can be seen to be almost the same as those in the case without damping except near the cut-on frequencies. The imaginary parts can be seen to be higher before the cut-on frequencies and much lower after the cut-on frequencies; they decrease dramatically near their cut-on frequencies. The decay rate curves of various waves in Figure 3.9 show this more noticeably. In Figure 3.9 it can be seen that the decay rate of the lateral bending wave has a steady increase from 0.5 dB/m to 2.5 dB/m in the frequency region of 1500 – 3000 Hz, while the torsional wave's decay rate has a peak of 2.1 dB/m appearing at about 2300 Hz.

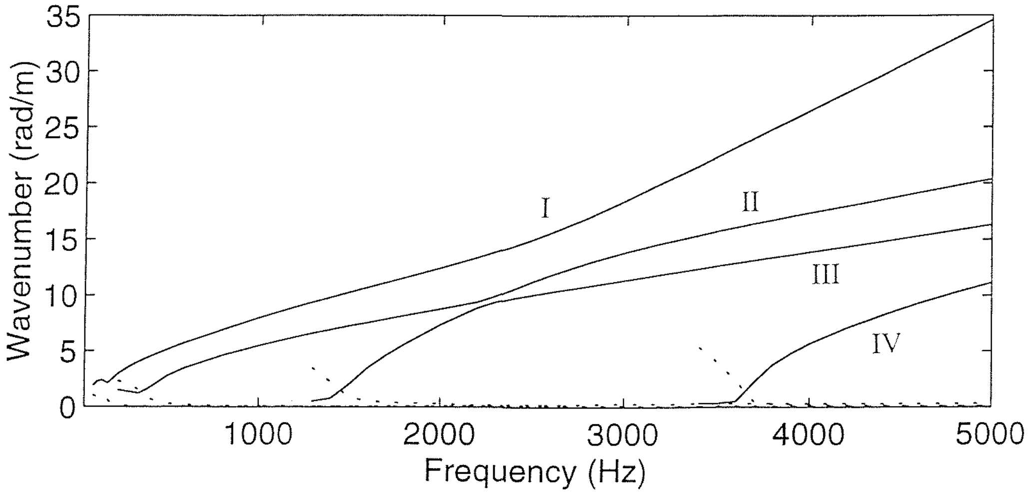

Figure 3.8. Dispersion relation of waves in a continuously supported rail with damping for lateral vibration. — real part of the wavenumber, ······ imaginary part of the wavenumber.

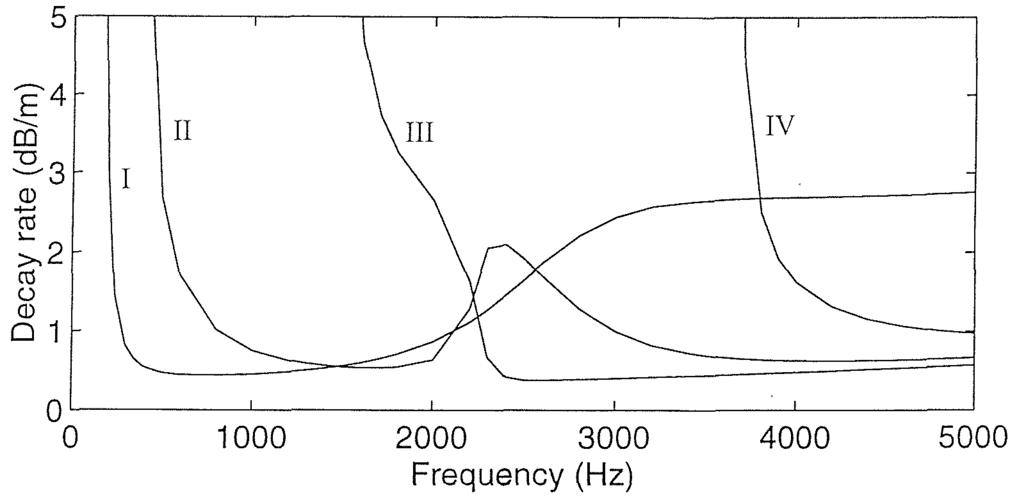

Figure 3.9. Decay rates of different waves in a continuously supported rail.

3.4. Receptance of continuously supported rail

A continuously supported rail model can avoid the complication of the periodic support nature and to some extent, the results from the continuously supported rail model are still acceptable. In this section, the continuously supported model is employed for calculating receptances and thus the pad, sleeper and ballast are replaced by equivalent continuous layers of mass and stiffness. The parameters of these layers used in this section are the same as above.

3.4.1. *Equation of motion*

In the rest of this chapter, it will be assumed that forces and responses are harmonic, so the $e^{i\omega t}$ term will usually be omitted. Considering the continuously supported rail subjected to a lateral harmonic excitation $Fe^{i\omega t}$ acting on top of the rail head at the point $z = 0$, the equation of motion can be given as follows:

$$-\mathbf{D}\mathbf{q}'' - \mathbf{G}\mathbf{q}' - (\omega^2\mathbf{M} - \mathbf{K})\mathbf{q} = \delta(z)\begin{pmatrix} F & 0 & F\dfrac{h_h}{2} & 0 & 0 & 0 \end{pmatrix}^{\mathrm{T}} \tag{3.16}$$

Equation (3.16) can be written in the state space form:

$$\mathbf{X}' = \mathbf{A}\mathbf{X} + \mathbf{P}\delta(z) \tag{3.17}$$

where

$$\mathbf{X} = \begin{bmatrix} \mathbf{q}(z) \\ \mathbf{q}'(z) \end{bmatrix} \tag{3.18a}$$

$$\mathbf{A} = \begin{bmatrix} \mathbf{0} & \mathbf{I} \\ -\mathbf{D}^{-1}(\omega^2\mathbf{M} - \mathbf{K}) & -\mathbf{D}^{-1}\mathbf{G} \end{bmatrix} \tag{3.18b}$$

$$\mathbf{P} = [\ \mathbf{0}\ \ -\mathbf{D}^{-1}\mathbf{F}]^{\mathrm{T}} \tag{3.18c}$$

$$\mathbf{F} = \begin{bmatrix} F & 0 & \dfrac{Fh_h}{2} & 0 & 0 & 0 \end{bmatrix}^{\mathrm{T}} \tag{3.18d}$$

3.4.2. *Point and cross receptances*

Taking the Laplace transform of equation (3.17) gives

$$(s\mathbf{I} - \mathbf{A})\mathbf{X}(s) = \mathbf{P} \tag{3.19}$$

According to Cramer's rule the Laplace transform of the rail head displacement and rotation, respectively, has the form of

$$V_h(s) = \frac{\Delta_1(s)}{\Delta(s)}, \qquad \Theta_h(s) = \frac{\Delta_3(s)}{\Delta(s)} \tag{3.20, 3.21}$$

where, $\Delta(s)$ is the determinant of matrix $s\mathbf{I} - \mathbf{A}$. $\Delta_1(s)$ and $\Delta_3(s)$ are the determinants of the matrices which are obtained from $s\mathbf{I} - \mathbf{A}$ by replacing its first column and third column by **P** respectively. The lateral responses of the rail head are found by performing the Laplace inverse transform using contour integration:

$$v_h(z) = \frac{1}{2\pi i}\int_{\gamma - i\infty}^{\gamma + i\infty} V_h(s)e^{sz}ds = \sum_{\substack{k \text{ with } \mathrm{Re}(s_k)<0 \text{ or} \\ \mathrm{Im}(s_k)<0 \text{ if } \mathrm{Re}(s_k)=0}} \mathrm{Res}[V_h(s_k)e^{s_k z}] \qquad z > 0 \tag{3.22}$$

$$\theta_h(z) = \frac{1}{2\pi i}\int_{\gamma - i\infty}^{\gamma + i\infty} \Theta_h(s)e^{sz}ds = \sum_{\substack{k \text{ with } \mathrm{Re}(s_k)<0 \text{ or} \\ \mathrm{Im}(s_k)<0 \text{ if } \mathrm{Re}(s_k)=0}} \mathrm{Res}[\Theta_h(s_k)e^{s_k z}] \qquad z > 0 \tag{3.23}$$

where the residues at the poles s_k are given by

$$\mathrm{Res}[V_h(s_k)e^{s_k z}] = \frac{\Delta_1(s_k)}{\Delta'(s_k)}e^{s_k z} \tag{3.24}$$

$$\mathrm{Res}[\Theta_h(s_k)e^{s_k z}] = \frac{\Delta_3(s_k)}{\Delta'(s_k)}e^{s_k z} \tag{3.25}$$

In a similar way the lateral responses of the rail foot can be obtained. The point receptance at the top of the rail head at $z = 0$ is given by

$$\alpha(\omega) = \frac{v_h(0) + h_h\theta_h(0)/2}{F} \tag{3.26}$$

3.4.3. *Numerical results*

The amplitude and phase of the lateral point receptance are shown in Figure 3.10. Three well-damped resonances can be seen at about 100 Hz, 160 Hz and 380 Hz. At 100 Hz the whole track bounces on the lateral stiffness of the ballast, whereas at 160 Hz the rail vibrates laterally on the stiffness of the pad. These two resonances occur at the cut-on frequencies of the lateral bending wave which can be seen in Figure 3.7. At 380 Hz the rail rotates on the pad rotational stiffness. This can be identified as the cut-on of the torsional wave. The other two peaks at about 1400 Hz and 3600 Hz can be identified as the cut-on of the web bending waves III

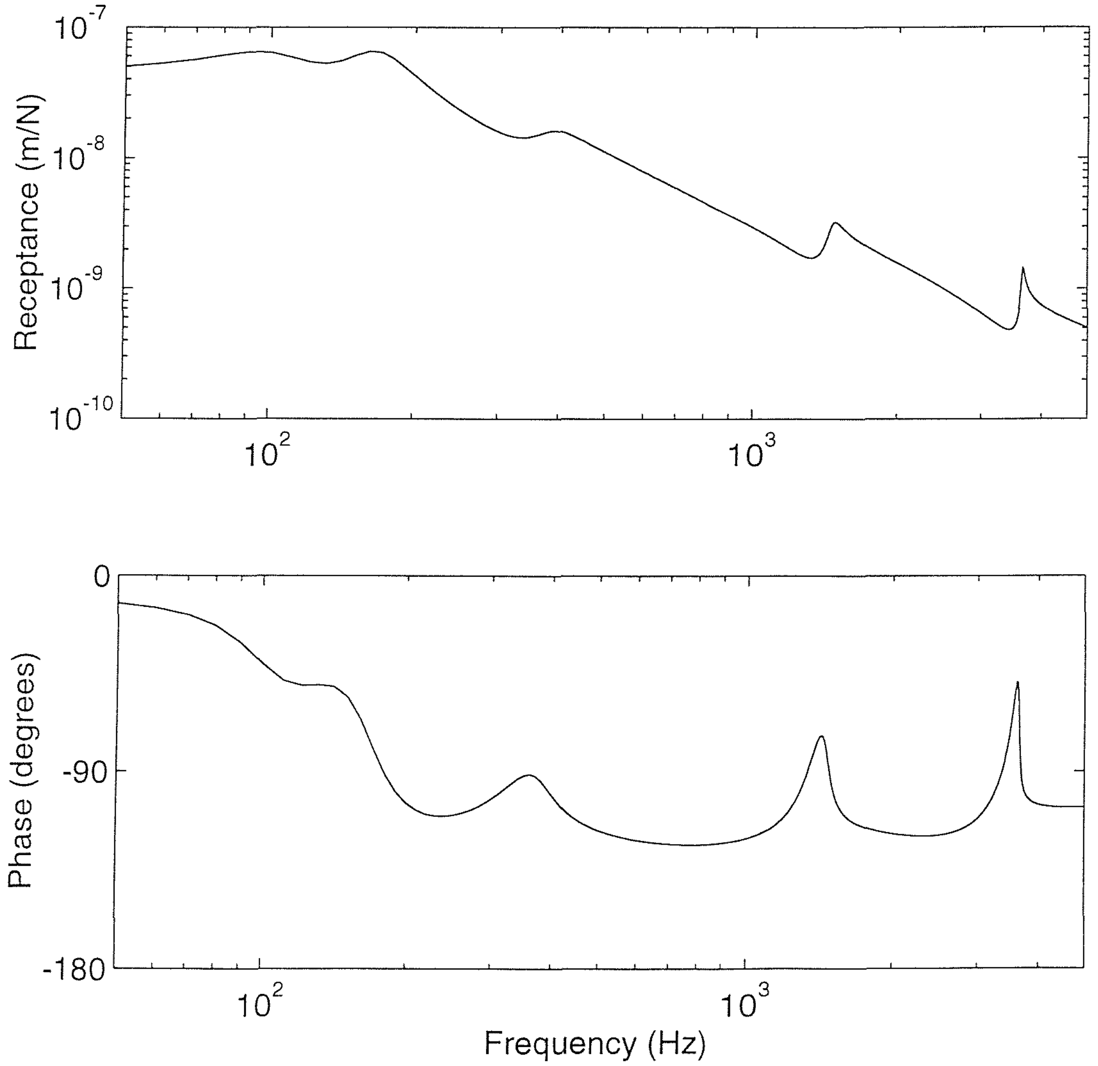

Figure 3.10. Amplitude and phase of the point receptance for lateral vibration of the continuously supported rail.

and IV respectively. These are damped by both the pad loss factor (rotational) and the rail loss factor, although the second one is sharper, suggesting that the pad loss factor has less effect here.

Various “cross” receptances are shown in Figure 3.11. (The term cross receptance is used here to mean the response at some other positions at $z = 0$ to a force at the top of the head. The term transfer receptance is reserved for the response at $z \neq 0$.) Figures 3.11(a) and 3.11(b) show the lateral displacement (in the centre of the head or foot) and rotation respectively. The solid lines are for the head and the dashed lines for the foot. It can be observed that the responses of the rail

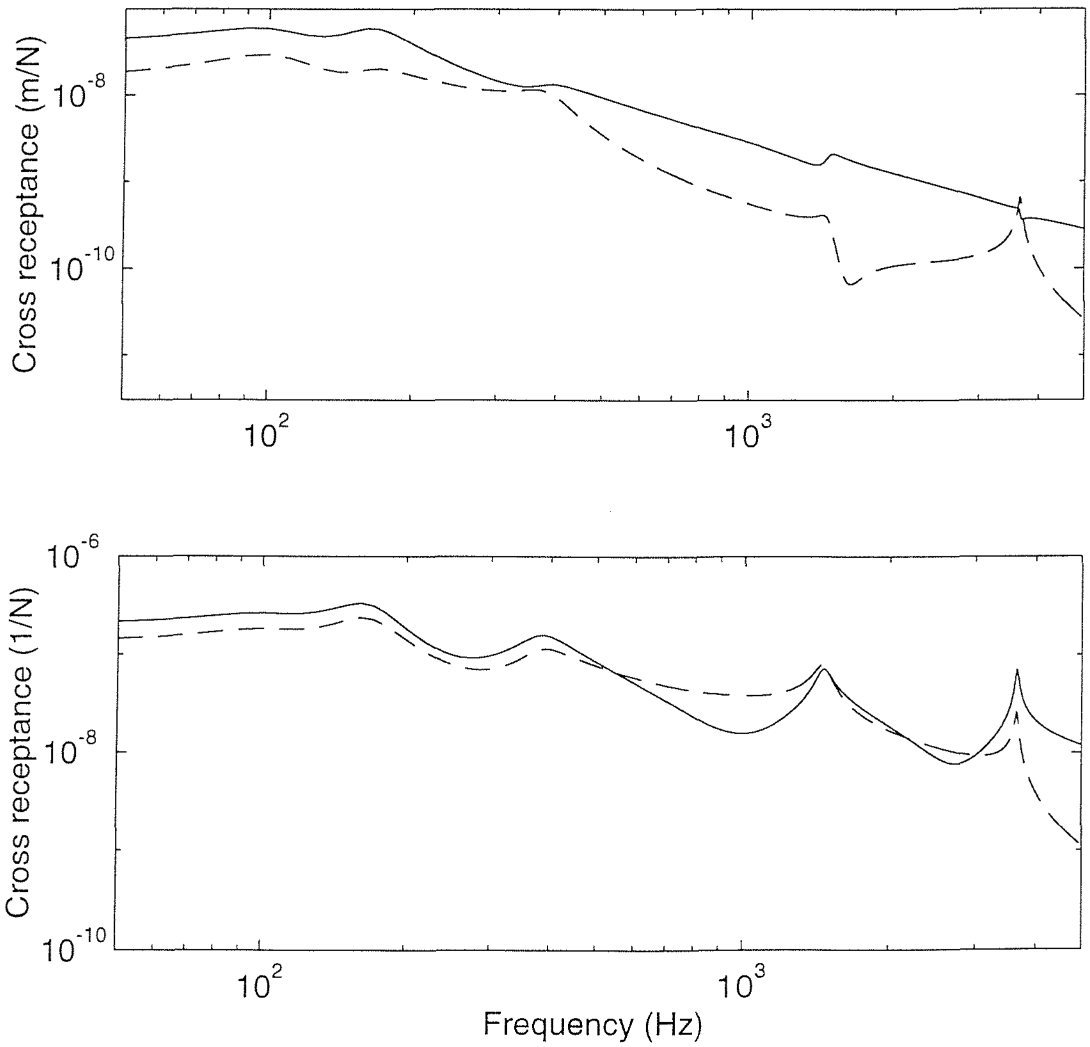

Figure 3.11. Cross receptances for lateral vibration of the continuously supported rail. Force acts at the top of the rail head. (a) translational response, (b) rotational response. — for rail head, - - - for rail foot.

head usually are higher than those of the foot. At low frequencies the lateral displacement and rotation curves have similar tendencies, whereas at the web bending cut-on frequencies the peaks are more noticeable in the rotation than in the displacement. This is because the web bending strongly involves the rotation of the head and foot. The rail head displacement curve can be seen to be quite smooth at high frequencies and there is almost no peak appearing at the second web bending cut-on frequency.

3.5. Receptance of discretely supported rail

Although the above analysis is for a continuously supported rail, in fact a rail is discretely supported by pads, sleepers and ballast. A more realistic model for railway track vibration should therefor be an infinite rail with periodic supports. Some important characteristics, for example, pinned-pinned resonances can only be obtained using a discretely supported model. For the lateral vibration of the rail, the pinned-pinned resonance may appear in a more complicated form than for the vertical vibration because there are various waves in the rail as shown in previous sections. In this section a periodically supported lateral rail model is considered.

3.5.1. *Equation of motion*

An infinite periodically supported rail model is shown in Figure 2.11 in the last chapter, but now the reference direction is lateral and thus the displacements should be v and θ instead of u_h and u_f. The supports are characterised by pad stiffnesses (both lateral and rotational), K_{pn} and K_{prn}, sleeper mass, M_s and ballast stiffness, K_{bn}. Damping is considered by introducing loss factors η_r into the Young's modulus E and shear modulus G of the rail, η_p into the pad stiffnesses K_{pn} and K_{prn}, η_b into the ballast stiffness K_{bn}, and making E, G, K_{pn}, K_{prn} and K_{bn} complex with the appropriate factor $(1+i\eta)$. Assuming the n-th support is at the position $z = z_n$ and a single external harmonic force $Fe^{i\omega t}$ acts at the top of the rail head at the point $z = z_F$, the equation of motion of the discretely supported rail is given as

$$-\mathbf{Dq}'' - \mathbf{Gq}' - (\omega^2\mathbf{M} - \mathbf{K}_R)\mathbf{q} = \begin{pmatrix} F\delta(z-z_F) & 0 & F\frac{h_h}{2}\delta(z-z_F) & F_s & 0 & T_s \end{pmatrix}^T \quad (3.27a)$$

where

$$F_s = -\sum_{\substack{n=-\infty \\ n\neq 0}}^{\infty}[Z_{tn}(v_{fn} - \frac{h_f\theta_{fn}}{2})\delta(z-z_n)] \tag{3.27b}$$

$$T_s = -\sum_{\substack{n=-\infty \\ n\neq 0}}^{\infty}\{[Z_{rn}\theta_{fn} - Z_{tn}(v_{fn} - \frac{h_f\theta_{fn}}{2})\frac{h_f}{2}]\delta(z-z_n)\} \tag{3.27c}$$

F_s and T_s represent infinite sets of reaction forces and moments from the supports respectively. Z_{tn} and Z_{rn} are the translational and rotational dynamic stiffnesses at the n-th support respectively and given as

$$Z_{tn} = \frac{K_{pn}(K_{bn} - M_s\omega^2)}{K_{pn} + K_{bn} - M_s\omega^2} \tag{3.28a}$$

$$Z_{rn} = K_{pr} \tag{3.28b}$$

3.5.2. *Response to a harmonic excitation*

The discretely supported railway track may be simplified to an infinite rail with a finite number of discrete supports. This is because the supports at large distances from the point at which the response is to be calculated can be neglected due to the wave propagation decay. The number of supports should be chosen large enough to guarantee an acceptable approximate solution. To calculate the response of the rail the discrete supports can be replaced by a series of point forces. Based on the Green's function and the superposition principle the stationary response of the rail to the harmonic excitation can be obtained, using a similar method to section 2.5.

The Green's function $g_{ij}(z,z')$ for the infinite rail is the response of the i-th component of the displacement vector $\mathbf{q}(z)$ at z caused by a unit harmonic force/moment of the j-th component of the excitation $\mathbf{F}$ at z'. It is chosen here that when $j = 1$ or 4 the forces act at the top of the rail head or at the bottom of the rail foot respectively rather than at the centre of the head or foot. The procedure to determine a Green's function $g_{ij}(z,z')$ is shown in Appendix B.

Using the superposition principle the displacement and rotation of the rail head are given by

$$v_h(z) = -\sum_{\substack{n=-N\\n\neq 0}}^{N} Z_{tn}[v_f(z_n) - \frac{h_f}{2}\theta_f(z_n)]g_{14}(z,z_n) - \sum_{\substack{n=-N\\n\neq 0}}^{N} Z_{rn}\theta_f(z_n)g_{16}(z,z_n) + Fg_{11}(z,z_F) \tag{3.29}$$

$$\theta_h(z) = -\sum_{\substack{n=-N\\n\neq 0}}^{N} Z_{tn}[v_f(z_n) - \frac{h_f}{2}\theta_f(z_n)]g_{34}(z,z_n) - \sum_{\substack{n=-N\\n\neq 0}}^{N} Z_{rn}\theta_f(z_n)g_{36}(z,z_n) + Fg_{31}(z,z_F) \tag{3.30}$$

respectively or in matrix form

$$\begin{pmatrix} v_h(z) \\ \theta_h(z) \end{pmatrix} = -\sum_{\substack{n=-N\\n\neq 0}}^{N} \begin{bmatrix} Z_{tn}g_{14}(z,z_n) & Z_{rn}g_{16}(z,z_n) - \frac{h_f}{2}Z_{tn}g_{14}(z,z_n) \\ Z_{tn}g_{34}(z,z_n) & Z_{rn}g_{36}(z,z_n) - \frac{h_f}{2}Z_{tn}g_{34}(z,z_n) \end{bmatrix} \begin{pmatrix} v_f(z_n) \\ \theta_f(z_n) \end{pmatrix} + F\begin{pmatrix} g_{11}(z,z_F) \\ g_{31}(z,z_F) \end{pmatrix} \tag{3.31}$$

Equation (3.31) can be presented in the following compact form:

$$\mathbf{q}_h(z) = -\sum_{\substack{n=-N\\n\neq 0}}^{N} \mathbf{G}_{hf}(z,z_n)\mathbf{q}_f(z_n) + F\mathbf{G}_{hF}(z,z_F) \tag{3.32}$$

Similarly, the displacement and rotation of the rail foot are given by

$$v_f(z) = -\sum_{\substack{n=-N\\n\neq 0}}^{N} Z_{tn}[v_f(z_n) - \frac{h_f}{2}\theta_f(z_n)]g_{44}(z,z_n) - \sum_{\substack{n=-N\\n\neq 0}}^{N} Z_{rn}\theta_f(z_n)g_{46}(z,z_n) + Fg_{41}(z,z_F) \tag{3.33}$$

$$\theta_f(z) = -\sum_{\substack{n=-N\\n\neq 0}}^{N} Z_{tn}[v_f(z_n) - \frac{h_f}{2}\theta_f(z_n)]g_{64}(z,z_n) - \sum_{\substack{n=-N\\n\neq 0}}^{N} Z_{rn}\theta_f(z_n)g_{66}(z,z_n) + Fg_{61}(z,z_F) \tag{3.34}$$

$$\begin{pmatrix} v_f(z) \\ \theta_f(z) \end{pmatrix} = -\sum_{\substack{n=-N\\n\neq 0}}^{N} \begin{bmatrix} Z_{tn}g_{44}(z,z_n) & Z_{rn}g_{46}(z,z_n) - \frac{h_f}{2}Z_{tn}g_{44}(z,z_n) \\ Z_{tn}g_{64}(z,z_n) & Z_{rn}g_{66}(z,z_n) - \frac{h_f}{2}Z_{tn}g_{64}(z,z_n) \end{bmatrix} \begin{pmatrix} v_f(z_n) \\ \theta_f(z_n) \end{pmatrix} + F\begin{pmatrix} g_{41}(z,z_F) \\ g_{61}(z,z_F) \end{pmatrix} \tag{3.35}$$

$$\mathbf{q}_f(z) = -\sum_{\substack{n=-N\\n\neq 0}}^{N} \mathbf{G}_{ff}(z,z_n)\mathbf{q}_f(z_n) + F\mathbf{G}_{fF}(z,z_F) \tag{3.36}$$

If $Fe^{i\omega t}$ acts at mid-span ($z = 0$), the following symmetric relationship holds:

$$\mathbf{q}(z) = \mathbf{q}(-z) \tag{3.37a}$$

$$Z_{tn} = Z_{-tn}, \quad Z_{rn} = Z_{-rn} \tag{3.37b,c}$$

$$g_{ij}(z,z') = g_{ij}(-z,-z') \tag{3.37d}$$

Equations (3.32) and (3.36) can be simplified to give

$$\mathbf{q}_h(z) = -\sum_{n=1}^{N}[\mathbf{G}_{hf}(z,z_n) + \mathbf{G}_{hf}(z,-z_n)]\mathbf{q}_f(z_n) + F\mathbf{G}_{hF}(z,0) \tag{3.38}$$

$$\mathbf{q}_f(z) = -\sum_{n=1}^{N}[\mathbf{G}_{ff}(z,z_n) + \mathbf{G}_{ff}(z,-z_n)]\mathbf{q}_f(z_n) + F\mathbf{G}_{fF}(z,0) \tag{3.39}$$

At each support point $z = z_m$ the displacement and rotation of the rail foot can be written as follows:

$$\mathbf{q}_f(z_m) = -\sum_{n=1}^{N}[\mathbf{G}_{ff}(z_m,z_n) + \mathbf{G}_{ff}(z_m,-z_n)]\mathbf{q}_f(z_n) + F\mathbf{G}_{fF}(z_m,0) \quad m = 1, 2, \cdots, N \tag{3.40}$$

From equation (3.40) the displacement and rotation of the foot at each support point can be solved in terms of F by taking the sum to the left-hand side and then inverting the matrix of coefficients of $\mathbf{q}_f(z_m)$ as in section 2.5.2. Substituting them into equations (3.38) and (3.39), one can obtain the displacement and rotation at any point on the rail head and foot.

For $Fe^{i\omega t}$ acting above a sleeper (this sleeper is chosen as $n = 0$ and also $z = 0$) the similar equations for the displacements and rotations of the rail head and foot can be given as follows:

$$\mathbf{q}_h(z) = -\mathbf{G}_{hf}(z,0)\mathbf{q}_f(0) - \sum_{n=1}^{N}[\mathbf{G}_{hf}(z,z_n) + \mathbf{G}_{hf}(z,-z_n)]\mathbf{q}_f(z_n) + F\mathbf{G}_{hF}(z,0) \tag{3.41}$$

$$\mathbf{q}_f(z) = -\mathbf{G}_{ff}(z,0)\mathbf{q}_f(0) - \sum_{n=1}^{N}[\mathbf{G}_{ff}(z,z_n) + \mathbf{G}_{ff}(z,-z_n)]\mathbf{q}_f(z_n) + F\mathbf{G}_{fF}(z,0) \tag{3.42}$$

$$\mathbf{q}_f(z_m) = -\mathbf{G}_{ff}(z_m,0)\mathbf{q}_f(0) - \sum_{n=1}^{N}[\mathbf{G}_{ff}(z_m,z_n) + \mathbf{G}_{ff}(z_m,-z_n)]\mathbf{q}_f(z_n) + F\mathbf{G}_{fF}(z_m,0)$$

$$m = 0, 1, 2, \cdots, N \tag{3.43}$$

In a similar way the displacement and rotation of the foot at each support point can be solved from equation (3.43). Substituting them into equations (3.41) and (3.42), the displacement and rotation at any point on the rail head and foot can be obtained.

3.5.3. *Numerical results*

The point and cross receptances of the discretely supported rail for lateral vibration are calculated in the frequency range from 50 Hz to 5000 Hz for an external excitation acting at the top of the rail head either above a sleeper or at mid-span. Parameters for each support are chosen as follows (to correspond to those used earlier for the continuous support):

$K_p = 50$ MN/m $\quad K_b = 80$ MN/m $\quad K_{pr} = 0.654$ MNm $\quad M_s = 162$ kg

Other parameters such as loss factors are the same as used in the previous sections for the continuously supported rail. The span length (the distance between two sleepers) is chosen as $d = 0.6$ m, and the support number $2N = 80$ for the excitation acting at mid-span, $2N + 1 = 81$ for the excitation acting above a sleeper.

The amplitude and phase of the lateral point receptance are shown in Figure 3.12. Solid and dashed lines are the results from the excitation acting at mid-span and above a sleeper respectively. In the low frequency region up to about 400 Hz the responses to the excitation acting both at mid-span and above a sleeper are almost the same and similar to the continuous track response in Figure 3.10. Three well-damped resonances below 400 Hz and two sharp resonances at about 1400 and 3600 Hz can be seen. These resonances can be identified as the cut-on of the lateral bending wave (including its branch at 100 – 150 Hz), the torsional wave and two web bending waves as predicted in the continuously supported rail model in section 3.4.3. Two pinned-pinned resonances marked with a and a', c and c' can be seen clearly in Figure 3.12. The a-a' pinned-pinned resonance occurs at about 500 Hz when the lateral bending wavelength is equal to twice the span length (this corresponds to a wavenumber of 5.2 rad/m in Figure 3.7). When the wavelength of the first order web bending (rail head and foot rotation out of phase with each other) is equal to twice the span length, at about 1700 Hz, the c-c' pinned-pinned resonance appears. There should be two other pinned-pinned resonances since there are four types of propagating wave in the rail. The pinned-pinned resonance due to the torsional wave should occur at around 900 Hz but it is not noticeable in Figure 3.12. However, it can be identified in the cross receptance plots later on. The pinned-pinned resonance from the second order web bending wave (rail head and

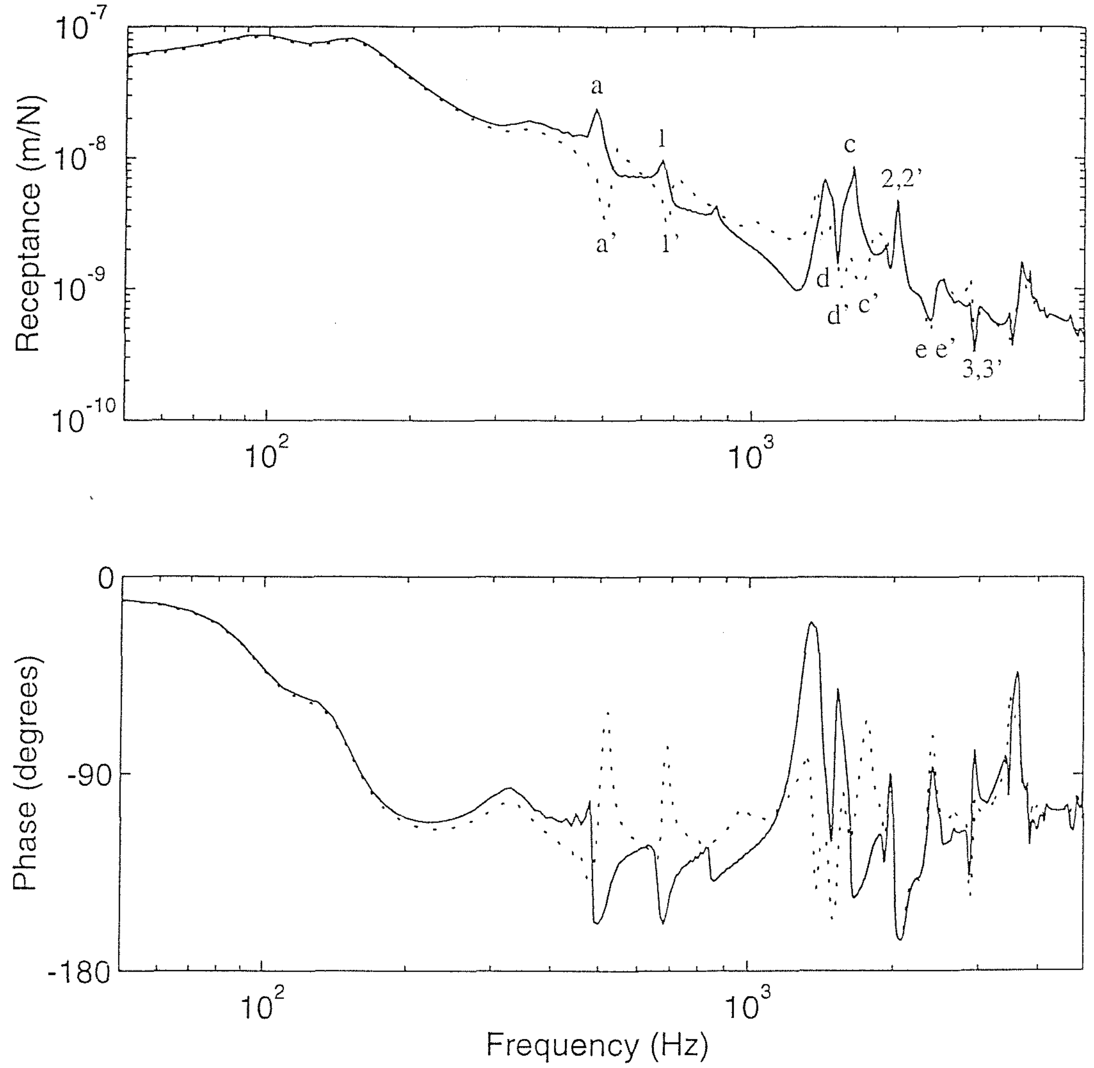

Figure 3.12. Amplitude and phase of the point receptance for lateral vibration of the discretely supported rail. — for excitation acting at mid-span, ······ for excitation acting above a sleeper. (for meaning of symbols see text).

foot rotation in phase with each other), which should occur at about 3900 Hz, does not appear because this wave is almost not affected by the supports. It is because the high frequency vibration of the rail is less affected by the supports, that the receptances in the high frequency region are quite similar for the excitation acting either at mid-span or above a sleeper, also similar to Figure 3.10.

When the wavelength is equal to the span length (this corresponds to a wavenumber of 10.4 rad/m in Figure 3.7), the magnitude of the point receptance should be minimum for excitation acting either at mid-span or above a sleeper. For the lateral bending wave the frequency corresponding to this situation is about

1600 Hz, while for the torsional wave and the first order web bending wave the corresponding frequencies are about 2400 Hz and 2600 Hz respectively. The troughs near these frequencies can be observed in Figure 3.12, which are marked with d, e and d', e' for the excitation acting at mid-span and above a sleeper respectively. Because 2400 Hz and 2600 Hz are very close, the two troughs corresponding to the torsional wave and the first order web bending wave are combined. For the second web bending wave no trough is observed because vibration at very high frequency is less affected by the supports. Unfortunately, for other peaks and troughs marked with 1 – 3 and 1'– 3' no clear physical explanations can be found. They are possibly due to the superposition of different waves and related to the periodic supports. Figure 3.13 shows the point receptances from the track with the span length d = 0.7 m instead of d = 0.6 m. It is clear from Figure 3.13 that the peaks and troughs marked with 1 – 3 and 1'– 3' appear at lower frequencies due to the larger span length.

The cross receptances are shown in Figures 3.14 and 3.15 which are the responses to the excitation acting at mid-span and above a sleeper respectively. Figures 3.14(a) and 3.15(a) show the translational cross receptance, Figures 3.14(b) and 15(b) the rotational cross receptance. Solid lines and dashed lines represent the responses of the rail head and foot respectively to a force at the top of the rail head. The lateral displacements are the responses in the centre of the rail head or foot.

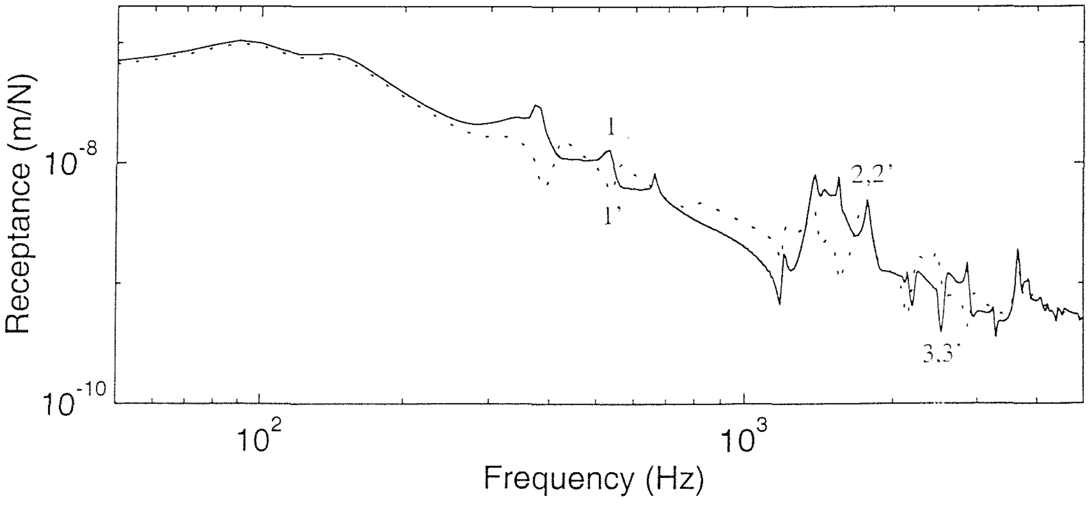

Figure 3.13. Amplitude of the point receptance for lateral vibration of the discretely supported rail, span length d = 0.7 m. Keys as for Figure 3.12.

Compared with the continuously supported rail model (Figure 3.11), some similar properties can be seen in Figures 3.14 and 3.15. The responses of the rail head are generally higher than those of the foot in most frequency regions. At low frequencies both the lateral displacement and the rotation curves fluctuate smoothly. However, at high frequencies these curves fluctuate sharply with many peaks and troughs because of the effects of the discrete supports.

Although the cross receptances seem to be more complicated than the point receptances, some specific points can still be observed. The pinned-pinned resonance due to the torsional wave can be seen clearly at about 850 Hz in terms of

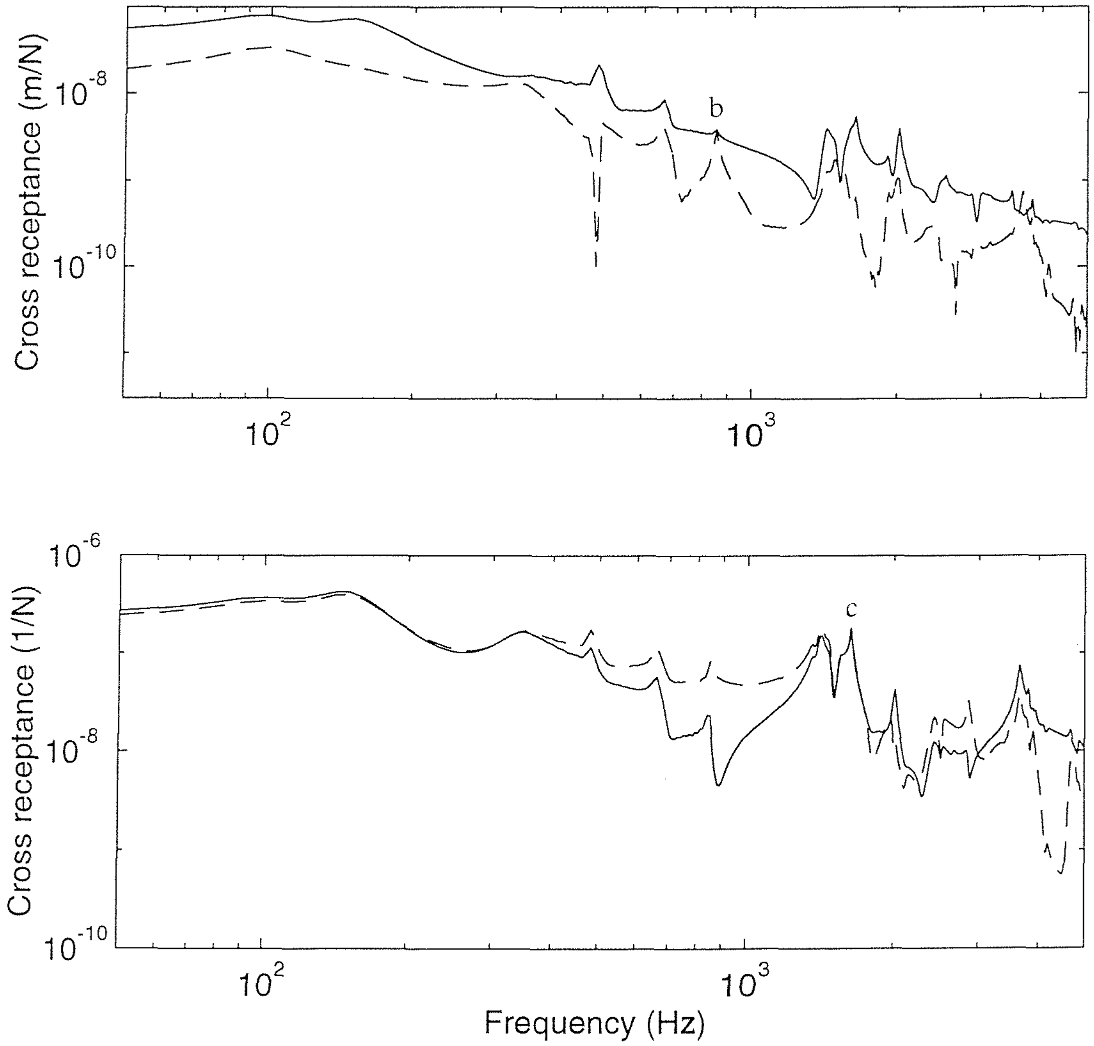

Figure 3.14. Cross receptances for lateral vibration of the discretely supported rail with excitation acting at mid-span at the top of the rail head. (a) translational response, (b) rotational response. — for rail head, - - - for rail foot.

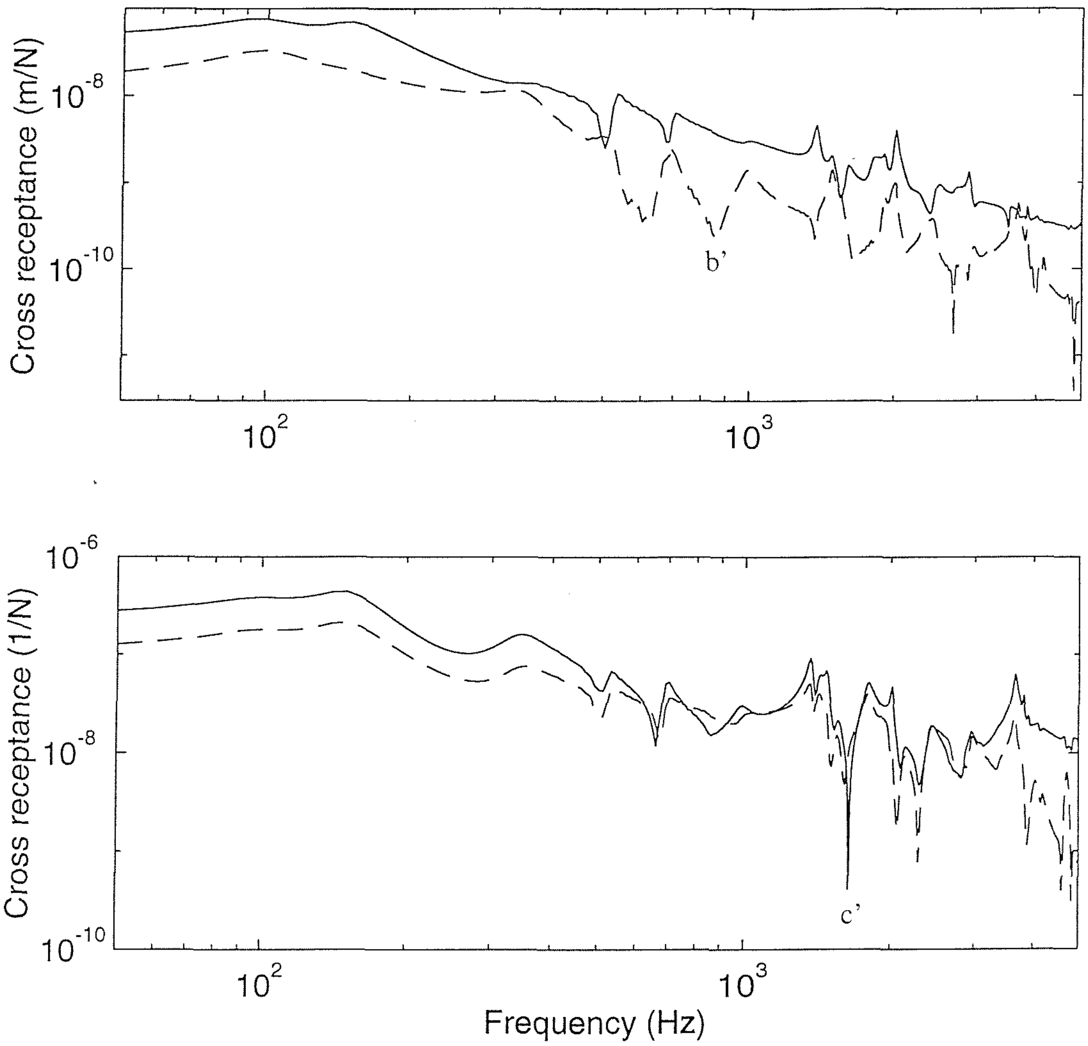

Figure 3.15. Cross receptances for lateral vibration of the discretely supported rail with excitation acting above a sleeper at the top of the rail head. (a) translational response, (b) rotational response. — for rail head, - - - for rail foot.

the rail foot displacements from Figures 3.14(a) and 3.15(a), and is marked with b and b'. Another pinned-pinned resonance due to the first order web bending wave at about 1700 Hz can be seen much more sharply in terms of the rotations, and is marked with c and c' in Figures 3.14(b) and 3.15(b). The cross receptance curves of the rail head displacement in Figures 3.14(a) and 3.15(a) can be seen to be similar to the point receptance curves shown in Figure 3.12 but are smoother at high frequencies. As in the continuously supported rail model there is again almost no peak appearing for the rail head displacement at the second web bending cut-on frequency.

3.5.4. *Comparison with experimental results*

While no new measurements have been made for this part of the study, some experimental results are available in [95]. One of them was obtained from UIC 60 rail with concrete monobloc sleepers. The measurements were carried out on unloaded tracks by means of impact excitation using an instrumented hammer. For lateral vibration the excitation acted in the centre of the rail head and the accelerance at the same place on the opposite side was measured. The measured and

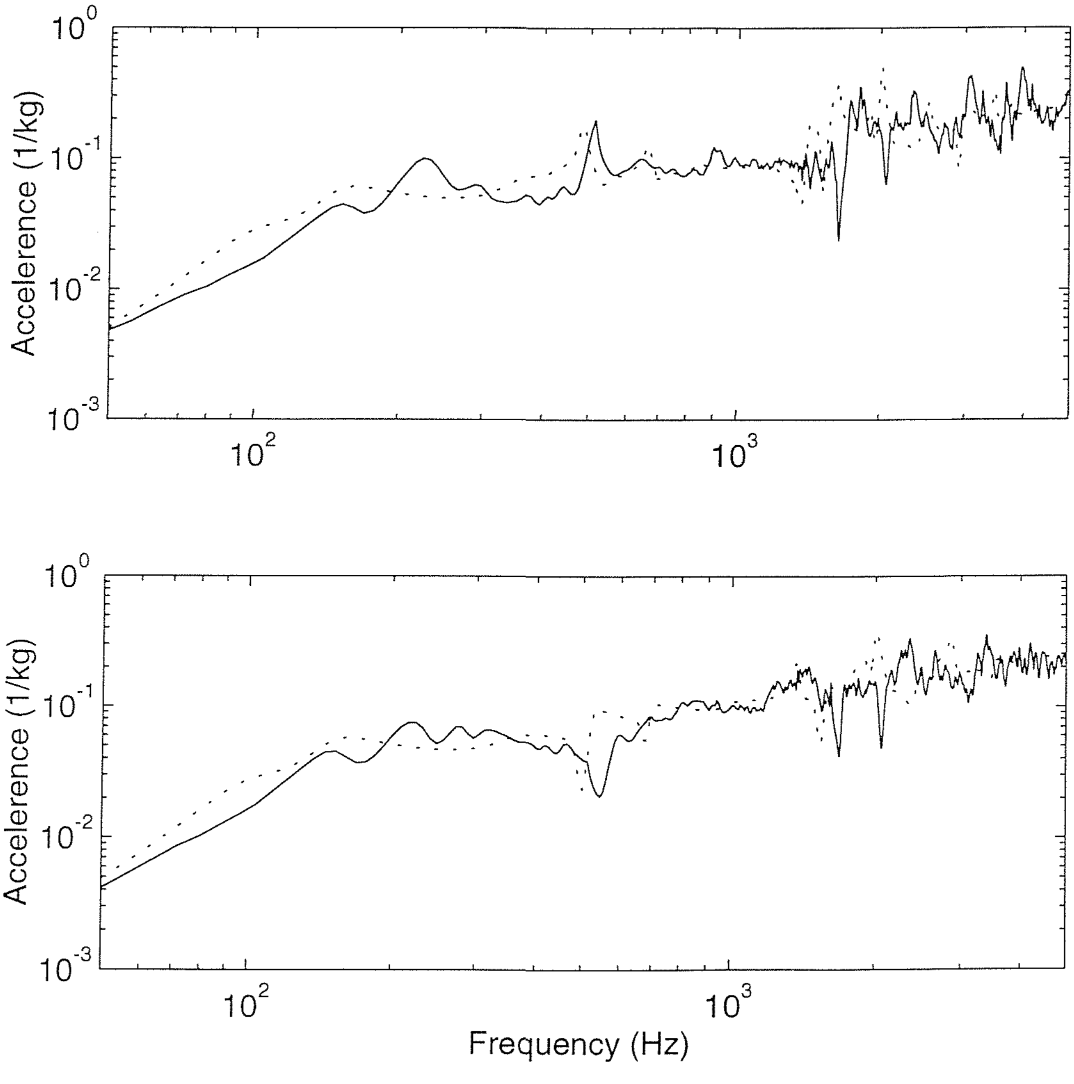

Figure 3.16. Comparison of predictions from the discretely supported rail model and measurements. Both excitation and response are at the centre of the rail head. (a) excitation acting at mid-span, (b) excitation acting above a sleeper. — from measurements (from [95]), ······ from predictions.

predicted lateral accelerances in the centre of the rail head are compared in Figures 3.16(a) and 3.16(b) which are for the excitation acting at mid-span and above a sleeper respectively. The input parameters for the track are as in previous sections. A good agreement can be seen from Figure 3.16 throughout the frequency region from 50 Hz to 5000 Hz. The main deviation is that the response peaks in the predictions from the multiple beam model are shifted towards lower frequencies. This is probably due to the simplification of the rail cross-section. The connections between the web and head and between the web and foot of an actual rail have a tapered transition so that the real rail is stiffer than the simplified version and thus the response peaks appear at higher frequencies in the measurements. Furthermore, the parameters of the track foundation used in the model, which are based on those given in [95], seem to be lower than the realistic values and this results in a higher accelerance at low frequencies from the predictions.

3.6. Transfer receptance and vibration decay along the rail

The lateral vibration decay along the rail can be investigated through the transfer receptance of the rail, which represents the combined wave (the lateral bending wave, the torsional wave and the web bending waves) propagation decay along the rail. Figure 3.17 shows the transfer receptances for the continuously supported rail at selected frequencies. Figure 3.18 shows equivalent results for the discretely supported rail with the external excitation acting at mid-span. Each Figure contains six parts for excitation frequencies at 200 Hz, 500 Hz, 1200 Hz, 1600 Hz, 3200 Hz and 3800 Hz. Both the excitation and the response are at the top of the rail head in each case. In Figures 3.17 and 3.18 the upper line represents the receptance amplitude, while the lower line represents the real part of the receptance. From the real part the variation of wavelength with frequency can be observed. In the continuously supported model the interval between two points, at which the receptances are calculated, is 0.06 m, while in the discretely supported model it is 0.15 m. Although this is sufficient to resolve the wavelengths at the lower frequencies, at the highest frequencies it can lead to some spatial aliassing effects (compare Figures 3.17 with 3.18). Nevertheless the global effects can be detected in

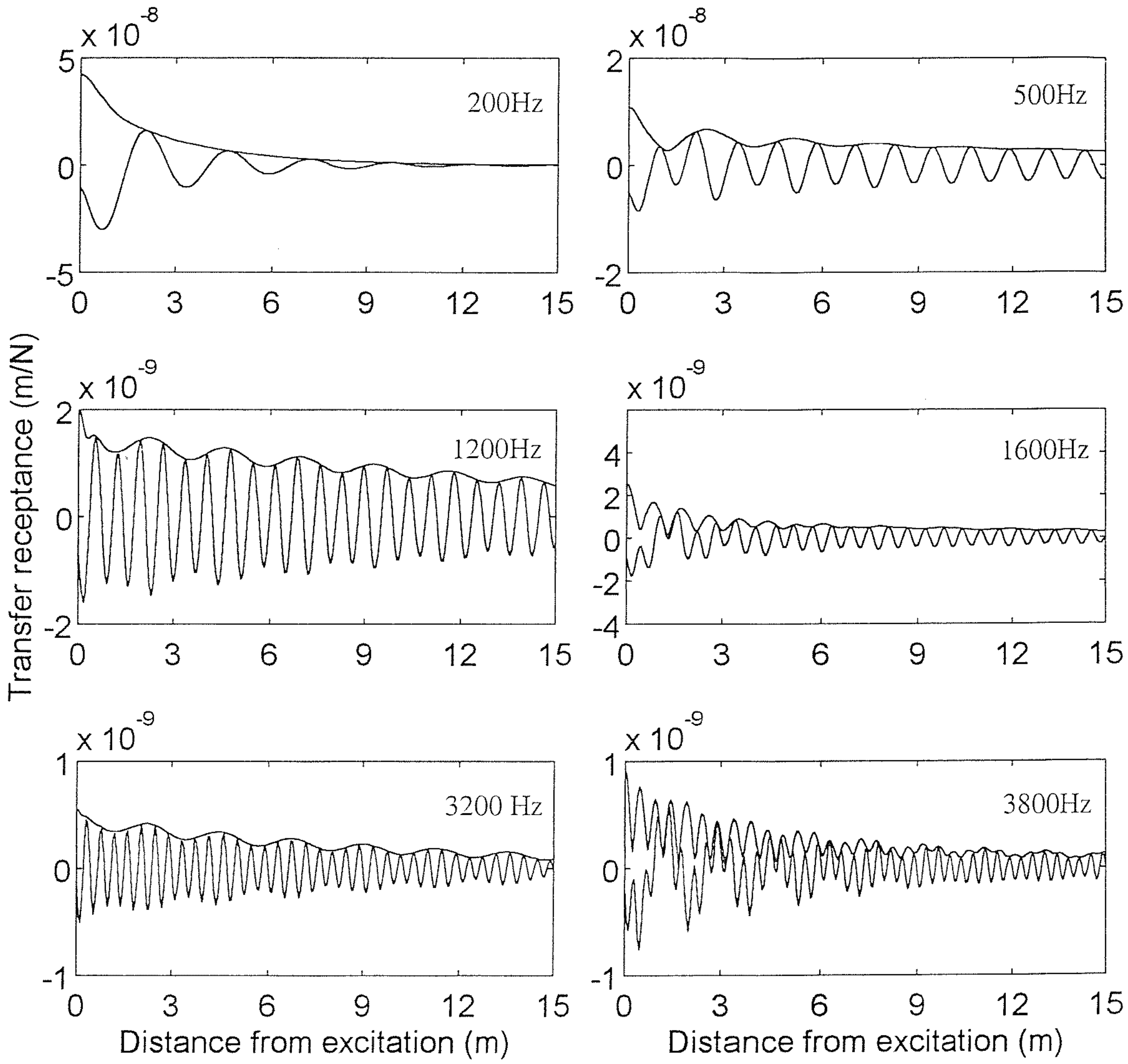

Figure 3.17. Combined wave propagation decay in the continuously supported rail. upper lines: amplitude of transfer receptance, lower lines: real part of transfer receptance.

these graphs.

It can be seen from Figures 3.17 and 3.18 that the lateral vibration decay becomes more and more complicated with increasing frequency because after each cut-on frequency one more propagating wave will be added to the response and each wave has its own decay rate (see Figure 3.9). The superposition of different waves can lead to a 'beating' effect, see for example the result at 1200 Hz in Figure 3.17. At this frequency the difference between the wavenumbers of the lateral and torsional waves is about 2.7 rad/m (see Figure 3.8) which corresponds to a 'beating wavelength' of 2.3 m which is observed in the receptance amplitude. In general, the

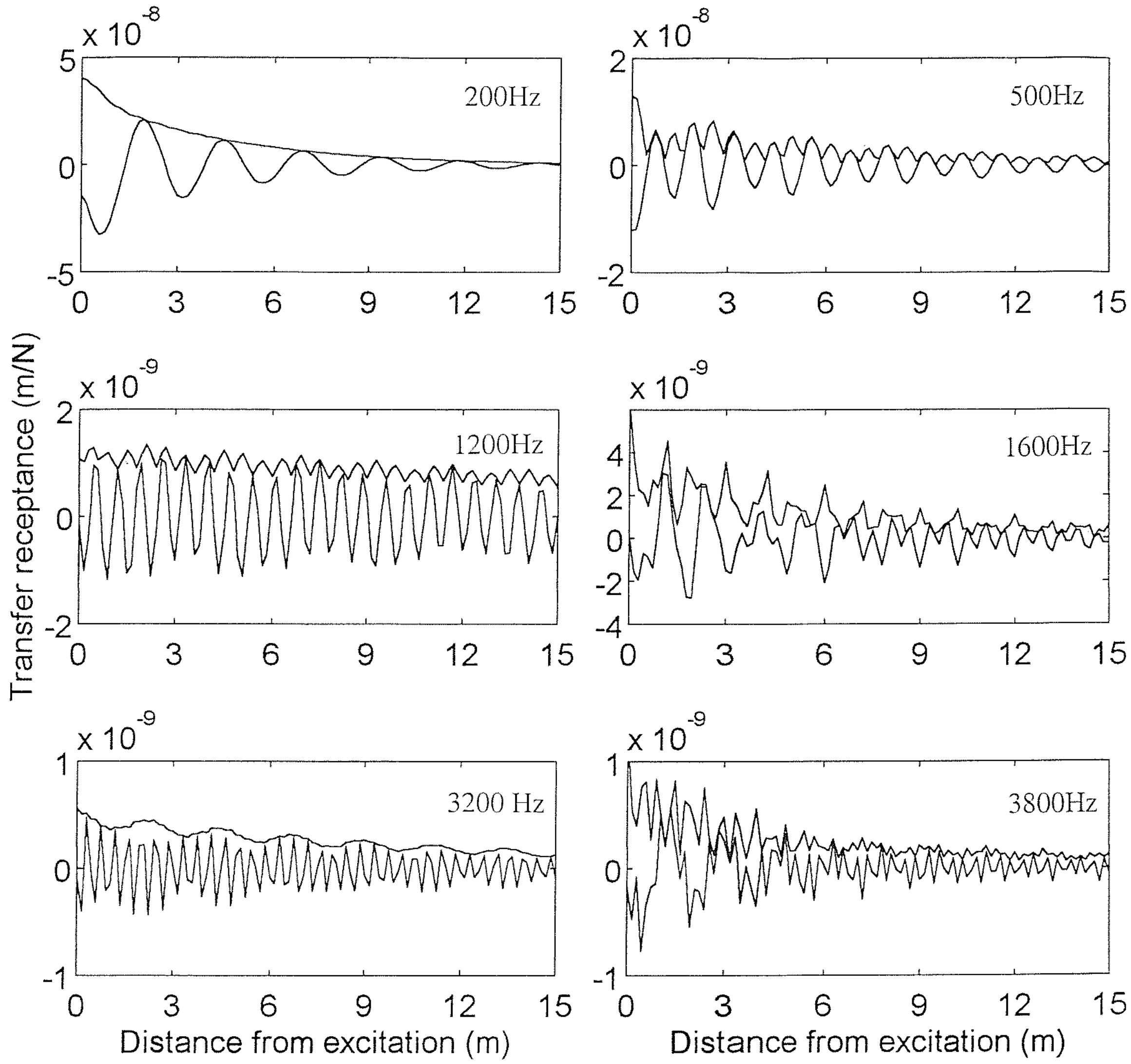

Figure 3.18. Combined wave propagation decay in the discretely supported rail with excitation acting at mid-span. upper lines: amplitude of transfer receptance, lower lines: real part of transfer receptance.

vibration decay gradually reduces from low frequencies to high frequencies except at the cut-on frequencies. Around the cut-on frequencies the transfer receptances experience a noticeable change. After each cut-on frequency a new wave joins the response with its initial long wavelength (low wavenumber). This new wave combined with other relatively short waves forms a compound wave. On the other hand, the new wave has a higher decay rate near its cut-on frequency (see Figures 3.8 and 3.9), so that it decays more quickly than other short waves and at larger distances the short waves are dominant. This can be seen in the graphs for 500 Hz, 1600 Hz and 3800 Hz in Figures 3.17 and 3.18. For example, it can be seen from Figure 3.17 that at 3800 Hz the second web bending wave is a new contributed wave with long wavelength and decays quickly, so that the short waves are dominant at larger distances. Because of the higher decay rate of the new wave near the cut-on frequency the initial decay rate of the compound wave also becomes higher shortly after the cut-on frequency.

The pinned-pinned vibration behaviour can be observed in the transfer receptances of the discretely supported model, a feature not seen in the results of the continuously supported rail model. From Figure 3.18 it can be seen that the transfer receptance amplitude fluctuates with a period length related to the span length particularly at 500 Hz (first lateral pinned-pinned resonance) and 1200 Hz.

The decay rates of different waves in the continuously supported rail are compared with the measurement data from [95] in Figure 3.19. The measured results represent the average decay rate of the compound wave whereas the predictions show the result for each wave separately. The measurement will tend to be dominated by the wave with the lowest decay rate. It can be seen that the tendency of the decay rates from the theoretical model is consistent with the measurement, apart from the high frequency region. Above 3500 Hz the theoretical model is over damped by the loss factor for the rail which has been chosen as

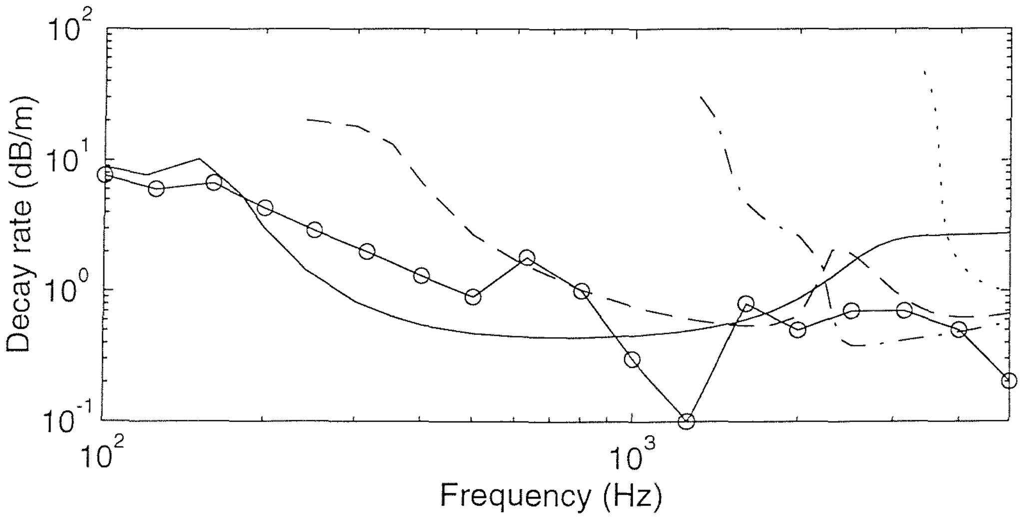

Figure 3.19. Decay rates of rail vibration, $\eta_r = 0.01$. o—o measured (from [95]), — wave I, - - - wave II, -·-·- wave III, ······ wave IV (from continuously supported rail model).

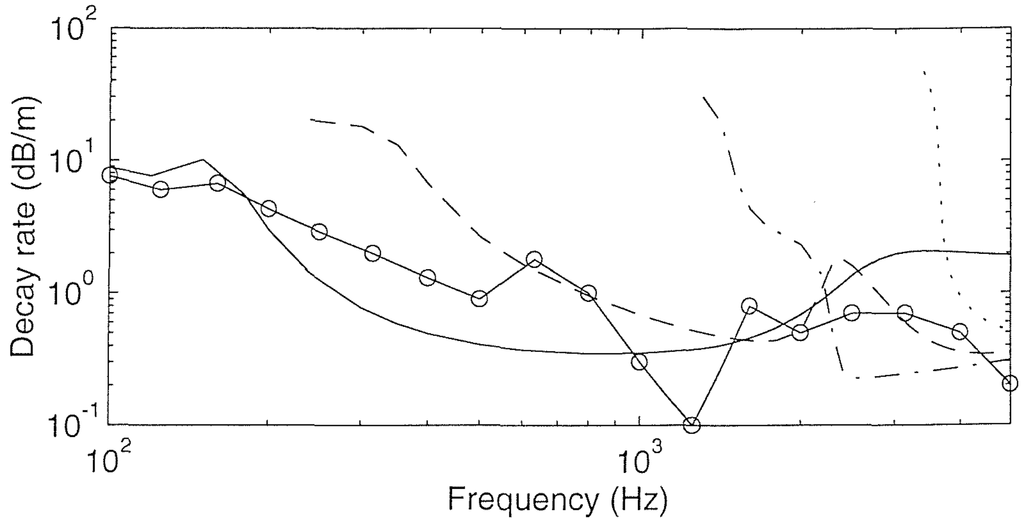

Figure 3.20. Decay rates of rail vibration, $\eta_r = 0.005$. Keys as for Figure 3.19.

$\eta_r = 0.01$. However, setting $\eta_r = 0$ led to very low decay rate in this high frequency region. Figure 3.20 shows the results from $\eta_r = 0.005$. The decay rates above 3500 Hz can be seen to be closer to the measurement data compared with $\eta_r = 0.01$.

3.7. Conclusions

In this chapter a multiple (interconnected) beam model has been presented for studying the lateral vibration behaviour of railway track. This simplified model is less complex than the commonly used FE models but all essential cross-sectional deformations of the rail can be included. Detailed investigation of the lateral vibration for both continuously and discretely supported rail has been carried out efficiently using this model. The results of the free wave dispersion relation from this model have shown a good agreement with an FE model which justifies the neglect of the web twisting and bending stiffnesses in the direction of the rail axis. Good agreement between the predictions and measurement data has also been reached in terms of accelerance.

Compared with the continuously supported rail model, the predictions from the discretely supported rail model show that the track support has significant effects on the lateral vibration in the frequency region from about 400 Hz to 3000 Hz which is of most importance for noise radiation. Many peaks or troughs of the receptance appear in this region. Among them are three pinned-pinned resonances corresponding to the bending wave, torsional wave and the first web bending wave, so that for the lateral vibration the pinned-pinned effects are more complicated than for vertical vibration due to the presence of multiple waves. All these suggest that a discretely supported rail model is more appropriate in this frequency range. The decay of the lateral vibration with distance also has complicated behaviour due to the presence of multiple waves. In general the lateral vibration decay rate decreases from low frequency to high frequency, with some temporary increase near cut-on frequencies.

The parameter identification of a realistic rail and its support is crucial for an improved prediction from the model. An initial FE calculation of the cross-section of a rail shows that the cut-on frequencies of the web bending of a realistic UIC 60 rail are 1358 Hz and 4192 Hz, whereas the results from the simplified cross-section version of Figure 4 are 1300 Hz and 3623 Hz (also from an FE calculation). The differences in terms of the wave dispersion relation are shown in Appendix C between the FE models of the simplified cross-section and the original cross-section for UIC 60 rail. The wave dispersion relation from the multiple beam model with improved parameters in accordance with the original UIC 60 rail is also presented in Appendix C.

CHAPTER 4

The Effects of a Single Wheel Load on the Foundation Stiffness and Rail Vibration

In this chapter the preloads in the pad and ballast caused by a single wheel load are studied by considering the non-linear properties of the track foundation, and thus the preloaded pad and ballast stiffnesses are determined. A model of the track dynamics based on an infinite discretely supported Timoshenko beam with preloaded pad and ballast dynamic stiffnesses is developed. Its vertical vibration behaviour under the influence of the local wheel load is investigated. It is shown that the point receptance for vertical vibration is strongly affected by the local wheel load at low frequencies, but the effect of the local wheel load on the average wave propagation decay rate along the rail is very limited.

4.1. Introduction

As discussed in chapter 1 many different models have been developed to investigate the dynamic properties of railway track over the years. In all these models the resilient components in the foundation layers or at the periodic supports such as the railpad and the ballast have significant effects on the track vibration, noise radiation, the contact force between rail and wheel and the generation of rail corrugations. Usually, their parameters are considered uniform in these models. For example, the pad stiffness and the ballast stiffness are regarded as constant along the whole railway track or assigned the same value at each support. In fact these parameters vary with load and frequency. Measurements by Thompson et al. [89] (see also [10]) have shown that the pad stiffness can vary dramatically with preload and also varies with vibration frequency. The ballast stiffness is also strongly dependent upon load and frequency, see Frémion [12]. When a train moves along the rail, it applies a preload on the rail and its foundation in a local area around each wheel. Therefore, the pad and ballast stiffness near the wheel are different from those which apply at a distance along the rail. This affects the dynamic behaviour of the track, and thus the rail vibration and noise radiation etc.

The aim of this chapter is to study the vertical rail vibration properties considering the pad and ballast stiffness variations due to wheel preload. Although the behaviour of pads and ballast is non-linear, it is assumed that the dynamic behaviour can be represented by a linear model with stiffnesses that are chosen according to the quasi-static load, since the dynamic displacements are small. Firstly the non-linear load-deflection and load-stiffness laws for both railpad and ballast are introduced according to Thompson [89] and Frémion [12]. Then they are combined to obtain the load-deflection property of the whole rail foundation. After this, the rail deflection and the reaction force in the foundation under a wheel load are calculated in order to obtain the different preloads in the pad and ballast at the different supports along the track. Knowing the preloads in the pad and ballast, the dynamic stiffness of the preloaded pad and ballast can be determined from data in references [89] and [12]. Finally a discretely supported Timoshenko beam model is employed for the dynamic behaviour of the track and the receptances and the wave propagation decay rates for vertical rail vibration are calculated considering the preloaded pad and ballast stiffnesses which have different values at different supports. The method derived here is applied to a track consisting of UIC 60 rails on monobloc concrete sleepers. The railpads are Pandrol studded 10 mm pads because the available measurement data in [89] is for these pads. However, the principles involved can be applied to any pad. The study in this chapter shows that when the preloaded pad and ballast stiffness are considered, the results are quite different from the model in which only the uniform values of the pad and ballast stiffness are employed. However, it is possible to derive an approximate method for using the simpler model by a combination of loaded and unloaded parameter values.

4.2. Stiffness of railway track foundation

In order to determine the preloaded pad and ballast stiffnesses, the values of preload in the pad and ballast should be known in advance. In practice this preload is caused by the weight of a train and is transmitted through the wheels to the rail and its foundation. It is effectively a static problem to determine the preload in the pad and ballast. It is therefore assumed that the quasi-static behaviour of the pad and ballast can be approximated by that under a static wheel load. Although this assumption is not strictly correct, since the loading/unloading due to a wheel occurs within about 0.1 second, it is sufficient for a first study. Only one wheel load is considered for simplicity and at this stage the railway track is simplified to an infinite uniform beam on a continuous elastic foundation. However, this foundation, composed of railpads and ballast, has a non-linear behaviour because both railpad and ballast stiffnesses are non-linear. Therefore, the non-linearity of the railway track foundation should be studied first.

4.2.1. *Pad stiffness*

Both the static and dynamic stiffness of the railpad considered here have been measured by Thompson et al. [89]. The static load-deflection and load-stiffness curves are shown in Figure 4.1, the stiffness being defined here as the inverse of the gradient of the load-deflection curve. The static stiffness can be seen to be relatively constant for preloads up to 20 kN, above which it increases sharply. Values of the static and dynamic stiffness at selected preloads are given in Table 4.1. The dynamic stiffness is mildly frequency dependent and the values given in Table 4.1 apply at the

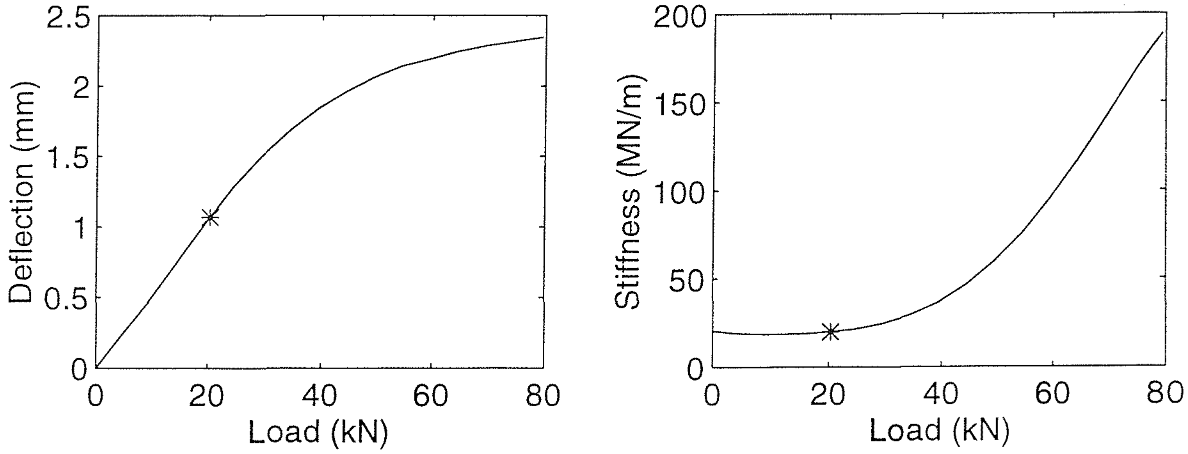

Figure 4.1. Static load-deflection and load-stiffness curves for Pandrol studded 10 mm railpad (redrawn from [89]). * initial preload point.

frequencies listed. It can be seen that the dynamic stiffness is much higher than the static stiffness at the same preload level. The dynamic/static stiffness ratio has been derived from the data from [89]. It is used in sections 4.4. and 4.5. In general, the rail is fixed to the sleepers by clips. The clip applies a preload on the railpad which is about 20 kN for each pad. In addition the weight of the rail is also applied onto the pad as a preload. For UIC 60 rail (60 kg/m) and a 0.6 m distance between two sleepers each railpad is subjected to about 0.36 kN rail weight load. Thus the initial preload in the railpad is about 20.36 kN. In Figure 4.1 this preload point is marked by '*'.

4.2.2. *Ballast stiffness*

Detailed data for the ballast stiffness are not available at present, but some work on the ballast stiffness is helpful to estimate the elastic properties of the railway foundation. According to direct dynamic measurements, an indication of the ballast stiffness variation has been given by Frémion et al. [12]. It is found that vertical stiffness of the ballast is influenced by a static preload and increases significantly with frequency. They suggested that the ballast stiffness may be assumed to follow the Hertz law ($W^{1/3}$ where W is the static preload) because this is consistent with the experimental results. A summary of the direct stiffness measurements from [12] is given in Table 4.2. It can be seen that a doubling of the ballast stiffness occurs from

Table 4.1

Static and dynamic stiffness of Pandrol studded 10 mm railpad (from [89])

Preload (kN)	20	30	40	60	80
Static stiffness (MN/m)	19	25	37	95	200
Dynamic stiffness at 50 Hz (MN/m)	61	82	130	300	650
Dynamic stiffness at 200 Hz (MN/m)	69	92	140	330	690
Dynamic stiffness at 500 Hz (MN/m)	81	110	170	390	780
Dynamic/static stiffness ratio at 50 Hz	3.2	3.3	3.5	3.2	3.3
Dynamic/static stiffness ratio at 200 Hz	3.6	3.7	3.8	3.5	3.6
Dynamic/static stiffness ratio at 500 Hz	4.3	4.4	4.6	4.1	3.9

50 Hz to 200 Hz and again from 200 Hz to 500 Hz, and changing the preload from 1.2 kN to 11 kN leads to a doubling of the vertical stiffness. However, when the preload increases from 11 to 21 kN, the vertical stiffness increases only by about 15 %.

By use of the data in Table 4.2 and the suggestion that the vertical stiffness follows the Hertz law, it may be assumed that the ballast stiffness k_b can be represented by

$$k_b = a\sqrt[3]{F_b} \tag{4.1}$$

where F_b and a are the load and the constant coefficient respectively. Because stiffness is the derivative of the load with respect to the deflection u:

$$k_b = \frac{dF_b}{du}$$

the load-deflection law for ballast can be derived from it and has the form of

$$u = \frac{1.5}{a}\sqrt[3]{F_b^{\,2}} \tag{4.2}$$

The load-stiffness and load-deflection curves for the ballast at 50 Hz and 200 Hz are shown in Figure 4.2, where the constant coefficient a is determined using the data at the static load of 11 kN. The ballast stiffness can be seen to increase very sharply when the preload increases from zero and the rate of increase becomes smaller as the preload increases further. Therefore, the incremental tendency of the ballast stiffness is the opposite to that of the pad stiffness. The initial preload in the ballast is from the rail weight and the sleeper weight. A concrete sleeper weighs about 3 kN. The weight of half a sleeper and 0.6 m rail forms the initial preload in

Table 4.2

Vertical ballast stiffness for a sleeper block with an area of 0.23m^2 (from [12])

Static load (kN)	50 Hz (MN/m)	200 Hz (MN/m)	500 Hz (MN/m)
1.2	50	130	-
11	120	210	420
21	125	240	480

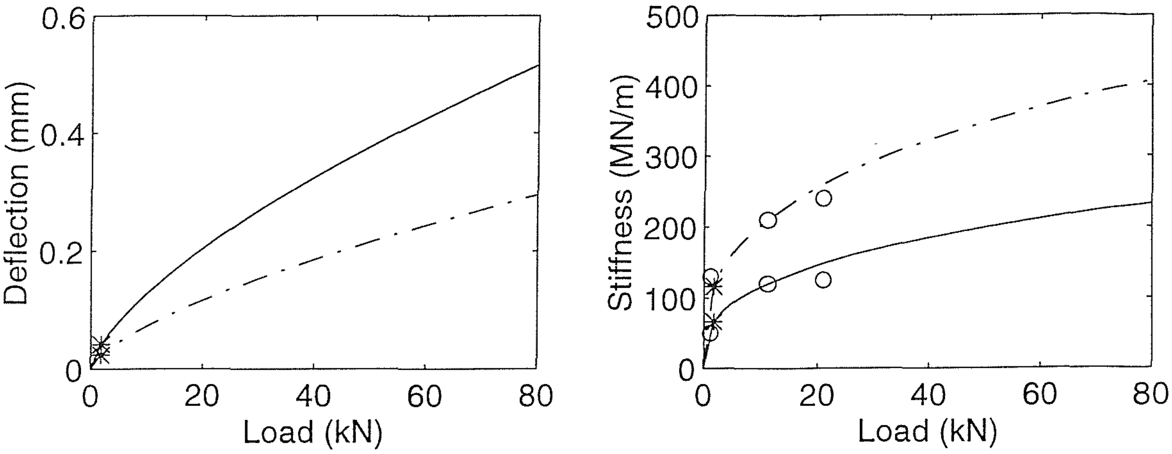

Figure 4.2. Dynamic load-deflection and load-stiffness curves for ballast at 50 Hz and 200 Hz. — at 50 Hz, – · – , at 200 Hz, * initial preload point, o points from Table 4.2.

the ballast at each support, which is about 1.86 kN and marked by '*' in Figure 4.2. Some other data about the ballast stiffness can be found in Appendix D, which confirm the load-deflection relationship given above.

4.2.3. *Railway track foundation stiffness*

The elasticity of the rail foundation is formed by both railpad and ballast, but here the superposition principle does not hold because of their non-linearity. To obtain the load-deflection and load-stiffness laws of the foundation the whole evolution of the deformation from zero in the pad and ballast should be taken into consideration. Figure 4.3 shows the loads on the pad and the ballast. W_r and W_s represent the weights of the rail in one span and of the sleeper respectively, F_c is the preloads from the clips, F is the external load and Δu_p and Δu_b represent deflections of the pad and the ballast respectively caused by F. The following values are used for the parameters (as above):

$$W_r = 0.36 \text{ kN}, \qquad W_s = 1.5 \text{ kN}, \qquad F_c = 20 \text{ kN}$$

The total foundation deflection u should be equal to the sum of the pad deflection and the ballast deflection:

$$u = \Delta u_p + \Delta u_b \tag{4.3}$$

Since the clip is much softer than the pad, F_c can be regarded as constant when the pad is subjected to a deformation caused by the external load F. Thus the pad

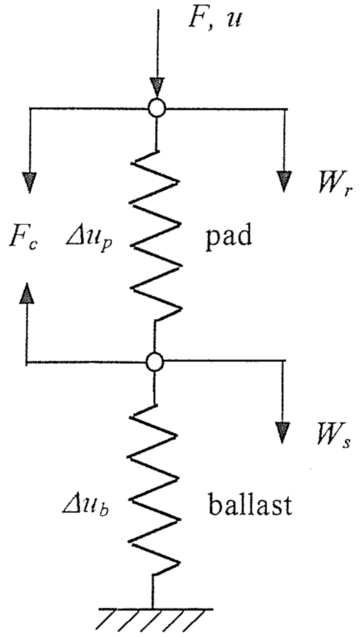

Figure 4.3. Loads on the pad and ballast.

deflection Δu_p and the ballast deformation Δu_b under the external load F can be written as

$$\Delta u_p = u_p(F + F_c + W_r) - u_p(F_c + W_r) \tag{4.4a}$$

$$\Delta u_b = u_b(F + W_r + W_s) - u_b(W_r + W_s) \tag{4.4b}$$

where $u_p(F)$ and $u_b(F)$ are the deflections as a function of load of the pad and ballast respectively.

Because data for the ballast static stiffness are not available, it is assumed here that the ballast static stiffness may be estimated to have values that are 25 %, 50 % or 100 % of the dynamic stiffness at 50 Hz, which are represented as soft, medium and stiff ballast assumptions respectively. The stiff ballast assumption partly takes account of the fact that a monobloc sleeper has a larger base area in contact with ballast, whereas the values in Table 4.2 were measured with bibloc sleepers. Using the load-deflection curves in Figure 4.1 for the pad and the load-deflection law in equation (4.2) for the ballast, the load-deflection law for the complete rail foundation can be obtained by equations (4.3) and (4.4). Figure 4.4 shows these combined load-deflection and load-stiffness curves of the rail foundation. The load-stiffness curve is derived from the load-deflection curve. Three graphs are shown,

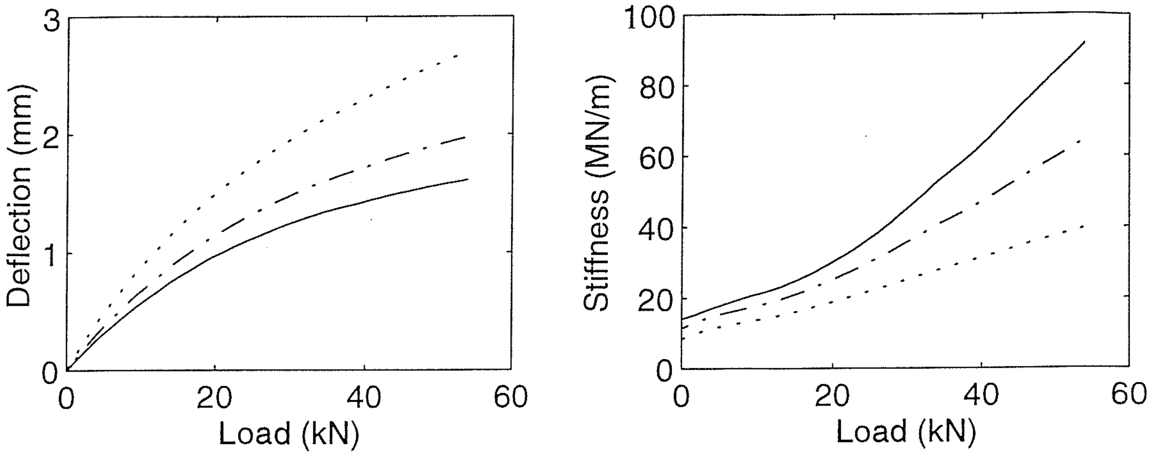

Figure 4.4. Foundation load-deflection and load-stiffness curves. — stiff ballast, - · - medium ballast, ······ soft ballast.

respectively, the soft, medium and stiff ballast assumptions. It can be seen that the rail foundation retains non-linearity through the combination of pad and ballast behaviour.

4.3. Deflection and reaction force in the track foundation under the wheel load

4.3.1. *Equation for the beam on a non-linear elastic foundation*

In order to determine the deflection and reaction force in the track foundation due to a wheel load, the wheel load can be represented by a concentrated load and the railway track is simplified to an infinite uniform beam supported by a continuous elastic foundation. For the beam on a linear elastic foundation Timoshenko gave an exact solution in [94]. However, the railway track foundation considered here is non-linear rather than having a constant modulus. This makes the problem much more difficult to solve than the linear elastic case.

The differential equation for the rail deflection has the form of

$$EI\frac{d^4u}{dz^4} = -\frac{F(u)}{d} \tag{4.5}$$

where *F(u)* is the reaction force in the foundation of one span as a function of deflection *u* and *d* is the span length. *EI* is the bending stiffness of the beam and *z* is the distance along the track. *F(u)* is determined by the load-deflection law in Figure

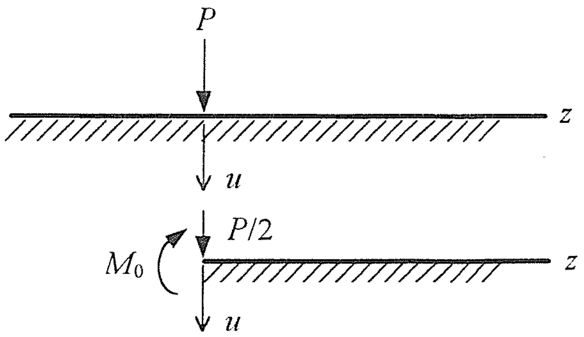

Figure 4.5. Beam on the elastic foundation. By symmetry with suitable boundary conditions the upper system can be replaced by the lower system.

4.4. The rail and sleeper weights vanish now because their effect has already been included in the procedure for deriving the load-deflection law of the foundation. Only half of the beam need be considered due to the symmetry condition at the load point, see Figure 4.5. The boundary conditions for equation (4.5) are:

$$u'(0) = 0 \tag{4.6a}$$

$$u'''(0) = \frac{P}{2EI} \tag{4.6b}$$

$$u(\infty) = 0 \tag{4.6c}$$

$$u'(\infty) = 0 \tag{4.6d}$$

where P is the wheel load acting at the position $z = 0$ and $'$ indicates the derivative with respect to z. Boundary conditions (4.6c) and (4.6d) mean that at points infinitely distant from the load P the deflection and the slope vanish.

4.3.2. *Numerical solutions—deflection and reaction force in foundation*

Equation (4.5) with the boundary conditions (4.6) forms a non-linear boundary value problem which may be solved numerically. It is difficult to solve because equation (4.5) is a fourth order differential equation and some boundary conditions in (4.6) should be satisfied at the infinitely distant points. The starting point for the numerical calculation should be chosen at $z = 0$. There are two parameters at $z = 0$ which have to be estimated in order to meet the boundary conditions at $z = \infty$. These are $u(0)$ and $u''(0)$. For performing the numerical calculation some points should be considered:

(1) It is impossible to meet the boundary conditions at $z = \infty$ because the errors introduced by numerical approximations will ruin the solution as z becomes very large. By referring to the analytical solution of the beam on a linear elastic foundation, a reasonable value may be estimated for z, at which the boundary conditions should be satisfied instead of at $z = \infty$. In the case of the linear elastic foundation the beam deflection is given as follows [94]:

$$u = \frac{P\beta}{2k} e^{-\beta z} (\cos\beta z + \sin\beta z) \tag{4.7}$$

where $\beta = \sqrt[4]{k/(4EI)}$, k is the constant modulus of the foundation. The deflection can be seen to decay very quickly with the power of $-\beta z$. u', u'' and u''' have the same decay rate as u. From the author's experience, the boundary conditions at $z = \infty$ may be regarded as the boundary conditions at $z = 4 \sim 5$ m, and will be shown in the results below.

(2) Since there are two values required at the beginning, $u(0)$ and $u''(0)$, the normal 'shooting method' [2] is not appropriate. Here a simple direct 2-D searching method is developed. It is divided into two stages. Firstly, the searching procedure is performed in a larger area with a large step size to obtain a rough solution. Then the same procedure is performed but in a small area and with a fine step size. This method is found to be quite effective for 2-D searching.

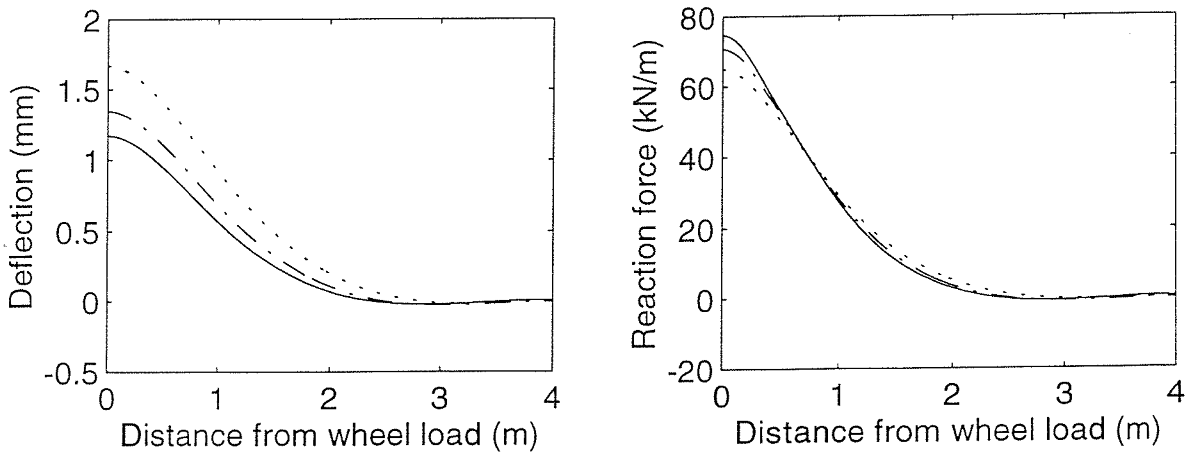

Figure 4.6. Foundation deflection and reaction force under 75 kN wheel load. — stiff ballast, - · - medium ballast, ······ soft ballast.

The numerical results of both the foundation deflection and the reaction force in the foundation are shown in Figure 4.6, where the span length $d = 0.6$ m, the wheel load $P = 75$ kN and $EI = 6.4 \times 10^6$ Nm^2 for UIC 60 rail. Three curves are shown representing the results from the soft, medium and stiff ballast stiffness assumptions. It can be seen that the foundation deformation occurs only in the near field of the wheel load. At $z = 0$, where the load P acts, the deflection has its maximum value, but from about $z = 2.3$ m for the stiff ballast, $z = 2.5$ m for the medium one and $z = 3$ m for the soft one the foundation deflection is almost zero (Note—although negative deflection occurs, neither the ballast nor the pad unload completely). The stiffer the foundation is, the smaller the maximum deflection at $z = 0$, and the quicker the decay of the deflection. The decay rate of the deflection is similar to that in the case of the linear elastic foundation, in which it is $e^{-\beta z}$. The curve of the reaction force in the foundation is similar to the deflection. The reaction force also occurs only in the near field of the wheel load and has the maximum value at $z = 0$. The stiffer foundation has a larger maximum reaction force. For the reaction force the decay rate is also higher for the stiffer foundation, but in the area near to $z = 0$ it is noticeably sharper than the deflection decay. This is because the stiffness of the foundation increases with increasing deflection. For smaller deflections the foundation is softer, and thus the reaction force is smaller still.

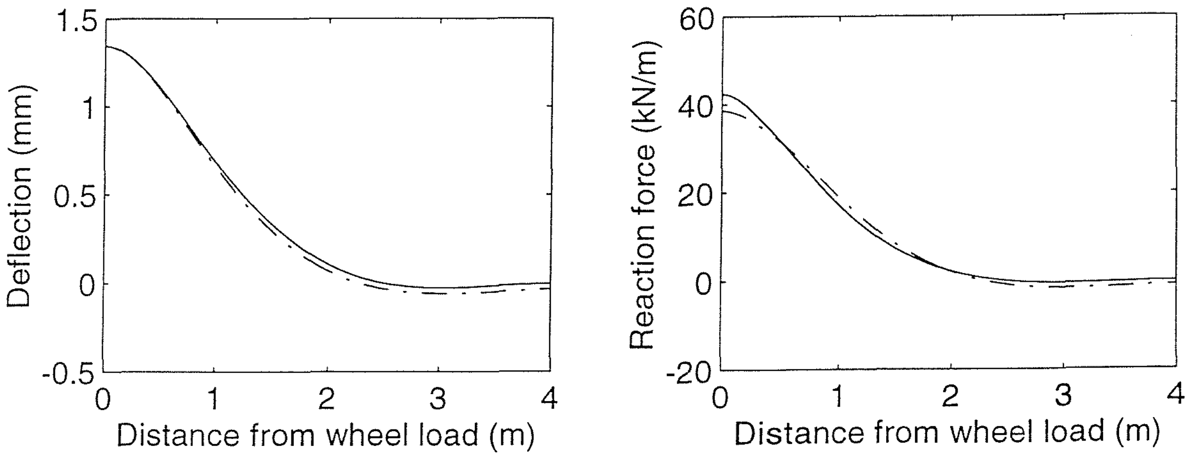

Figure 4.7. Comparison of the results from non-linear foundation model and equivalent linear foundation model, P = 75 kN, medium ballast. — non-linear foundation, -·-·- linear foundation (k = 28.71 MN/m^2).

For comparison, Figure 4.7 shows the foundation deflection and the reaction force from a linear elastic foundation model having a constant modulus k equivalent to the medium ballast assumption and the wheel load $P = 75$ kN. k is chosen to give the same maximum deflection as the non-linear elastic foundation using the following formula,

$$u(0) = \frac{P\beta}{2k} \tag{4.8}$$

where $u(0)$ is the deflection at $z = 0$ from the non-linear foundation model, and $\beta = \sqrt[4]{k/(4EI)}$. It can be seen from Figure 4.7 that the foundation deflection of the linear model is quite close to that of the non-linear model, but the reaction force is not as sharp as in the non-linear model. The region with negative deflection and reaction force is greater in the linear case than in the non-linear case. It should be pointed out that there is no general approximate linear solution for the non-linear elastic foundation model because the equivalent constant stiffness needs to be determined using the deflection at $z = 0$ from the non-linear model.

4.4. Pad and ballast stiffness under preload

4.4.1. *Preload in pad and ballast*

The pad and ballast stiffnesses are dependent on the preload in them. Under the wheel load, the foundation deflection and reaction force have different values at different places so that the railpads and ballast are subjected to different preloads at different supports. The preloads in the pad and ballast can be calculated on the basis of the foundation deflection $u(z)$ and the load-deflection law $F[u(z)]$ as derived in the previous sections. Two situations are considered here to determine the preloads in the pad and the ballast. In the first the wheel load is acting at mid-span (half way between two sleepers), and in the other the wheel load is acting above a sleeper.

The preload P_f in the foundation at different supports can be obtained by performing the following definite integral between corresponding limits z_1 and z_2:

$$P_f = \int_{z_1}^{z_2} \frac{F[u(z)]}{d} dz \tag{4.9}$$

Figure 4.8 shows schematically the integral limits for calculating the preload at each

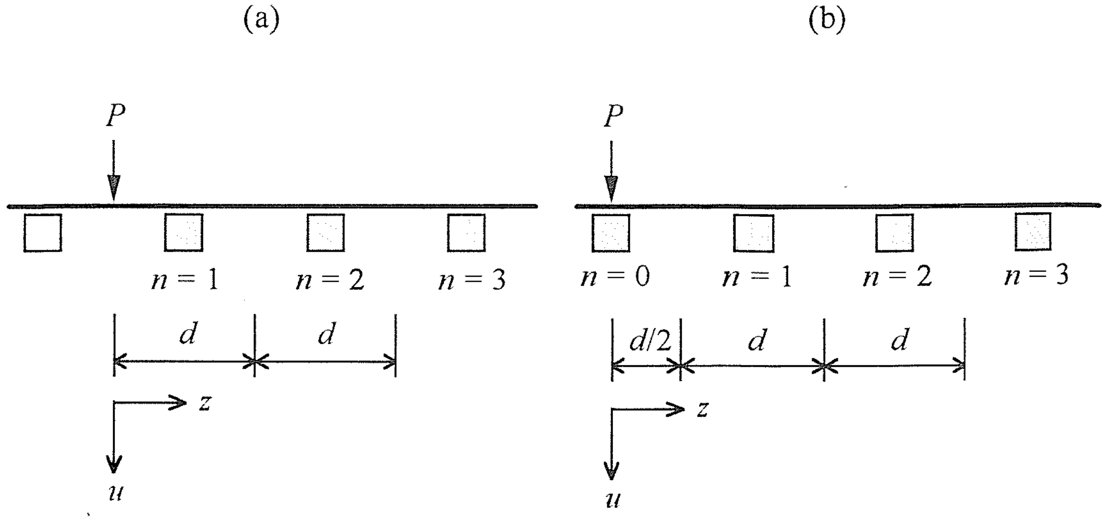

Figure 4.8. Integral limits for calculating the preload at each support. (a) load at mid-span, (b) load above a sleeper.

support in the two wheel load situations. For the wheel load acting at mid-span, the integral limits are from $(n-1)d$ to nd for the n-th support. For the wheel load acting above a sleeper the integral limits are from 0 to $d/2$ for the first support (n = 0) and the integral should be doubled. For the others the integral limits are from $(2n-1)d/2$ to $(2n+1)d/2$ for the n-th support.

The results of the preloads in pad and ballast at different supports are listed in Tables 4.3 and 4.4 for the wheel loads P = 75 kN and P = 125 kN respectively. The same parameters as in the previous sections are used. The preload in the pad P_p includes the clip load F_c and the rail weight. The preload in the ballast P_b includes the rail and sleeper weights. They are calculated using following equations:

$$P_p = P_f + F_c + W_r \tag{4.10a}$$

$$P_b = P_f + W_r + W_s \tag{4.10b}$$

It can be seen from Tables 4.3 and 4.4 that the preloads in the pad and ballast reach the maximum values at the nearest support to the wheel load, and decrease with increasing distance from the wheel load. The effects of the wheel load on the preloads in the pad and ballast are seen only at a limited number of supports, for example, five supports at each side of the wheel load. Except for these supports, the preload at other supports further away from the wheel load may be approximately

Table 4.3

Preloads (kN) in pad and ballast caused by a wheel load of 75 kN

Wheel load		above a sleeper (P = 75 kN)			at mid-span (P = 75 kN)		
Static ballast stiffness		soft	medium	stiff	soft	medium	stiff
Pad position	0	43.84	45.66	46.88	—	—	—
	1	36.86	37.28	37.47	41.54	42.86	43.71
	2	28.46	27.94	27.54	32.34	32.13	31.90
	3	23.28	22.67	22.33	25.45	24.81	24.40
	4	20.96	20.54	20.41	21.84	21.31	21.08
	5	20.30	20.08	20.13	20.50	20.18	20.14
	6	—	—	—	20.27	20.12	20.26
	∞	20.36	20.36	20.36	20.36	20.36	20.36
Ballast position	0	25.34	27.16	28.38	—	—	—
	1	18.36	18.78	18.97	23.04	24.36	25.21
	2	9.96	9.44	9.38	13.84	13.63	13.40
	3	4.78	4.17	3.83	6.95	6.31	5.90
	4	2.46	2.04	1.91	3.34	2.81	2.58
	5	1.80	1.58	1.63	2.00	1.68	1.64
	6	—	—	—	1.77	1.62	1.76
	∞	1.86	1.86	1.86	1.86	1.86	1.86

regarded as only having rail weight and clip loads for the pad, rail and sleeper weight loads for the ballast. Therefore, the influence of the wheel loads on the preloads in the pad and ballast is local. Compared with the wheel loads acting at mid-span, when the wheel load acts above a sleeper, the pad and the ballast at that support bear a larger preload. The changing of the ballast stiffness from soft to stiff only causes a slight difference in the preloads of the pad and ballast. When the ballast stiffness changes from soft to stiff, the preload distribution at different supports becomes slightly more localised in the vicinity of the wheel.

Table 4.4

Preloads (kN) in pad and ballast caused by a wheel load of 125 kN

Wheel load		above a sleeper (P = 125 kN)			at mid-span (P = 125 kN)		
Static ballast stiffness		soft	medium	stiff	soft	medium	stiff
Pad position	0	63.01	67.52	71.14	—	—	—
	1	48.20	48.39	48.07	58.07	60.92	62.89
	2	32.51	31.21	30.26	39.32	38.25	37.27
	3	24.36	23.36	22.79	27.67	26.46	25.67
	4	21.02	20.48	20.29	22.25	21.48	21.13
	5	20.16	19.96	20.03	20.40	20.04	19.99
	6	—	—	—	20.14	20.07	20.24
	∞	20.36	20.36	20.36	20.36	20.36	20.36
Ballast position	0	44.51	49.02	52.64	—	—	—
	1	29.70	29.89	29.57	39.57	42.42	44.39
	2	14.01	12.71	11.76	20.82	19.75	18.77
	3	5.86	4.86	4.29	9.17	7.96	7.17
	4	2.52	1.98	1.79	3.75	2.98	2.63
	5	1.66	1.46	1.53	1.90	1.54	1.49
	6	—	—	—	1.64	1.57	1.74
	∞	1.86	1.86	1.86	1.86	1.86	1.86

4.4.2. *Preloaded pad and ballast stiffness*

The preloaded pad and ballast stiffnesses can be determined from their load-stiffness laws. In reference [89] it is found that the pad dynamic stiffness varies slightly with frequency. At 200 Hz the dynamic stiffness to static stiffness ratio is about from 3.5 to 3.8 and this can be used to derive a load-dependent but frequency-independent approximation (see Table 4.1). For higher frequency it is slightly higher than this. Here a ratio of 3.6 is used for the pad dynamic stiffness. The ballast stiffness is also frequency-dependent, but less data are available. The

Table 4.5

Preloaded pad and ballast dynamic stiffness (MN/m) for wheel load 75 kN

Wheel load		above a sleeper (P = 75 kN)			at mid-span (P = 75 kN)		
Static ballast stiffness		soft	medium	stiff	soft	medium	stiff
Pad position	0	161.4	174.4	183.7	—	—	—
	1	119.7	121.9	122.9	146.7	155.1	160.5
	2	86.9	85.3	84.1	99.6	98.9	98.1
	3	73.2	72.3	71.8	78.0	76.1	74.9
	4	69.8	69.1	68.8	71.0	70.2	69.9
	5	68.7	68.3	68.4	69.0	68.5	68.4
	6	—	—	—	68.6	68.4	68.6
	∞	68.8	68.8	68.8	68.8	68.8	68.8
Ballast position	0	360.6	369.0	374.5	—	—	—
	1	323.9	326.3	327.4	349.3	355.9	360.0
	2	264.1	259.4	255.7	294.8	293.2	291.6
	3	206.8	197.5	192.1	234.2	226.9	221.9
	4	165.8	155.8	152.3	183.4	173.3	168.3
	5	149.3	142.9	144.6	154.6	146.0	144.9
	6	—	—	—	148.4	144.2	148.2
	∞	151.0	151.0	151.0	151.0	151.0	151.0

load-dependent ballast stiffness measured at 200 Hz in Table 4.2 is chosen to calculate the ballast stiffness for the whole frequency region. In addition, its value which was measured with bibloc sleepers has been multiplied by 1.3 to allow for the larger area of ballast in contact with a monobloc sleeper. Note that the soft, medium and stiff approximations apply only to the static ballast stiffness and not the dynamic stiffness, which is the same in each case.

The preloaded pad and ballast dynamic stiffnesses in different wheel load situations are listed in Tables 4.5 and 4.6. The stiffness variation is similar to the

Table 4.6

Preloaded pad and ballast dynamic stiffness (MN/m) for wheel load 125 kN

Wheel load		above a sleeper (P = 125 kN)			at mid-span (P = 125 kN)		
Static ballast stiffness		soft	medium	stiff	soft	medium	stiff
Pad position	0	376.3	473.7	551.1	—	—	—
	1	193.6	195.0	192.6	330.2	357.5	375.2
	2	100.2	95.7	92.6	132.8	127.1	121.9
	3	74.8	73.3	72.4	84.5	81.0	78.6
	4	69.8	69.0	68.7	71.6	70.5	69.9
	5	68.5	68.2	68.3	68.8	68.3	68.2
	6	—	—	—	68.4	68.3	68.6
	∞	68.8	68.8	68.8	68.8	68.8	68.8
Ballast position	0	435.1	449.3	460.1	—	—	—
	1	380.2	381.0	379.6	418.3	428.1	434.7
	2	296.0	286.5	279.2	337.7	331.8	326.3
	3	221.3	207.9	199.5	256.9	245.1	236.7
	4	167.1	154.1	149.1	190.7	176.7	169.4
	5	145.3	139.2	141.5	152.0	141.9	140.3
	6	—	—	—	144.8	142.6	147.7
	∞	151.0	151.0	151.0	151.0	151.0	151.0

preload variation in Tables 4.3 and 4.4. At the nearest support to the wheel load the pad and ballast stiffnesses have the maximum values, and gradually reduce to some stable value with increasing distance from the wheel load. These stable values are the stiffness of the pad under the clip load and the rail weight and the stiffness of the ballast under the rail and sleeper weights. The effects of the wheel load on the pad and ballast stiffness are also local, for example, on five pads and the ballast under five sleepers at each side of the wheel load. For other pads and sleepers more distant from the wheel load, their stiffness may approximately be regarded as uniform.

Comparing the data in Table 4.5 to those in Table 4.6 one can see that the stiffness of the preloaded pads at the supports near the wheel load dramatically increases when the wheel load increases from 75 kN to 125 kN. This is because the pad stiffness increases sharply if the preload is above 40 kN (see Figure 4.1). The ballast stiffness also increases when the wheel load goes up, but not so sharply (Figure 4.2).

4.5. Rail vibration considering preloaded pad and ballast stiffness

4.5.1. *Discretely supported railway track model*

The dynamic railway track model used for exploring the vertical vibration behaviour under the local wheel load is shown in Figure 4.9. For simplicity a simple Timoshenko beam is used to represent the rail other than the double beam model developed in chapter 2. This is because the track foundation mainly affects rail vibration at lower frequencies and a simple Timoshenko beam model can be used for rail vibration at least up to 2 kHz, see chapter 2. In Figure 4.9 the track is represented by an infinite uniform Timoshenko beam which is discretely supported by a finite number of railpads, sleepers and ballast. The beam is characterised by EI, the bending stiffness, G, the shear modulus, ρ, the density, A, the cross-sectional area, κ, the shear coefficient and η_r, the damping loss factor. The n-th railpad is modelled by a stiffness K_{pn} and a damping loss factor η_p. The subscript n indicates

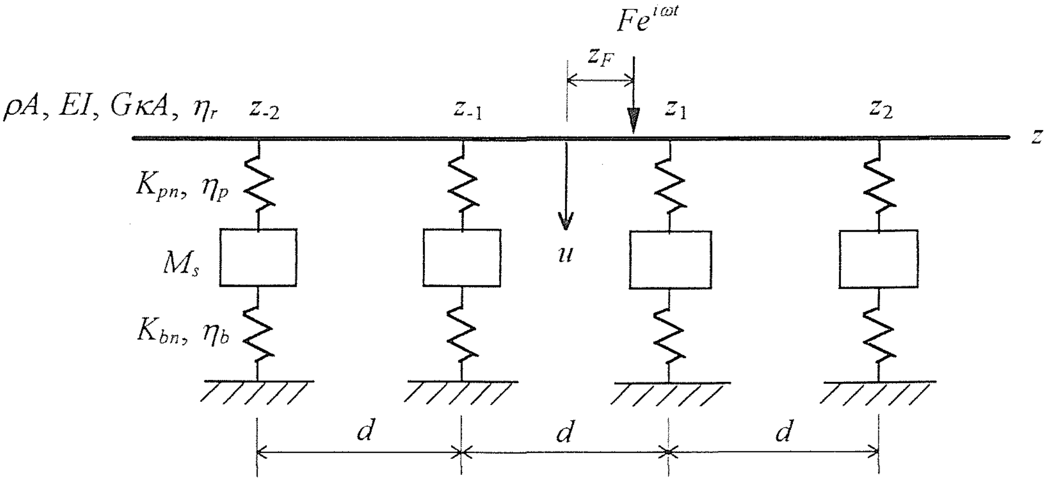

Figure 4.9. Discretely supported railway track model.

that the pad stiffness may have different values at different supports because the pads are subjected to the preloads due to the local deformation of the track foundation caused by the train weight. The pad loss factor is assumed constant, consistent with measurements in [89]. The sleeper is modelled as a mass M_s. The ballast is modelled by a stiffness K_{bn} and a damping loss factor η_b. The subscript n again indicates that the ballast stiffness may have different values at different supports due to the preload. Since the train speed is much lower than the flexural wave propagation speed in the rail, the dynamic excitation imposed by the rolling wheel is represented by a stationary harmonic force $Fe^{i\omega t}$, where $i = \sqrt{-1}$ and ω is the angular frequency of the harmonic excitation.

The vibration response of the rail to the harmonic force can be calculated using the Green's function and the superposition principle [28]. The Green's function $g(z, z')$ for an infinite Timoshenko beam is the response at point z to a unit harmonic force at z' [84]:

$$g(z,z') = \left(u_1 e^{-ik_1|z-z'|} + u_2 e^{-k_2|z-z'|}\right)e^{i\omega t} \tag{4.11}$$

where k_1 and k_2 are the respective complex wavenumbers of the propagating and evanescent waves in the free Timoshenko beam, given by

$$k_1 = \frac{\omega}{\sqrt{2}}\left\{\frac{\rho}{E} + \frac{\rho}{G\kappa} + \left[\left(\frac{\rho}{E} - \frac{\rho}{G\kappa}\right)^2 + \frac{4\rho A}{EI\omega^2}\right]^{\frac{1}{2}}\right\}^{\frac{1}{2}} \tag{4.12a}$$

$$k_2 = \frac{\omega}{\sqrt{2}}\left\{-\left(\frac{\rho}{E} + \frac{\rho}{G\kappa}\right) + \left[\left(\frac{\rho}{E} - \frac{\rho}{G\kappa}\right)^2 + \frac{4\rho A}{EI\omega^2}\right]^{\frac{1}{2}}\right\}^{\frac{1}{2}} \tag{4.12b}$$

and u_1 and u_2 are defined by

$$u_1 = \frac{i}{EG\kappa}\,\frac{\rho I\omega^2 - G\kappa A - EIk_1^{\,2}}{2Ak_1\left(k_1^{\,2} + k_2^{\,2}\right)} \tag{4.13a}$$

$$u_2 = \frac{1}{EG\kappa}\,\frac{\rho I\omega^2 - G\kappa A - EIk_2^{\,2}}{2Ak_2\left(k_1^{\,2} + k_2^{\,2}\right)} \tag{4.13b}$$

Here the formulation given in [28] has been modified by the inclusion of the shear coefficient κ and more convenient notation as in [84]. The rail loss factor is included in these equations by making E and G complex with the factor $(1+i\eta_r)$.

Consider now such a beam attached to the supports with dynamic stiffness Z_{sn} at the position $z = z_n$, see Figure 4.9. A single external harmonic force $Fe^{i\omega t}$ acts at the point $z = z_F$. The dynamic stiffness Z_{sn} is the ratio of force to the displacement caused by that force and given by

$$Z_{sn} = \frac{K_{pn}\left(1+i\eta_p\right)\left[K_{bn}\left(1+i\eta_b\right) - M_s\omega^2\right]}{K_{pn}\left(1+i\eta_p\right) + K_{bn}\left(1+i\eta_b\right) - M_s\omega^2} \tag{4.14}$$

The total displacement u at a point z is given by the superposition of the response to the external force $Fe^{i\omega t}$ and the response to the forces from all the support points:

$$u(z) = -\sum_{\substack{n=-N \\ n\neq 0}}^{N} Z_{sn} u(z_n) g(z, z_n) + F g(z, z_F) \tag{4.15}$$

The displacement at each support point $z = z_m$ are given by

$$u(z_m) = -\sum_{\substack{n=-N \\ n\neq 0}}^{N} Z_{sn} u(z_n) g(z_m, z_n) + F g(z_m, z_F), \quad m = \pm 1, \pm 2, \cdots, \pm N \tag{4.16}$$

When $Fe^{i\omega t}$ acts at mid-span where $z = 0$ and thus $z_F = 0$, the displacements are symmetric with respect to the point $z = 0$. From equation (4.16) the displacements at each support point can be solved in terms of F by taking the sum to the left-hand

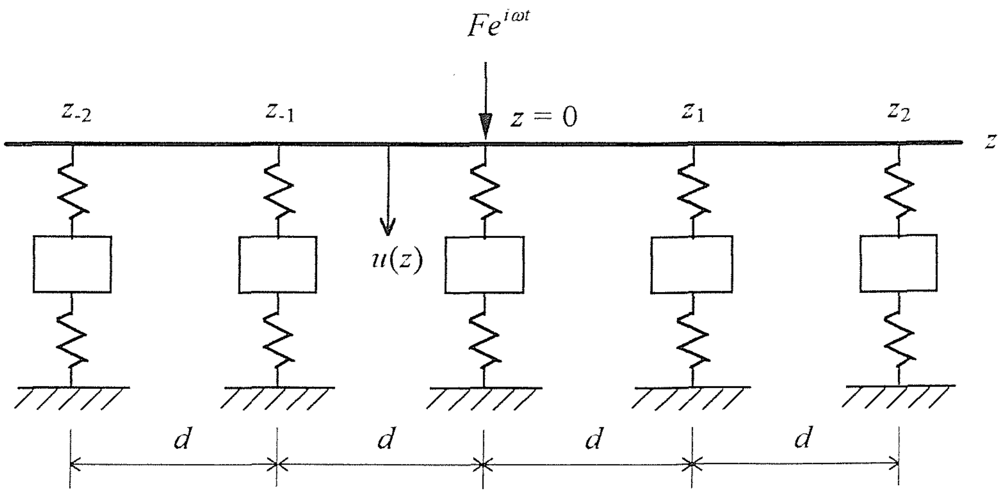

Figure 4.10. Special case of discretely supported track model where external force acts above a sleeper.

side and then inverting the matrix of coefficients of $u(z_m)$. Substituting them into equation (4.15), one can obtain the displacement at any point on the rail.

For the external force $Fe^{i\omega t}$ acting above a sleeper, again taking the forcing point as $z = 0$, see Figure 4.10, the displacements can be determined by the following equations:

$$u(z) = -\sum_{n=-N}^{N} Z_{sn} u(z_n) g(z, z_n) + Fg(z, 0) \tag{4.17}$$

where $z_0 = 0$. The displacement at each support point $z = z_m$ can be obtained by solving the following equations:

$$u(z_m) = -\sum_{n=-N}^{N} Z_{sn} u(z_n) g(z_m, z_n) + Fg(z_m, 0), \quad m = 0, \pm 1, \pm 2, \cdots, \pm N \tag{4.18}$$

For the external force acts at mid-span or above a sleeper, the symmetry of the problem can be used to reduce the dimension of equations (4.15) – (4.18), as used in chapter 2 and chapter 3.

4.5.2. *Numerical results*

The point receptance of the track for vertical vibration is calculated for the external excitation acting either above a sleeper or at mid-span in the frequency range from 50 Hz to 1500 Hz. The wave propagation decay rate along the rail is examined in the same frequency range. To investigate the effects of the local wheel load on the track vertical vibration behaviour the preloaded pad and ballast stiffnesses listed in Tables 4.5 and 4.6 are employed in the numerical calculation and the results are compared to those from the track model having uniform pad and ballast stiffnesses. The following parameters are used in numerical calculations:

$E = 2\times10^{11}$ N/m^2 $G = 0.77\times10^{11}$ N/m^2 $\eta_r = 0.01$
$\rho = 8000$ kg/m^3 $A = 0.75\times10^{-2}$ m^2 $I = 3.2\times10^{-5}$ m^4
$\kappa = 0.4$ $M_s = 150$ kg $\eta_p = 0.25$
$\eta_b = 0.6$ $d = 0.6$ m $N = 40$ (for receptance)
$N = 60$ (for decay rate)

These are chosen to represent UIC 60 rail [95] and the sleeper mass represents half of the mass of a concrete monobloc sleeper. The ballast loss factor is chosen lower than in [95] in order to make effects in the response more visible.

Because the deformation of the track foundation caused by the wheel load is local and only a limited number of pads and ballast springs are preloaded by the wheel load, the pad and ballast stiffnesses are assigned different values at only the first six supports on each side of the wheel load (including $n = 0$ for the case of excitation above a sleeper) and from the seventh support they have uniform values. The preloaded pad and ballast stiffnesses listed in Tables 4.5 and 4.6 for the stiff ballast assumption are used in the calculation.

(*a*) Receptance

The amplitude and phase of the point receptances of the track are shown in Figures 4.11 and 4.12 which give the results for the wheel load P = 75 kN and P = 125 kN respectively. Figures 4.11(a) and 4.12(a) show the results when the

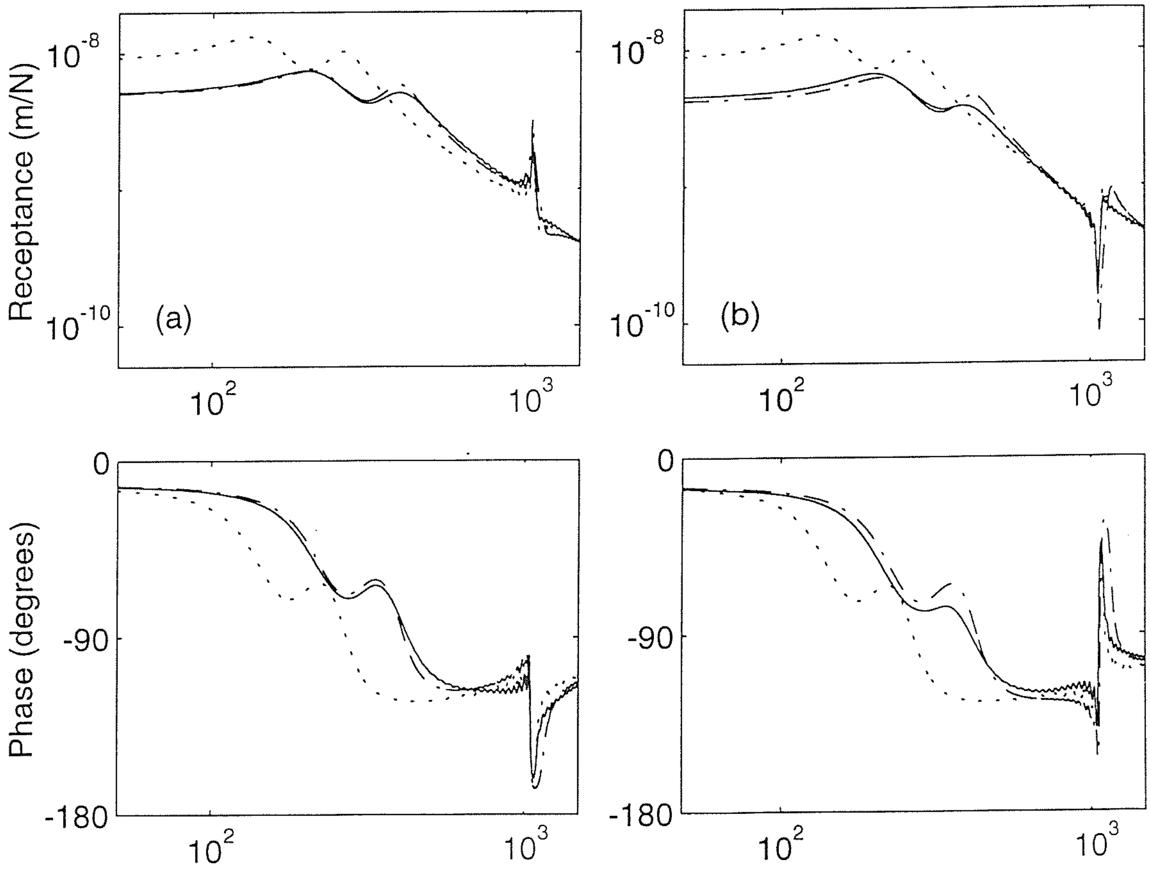

Figure 4.11. Amplitude and phase of the point receptances, for P = 75 kN. (a) load at mid-span, (b) load above a sleeper. — varying stiffness foundation, – · – uniform stiff foundation, ······ uniform soft foundation.

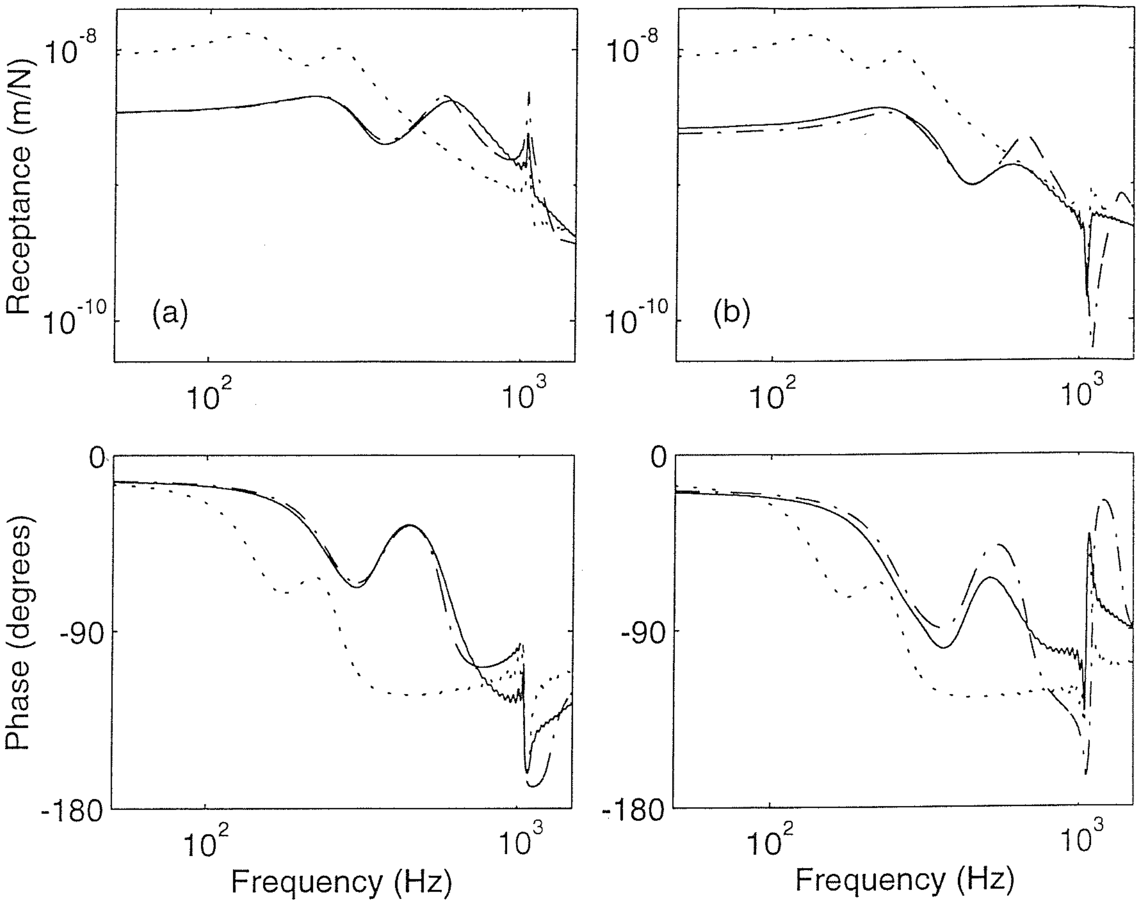

Figure 4.12. Amplitude and phase of the point receptances, for P = 125 kN. (a) load at mid-span, (b) load above a sleeper, key as for Figure 4.11.

wheel load acts at mid-span and Figures 4.11(b) and 4.12(b) show the results when the wheel load acts above a sleeper. The solid lines in Figures 4.11 and 4.12 are the results from the model having different pad and ballast stiffness at different supports near the wheel load. The dotted lines are the results from the model having uniform pad and ballast stiffness at each support point which has the values as at the seventh support point—this case represents a uniform soft or unloaded foundation. The dotted-dashed lines also are the results from the model having uniform pad and ballast stiffness but which has the values as at the first support point—this case represents the uniform stiff or loaded foundation.

Two well-damped resonances can be seen, at about 130 Hz and 260 Hz for the uniform soft foundation model. These occur at higher frequencies for both the uniform stiff foundation and the varying stiffness foundation models—in Figure 4.11 where P = 75 kN they occur at about 200 Hz and 400 Hz, and in Figure 4.12 where P = 125 kN they occur at about 220 Hz and 600 Hz. At the first resonance the whole track bounces on the ballast stiffness, whereas at the second the rail vibrates on the pad stiffness. At about 1050 Hz the pinned-pinned resonance, which corresponds to a standing wave with nodes at the sleepers, can be seen for all the models although there are different peak values from different models.

It can be seen from Figures 4.11 and 4.12 that the uniform stiff foundation model and the varying stiffness foundation model have almost the same receptance curves in the frequency range up to about 1000 Hz. Based on this it may be considered that *the point receptances of a railway track at low frequencies are governed by the local supports near the wheel load.* This point can be further verified by the curves in Figure 4.13. The solid lines in Figure 4.13 come from the rail on the uniform stiff foundation under the wheel load P = 75 kN, and the dotted lines come from the same rail but having only three uniform supports for the wheel load acting above a sleeper (n = 0, ±1), or four uniform supports for the wheel load acting at mid-span (n = ±1, ±2). The fact that these two lines almost overlap each other except near the pinned-pinned frequency indicates again that the receptances of a railway track at low frequencies are controlled by only a few supports near the wheel load. In addition it can be seen from Figures 4.11 and 4.12 that the stiffer the foundation is, the lower the receptances in the low frequency region and the higher the frequencies corresponding to the two low frequency resonances of the rail vibration.

With regard to the pinned-pinned resonance peaks, it can be seen from Figures 4.11 and 4.12 that the peak is higher in the case of the uniform stiff foundation than the uniform soft or varying stiffness foundations, whereas in the latter two cases the peaks are equally high. The first fact implies that the pinned-pinned resonance is stronger when the rail foundation is stiffer and the second implies that *the local stiffness variation in the rail foundation near the wheel load has no obvious effects on the pinned-pinned resonance.*

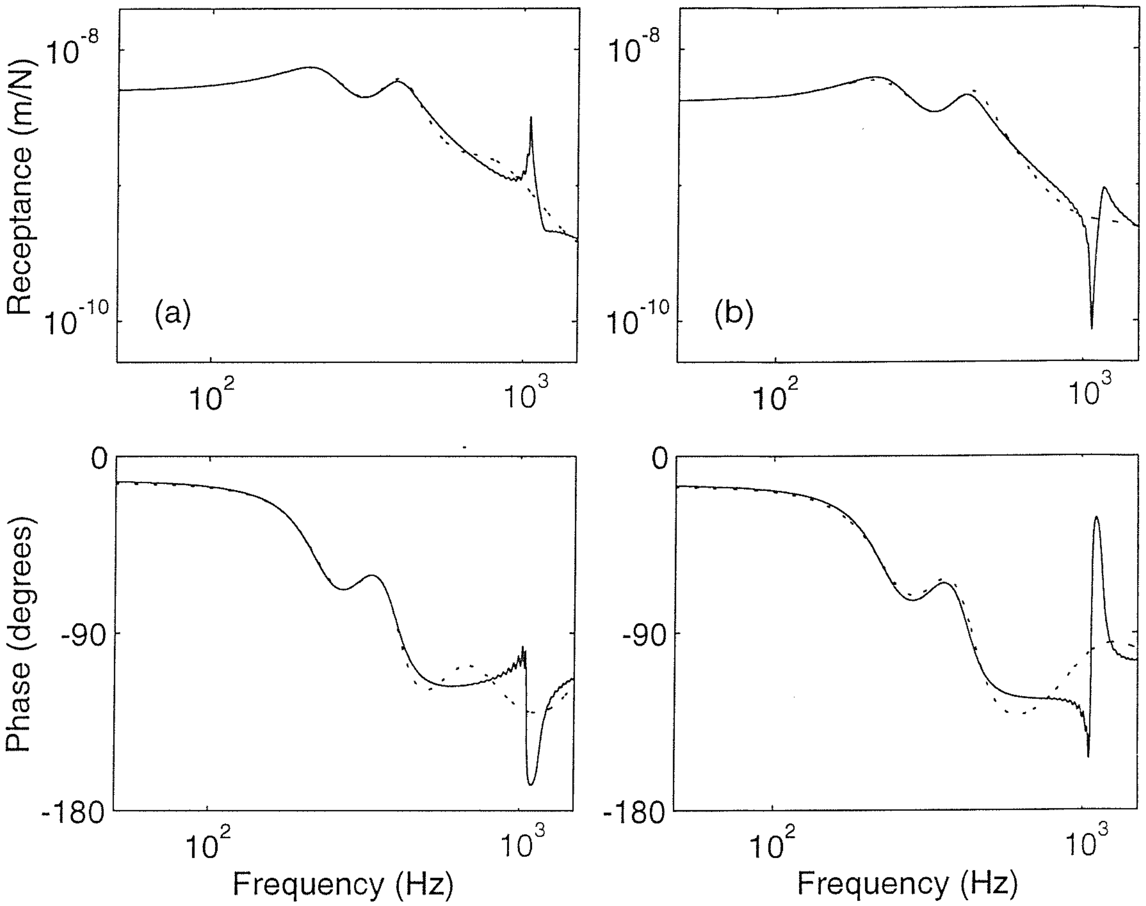

Figure 4.13. Amplitude and phase of the point receptances, for P = 75 kN. (a) load at mid-span, (b) load above a sleeper. — uniform stiff foundation, ······ four uniform supports for load at mid-span and three uniform supports for load above a sleeper.

(*b*) Decay rate

The decay rates of the wave propagation along the rail for different models are shown in Figures 4.14 and 4.15. These are calculated from the decay in vibration level over a thirty span length from the excitation point divided by this distance (18 m). The curves in Figure 4.14 are for the wheel load P = 75 kN and in Figure 4.15 for P = 125 kN. Figures 4.14(a) and 4.15(a) show the results when the wheel load acts at mid-span and Figures 4.14(b) and 4.15(b) show the results when the wheel load acts above a sleeper. The solid lines here again represent the varying stiffness foundation model. The dotted lines represent the uniform soft foundation model and the dotted-dashed lines represent the uniform stiff foundation model. In

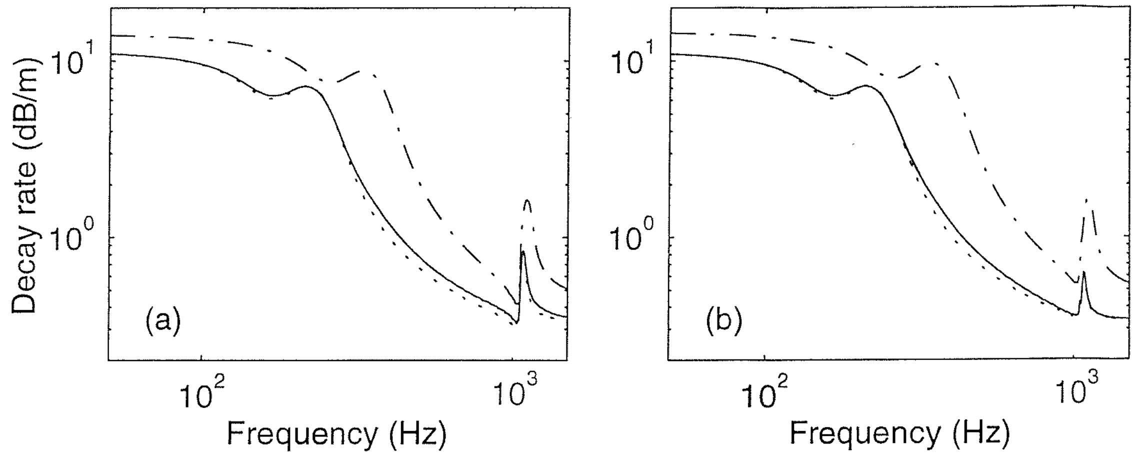

Figure 4.14. Decay rates of the wave propagation along the rail, for P = 75 kN. (a) load at mid-span, (b) load above a sleeper. — varying stiffness foundation, – · – uniform stiff foundation, ······ uniform soft foundation.

general for all models, the decay rates can be seen to be very high in the low frequency region and very low in the high frequency region. They gradually decrease with increasing frequency and then reach a local trough and a local peak. For the uniform foundation models this peak corresponds to a trough in the receptance. After the peak the decay rates drop steeply, and then have a sharp peak just above the pinned-pinned resonance frequency. It can be seen from Figures 4.14 and 4.15 that the decay rate is higher in the case of the uniform stiff foundation than the

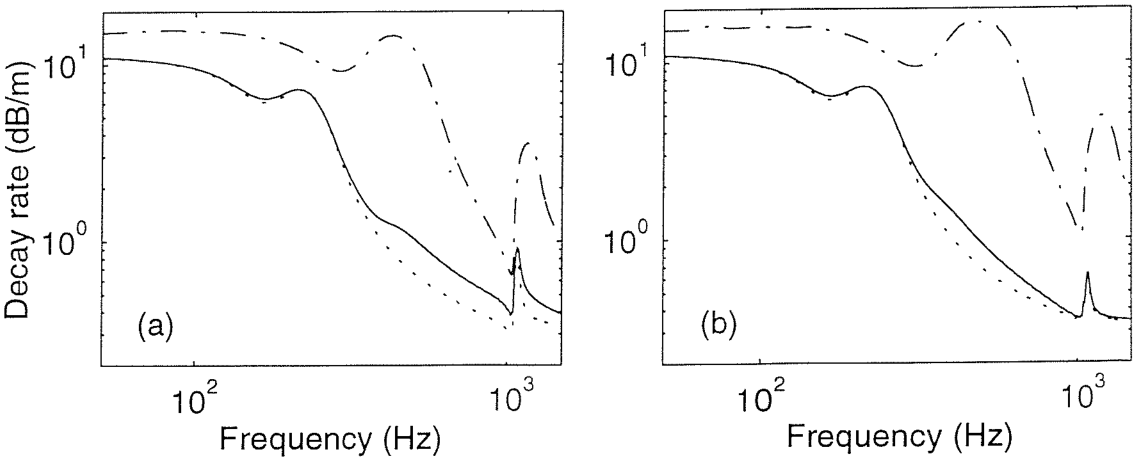

Figure 4.15. Decay rates of the wave propagation along the rail, for P = 125 kN. (a) load at mid-span, (b) load above a sleeper, key as for Figure 4.14.

uniform soft and varying stiffness foundations, whereas in the latter foundations the decay rates are almost the same for both values of the wheel load P = 75 or 125 kN. This implies that *the effect of the local stiffness variation in the track foundation near the wheel load on the average wave propagation decay rate is very limited.* The reason for this is that the pad and ballast are stiffened only at a few supports near the wheel load and therefore their effects on the average decay rate within a certain distance are not very noticeable. However, within about two or three spans from the wheel load the local decay rate is higher than in distant area due to the local loaded and thus stiffer supports. As an example Figure 4.16 shows the amplitude decay of the transfer receptance which represents the response at other positions along the rail to a unit harmonic force acting at $z = 0$. In this case the excitation frequency is 600 Hz. The solid lines in Figure 4.16 represent the varying stiffness foundation model, the dotted lines the uniform soft foundation model and the dotted-dashed lines the uniform stiff foundation model. Figure 4.16(a) is for the wheel load P = 75 kN and Figure 4.16(b) for the wheel load P = 125 kN. The amplitude decay rate can be seen to be higher only in a local area near the excitation point for the varying stiffness foundation model and to be almost equal far from the excitation point for both varying stiffness foundation and uniform soft foundation. This example at 600 Hz corresponds to a region in Figures 4.14 and 4.15 where the varying stiffness and uniform soft foundation results differed most.

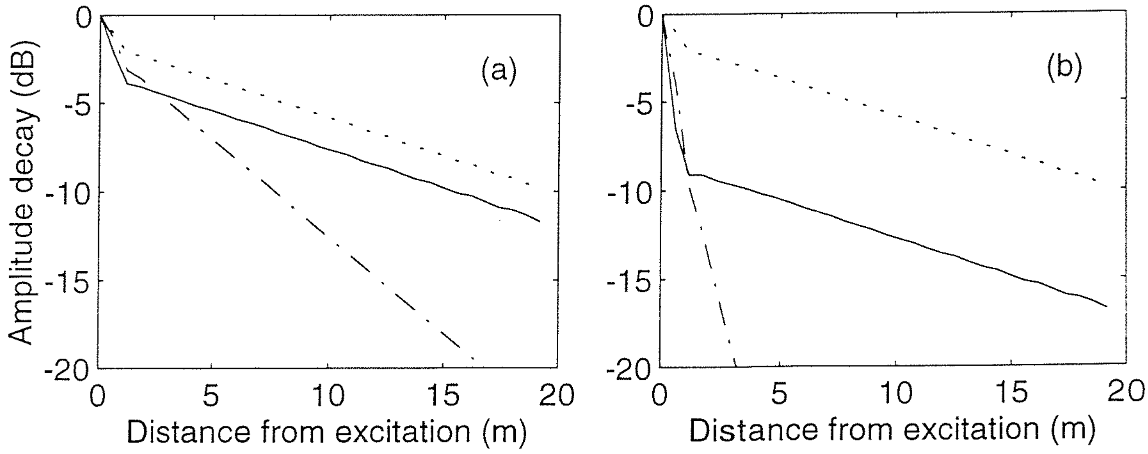

Figure 4.16. Amplitude of the Transfer receptance at 600 Hz, load at mid-span. (a) for P = 75 kN, (b) for P = 125 kN, key as for Figure 4.11.

It has been seen that the point receptances at low frequencies are governed by the local supports near the wheel load, whereas the pinned-pinned resonance and the average decay rate of the wave propagation are determined by the unloaded supports. Based on the these facts a simpler vertical track vibration model may be appropriate such as a combination of a few (three or four) preloaded supports near the external excitation and unloaded supports at the other points along the rail. It would also be possible to approximate the vertical track vibration using a combination of a model with loaded supports to represent the receptance and a model with unloaded supports to represent the average decay rate. Nevertheless, such an approximation would overestimate the receptance at the rail-on-pad resonance, here between 400 and 700 Hz, by up to about 4 dB (see Figure 4.12).

4.6. Conclusions

In this chapter the effects of a single wheel preload on the railway foundation stiffness and vertical vibration have been studied. Firstly the non-linear load-deflection relationship of the whole track foundation has been obtained by combining the pad and ballast load-deflection laws. Based on this load-deflection law of the track foundation, the local foundation deformation caused by a single static wheel load has been calculated using a non-linear track model and hence the preloads in the pad and ballast are known. From a knowledge of the load-frequency-stiffness laws of the pad and ballast, their dynamic stiffness at different supports around the wheel load can be determined. To investigate the effect of the preloaded pad and ballast stiffness on the track vertical vibration an infinite discretely supported Timoshenko beam model has been employed, and the point receptance of the rail and the wave propagation decay rate have been calculated using different track foundation models including the uniform soft, uniform stiff and varying stiffness foundations.

The results show that the deformations of the track foundation under a single static wheel load are local and near the wheel load, so only a limited number of railpads and ballast springs are preloaded by the wheel load. The preloaded pads and ballast become stiffer and thus affect the railway vertical vibration behaviour to some extent. The numerical predictions show that the track vertical vibration properties below the pinned-pinned resonance frequency are noticeably influenced through the stiffened pad and ballast due to the static wheel preload. The receptance of the rail vibration is reduced at low frequency and the first two resonance frequencies are increased when the preloaded pad and ballast stiffnesses are employed in the vertical track vibration model. A good approximation to the receptance is given by using the loaded stiffness throughout. On the other hand, the local static wheel load does not affect the pinned-pinned resonance and affects the average wave propagation decay rate along the rail only to a very limited extent, and these can be predicted from the uniform unloaded (soft support) track model.

This chapter has given a general approach to investigate the influence of the local preload on track vertical vibration and useful results have been obtained. The method can readily be applied to other pads if the load-deflection law is known. Further practical measurements need to be carried out to validate the predictions and also essentially, more detailed information about the ballast static and dynamic stiffness is needed. Moreover, in practice the preload in the track foundation is caused by multiple wheel loads rather than a single wheel load. The effects of multiple wheel loads on the track foundation stiffness and rail vibration will be studied in chapter 7 below.

CHAPTER 5

The Influence of Random Sleeper Spacing and Ballast Stiffness on Rail Vibration

In this chapter the sleeper spacing and ballast stiffness are treated as random variables and their effects on the rail vibration are explored through numerical simulations. The statistical results show that the point receptance and the vibration decay rate are distributed in a certain area instead of having a fixed value due to the variability in the sleeper spacing and ballast stiffness. It is found that the phenomenon of the pinned-pinned resonance may be suppressed by the random sleeper spacing. By studying the average vibration due to the interaction with a wheel it is shown that the random foundation has no significant effect on the average noise radiated by the track.

5.1. Introduction

The foundation of a railway track, formed of railpads, sleeper and ballast, has crucial effects on the rail vibration properties as shown in the last chapter. Usually, the sleeper spacing and ballast stiffness are treated as uniform and represented by constant parameters in theoretical analyses. However, in reality they are irregular and should be represented by different values at each support point. The aim of this chapter is to explore the effects on the rail vibration of random variations in sleeper spacing and ballast stiffness.

The sleeper spacing is found not to be constant even for a newly built railway track, see de France [8]. In fact it is in a certain region rather than having a fixed value. Therefore the sleeper spacing of a railway track should be regarded as random instead of deterministic and constant. The ballast stiffness also varies between different support positions because the contact state between the sleeper and the ballast is affected by many uncertain factors and the ballast stiffness depends upon the contact state. In order to obtain a better understanding of the track dynamic behaviour, it would be better to take the sleeper spacing and ballast stiffness as random variables since they have significant effects on the track vibration. A random sleeper spacing was studied by Heckl [28] in several specific numerical calculations. Also the effect of random sleeper spacing, ballast and pad stiffness on parametric excitation of track support irregularities was studied by Nordborg [54]. However, these studies are limited by their use of a few specific samples which are insufficient to draw general conclusions for such a random phenomenon. It is preferable if some statistical results, such as the mean value and the standard deviation are given to describe a set of random events.

In this chapter the influence of the random sleeper spacing and ballast stiffness is studied. A simple and effective methodology to generate an arbitrary distribution using a commonly used uniform distribution generator is developed for numerical simulation. Based on these and a discretely supported rail model, the effects on the track vibration of the random sleeper spacing and ballast stiffness are investigated through extensive numerical calculations.

To obtain a reliable statistical result many numerical calculations have to be carried out. To minimise the computing time required for the numerical simulations, only a simple Timoshenko beam model is employed for the rail and only the vertical vibration of the rail is considered. Moreover, the frequency region is limited to 50 – 1500 Hz because at higher frequencies the rail vibration is less affected by the track foundation.

5.2. Distribution of random sleeper spacing and ballast stiffness

The sleeper spacing of a railway track is generally not constant and its values vary irregularly in a certain range. This occurs due to limited precision during track installation, and is further increased by movement in service and maintenance operations. Little data are available quantifying these effects. However, as an example Figure 5.1 shows the disparity of the sleeper spacing for a test track at Chilworth, Southampton [8], which was laid accordingly to normal procedures. This had a mean spacing of 62.8 cm and a standard deviation of 3.9 cm.

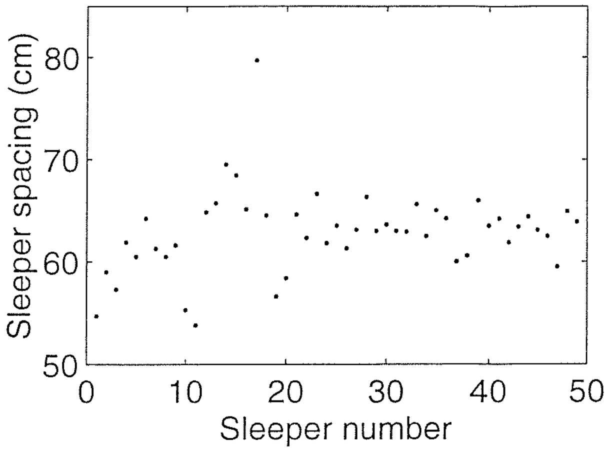

Figure 5.1. Sleeper spacing measurement result on a 33 m test track (from de France [8]).

It is known from chapter 4 that the ballast stiffness at each support depends upon the preload at the support, and the preload is related to the contact state of the sleeper with the ballast. As the contact state of a sleeper with the ballast is not uniform at each support position, the ballast stiffness at different sleepers is also variable. Significant differences in the static force-deflection relation for the ballast between adjacent sleepers were found by Igeland and Oscarsson [30]. Figure 5.2 shows the measured force-deflection curves at three almost adjacent sleepers from [30]. Since the contact state between a sleeper and the ballast is not predictable, the ballast stiffness at each support should also be seen as irregular. In an extreme case, a sleeper may be out of contact with the ballast. Thus the ballast stiffness could be

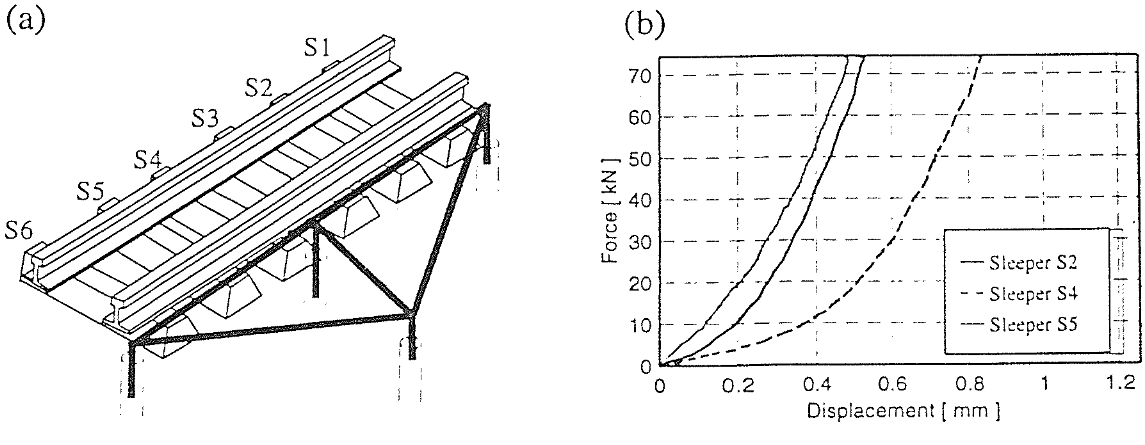

Figure 5.2. (a) Measurement arrangement at Goose Hill, Sweden, 1995, (b) load applied to concrete sleeper at each rail seat versus deflection at sleeper end (from Igeland [30]).

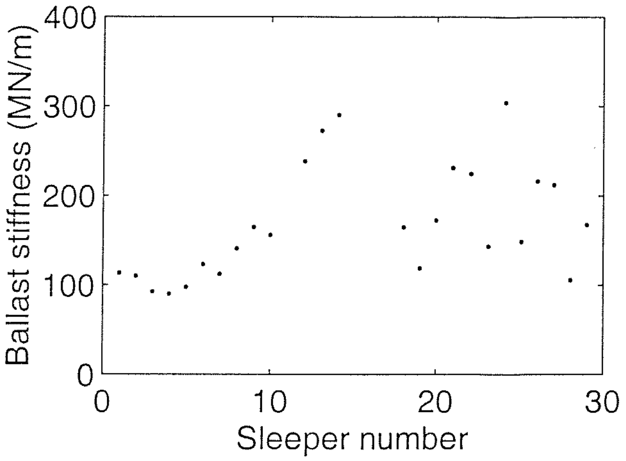

Figure 5.3. Dynamic ballast stiffness at different positions, averaged over 50 – 90 Hz, for a test track at Chilworth, Southampton (from [8]).

zero at some support positions. Figure 5.3 shows another example of variations in the ballast stiffness [8]. In this case the ballast stiffness is taken from the frequency responses of the sleepers in the frequency range 50 – 90 Hz. For these measurements the sleepers were uncoupled from the rail. The standard deviation of these results is 38% of the mean value. The results appear to show some long wavelength variations but these are likely to be specific to this short test track.

The pad stiffness could also be considered to vary randomly but there is less evidence that this is the case, so in this study the pad stiffness is taken as constant.

Since the sleeper spacing and the ballast stiffness are irregular, they both should be seen as random variables. It is important in dealing with random variables to know their distribution. Although detailed data for sleeper spacing and ballast stiffness are not available, it may be acceptable to assume that both the sleeper spacing and the ballast stiffness can be represented by a Gaussian distribution. However, for an engineering application, the disadvantage of the Gaussian distribution is that the random variables may tend towards either negative or positive infinity. This is not the case in practice where realistic limits exist. To avoid this, the following probability density function, defined in an interval [0 1], is employed:

$$p(x) = \begin{cases} 2\sin^2 \pi x & 0 \le x \le 1 \\ 0 & \text{elsewhere} \end{cases} \tag{5.1}$$

This function is known as the Hanning window in signal processing when the factor two is omitted. It is very close to the Gaussian distribution with $(\mu, \sigma) = (0.5, 0.2)$ in [0 1] but the probability density is zero outside the range [0 1]. Figure 5.4 shows this probability density function and the corresponding Gaussian distribution in [0 1].

Another important problem to be addressed from an application point of view is how to generate a set of data according to an arbitrary probability distribution. This is necessary because the distribution of practical samples may be found to be different from the theoretical distributions such as the Gaussian or uniform distributions. Although the analysis in this chapter is based on equation (5.1), the methodology can be used for an arbitrary distribution. Often, built-in computer codes sample only uniform or normal distributions, for example, 'rand' and 'randn' in Matlab [75]. In order to generate an arbitrary distribution, a simple but effective technique is developed as below. This technique only uses the sampling of a uniform distribution. First, create a set of samples $x_1, x_2, \ldots, x_N$, such that the distribution of these samples is the same as that needed, for example, represented by equation (5.1). These can be obtained by dividing the range [0 1] of $P(x)$ in Figure 5.4(b) into

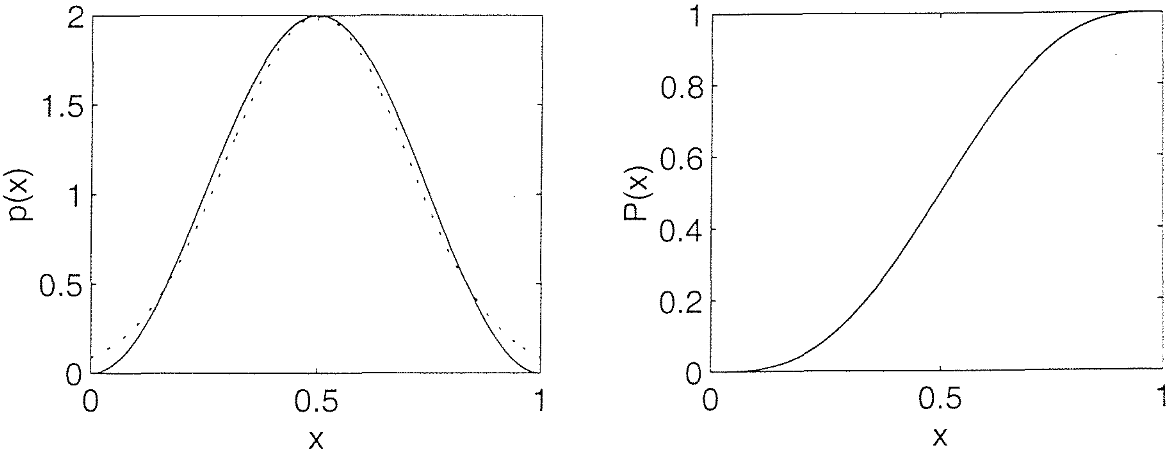

Figure 5.4. Probability density and probability distribution functions for $p(x) = 2\sin^2 \pi x$. Dotted line represents Gaussian distribution $(\mu, \sigma) = (0.5, 0.2)$ in [0 1].

N equal steps and selecting the corresponding x values. Then generate uniformly distributed random integers in the interval [1 N] M times using the built-in computer code. Each random integer is used to select an element from the samples $x_1, x_2, \ldots, x_N$. If $M >> N$, the sampling procedure should produce a good approximation of the distribution defined by the samples $x_1, x_2, \ldots, x_N$. The tricky point is how to choose N and M properly. N should be as small as possible, but not too small to set up a designed distribution. M should be large enough so that each element of the samples $x_1, x_2, \ldots, x_N$ can be uniformly experienced. Figure 5.5(a) shows a bar chart of a distribution designed by equation (5.1) and composed of 100 samples (N = 100). Figure 5.5(b) displays a sample of the computer generated distribution with sampling 10,000 times (M = 10,000). The sampling distribution can be seen to be close to that intended.

In this chapter both the random sleeper spacing and the ballast stiffness are designated as having the distribution described by equation (5.1). Two sets of the random sleeper spacing and the ballast stiffness are used. In one set the sleeper spacing is distributed in [0.3 0.9] with a mean value 0.6 m and a standard deviation 0.11m. In the other it is distributed in [0.45 0.75] with the same mean value 0.6 m but a standard deviation of 0.05 m. The latter is close to the variation measured on the new track in [8] (see Figure 5.1). The ballast stiffness is treated by multiplying

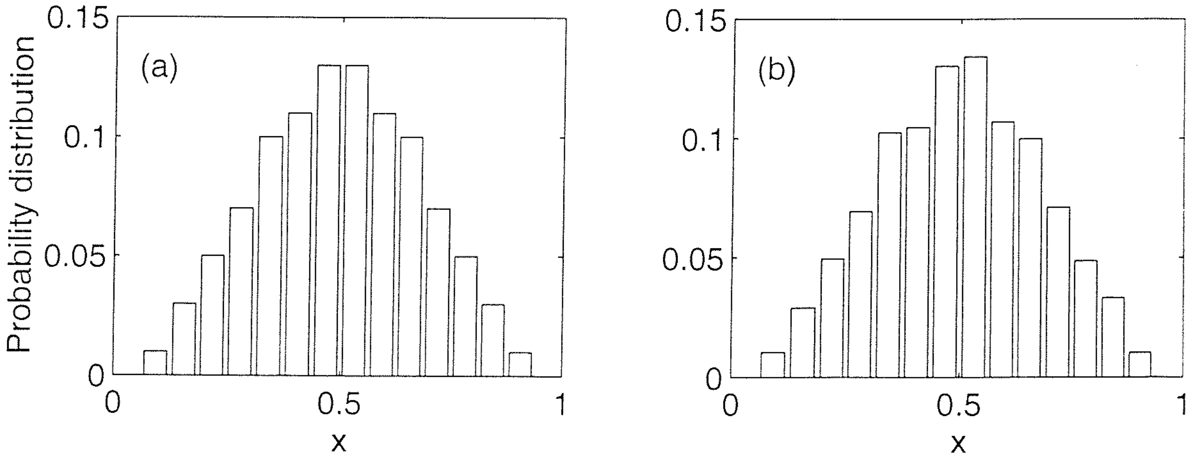

Figure 5.5. (a) Bar chart of the distribution designed by $p(x) = 2\sin^2 \pi x$ and composed of 100 samples (N = 100), (b) a sample of the computer generated distribution with sampling 10,000 times (M = 10,000).

a constant ballast stiffness by a random factor distributed in [0 2] and [0.5 1.5] with a mean value 1 and standard deviations 0.35 and 0.18 for the two sets respectively. The larger of these corresponds closely to the variation measured in [8] (see Figure 5.3). The ballast stiffness K_b will be given in section 5.4.

5.3. Railway track vibration model

In order to obtain a reliable statistical result (mean value and standard deviation) of the rail vibration response, a great deal of numerical calculations have to be carried out. To minimise the computation time required for the numerical calculations, only a conventional Timoshenko beam model with discrete supports is used to represent the vertical vibration behaviour of the railway track. Although simple, a Timoshenko beam model can be used very well up to 2000 Hz for the vertical vibration of a rail as shown in chapter 2.

A discretely supported railway track model is shown in Figure 4.9, where K_p and η_p are the pad stiffness and loss factor, K_b and η_b are the ballast stiffness and loss factor, M_s is the sleeper mass. To calculate the rail response the discrete supports are replaced by corresponding external forces, and thus the railway track can be simply considered as an infinite beam with many point forces acting on it. Based on the Green's function and the superposition principle the stationary response of the rail to the harmonic excitation can be obtained. This approach is used in the previous chapters and also used in this chapter. In Figure 4.9 the discretely supported railway track is modelled with an infinite rail and a finite number of discrete supports. This is because the supports at large distances from the point at which the response is to be calculated, can be neglected due to the wave propagation decay. The number of supports to be considered depends on the wave propagation decay rate along the track. At low frequencies, for example, four supports may be enough to calculate the point receptance due to the high decay rate, see chapter 4. At high frequencies, however, it should be large enough to guarantee an acceptable approximate solution because of the low decay rate. The number required depends on the pad stiffness. Based on the superposition principle the responses of the rail at the support points to a unit force acting at z_F can be written as

$$u(z_m) = -\sum_{n=1}^{N} Z_{sn} u(z_n) g(z_m, z_n) + g(z_m, z_F) \qquad m = 1, 2, \cdots, N \tag{5.2}$$

where $g(z_m, z_n)$ and $g(z_m, z_F)$ are the Green's functions for an unsupported rail—the responses at point z_m to a unit harmonic force acting at z_n and z_F respectively, and can be calculated using the method in chapter 4 or the Laplace transform method in chapter 2. N is the number of the discrete supports, Z_{sn} is the dynamic stiffness of the n-th support and is given as the following:

$$Z_{sn} = \frac{K_p(1+i\eta_p)[K_{bn}(1+i\eta_b) - M_s\omega^2]}{K_p(1+i\eta_p) + K_{bn}(1+i\eta_b) - M_s\omega^2} \tag{5.3}$$

The dynamic stiffness Z_{sn} may have different values at different supports because the ballast stiffness at the n-th support K_{bn} is generated by multiplying K_b by a random factor.

Equation (5.2) can be solved to give $u(z_m)$ by taking the sum to the left-hand side and then inverting the matrix of coefficients of $u(z_m)$. Then the displacement at any point on the rail can be obtained by substituting $u(z_m)$ into the following equation:

$$u(z) = -\sum_{n=1}^{N} Z_{sn} u(z_n) g(z, z_n) + g(z, z_F) \tag{5.4}$$

Thus the point receptance at $z = z_F$ and the transfer receptance at z for the rail vertical vibration are given as

$$\alpha^R = u(z_F), \quad \alpha^{RT}(z) = u(z) \qquad (5.5, 5.6)$$

5.4. Numerical results

The following parameters are used for the railway track vibration model:

$E = 2.1\times10^{11}$ N/m^2, $G = 0.77\times10^{11}$ N/m^2, $\rho = 8000$ kg/m^3

$A = 7.69\times10^{-3}$ m^2, $I = 30.55\times10^{-6}$ m^4, $\kappa = 0.4$

$K_p = 68.8$ MN/m, $K_b = 151$ MN/m, $M_s = 150$ kg

$\eta_r = 0.01$, $\eta_p = 0.25$, $\eta_b = 0.6$

The pad and ballast stiffness used here correspond to an unloaded track with soft railpads. In practice, however, a track is preloaded by the wagons through wheels. This leads to increased track foundation stiffness in the area close to the wheels. The effects of the wheel preloads on the foundation stiffness and track vibration have been studied in chapter 4. For simplicity, however, only an unloaded track is considered in this chapter.

The random sleeper spacing is directly generated in [0.3 0.9] or [0.45 0.75] with the distribution described by equation (5.1) using the methodology introduced in section 5.2. The random ballast stiffness K_{bn} is generated by multiplying K_b by a random factor r distributed in [0 2] or [0.5 1.5] with the same distribution as the random spacing. As a result, the support positions z_m and z_n in equations (5.2) and (5.4) now are random, and the dynamic stiffness Z_{sn} in equation (5.3) also randomly varies for each value of n.

The point receptance and the wave propagation decay rate in the rail are calculated with the excitation acting either at mid-span or above a sleeper. The number of the discrete supports is chosen $N = 80$ for the whole track. The decay rate of the wave propagation is calculated from the decay in vibration level over a twenty-five span length from the excitation point divided by this distance. Although the wave attenuation is greater in the near field or in the loaded area (which is not taken account of in this chapter), compared to that in the far field or in the unloaded area, a general view of the vibration decay can be obtained from the average decay rate in the frequency range considered. By taking an average over 25 spans the result is representative of the far field wave propagation in the rail. The amplitude and the phase of the point receptance and the wave propagation decay rate are given in terms of their mean value and standard deviation. These statistical results come from an average of one hundred calculation samples. For each case the results for a specific random sample are also presented for comparison with the constant sleeper spacing and ballast stiffness case.

5.4.1. *Effects on receptance and decay rate*

Figure 5.6 shows the statistical results for the random ballast stiffness only (i.e. constant sleeper spacing). It can be seen that the random ballast stiffness only

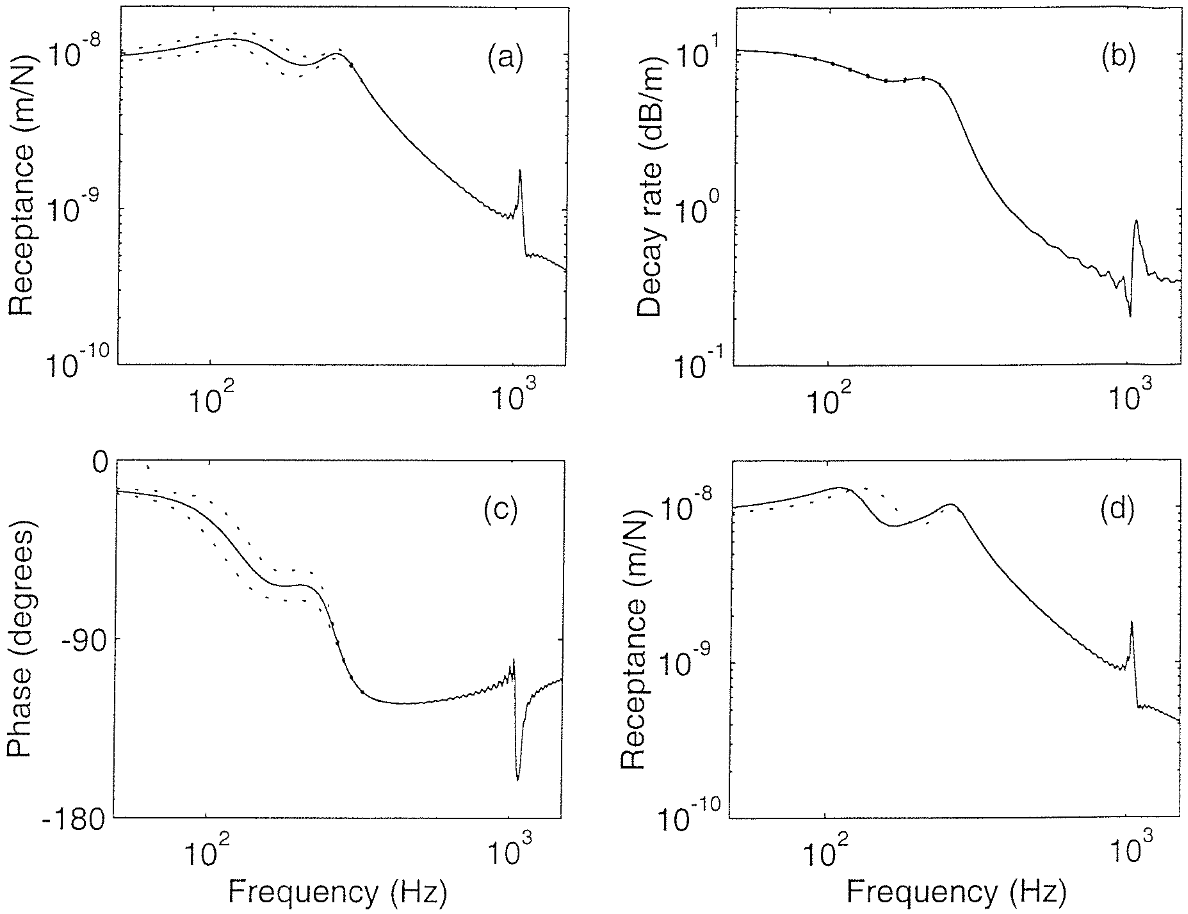

Figure 5.6. Results for random ballast stiffness with random factor r distributed in [0 2], sleeper spacing d = 0.6m, excitation acting at mid-span. — mean value, ····· mean value plus or minus standard deviation. (a) Amplitude of point receptance, (b) wave propagation decay rate, (c) phase of point receptance, (d) amplitude of point receptance, ····· result from constant sleeper spacing and ballast stiffness, — result from a specific random sample.

affects the rail vibration below about 300 Hz for the mean value of ballast stiffness considered. Because of the random ballast stiffness, the first track resonance, at which the whole track bounces on the ballast stiffness, now appears randomly in a certain frequency region rather than at about 130 Hz for the deterministic uniform ballast stiffness case. The second resonance, at which the rail vibrates on the pad stiffness, is less affected by the random ballast stiffness. Moreover, since the random ballast stiffness has no effects on the high frequency vibration of the track, the pinned-pinned resonance (the peak at about 1000 Hz) is not affected by the random

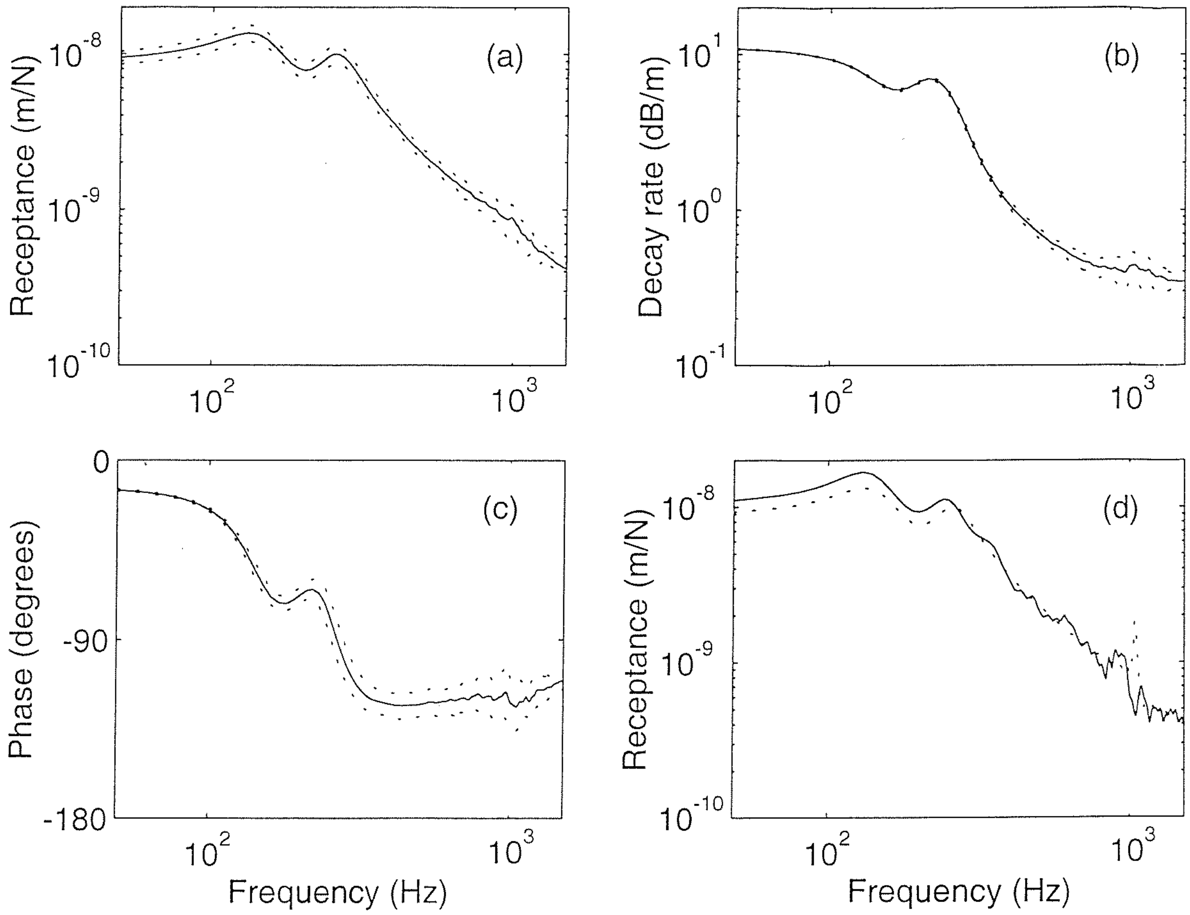

Figure 5.7. Results for random sleeper spacing distributed in [0.3 0.9], excitation acting at mid-span, key as for Figure 5.6.

ballast stiffness. The wave propagation decay rate at low frequencies is almost unaffected by the random ballast stiffness. This is because the decay rate is calculated over many spans along the track and therefore it is determined by the average of the random ballast stiffness (damping) over these spans.

Figure 5.7 shows the statistical results for the random sleeper spacing only. It can be seen that the point receptance of the rail vibration is affected by the random sleeper spacing in the whole frequency region. The pinned-pinned resonance peak is now not noticeable *even for the single sample in Figure 5.7(d)* and instead, many small peaks are spread in a wide frequency region due to the random sleeper spacing. At the first pinned-pinned resonance for a fixed sleeper spacing, the wavelength is equal to twice the span length and all the directly reflected waves (reflected only once by the support points) are superposed at the excitation point in the same phase so that the pinned-pinned resonance peak is formed. For the random sleeper spacing, however, this condition does not occur or is very weak and so the pinned-pinned resonance is not noticeable. The low frequency vibration is also affected by the random sleeper spacing because the average stiffness of the track foundation per unit length near the excitation point is now random due to the random sleeper spacing. The decay rate is affected by the random sleeper spacing mainly near the pinned-pinned resonance area.

Figure 5.8 shows the statistical results for the random ballast stiffness combined with the random sleeper spacing. Comparing Figure 5.8 with Figures 5.6 and 5.7,

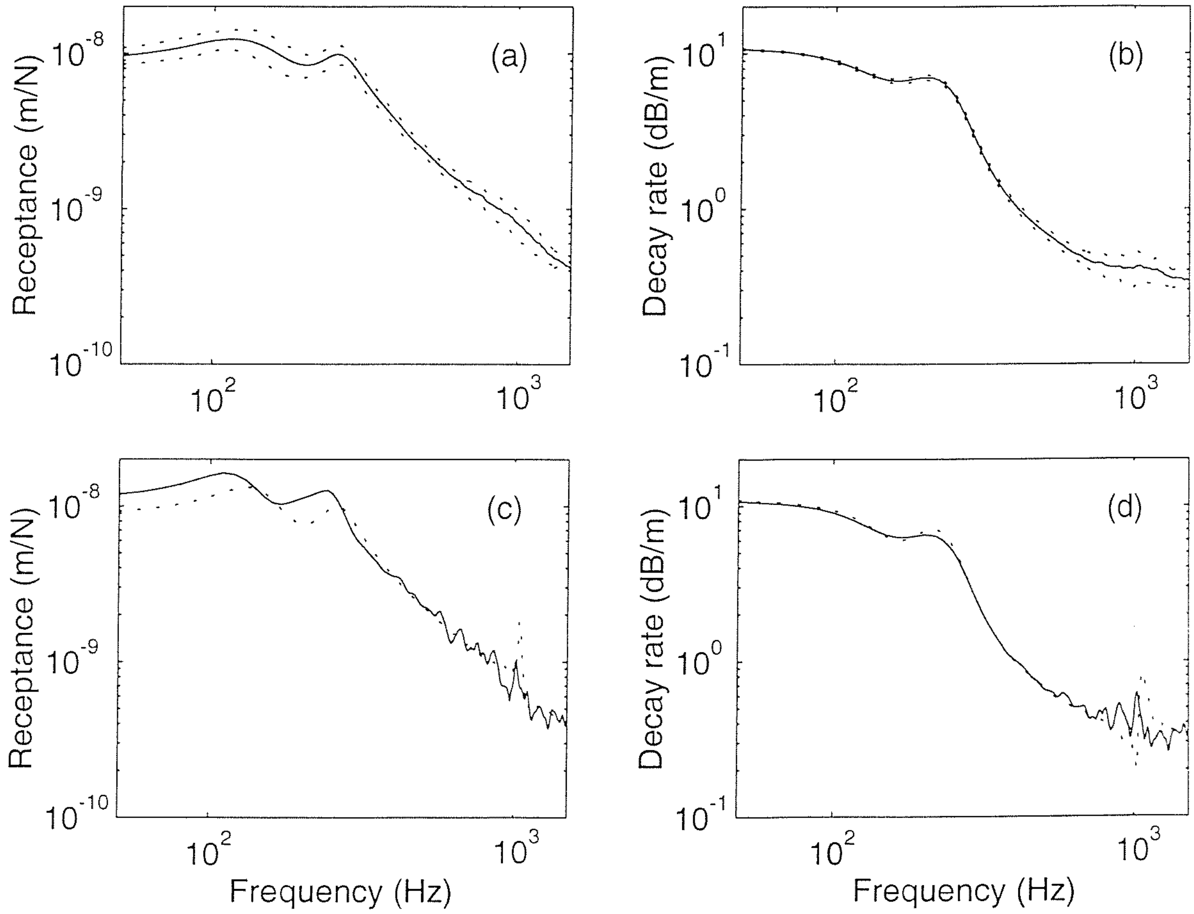

Figure 5.8. Results for random sleeper spacing distributed in [0.3 0.9] and ballast stiffness with random factor *r* distributed in [0 2], excitation acting at mid-span, key as for Figure 5.6. (a) Amplitude of point receptance, (b) wave propagation decay rate, (c) and (d) results from a specific random sample and from the track with constant sleeper spacing and ballast stiffness.

the random sleeper spacing can be seen to have more significant effects on the rail vibration than the random ballast stiffness.

It should be emphasised that the mean value and the standard deviation of the point receptance and the decay rate only have a statistical meaning. The mean value is averaged at each frequency in the whole frequency range 50 – 1500 Hz. Since the resonance peaks and troughs for each sample may appear at different frequencies due to the random sleeper spacing and ballast stiffness, they could cancel each other when averaged. Thus the mean value graph might be very smooth. However, for a specific random sample, both the point receptance and the decay rate can have many peaks and troughs, and their amplitude may exceed the limits of the mean value plus

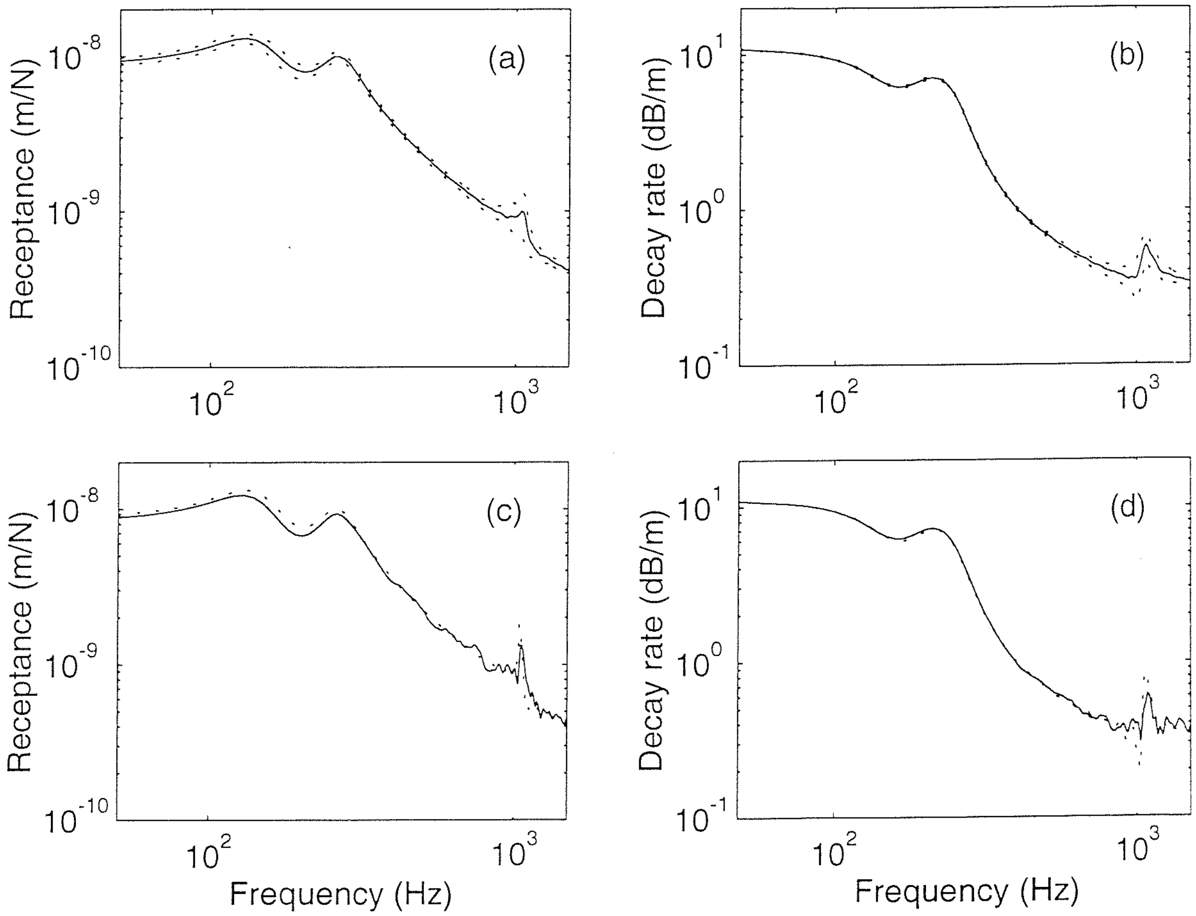

Figure 5.9. Results for random sleeper spacing distributed in [0.45 0.75] and ballast stiffness with random factor r distributed in [0.5 1.5], excitation acting at mid-span, key as for Figure 5.8.

or minus the standard deviation at some frequencies. All these points can be observed from Figure 5.8 by comparing the specific random samples with the statistical results.

Figure 5.9 also shows the results for the random ballast stiffness combined with the random sleeper spacing but the random sleeper spacing is distributed in [0.45 0.75] instead of [0.3 0.9] and the random factor *r* for the ballast stiffness is now distributed in [0.5 1.5]. Therefore, the deviations now are smaller than the case of Figure 5.8. Furthermore, there is a noticeable pinned-pinned resonance peak for the mean value of the point receptance, though it is not as sharp as for the uniform sleeper spacing case.

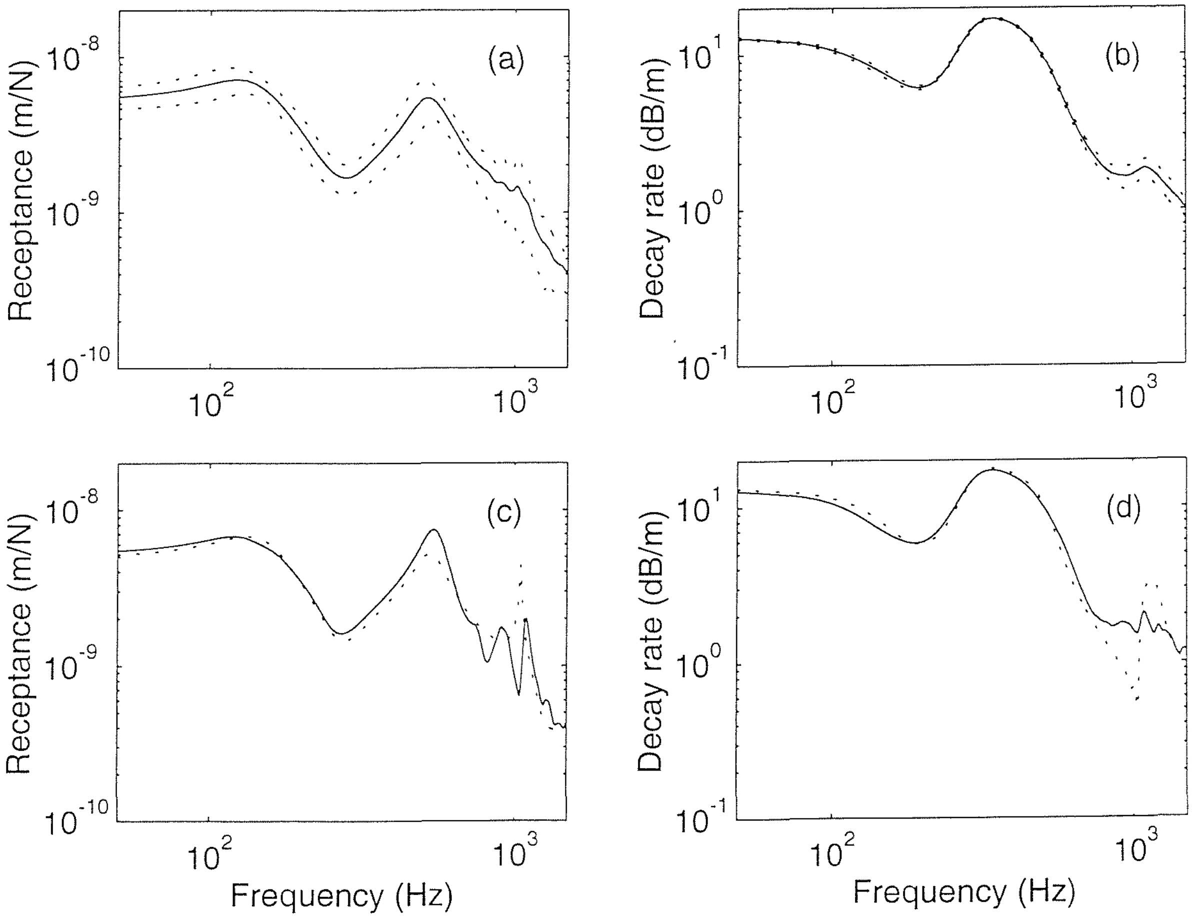

Figure 5.10. Results for random sleeper spacing distributed in [0.3 0.9] and ballast stiffness with random factor *r* distributed in [0 2], for stiffer pad K_p = 344 MN/m with excitation acting at mid-span, key as for Figure 5.8.

Figure 5.10 shows the results for a case of a five times higher pad stiffness (344 MN/m) and with both the sleeper spacing and the ballast stiffness being random. The deviation of the statistical results in Figure 5.10 becomes much larger than the track with the softer pad stiffness, especially in the pinned-pinned resonance area. In addition, the vibration decay rate can be seen to be much higher at high frequencies, compared with Figure 5.8 for the softer pad stiffness. Significantly, the sharp dip and rise in decay rate found at the pinned-pinned resonance of a periodic track (see Figure 5.10(d)) are suppressed by random sleeper spacing.

5.4.2. *Effect on noise radiation*

Another aim of the study in this chapter is to determine the effect of the irregularities of the sleeper spacing and ballast stiffness on the noise radiated by the track. The noise energy radiated by the rail and sleepers is directly related to the integral/sum of squared velocity of the rail and sleepers [84]. The vibration of the rail and sleepers is therefore calculated for the 'passage' of a single wheel on the basis of a relative displacement excitation between the wheel and rail. The 'moving irregularity' model is used [40] in which the wheel and rail are assumed stationary with the roughness moving between them. The excitation force, F, is determined from the following formula [16]:

$$F = -\frac{r}{\alpha^{W} + \alpha^{C} + \alpha^{R}} \tag{5.7}$$

where r is the relative displacement (roughness) between the wheel and rail and α^{W}, α^{C} and α^{R} are the point receptances of the wheel, contact spring and rail respectively. Values for α^{W} and α^{C} will be derived in chapter 7. For each of the samples of the random distribution, the rail vibration velocity $v(z)$ is calculated over a 39 span length at intervals of a quarter span length, the force being applied approximately at the centre of this length. The rail vibration level is then formed from the sum of

$$\sum \left|v(z)\right|^{2} \Delta z \tag{5.8}$$

over the 39 span length (approximately 23.4 m), where Δz is equal to a quarter span length. The sleeper response is calculated as the sum of the squared vibration velocity of 40 sleepers.

Figure 5.11 shows the rail vibration level and the summed vibration of the sleeper for a 1 μm relative displacement input at each frequency. Results are shown for the track with uniform sleeper spacing and ballast stiffness, and the mean and one standard deviation range are shown from a population of 100 tracks with

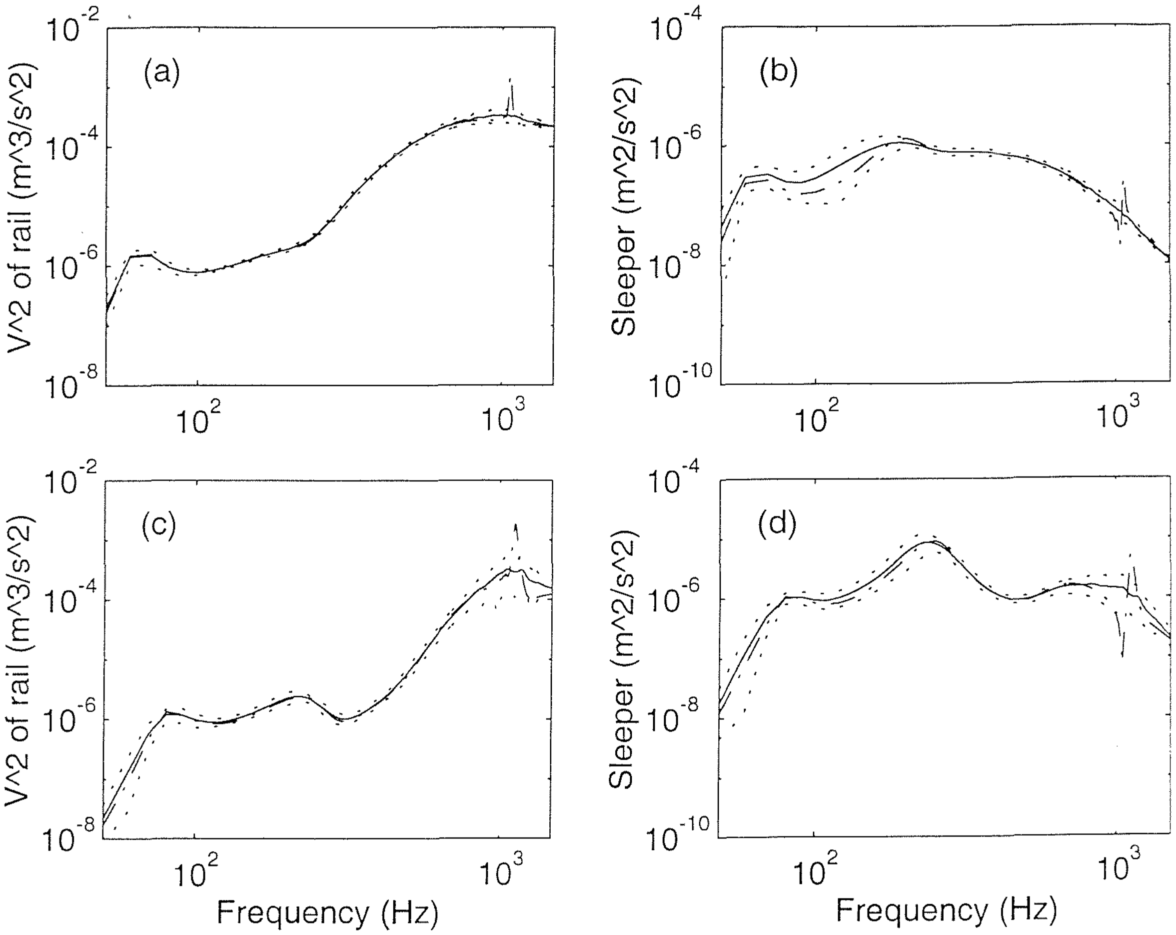

Figure 5.11. Vibration levels of the rail and sleepers due to 1 μm relative displacement excitation for random sleeper spacing distributed in [0.3 0.9] and ballast stiffness with random factor r distributed in [0 2], excitation acting at mid-span. — mean value, ····· mean value plus or minus standard deviation, -·-· result from constant sleeper spacing and ballast stiffness. (a) and (b) For the track with the soft pad (68.8 MN/m), (c) and (d) for the track with the stiffer pad (344 MN/m).

random sleeper spacing and ballast stiffness. In all cases the excitation was located at mid-span. The results for the uniform track contain a sharp peak close to the pinned-pinned frequency—in fact the peak is at 1065 Hz for the track with the soft pad (68.8 MN/m) and at 1125 Hz for the track with the stiffer pad (344 MN/m) whereas the peak in the receptance is at 1045 Hz (pinned-pinned frequency). The results for the randomised tracks do not contain this peak, mainly because the pinned-pinned effect is weaker (see Figure 5.7) but also because it occurs at different frequencies in each sample. However, since the peak for the regular track is rather sharp, it has only a small effect on the overall vibration level. The 1/3 octave band average response at 1 kHz is only 1 dB lower for the mean response of the random track than for the regular track for either pad.

The standard deviation of the vibration results is very small, corresponding mostly to less than ±1 dB variations in response. In the sleeper response below 200 Hz for the soft pad, the random effects lead to a higher standard deviation and an increase of about 2 dB in the average sleeper response compared with the regular track. For the stiffer pad, between 800 and 1500 Hz the standard deviation range of the rail response increases to about ±3 dB.

Altogether, it is found that the random sleeper spacing and ballast stiffness leads to only small variations in the noise from the track, and no net increase or decrease in the track noise. The reduction associated with the removal of the peak at 1 kHz is only 1 dB in 1/3 octave band level. Moreover, in practice the pinned-pinned effect is found to be cancelled anyway by the presence of multiple wheels on the track, see chapter 6.

5.5. Conclusions

The sleeper spacing and ballast stiffness of a railway track are irregular in reality and may be regarded as random variables in a certain region. The concept of the random sleeper spacing and ballast stiffness has been introduced into the track model and their distributions have been assumed. The same methodology could be used with a measured distribution. A simple Timoshenko beam model with discrete supports has been employed to represent the railway track for numerical simulations. The effects on the track vibration of the random sleeper spacing and ballast stiffness have been investigated through extensive numerical calculations.

The statistical results show the effect of the random sleeper spacing and ballast stiffness on the track vibration. The point receptance and the vibration decay rate are distributed in a certain area instead of having a fixed value due to the variations in the sleeper spacing and ballast stiffness. The random ballast stiffness mainly affects the low frequency vibration of the track below about 300 Hz for the mean value of ballast stiffness considered, whereas the random sleeper spacing affects the track vibration in the whole frequency region 50 – 1500 Hz studied. This is because the sleeper spacing affects the ballast stiffness, sleeper mass and pad stiffness per unit length, and the pinned-pinned resonance as well. Due to the random sleeper spacing the pinned-pinned resonance phenomenon is much less sharp than in the uniform sleeper spacing case and in some cases is completely suppressed. For a railway track with stiffer pads, its dynamic behaviour is more significantly affected by the random sleeper spacing, compared with the track with softer pads.

It is important that more extensive measurements of the variation in sleeper spacing, ballast stiffness and possibly pad stiffness be performed so that the actual statistical distributions can be established.

In terms of railway rolling noise, the randomness of the track foundation leads to only small effects and no significant increase or decrease in the track noise. The variations are limited to standard deviations corresponding mostly to only 1 dB. For the stiffer pad this increases to 3 dB close to 1 kHz. For the sleeper response with the soft pad below 200 Hz, the standard deviation is higher and there is also an increase of up to 2 dB in mean response. A small reduction is associated with the removal of the peak at 1 kHz, but this corresponds to only 1 dB in 1/3 octave band level for either pad.

CHAPTER 6

The Effects on Track Vibration of Multiple Wheel/Rail Interactions

In this chapter the effects on the rail vibration of multiple wheels on a rail are to be explored. Firstly the receptance of a rail with only a single additional wheel on it is studied using both continuously and discretely supported rail models to gain a physical insight. Then more complicated models are developed and used to investigate the effects of multiple wheels on a rail. Some useful conclusions are obtained through these calculations and through comparison and analysis of the rail vibration with and without additional wheel/rail interactions. Measurement data are also presented and shown to be in good agreement with the theoretical predictions.

6.1. Introduction

Structural vibration of the wheel and rail is generated by the combination of small scale undulations (roughnesses) on the wheel and rail contact surfaces. When a train runs on the track, these roughnesses produce dynamic interaction forces between the wheel and rail at the frequencies corresponding to the passage speed of the wheel/rail contact over the particular roughness wavelength so that the wheel and rail are excited, vibrate and radiate noise. The wheel/rail interaction force F can be calculated using a relative displacement (roughness) excitation model [16, 62]:

$$F = -\frac{r}{\alpha^W + \alpha^C + \alpha^R} \tag{6.1}$$

where r is the relative displacement (roughness) between the wheel and rail and α^W, α^C and α^R are the point receptances of the wheel, contact spring and rail respectively.

In order to determine the wheel/rail interaction force, knowledge of dynamic properties (receptances or impedances) of the wheel and rail is essential. Different models have been developed to investigate the track dynamic behaviour, see chapter 1. In most of these models, whether using finite elements or analytical representations of beams, the rail vibration behaviour is studied using a model in which the wheel/rail interaction is not considered, apart from at the single wheel/rail contact at which excitation takes place. If in equation (6.1) the rail receptance is used without taking account of wheels on the rail, the dynamic force between the wheel and rail that is calculated represents a situation in which only one wheel interacts with the rail, and all other wheels' interactions with the rail are neglected. Obviously this is not the case in practice. The main reason for calculating the rail receptance without taking wheel/rail interaction into account is to avoid the complicated nature of the interaction of multiple wheels with the rail. It is then assumed that the average response of the rail to multiple wheels can be obtained by combining the response to a series of single wheels.

In order still to use the relative displacement excitation (moving irregularity) models to calculate the wheel/rail interaction force and vibration of the wheel and rail, the various wheels should be included in the rail receptance calculation as additional passive systems coupling with the rail. Thompson [76] carried out some simple analysis of the effects of wheels on a rail, but it is very limited. Igeland [31], in a moving vehicle model, considered a two wheel bogie on a single rail and found some evidence of standing wave effects. Also multiple wheels are considered in multibody models of vehicles but these are used at low frequencies only, without any interaction through the track.

The aim of the study in this chapter is to explore the effects on the rail vibration of wheels on a rail by comparing the results from track models with and without considering multiple wheel/rail interactions. Firstly the receptance of a rail with a single additional wheel on it is studied using both continuously and discretely supported rail models to gain a physical insight. Then more complicated models are developed and used to investigate the effects of multiple wheels either on a continuously supported rail or on a discretely supported rail. Some useful conclusions are obtained through the calculations, comparison and analysis of the rail vibration in these situations. Measurement data are also presented and shown to be in good agreement with the theoretical predictions.

For simplicity a model based on an single Timoshenko beam is employed to represent the basic dynamic properties of a rail and only the vertical vibration of a rail is studied in this chapter. Some less important factors such as the cross-receptances of the wheel and rail are neglected. In a similar way as considered in this chapter, the effects of wheel/rail interactions on the lateral vibration can also be studied if an appropriate rail model is used for lateral vibration, for example the multiple beam model developed in chapter 3.

6.2. Model for vibration of a rail with a single wheel on it

6.2.1. *Model of a rail with a single wheel on it*

A vibration model of a rail with only one wheel on it is considered first as a simple case. Using this model, the receptances of the rail can be determined by means of the receptances of the wheel and the rail without the wheel on it and some most important characteristics of the effects of multiple wheel/rail interactions on the rail vibration can be obtained. For wagons which have only one wheelset at each end, this model can be used directly to obtain a practical solution. This is because, although a train contains many wheelsets running on the rail as will be seen later, the effect of one wheel on another can be ignored for wheels that are further apart than about 10 m, because the wave decay rate in the rail is in the range of 0.5 – 2 dB/m. The distance between the two wheelsets at opposite ends of a wagon is usually greater than 10 m.

Consider a rail having a single wheel (passive wheel) on it at $z = a$ and an external excitation (for example due to another wheel) applied at $z = 0$, as shown in Figure 6.1. Here only one direction of vibration of the rail is taken into account, which can be either vertical or lateral, and the cross-interaction of the vertical and lateral vibration is ignored for simplicity. Coupling with the far rail through sleepers and axle is also ignored. It is assumed that forces and responses are harmonic and both have an $e^{i\omega t}$ term, thus the $e^{i\omega t}$ term will usually be omitted. In Figure 6.1, F and u_i represent the external force and the incident wave produced by F respectively.

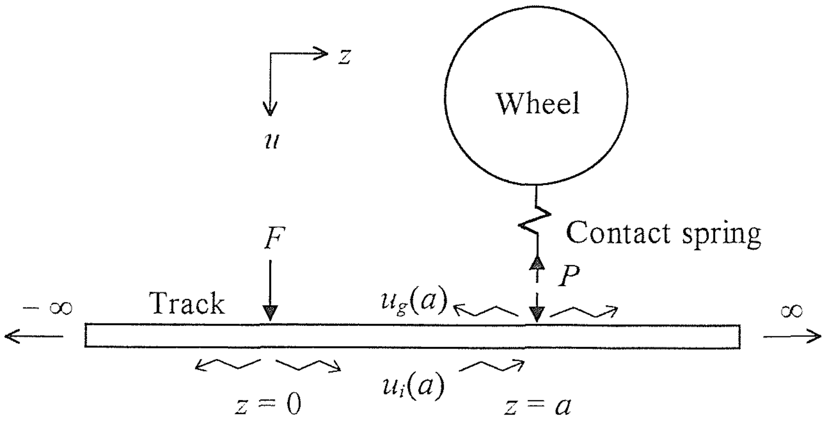

Figure 6.1. Railway track model with a single wheel on the rail.

The incident wave propagates along the rail and interacts with the wheel at $z = a$. This results in the generation of an interaction force P at the contact position. The generated wave produced by P is represented by u_g. Thus the vibration of the rail is a combination of the incident wave u_i and the generated wave u_g. The response of the rail at the wheel/rail contact point $z = a$ to the external force F at $z = 0$ is given as follows:

$$u(a) = u_i(a) + u_g(a) = F\alpha_F^{RT}(a) + P\alpha_P^R \tag{6.2}$$

where α_F^{RT} and α_P^R are the transfer and point receptances of the rail respectively. Equation (6.2) can be used for either a continuously supported or a discretely supported rail. For a discretely supported rail model, since F and P may act at different positions in a span between two sleepers, the receptances corresponding to F and P are generally not the same. Thus the subscripts F and P are used for marking the receptances corresponding to F and P respectively. For a continuously supported rail, or for a discretely supported rail where both F and P act either at mid-span or above a sleeper, the receptances for F and P are the same and the subscripts need not be used.

If the dynamic stiffness of the wheel, Z_w (including the wheel/rail contact spring stiffness), is known, the dynamic interaction force P can be represented by

$$P = -Z_w u(a) = -Z_w[u_i(a) + P\alpha_P^R] \tag{6.3}$$

Since $1/Z_w = \alpha^W + \alpha^C$, where α^W and α^C represent the receptances of the wheel and contact spring respectively, substituting it into (6.3) gives

$$P = -\frac{u_i(a)}{\alpha^W + \alpha^C + \alpha_P^R} = -\frac{\alpha_F^{RT}(a)}{\alpha^W + \alpha^C + \alpha_P^R} F \tag{6.4}$$

The wheel/rail interaction force can be seen from (6.4) to be related to the sum of point receptances of the wheel, contact spring and rail. This term also appears in the expression for roughness excitation, see equation (6.1). P also depends on the transfer receptance of the rail. If the point receptance of the wheel, contact spring or rail is high or the transfer receptance of the rail is low, the interaction force P will be small. Low transfer receptance occurs when the wave propagation decay rate is high, and thus the rail vibration at $z = a$ caused by the original force F is weak. As a result, the interaction force P is small.

When the generated interaction force P is known, the vibration displacement of the rail at any point can be obtained by superposing the incident and generated waves:

$$u(z) = F\alpha_F^{RT}(z) + P\alpha_P^{RT}(z-a) = F\left[\alpha_F^{RT}(z) - \frac{\alpha_F^{RT}(a)}{\alpha^W + \alpha^C + \alpha_F^R}\alpha_P^{RT}(z-a)\right] \tag{6.5}$$

Thus the transfer and point receptances of the rail with a single wheel on it are given as

$$\alpha_w^{RT}(z) = \frac{u(z)}{F} = \alpha_F^{RT}(z) - \frac{\alpha_F^{RT}(a)}{\alpha^W + \alpha^C + \alpha_P^R}\alpha_P^{RT}(z-a) \tag{6.6}$$

$$\alpha_w^R = \frac{u(0)}{F} = \alpha_F^R - \frac{\left[\alpha_F^{RT}(a)\right]\left[\alpha_P^{RT}(-a)\right]}{\alpha^W + \alpha^C + \alpha_P^R} = \alpha_F^R - \frac{\left[\alpha_F^{RT}(a)\right]^2}{\alpha^W + \alpha^C + \alpha_P^R} \tag{6.7}$$

where $\alpha_F^{RT}(a)$ and $\alpha_P^{RT}(-a)$ are equal because of reciprocity, and the subscript w means the rail having a wheel (or wheels) on it.

From (6.6) and (6.7) it can be observed that the receptances of the rail with a single wheel on it are determined by the point and transfer receptances of a 'bare' track (without any wheel/rail interaction), the receptance of the wheel and that of the contact spring. This is easy to understand in a physical sense. Thus the important point is that the receptances of a track with a single wheel (also multiple wheels) on it can be calculated through the receptances of the 'bare' track and the wheel.

Therefore, a knowledge of the receptances of the 'bare' track, wheel and contact spring is essential to calculate the receptances of a track with a wheel (or wheels) on it.

6.2.2. *Receptances of a rail without a wheel on it*

In this chapter a conventional Timoshenko beam model is employed to calculate the receptances of a rail without a wheel on it. Although a conventional beam model is only reliable below 2 kHz for the vertical vibration of the rail foot, it can be used for predicting the rail head response for frequencies up to close to the frequency when the higher-order 'foot flapping' wave cuts on, i.e. up to about 5 kHz, as shown in chapter 2. At high frequencies the wave propagation decay rate of a conventional beam model falls continuously, whereas in practice the decay rate increases slightly with increasing frequency above about 1 – 2 kHz [95]. Thus a small loss factor needs to be assigned to the rail to enhance the decay rate at high frequencies. The detailed procedures for calculating the receptance for either continuously or discretely supported rail can be found in chapter 2; here only the results are presented.

Figure 6.2 shows the point and transfer receptances of a continuously supported UIC 60 rail as well as the wave propagation decay rate. The transfer receptances are calculated at 0.9 m, 1.8 m and 3.6 m from the excitation point. The parameters for the rail are:

$$E = 2.1\times10^{11}\ \mathrm{N/m^2},\quad G = 0.77\times10^{11}\ \mathrm{N/m^2},\quad \rho = 7850\ \mathrm{kg/m^3},\quad \eta_r = 0.01,$$
$$A = 7.69\times10^{-3}\ \mathrm{m^2},\quad I = 30.55\times10^{-6}\ \mathrm{m^4},\quad \kappa = 0.4$$

and for the foundation:

$$k_p = 583\ \mathrm{MN/m^2},\quad \eta_p = 0.25,\quad k_b = 83.3\ \mathrm{MN/m^2},\quad \eta_b = 1.0,\quad m_s = 270\ \mathrm{kg/m}$$

where E is the Young's modulus, G the shear modulus, ρ the density, η_r the loss factor of the rail, A the cross-sectional area, I the area moment of inertia and κ the shear coefficient. For the track foundation k_p is the pad stiffness per unit length, η_p the loss factor of the pad, k_b the ballast stiffness per unit length, η_b the loss factor of the ballast and m_s the sleeper mass per unit length. These parameters correspond to a track with concrete sleepers and moderate stiffness rail pads. Similar parameters

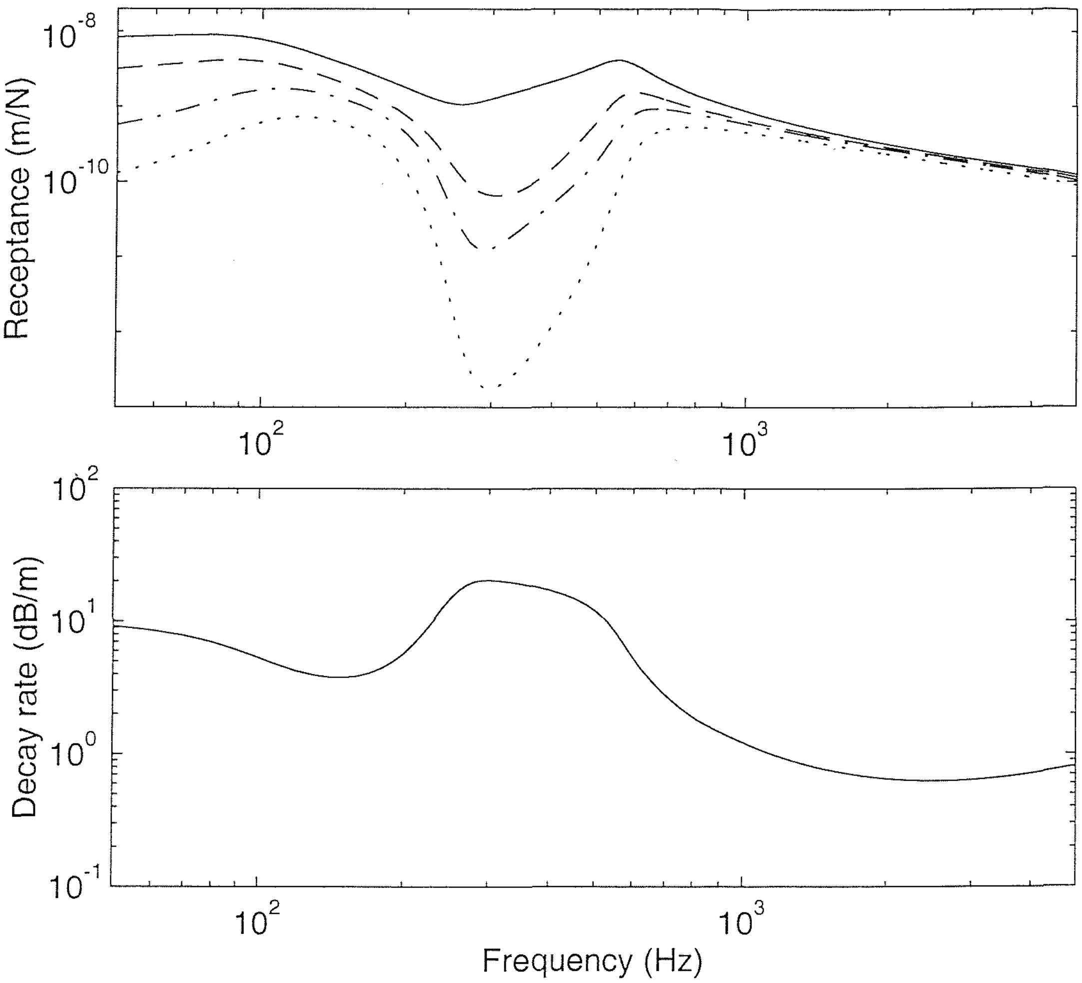

Figure 6.2. Magnitude of receptances and wave propagation decay rate of a continuously supported rail. — point receptance, - - - transfer receptance at 0.9 m, -·-·- transfer receptance at 1.8 m, ····· transfer receptance at 3.6 m.

are used in chapter 2 and in [95] for track C.

Figure 6.3 shows the point and transfer receptances of a discretely supported rail with the excitation acting either at mid-span or above a sleeper. The transfer receptances are also calculated at 0.9 m, 1.8 m and 3.6 m from the excitation. The parameters for the discrete support are:

$K_p = 350$ MN/m, $\eta_p = 0.25$, $K_b = 50$ MN/m, $\eta_b = 1.0$, $M_s = 162$ kg, $d = 0.6$ m

where K_p is the pad stiffness, K_b the ballast stiffness, M_s the sleeper mass and d the span length.

The point receptances for both the continuously supported and the discretely supported rails can be seen to reach resonances at about 80 Hz and 530 Hz, whereas

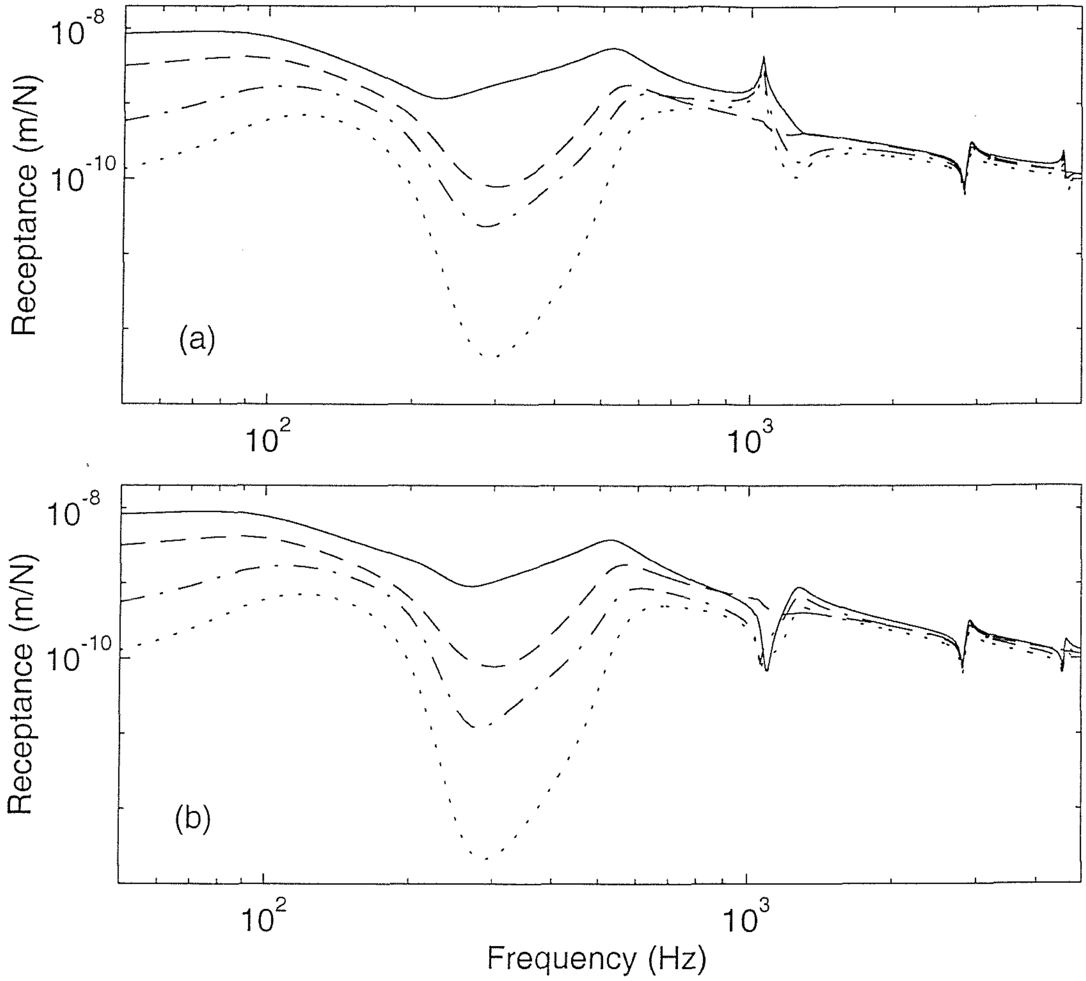

Figure 6.3. Magnitude of receptances of a discretely supported rail. (a) excitation at mid-span, (b) excitation above a sleeper. — point receptance, - - - transfer receptance at 0.9 m, -·-·- transfer receptance at 1.8 m, ····· transfer receptance at 3.6 m.

for the latter there are three pinned-pinned resonances which appear at about 1050 Hz, 2800 Hz and 4600 Hz. For detailed features of these resonances, see chapter 2. From Figure 6.2 it can be seen that the wave propagation decay rate is high at low frequencies and low at high frequencies. At about 300 Hz the decay rate is the highest, so that the responses around 300 Hz at the different positions dramatically decrease with increasing the distance from the excitation in both cases of the continuously and discretely supported rails. Whereas at high frequencies the responses at the different positions are similar due to the low decay rate. These features are very useful in understanding the results of the later analysis of the effects of the wheel/rail interaction on the rail vibration.

6.2.3. *Wheel receptance and contact spring receptance*

The wheel receptance can be obtained by either finite element analysis or experiment [78]. In theory it can be written as

$$\alpha_{ij}^{W}=\sum_{n=1}^{\infty}\frac{\Psi_{ni}\Psi_{nj}}{m_n(\omega_n^2-\omega^2+i\eta_n\omega_n^2)} \tag{6.8}$$

where ω_n is the n-th natural frequency, Ψ_{ni} and Ψ_{nj} are the n-th mode shape amplitudes for the i-th and j-th displacements, m_n is the modal mass for the n-th mode and η_n is the loss factor for the n-th mode. In practice, the infinite modal sum is often replaced by an approximation of a finite set of modes within the required frequency region. Here only the point receptance of a wheel in the radial direction at the contact point with the rail is needed.

The radial point receptance of a wheel can be approximated using the simple model shown in Figure 6.4. In this model the wheel is composed of a mass M_w (all the unsprung mass) and a modal spring K_M which represents the stiffness of high frequency modes. The point receptance is

$$\alpha^{W}=\frac{1}{K_M}-\frac{1}{M_w\omega^2} \tag{6.9}$$

From (6.9) the wheel can be seen to vibrate as a mass at low frequency and as a spring at high frequency. The receptance from the simple model is mainly used in this chapter, whereas that from the FE model (6.8) is only used for some comparisons. These comparisons show that this simple wheel model is acceptable for the purpose of the current study.

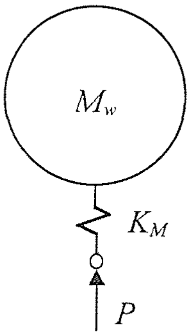

Figure 6.4. A simple model of the wheel (including unsprung mass).

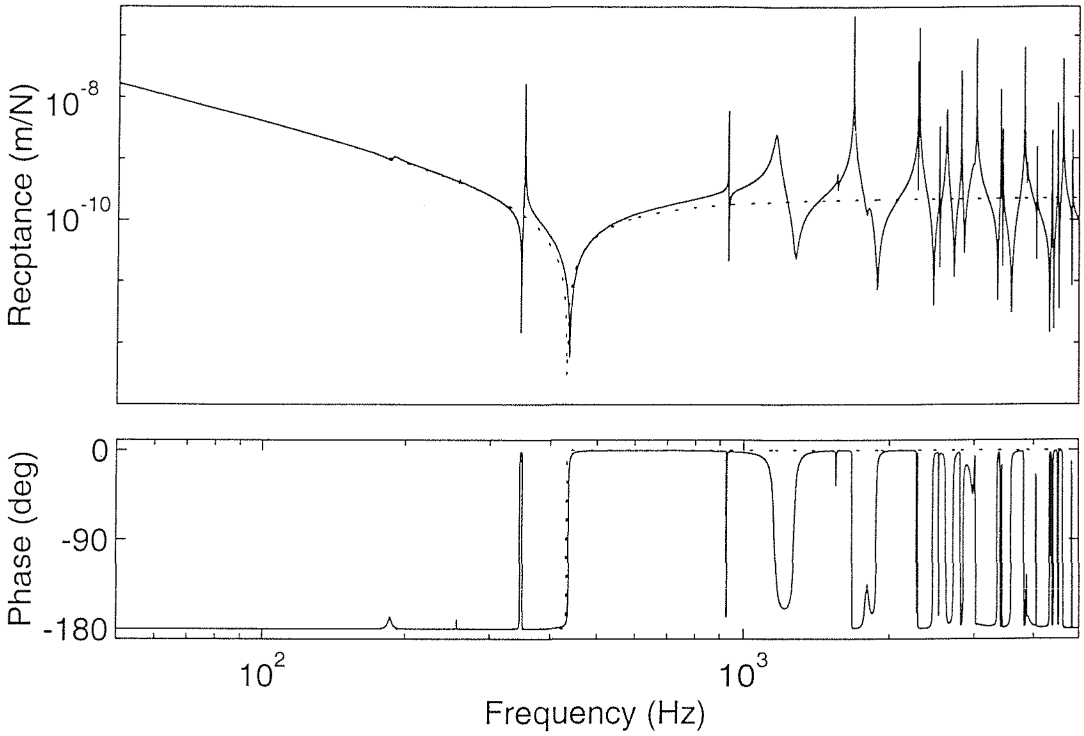

Figure 6.5. Receptance of the wheel (including unsprung mass). — from an FE model, ····· from the simple model.

Figure 6.5 shows the wheel receptances from an FE model (including the unsprung mass) and the simple model. The modal stiffness K_M of the simple model is chosen according to the mass M_w to match the main trough of the receptance from the FE model at the corresponding frequency of 430 Hz. The wheel parameters are chosen from a UIC 920 mm standard freight wheel. The unsprung mass is chosen as $M_w = 600$ kg.

It can be seen that there are a lot of sharp peaks and troughs in the wheel receptance at high frequencies due to the low damping of the wheel. Since a fairly large tolerance in web thickness is allowed in the wheel manufacturing and differences in diameter occur due to wear, the peaks or troughs in the high frequency region will occur at different frequencies for each individual wheel. The receptance of the simple model can be seen to be close to the average of the peaks and troughs of the FE model.

The contact spring between the wheel and the rail is effectively non-linear and follows the Hertz law. However, since the dynamic displacements are small, it is possible to treat the contact spring as a constant linear stiffness K_H. The value of K_H should be determined using the contact theory of Hertz according to the preload between the wheel and rail and their radii of curvature. Here the contact spring is calculated as in [76], giving $K_H = 1.14 \times 10^9$ N/m for a 50 kN preload. The contact spring receptance α^C is the inverse of K_H.

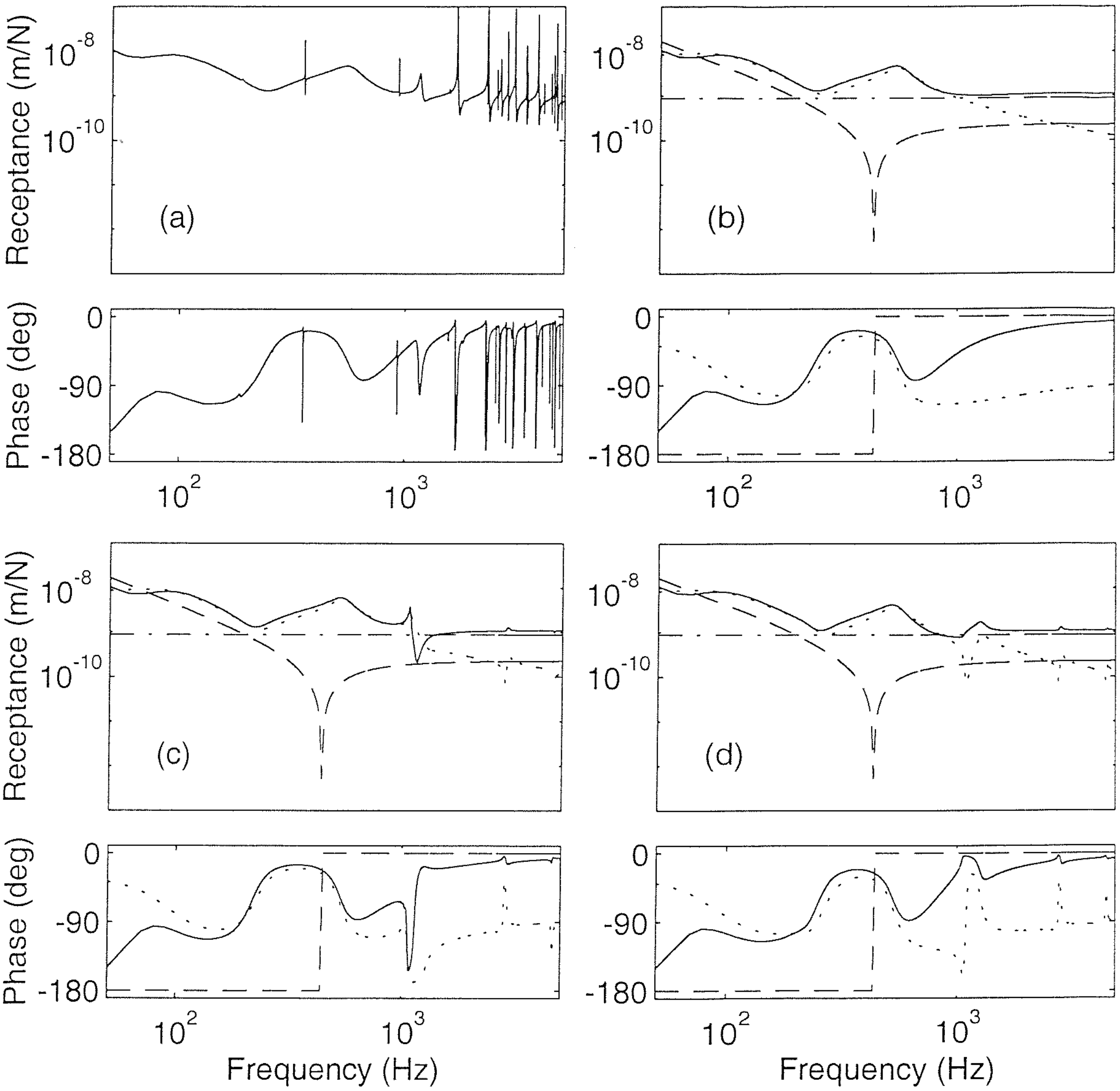

Figure 6.6. Point receptance sum of the wheel, contact spring and rail. (a) continuously supported rail and using FE wheel model, (b) continuously supported rail, (c) discretely supported rail with excitation at mid-span, (d) discretely supported rail with excitation above a sleeper, (b) – (d) include simple wheel models. — point receptance sum, - - - wheel receptance, ----- contact spring receptance, ····· rail receptance.

From equations (6.4), (6.6) and (6.7) it can be seen that the point receptance sum of the wheel, contact spring and rail plays a very important role in determining the wheel/rail dynamic interaction force and the point and transfer receptances of a rail with a wheel on it. Figure 6.6(a) shows the point receptance sum of the wheel (using the FE model), contact spring and continuously supported rail. Figures 6.6(b) – 6.6(d) show this sum along with the individual receptances for the cases of both continuously and discretely supported rails but using the simple wheel model. It can be seen that in all the cases in Figures 6.6(b) – 6.6(d) the sum of the receptances is similar except near the first pinned-pinned resonance at 1 kHz. In the frequency range 100 – 900 Hz the point receptance sum is high and almost the same as the rail receptance, whereas at high frequencies it becomes very close to the receptance of the contact spring and much higher than the rail receptance and wheel receptance. In Figure 6.6(a), using the FE model shows that the receptance sum is high at wheel resonances, but is well predicted by the simple model between resonances. For the discretely supported rail with the excitation acting at mid-span (Figure 6.6(c)) the point receptance sum can be seen to fall immediately after the first pinned-pinned resonance to a value close to the wheel receptance. The reason for this is that the amplitude of the rail receptance drops after the first pinned-pinned resonance and its phase is close to $-\pi$ so that at a certain frequency shortly above the pinned-pinned resonance the receptances of the rail and the contact spring are equal to each other in magnitude but out of phase, and thus cancel each other.

6.3. Rail vibration behaviour with a single wheel on it

In this section the dynamic behaviour of a rail with a single wheel on it is analysed using equations (6.6) and (6.7) in terms of the point and transfer receptances. First, the continuously supported rail is studied and then the discretely supported rail. Lastly, a specific case of a rail with two wheels located symmetrically on it is studied.

6.3.1. *Continuously supported rail*

For a continuously supported rail, equations (6.4), (6.6) and (6.7) can be rewritten as follows:

$$P=-\frac{u_i(a)}{\alpha^W+\alpha^C+\alpha^R}=-\frac{\alpha^{RT}(a)}{\alpha^W+\alpha^C+\alpha^R}F \tag{6.10}$$

$$\alpha_w^{RT}(z)=\frac{u(z)}{F}=\alpha^{RT}(z)-\frac{\alpha^{RT}(a)}{\alpha^W+\alpha^C+\alpha^R}\alpha^{RT}(z-a) \tag{6.11}$$

$$\alpha_w^R=\frac{u(0)}{F}=\alpha^R-\frac{[\alpha^{RT}(a)]^2}{\alpha^W+\alpha^C+\alpha^R} \tag{6.12}$$

where the subscripts F and P are removed because for a continuously supported infinite rail without a wheel on it the point receptance is the same at any position along the rail and the transfer receptance depends only upon the distance from the excitation.

Before calculating the point and transfer receptances by using equations (6.11) and (6.12), it is helpful to carry out some simple analysis in order to get a better understanding of the results. The ratio

$$\frac{\alpha_w^R}{\alpha^R}=1-\frac{[\alpha^{RT}(a)]^2}{\alpha^R(\alpha^W+\alpha^C+\alpha^R)} \tag{6.13}$$

may be used for quantifying the variation of the point receptances of the rail with a single wheel on it compared with the case without the wheel. Because the wave propagation decay rate in a supported rail is high at low frequencies, see Figure 6.2, the transfer receptance $\alpha^{RT}(a)$ is much smaller than the point receptance α^R when the distance a is large enough, for example greater than 1.8m. In addition the receptance sum $\alpha^W + \alpha^C + \alpha^R$ is very close to the point receptance α^R at low frequencies, see Figure 6.6(b). As a result, the second term in the right-hand side of equation (6.13) is close to zero, and thus the following approximation holds at low frequencies:

$$\frac{\alpha_w^R}{\alpha^R}\approx 1 \tag{6.14}$$

Therefore, at low frequencies the point receptance of a rail with a single wheel on it sufficiently far from the forcing point may be regarded as approximately equal to that of a rail without a wheel on it.

At high frequencies the following relationship holds, see Figure 6.6(b):

$$\left|\alpha^W + \alpha^C + \alpha^R\right| >> \left|\alpha^R\right| > \left|\alpha^{RT}(a)\right| \tag{6.15}$$

Thus the magnitude of the second term in the right-hand side of equation (6.13) is less than unity at high frequencies. In addition, although the distance a is constant, the phase of the second term continuously changes from $-\pi$ to π as the vibration frequency increases from low to high. This is because the wave number undergoes a continuous increase with increasing frequency and thus the phase of $\alpha^{RT}(a)$ continuously changes from $-\pi$ to π. Therefore, it is expected that *at high frequencies the point receptance of the rail with a single wheel on it will fluctuate around the point receptance of the rail without a wheel on it*. Moreover, *this fluctuation becomes smaller and smaller with increasing frequency* because the ratio of the rail receptance α^R (or $\alpha^{RT}(a)$) to the receptance sum $\alpha^W + \alpha^C + \alpha^R$ becomes smaller and smaller (see Figure 6.6).

Similarly, for the transfer receptance, the ratio

$$\frac{\alpha_w^{RT}(z)}{\alpha^{RT}(z)} = 1 - \frac{\alpha^{RT}(a)}{\alpha^W + \alpha^C + \alpha^R}\frac{\alpha^{RT}(z-a)}{\alpha^{RT}(z)} \tag{6.16}$$

can be used to examine the variation of the transfer receptance of a rail with a single wheel on it compared with the case without the wheel. However, situations are more complicated in terms of transfer receptance compared with the point receptance because both frequency and spatial position affect the transfer receptance. For example, when $z = a/2$, a, $2a$ and $-a$, the ratios are given as follows:

$$\frac{\alpha_w^{RT}(a/2)}{\alpha^{RT}(a/2)} = 1 - \frac{\alpha^{RT}(a)}{\alpha^W + \alpha^C + \alpha^R} \qquad z = a/2 \tag{6.17a}$$

$$\frac{\alpha_w^{RT}(a)}{\alpha^{RT}(a)} = 1 - \frac{\alpha^R}{\alpha^W + \alpha^C + \alpha^R} \qquad z = a \tag{6.17b}$$

$$\frac{\alpha_w^{RT}(2a)}{\alpha^{RT}(2a)} = 1 - \frac{[\alpha^{RT}(a)]^2}{\alpha^{RT}(2a)(\alpha^W + \alpha^C + \alpha^R)} \qquad z = 2a \tag{6.17c}$$

$$\frac{\alpha_w^{RT}(-a)}{\alpha^{RT}(-a)} = 1 - \frac{\alpha^{RT}(2a)}{\alpha^W + \alpha^C + \alpha^R} \qquad z = -a \tag{6.17d}$$

It may be expected that the variation at $z = a$ is greater than that at $z = a/2$, whereas the variation at z = $a/2$ is greater than that at $z = -a$ because $|\alpha^{R}| > |\alpha^{RT}(a)| > |\alpha^{RT}(2a)|$.

Figure 6.7 shows the dynamic interaction force between the wheel and rail and the point receptance of the rail with a single wheel on it. The dynamic interaction

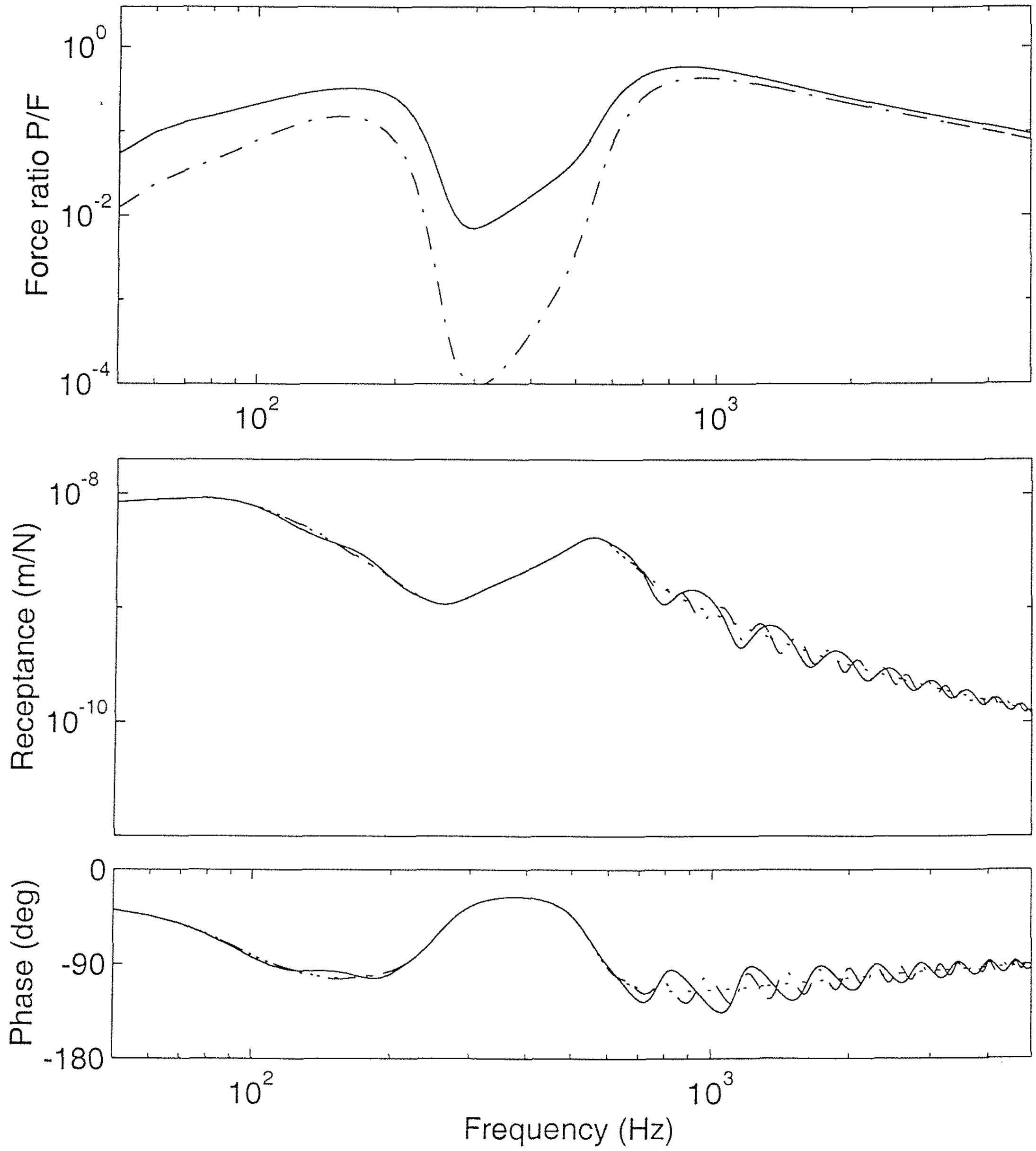

Figure 6.7. Wheel/rail interaction forces (magnitude) and point receptances of the continuously supported rail with a single wheel on it. — for excitation at 1.8 m from the wheel, ---- for excitation at 3.6 m, ····· for the case without wheel/rail interaction.

force is presented in terms of the ratio of the generated force P to the original force F. Two cases are calculated. The distance between the excitation and the wheel/rail interaction point is chosen as 1.8 m and 3.6 m for the two cases. The wheel/rail interaction force can be seen to have a similar trend to the transfer receptance of the rail without a wheel on it, see Figure 6.2, because the interaction force depends upon the transfer receptance according to equation (6.10). At about 850 Hz the interaction force reaches a peak value. This is because the point receptance sum of the wheel, contact spring and rail, the denominator in equation (6.10), is dominated by the rail receptance and tends to reach its minimum near this frequency, whereas the transfer receptance, the numerator, is fairly large and close to the rail point receptance due to a low decay rate. After this peak the wheel/rail interaction force comes down gradually with increasing frequency. Moreover, the interaction forces for distances of 1.8 m and 3.6 m are very close to each other above 1 kHz because the low decay rate of the wave propagation at high frequencies leads to the transfer receptances being similar in magnitude in each case, see Figure 6.2.

The point receptance of the rail with a single wheel on it can be seen from Figure 6.7 to be very close to that of the rail without the wheel at low frequencies as suggested above. At high frequencies, however, it fluctuates around the point receptance of the rail without a wheel/rail interaction. For the 1.8 m distance case the magnitude of the fluctuation is greater than for the 3.6m distance case. The maximum fluctuation occurs near 900 Hz because the wheel/rail dynamic interaction force reaches its peak around this frequency. As the wheel/rail interaction force decreases with increasing frequency after 900 Hz, so does the fluctuation of the point receptance. In addition the fluctuation levels in both cases become more similar to each other with increasing frequency.

Figure 6.8 shows the ratio of the point receptances of the rail with and without the wheel for both 1.8 m and 3.6 m distances. The variation in ratio can be seen to be smaller at low frequencies and larger at high frequencies. The largest variation appears near 900 Hz. It reaches about 138 % for the 1.8 m distance case and 125 % for the 3.6 m distance case. Above 3 kHz the ratios for both cases are approximately equal although the variation frequencies are different.

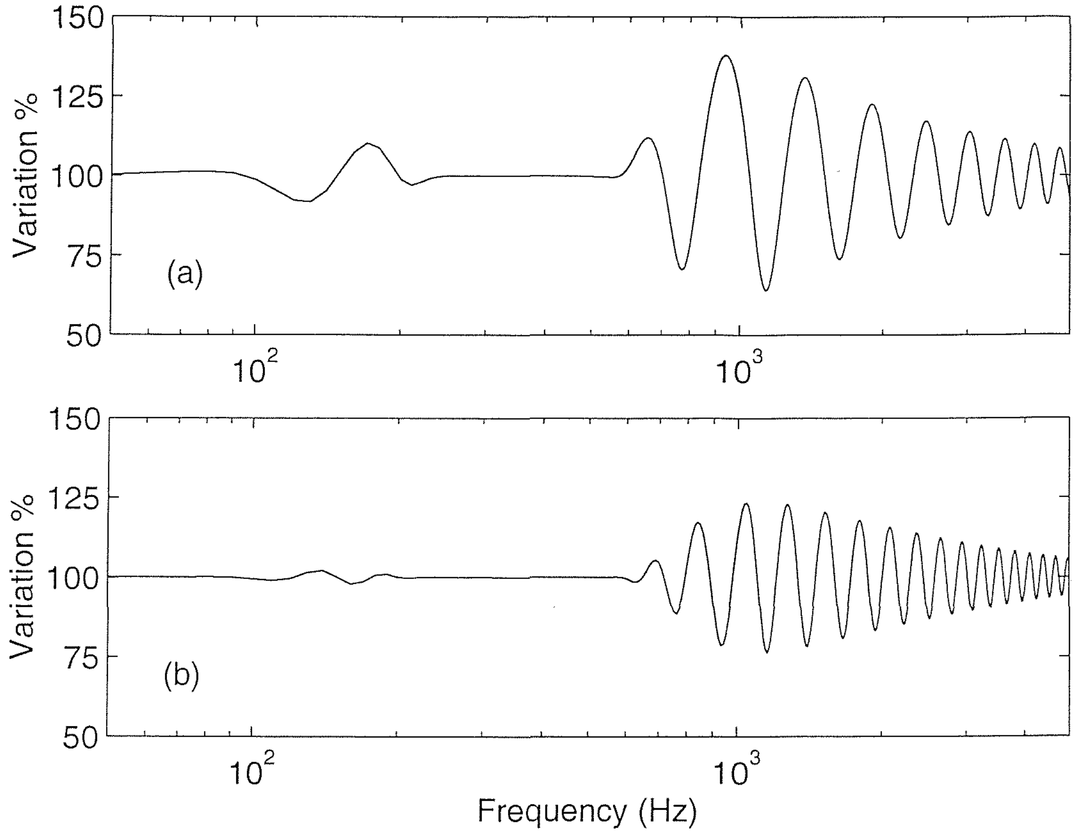

Figure 6.8. Ratio of the point receptance amplitude of the continuously supported rail with a single wheel on it to that of the rail without a wheel on it. (a) excitation at 1.8 m from the wheel, (b) excitation at 3.6 m from the wheel.

Figure 6.9 also shows the point receptance of the rail with a single wheel on it, but the wheel receptance α^W used now is from the FE model. Compared with the case using α^W from the simple wheel model, the point receptance can be seen to have some very sharp troughs and peaks corresponding to the sharp resonances and anti-resonances of the wheel. However, these can be neglected because their magnitude is small and they only appear in a very limited bandwidth. Thus the simple model of the wheel is in practice acceptable.

Figure 6.10 shows the transfer receptances at −1.8 m, 0.9 m, 1.8 m and 3.6 m away from the excitation with the wheel at 1.8 m. Compared with the rail without the wheel on it (Figure 6.2), the transfer receptances at high frequencies can be seen to be very similar in each case. The receptances at −1.8 m and 0.9 m are approximately equal to those of the rail without wheel/rail interaction in the whole frequency region. However, for the receptance at 1.8 m, the wheel/rail contact

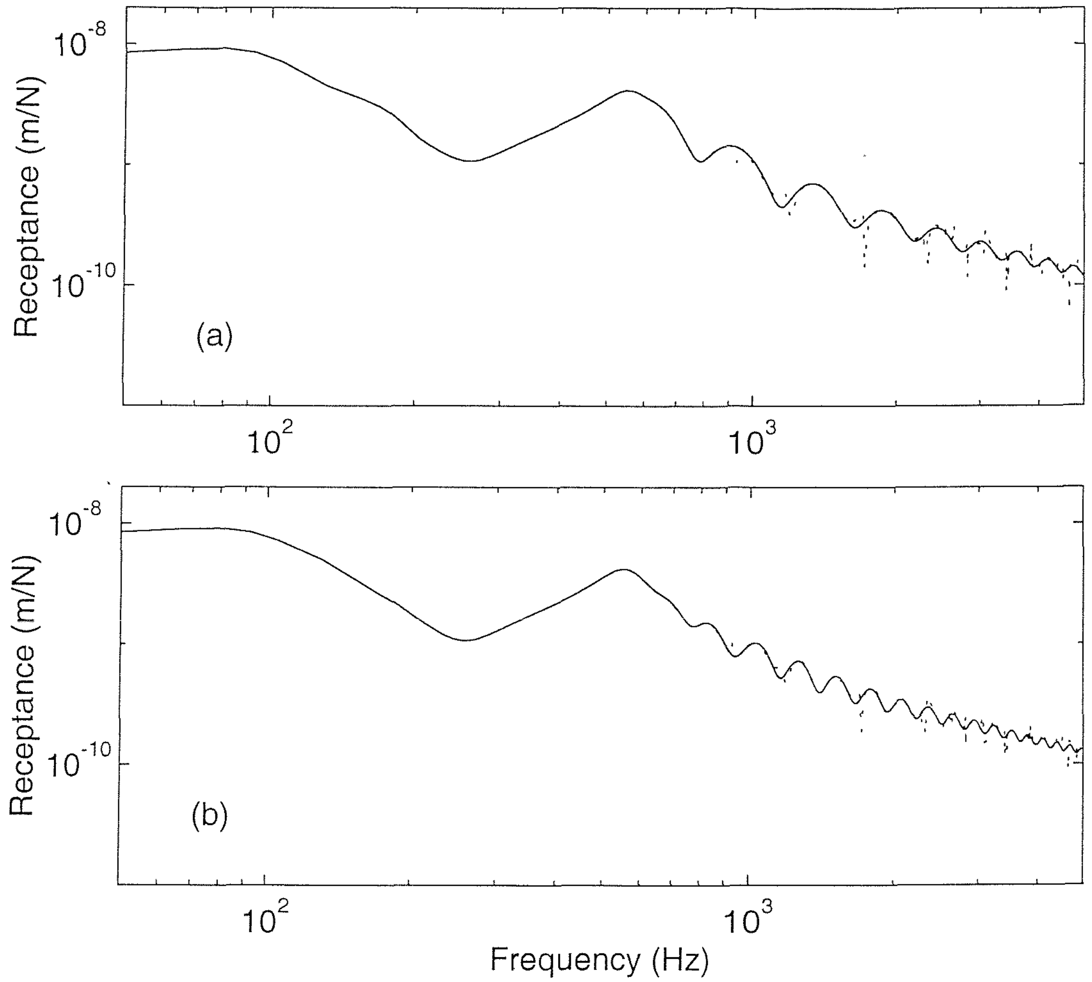

Figure 6.9. Magnitude of point receptances. (a) excitation at 1.8 m from the wheel, (b) excitation at 3.6 m from the wheel. — by using wheel receptance from the simple model, ····· by using wheel receptance from the FE model.

point, a considerable deviation between the two cases can be observed at low frequencies. For the receptance at 3.6 m the major deviation occurs in the frequency region 600 Hz – 1000 Hz.

6.3.2. *Discretely supported rail*

Using a discretely supported rail model the pinned-pinned resonance can be observed. To highlight the pinned-pinned resonance characteristic the external excitation and the additional wheel/rail interaction are assumed both to act either at mid-span or above a sleeper. For this special case equations (6.10 – 6.12) remain valid for the discretely supported rail model, but the receptances used in these

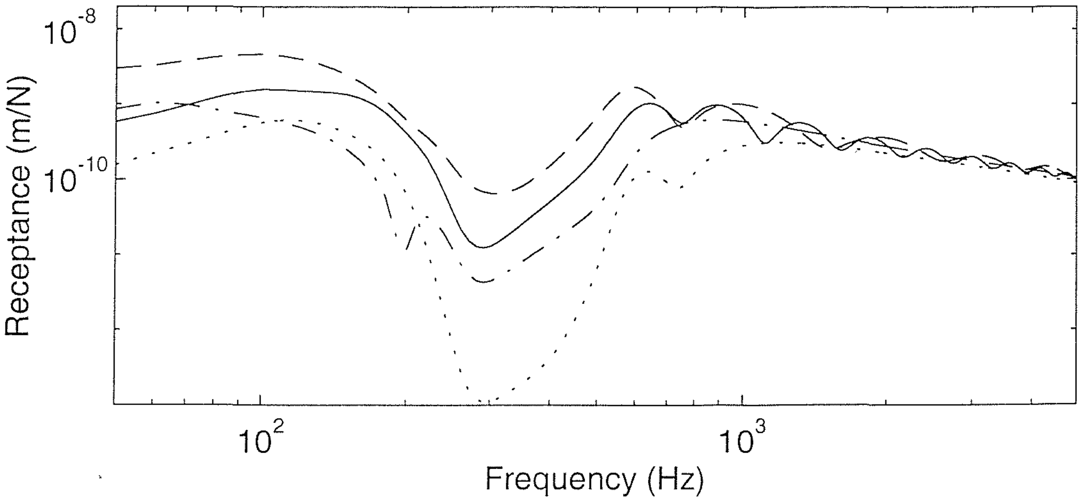

Figure 6.10. Magnitude of transfer receptances of the continuously supported rail with a single wheel on it. — receptance at −1.8 m, - - - at 0.9 m, -·-·- at 1.8 m, ····· at 3.6 m.

equations should be replaced by those from the discretely supported rail model. In addition the analysis carried out previously for the continuously supported rail is also valid for the discretely supported rail except for the pinned-pinned resonances. As above, two cases are calculated, for 1.8 m and 3.6 m distances between the excitation and the wheel. The span length between two sleepers is chosen as 0.6 m.

Figure 6.11 shows the wheel/rail interaction forces for the excitation acting either at mid-span or above a sleeper. As the interaction force is related to the rail receptance, the pinned-pinned vibration characteristic can also be recognised in Figure 6.11. The generated wheel/rail interaction force for the excitation acting at mid-span can be seen even to exceed the original force. This happens just above the first pinned-pinned resonance frequency, where the sum of the point receptances of the wheel, contact spring and rail has a sharp trough, see Figure 6.6(c) and equation (6.10).

Figure 6.12 shows the point receptances of the rail with and without the additional wheel on it. At low frequencies they are close to each other for both models, whereas at high frequencies the point receptances of the rail with a single wheel on it fluctuate around those of the rail without the wheel on it. The pinned-pinned resonance can also be seen clearly as a dip in each model for excitation above a sleeper. However, a cancellation of the first pinned-pinned resonance

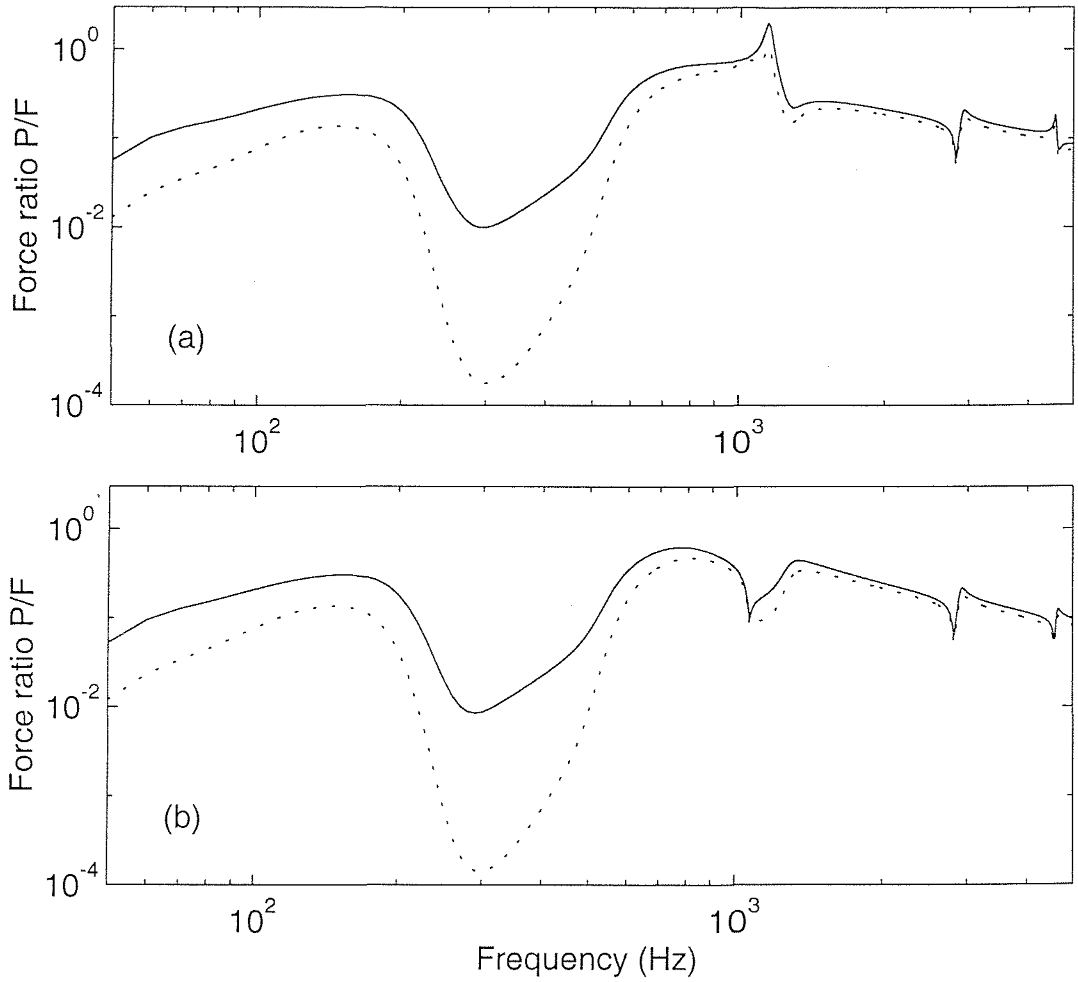

Figure 6.11. Wheel/rail interaction forces (magnitude) of the discretely supported rail with a single wheel on it. (a) excitation at mid-span, (b) excitation above a sleeper. — excitation at 1.8 m from the wheel, ····· excitation at 3.6 m from the wheel.

occurs in the case of the excitation acting at mid-span. This can be explained using equation (6.13). At the first pinned-pinned resonance the wavelength is equal to twice the span length and the 1.8 m and 3.6 m distances correspond to an integral number of spans. Thus the transfer receptance at the wheel/rail contact point is either in phase or exactly out of phase with the point receptance. On the other hand, the point receptance sum of the wheel, contact spring and rail is approximately equal to the rail point receptance at the first pinned-pinned resonance because the pinned-pinned resonance peak is much higher than both the wheel and the contact spring receptances (Figure 6.6(c)). For the 1.8 m distance the magnitude of the transfer receptance at the wheel/rail contact point is very close to that of the point

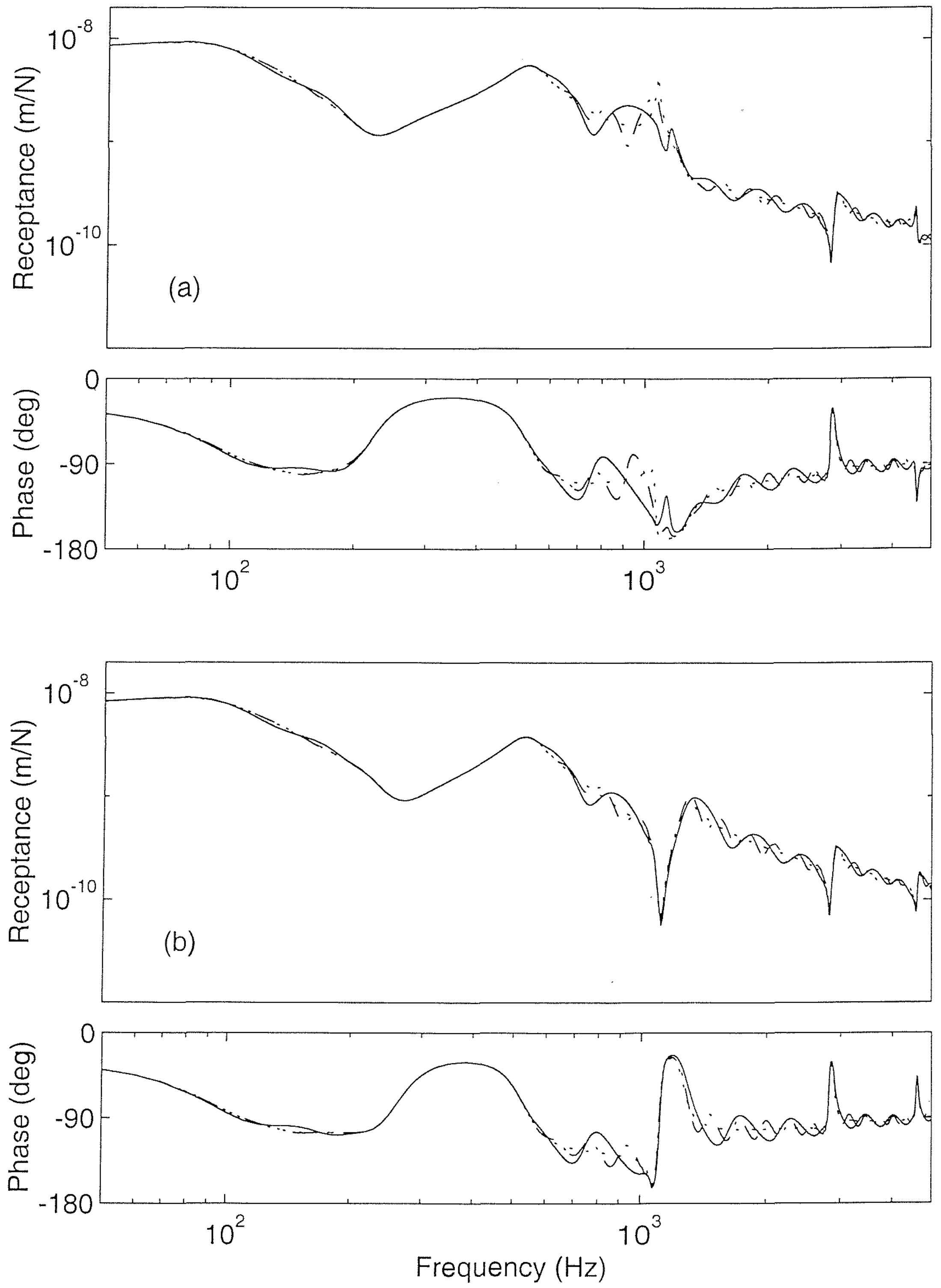

Figure 6.12. Point receptances of the discretely supported rail with a single wheel on it. (a) excitation at mid-span, (b) excitation above a sleeper. — for excitation at 1.8 m from the wheel, ----- for excitation at 3.6 m from the wheel, ····· for the case without wheel/rail interaction.

receptance at the first pinned-pinned resonance so that the second term in the right-hand side in equation (6.13) is approximately equal to unity. As a result, cancellation of the first pinned-pinned resonance occurs and the receptance of the rail with the wheel present is lower than without it. For the 3.6 m distance the cancellation is reduced because the transfer receptance at 3.6 m is smaller than at 1.8 m. In fact the cancellation of the first pinned-pinned resonance more or less happens as long as the rail has an additional wheel on it even if it is not at mid-span. This is because in the first pinned-pinned resonance the transfer receptance at the wheel/rail contact point is always approximately in phase or out of phase with the point receptance for most places in a span; the extent of the cancellation depends on the magnitude of the transfer receptance at the wheel/rail contact point. Figure 6.13 shows the pinned-pinned resonance cancellation for the excitation at mid-span and the additional wheel at 1.9 m or 2 m away from the excitation, the wheel being at 1/3 or 1/6 span respectively. The cancellation can still be observed for the wheel at 1/6 span, although it is much weaker compare to the wheel at 1/3 span.

Figure 6.14 shows the transfer receptances of the rail with a single wheel on it for excitation acting either at mid-span or above a sleeper. The transfer receptances

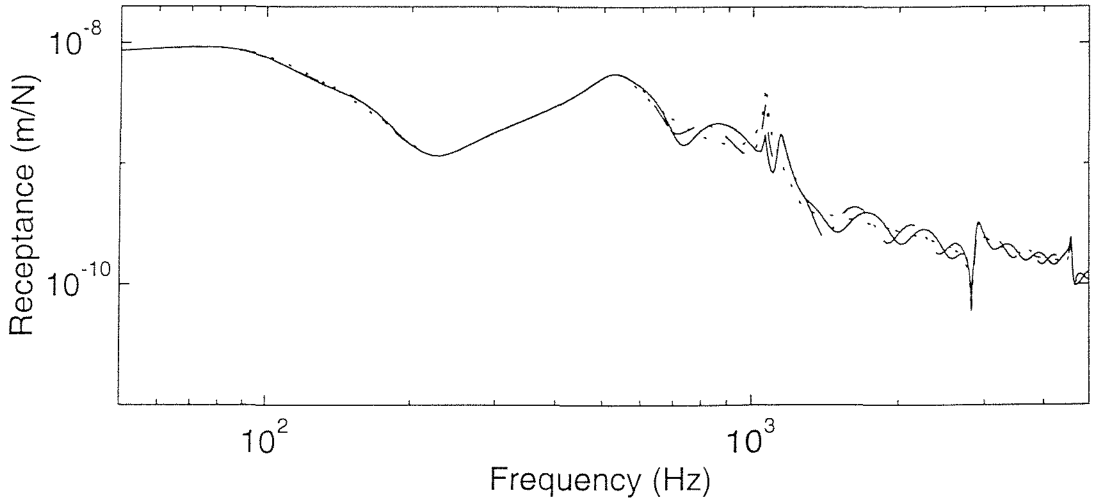

Figure 6.13. Amplitude of point receptances of the discretely supported rail with a single wheel on it. (a) excitation at mid-span, (b) excitation above a sleeper. — for excitation at 1.9 m from the wheel, -·-·- for excitation at 2 m from the wheel, ····· for the case without wheel/rail interaction.

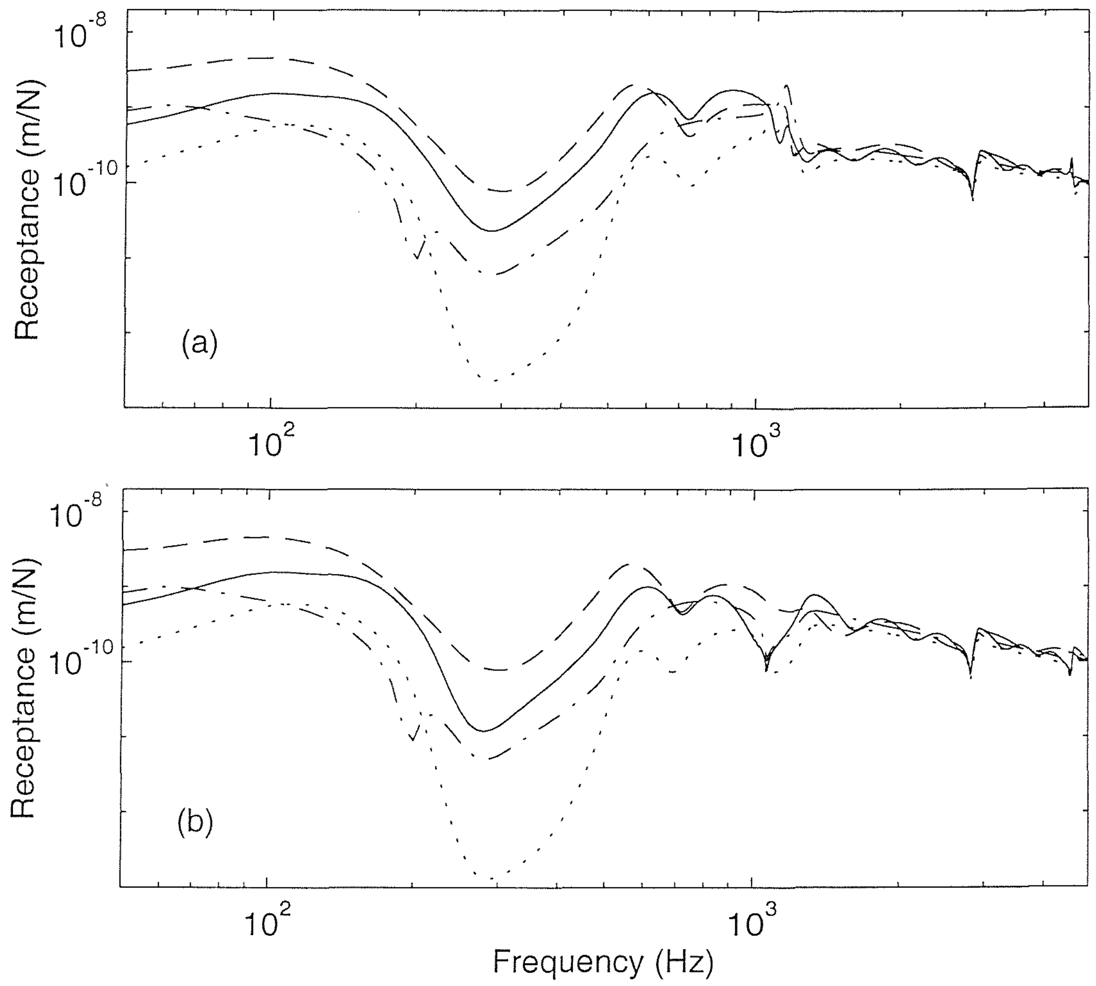

Figure 6.14. Magnitude of transfer receptances of the discretely supported rail with a single wheel on it. (a) excitation at mid-span, (b) excitation above a sleeper. — receptance at −1.8 m, - - - at 0.9 m, -·-·- at 1.8 m, ····· at 3.6 m.

are calculated at −1.8 m, 0.9 m, 1.8 m and 3.6 m away from the excitation with the wheel at 1.8 m. In low and high frequency regions the differences in the transfer receptance between the rails with and without the wheel (see Figure 6.3) on it are similar to the case of the continuously supported model (Figures 6.2 and 6.10). The deviations between the two models are only significant near the first pinned-pinned resonance. The cancellation of the first pinned-pinned resonance can also be observed in Figure 6.14(a) compared with Figure 6.3(a) and the peaks of the transfer receptances close to the first pinned-pinned resonance are due to the wheel/rail interaction force reaching its peak value shortly above the pinned-pinned resonance.

6.3.3. *Interaction with two wheels*

Prior to introducing multiple wheels, a simple extension of the above is considered in which it is assumed that there are two wheels on the rail, symmetrically located at $z = -a$ and a, one on each side of the external excitation F at $z = 0$. The responses at the wheel/rail interaction points to the external excitation for a continuously supported rail or a discretely supported rail with both the excitation and the wheels acting either at mid-span or above a sleeper can be given as

$$u(-a) = u(a) = F\alpha^{RT}(a) + P\alpha^{RT}(2a) + P\alpha^{R} \tag{6.18}$$

Using the same method as used in section 6.2.1, the wheel/rail interaction force, transfer receptance and point receptance can be derived as follows:

$$P = -\frac{\alpha^{RT}(a)}{\alpha^{W} + \alpha^{C} + \alpha^{R} + \alpha^{RT}(2a)}F \tag{6.19}$$

$$\alpha_w^{RT}(z) = \frac{u(z)}{F} = \alpha^{RT}(z) - \frac{\alpha^{RT}(a)}{\alpha^{W} + \alpha^{C} + \alpha^{R} + \alpha^{RT}(2a)}[\alpha^{RT}(z+a) + \alpha^{RT}(z-a)] \tag{6.20}$$

$$\alpha_w^{R} = \frac{u(0)}{F} = \alpha^{R} - \frac{2[\alpha^{RT}(a)]^2}{\alpha^{W} + \alpha^{C} + \alpha^{R} + \alpha^{RT}(2a)} \tag{6.21}$$

Because $\alpha^{RT}(2a)$ is much smaller than α^{R} at low frequencies and $\alpha^{W} + \alpha^{C} + \alpha^{R}$ at high frequencies, equation (6.21) may be written as

$$\alpha_w^{R} = \frac{u(0)}{F} \approx \alpha^{R} - \frac{2[\alpha^{RT}(a)]^2}{\alpha^{W} + \alpha^{C} + \alpha^{R}} \tag{6.22}$$

Thus at low frequencies the point receptance with two wheel/rail interactions still remains approximately equal to the point receptance of the rail without any wheel on it because the transfer receptance $\alpha^{RT}(a)$ is much smaller than the receptance sum $\alpha^{W} + \alpha^{C} + \alpha^{R}$, whereas at high frequencies the fluctuation of the point receptance is approximately doubled compared with the case of a single wheel on the rail.

According to this simple example it can be expected that for a rail with multiple wheels on it the point receptance will still be approximately equal to that of the rail without a wheel on it at low frequencies, whereas at high frequencies the point receptance fluctuation will be somewhat higher than that of the rail with only a single wheel on it.

6.4. Rail vibration behaviour with multiple wheels

In this section the rail vibration behaviour is studied taking account of multiple wheels on it. Models are developed for both continuously and discretely supported rails. The receptances at the wheel/rail interaction positions are calculated for each model. Numerical simulations show that, for a train of bogied wagons, taking four wheels into account which are in a pair of bogies at the adjacent ends of two wagons is enough to give a satisfactory approximation to the rail vibration with multiple wheels on it.

6.4.1. *Continuously supported rail with multiple wheels on it*

Figure 6.15 shows schematically a typical train on a discretely supported rail. The distances between wheels shown in Figure 6.15 are chosen to represent a bogie container wagon. The discrete rail supports may also be considered as continuous. Owing to the symmetrical arrangement of the wheels, the point receptance need be calculated only at two positions, z_{L1} and z_{L2} or z_{R1} and z_{R2}. To calculate the point receptance at z_{L1} or z_{L2} a unit force is applied at this position and the wheel at z_{L1} or z_{L2} should be omitted. The displacement at each wheel/rail contact position (including at z_{L1} or z_{L2}) is a superposition of the response to the unit force at z_{L1} or z_{L2} and of the contributions from the reactions at each wheel/rail contact (excluding at z_{L1} or z_{L2}). It can be written as

$$u(z_m) = \sum_{\substack{n=1 \\ n \neq Li}}^{M} P_n \alpha^{RT}(z_m, z_n) + \alpha^{RT}(z_m, z_{Li}) \qquad m = 1, 2, \cdots, M; \; i = 1, 2 \qquad (6.23)$$

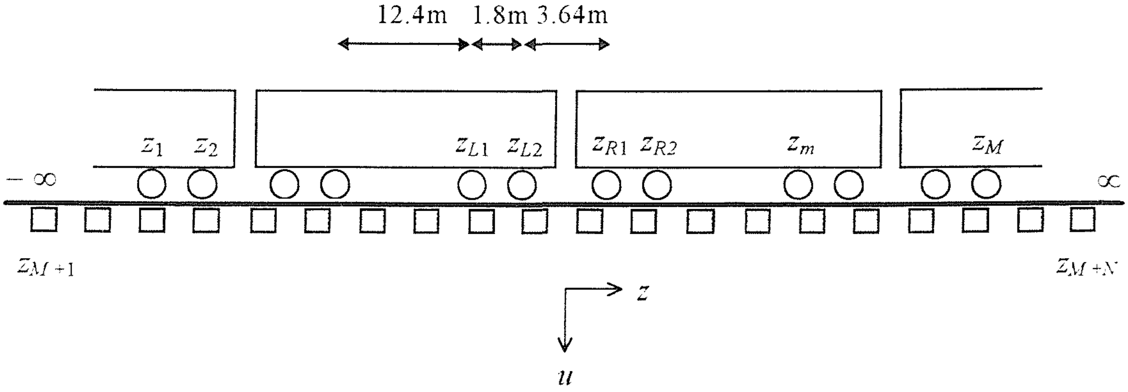

Figure 6.15. Railway track model with a train (multiple wheels) on the rail.

where $\alpha^{RT}(z_m, z_n)$ is the transfer receptance of a continuously supported rail without any wheels on it at z_m for a force acting at z_n, M is the number of wheel/rail interactions under consideration and P_n is the wheel/rail interaction force at z_n. This is given as

$$P_n = -Z_w u(z_n) \qquad n = 1, 2, \cdots, M\ ;\ n \neq L_i \tag{6.24}$$

where Z_w is the dynamic stiffness combination of the wheel and contact spring (see section 6.2.3):

$$Z_w = \frac{1}{\alpha^W + \alpha^C} = \frac{-K_H K_M M_w \omega^2}{K_H K_M - (K_H + K_M) M_w \omega^2} \tag{6.25}$$

Substituting equation (6.24) into (6.23) gives

$$u(z_m) = -\sum_{\substack{n=1 \\ n \neq Li}}^{M} Z_w u(z_n) \alpha^{RT}(z_m, z_n) + \alpha^{RT}(z_m, z_{Li}) \qquad m = 1, 2, \cdots, M \tag{6.26}$$

Equation (6.26) can be solved to give $u(z_m)$ in terms of $\alpha^{RT}(z_m, z_{Li})$ by taking the sum to the left-hand side and then inverting the matrix of coefficients of $u(z_m)$. Then the displacement at any point on the rail can be obtained by substituting $u(z_m)$ into the following equation:

$$u(z) = -\sum_{\substack{n=1 \\ n \neq Li}}^{M} Z_w u(z_n) \alpha^{RT}(z, z_n) + \alpha^{RT}(z, z_{Li}) \tag{6.27}$$

Thus the point receptance at $z = z_{Li}$ and the transfer receptance at z for the rail with multiple wheels on it are given as

$$\alpha_w^R = u(z_{Li}) \quad \text{and} \quad \alpha_w^{RT}(z) = u(z) \tag{6.28, 6.29}$$

Figure 6.16 shows the point receptances of a continuously supported rail having the same parameters as in the previous sections but with multiple wheels instead of only a single additional wheel on the rail. Two cases are calculated, in each case with the external excitation acting either at z_{L1} or z_{L2}. In one case only the wheel/rail interactions of a pair of bogies at the adjacent ends of two wagons are taken into account. In the other case two more pairs of bogies are added to take account of their wheel/rail interactions, see Figure 6.15. From Figure 6.16 the point receptance at low frequencies can be seen still to be almost equal to that of the rail without a wheel on it due to the high decay rate of the wave propagation (see Figure 6.2).

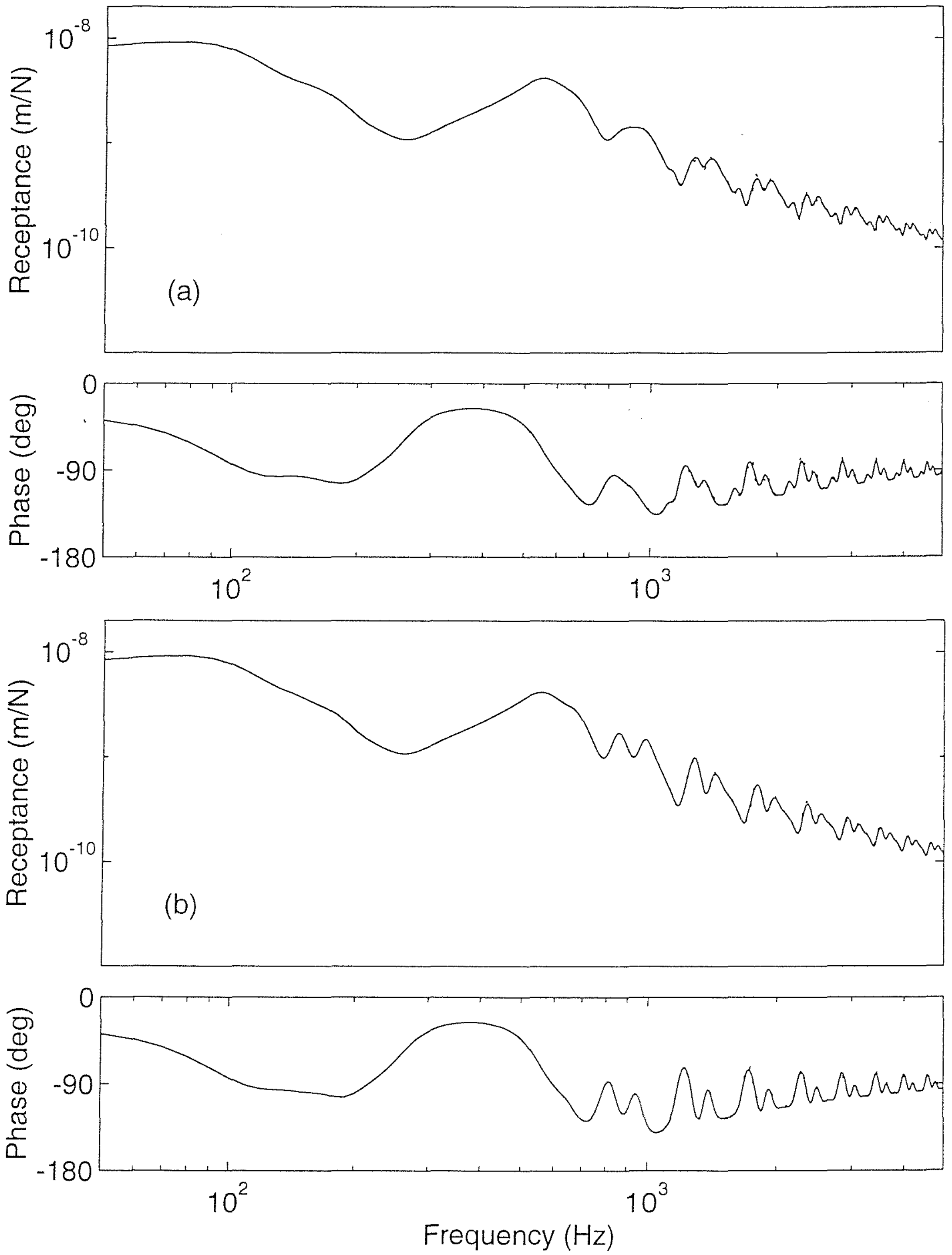

Figure 6.16. Point receptances of the continuously supported rail with multiple wheels on it. (a) excitation at z_{L1}, (b) excitation at z_{L2}. — a pair of bogies on the rail, ····· three pairs of bogies on the rail.

Compared to the single wheel/rail interaction case (see Figure 6.7), however, the fluctuations of the receptance at high frequencies are much stronger especially for the excitation acting at z_{L2} because of the multiple wheel/rail interactions. This was expected from section 6.3.3. An important question is how many wheels should be taken into account when calculating the point receptance of a rail with multiple wheels on it. For the track parameters considered, the effect of the wheel/rail interaction for any wheel more than about 10 m away from the point at which the point receptance is calculated may be neglected. This is shown to be the case in Figure 6.16 as the point receptances from the cases of one and three pairs of bogies on the rail only have a very slight difference between them. However, for a track with a softer foundation more wheel/rail interactions should be taken into account because the wave propagation decay rate is lower in such a track.

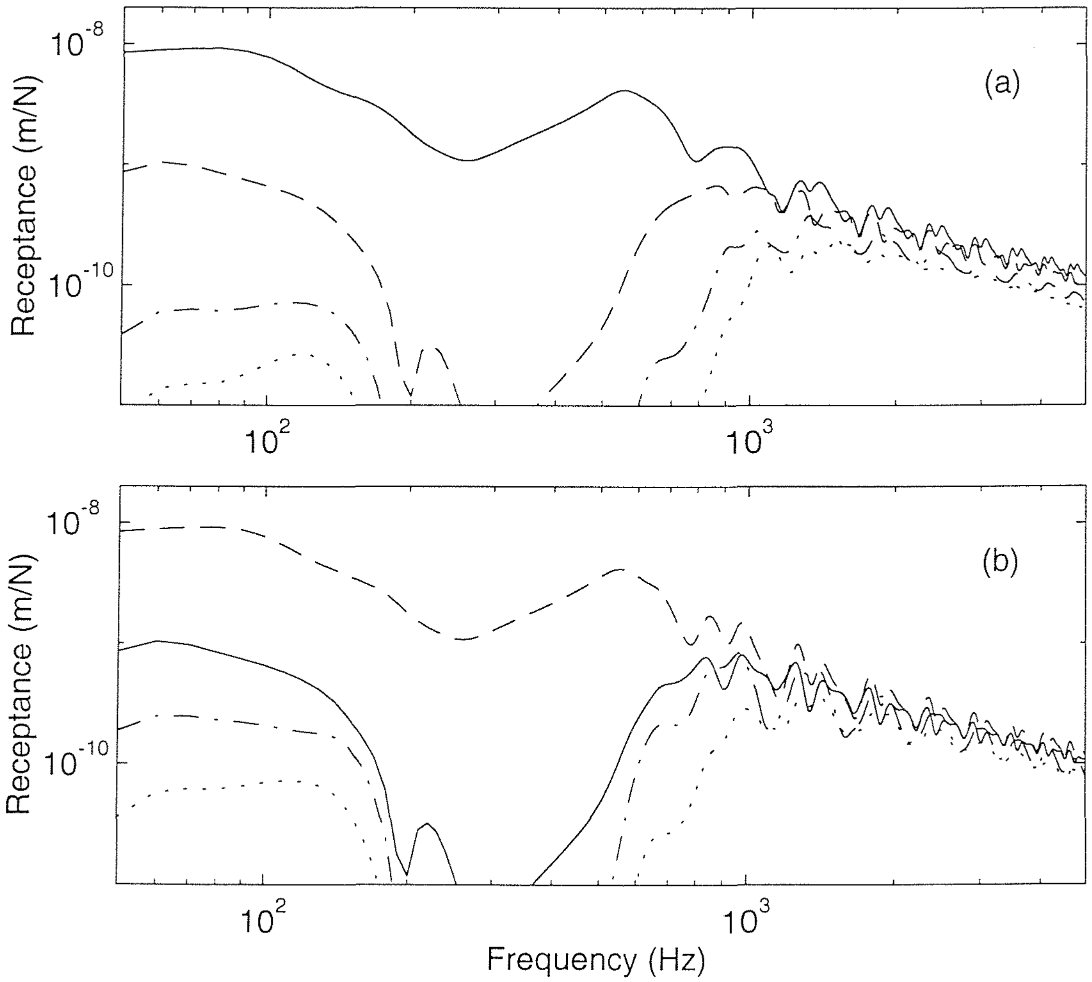

Figure 6.17. Magnitude of the receptances at four wheel/rail contact positions of the continuously supported rail with multiple wheels on it. (a) excitation at z_{L1}, (b) excitation at z_{L2}. — receptance at z_{L1}, - - - at z_{L2}, -·-·- at z_{R1}, ····· at z_{R2}.

Figure 6.17 shows the point and transfer receptances at four wheel/rail contact positions. The calculation is carried out only considering the wheel/rail interactions of a pair of bogies although there would be no difficulty in performing the calculation with more wheels on the rail. The external excitation acts at either z_{L1} or z_{L2}. From the receptances at the different positions the wave propagation decay rate can be observed to be high at low frequencies and low at high frequencies. This tendency is consistent with the case of the rail with only a single wheel on it. Because of the low decay rate at high frequencies the receptances at the different positions become closer and closer with increasing frequency. However, they fluctuate more rapidly and strongly with frequency due to the multiple wheel/rail interactions, compared with the case of a single wheel on the rail (Figure 6.10).

6.4.2. *Discretely supported rail with multiple wheels on it*

As shown in Figure 6.15 the discretely supported railway track is modelled with an infinite rail and a finite number of discrete supports. To calculate the response of the rail, both the discrete supports and the wheels can be replaced by many point forces in an extension of the method used in the previous chapters. Based on the superposition principle, the responses of the rail at the support points and the wheel/rail contact points to a unit force acting at z_{Li} can be written as

$$u(z_m) = \sum_{\substack{n=1 \\ n \neq L_i}}^{M} P_{wn} \alpha^{RT}(z_m, z_n) + \sum_{n=M+1}^{M+N} P_{sn} \alpha^{RT}(z_m, z_n) + \alpha^{RT}(z_m, z_{Li}) \quad m = 1, 2, \cdots, M+N \tag{6.30}$$

where $\alpha^{RT}(z_m, z_n)$ is the transfer receptance of a free rail at z_m with the force acting at z_n, M is the number of wheel/rail interactions under consideration, N is the number of the discrete supports, P_{wn} and P_{sn} are the wheel/rail interaction force and the reaction force of the support respectively and given as

$$P_{wn} = -Z_w u(z_n) \qquad n = 1, 2, \cdots, M \quad \text{and} \quad n \neq L_i \tag{6.31}$$

$$P_{sn} = -Z_s u(z_n) \qquad n = M+1, M+2, \cdots, M+N \tag{6.32}$$

where Z_s is the dynamic stiffness of the support:

$$Z_s = \frac{K_p (K_b - M_s \omega^2)}{K_p + K_b - M_s \omega^2} \tag{6.33}$$

Substituting equations (6.31) and (6.32) into (6.30) gives

$$u(z_m) = -\sum_{\substack{n=1 \\ n\neq Li}}^{M} Z_w u(z_n)\alpha^{RT}(z_m, z_n) - \sum_{n=M+1}^{M+N} Z_s u(z_n)\alpha^{RT}(z_m, z_n) + \alpha^{RT}(z_m, z_{Li})$$

$$m = 1, 2, \cdots, M + N \qquad (6.34)$$

Equation (6.34) can be solved in the same way as for equation (6.26). The displacement at any point on the rail can be obtained by substituting $u(z_m)$ into the following equation:

$$u(z) = -\sum_{\substack{n=1 \\ n\neq Li}}^{M} Z_w u(z_n)\alpha^{RT}(z, z_n) - \sum_{n=M+1}^{M+N} Z_s u(z_n)\alpha^{RT}(z, z_n) + \alpha^{RT}(z, z_{Li}) \qquad (6.35)$$

The point and transfer receptances are represented by equations (6.28) and (6.29).

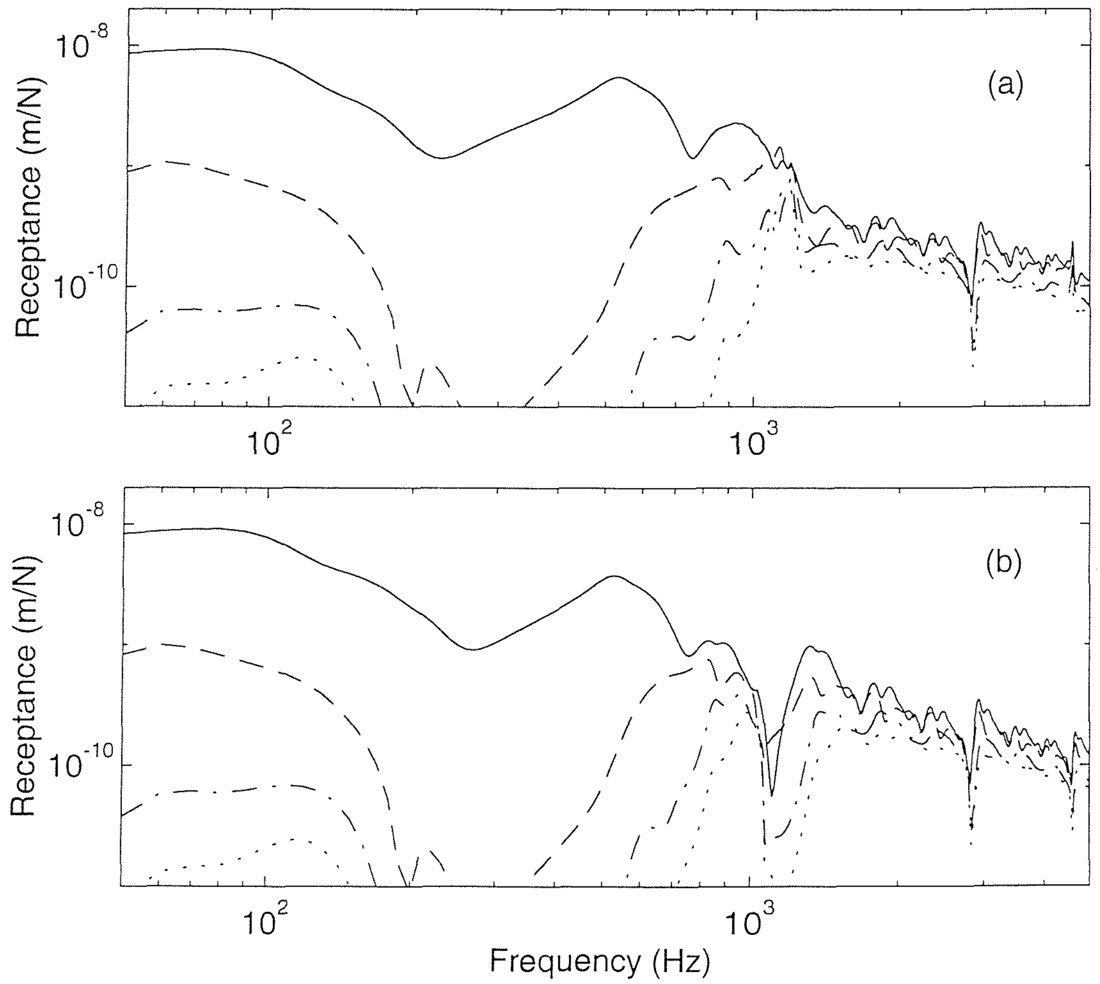

Figure 6.18. Magnitude of the receptances at four wheel/rail contact positions of the discretely supported rail with multiple wheels on it and with excitation at z_{L1}. (a) excitation at mid-span, (b) excitation above a sleeper, key as for Figure 6.17.

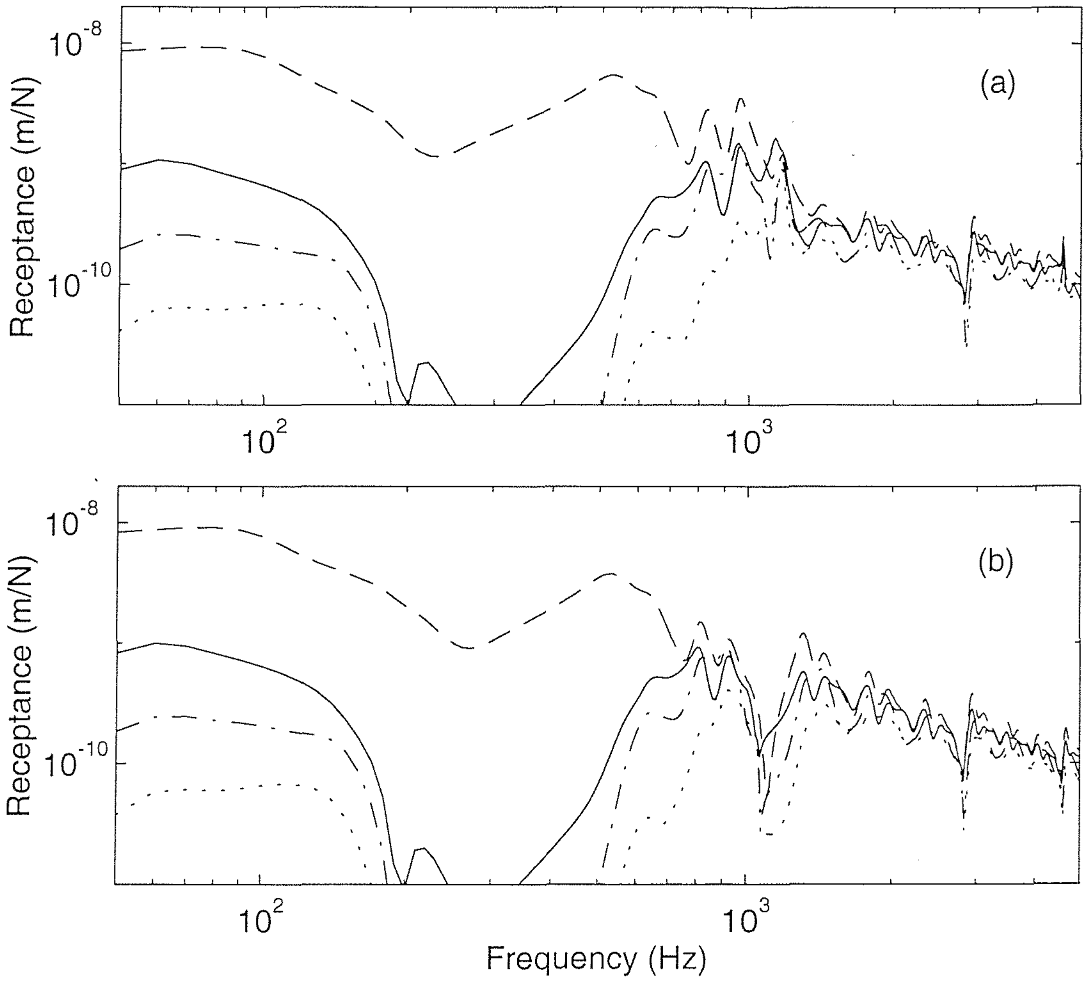

Figure 6.19. Magnitude of the receptances at four wheel/rail contact positions of the discretely supported rail with multiple wheels on it and with excitation at z_{L2}. (a) excitation at mid-span, (b) excitation above a sleeper, key as for Figure 6.17.

Figures 6.18 and 6.19 show the receptances at four wheel/rail contact positions for the external excitation acting at z_{L1} and z_{L2} respectively. z_{L1} and z_{L2} are chosen at mid-span or above a sleeper. The calculation is also carried out with only considering the wheel/rail interactions of a pair of bogies. Since the span length is chosen as d = 0.6 m and the distance between two wheels is 1.8 m or 3.64 m (see Figure 6.15) which is exactly or almost exactly equal to an integer times the span length, all the wheels are located at mid-span or above a sleeper when z_{L1} and z_{L2} are. Similarly to the continuously supported model the receptances at low frequencies can be seen from Figures 6.18 and 6.19 to be almost the same as those of the rail without a wheel on it. At high frequencies the pinned-pinned resonances can be observed, which can not be obtained using a continuously supported rail model. However, the first pinned-pinned resonance peak of the point receptance for an excitation acting at mid-span is not very noticeable because their cancellation occurs due to the wheel/rail interactions as discussed previously. Apart from the pinned-pinned resonance area, the results from the discretely supported rail model are fairly close to those from the continuously supported rail. Compared with the single wheel/rail interaction model, more fluctuations in the receptances are produced by the multiple wheel/rail interactions at high frequencies.

6.4.3. *Measurement results*

In order to validate the theoretical predictions, measurements have been carried on a test track at Chilworth, Southampton. A bogie was placed in the middle of the 36 m long test track to generate two wheel/rail interactions. Details about the measurements are given in Appendix E. An instrumented hammer was used to produce impact excitation. The distance between the excitation and the first wheel (close to the excitation) was three span lengths and equal to about 1.9 m. The distance between two wheels was 1.8 m. Since the span lengths of the test track are irregular, most of them being around 0.63 m (see chapter 5), only the first wheel was placed at mid-span and the other was at about one third of a span from the nearest sleeper. The impact excitation was applied at mid-span. The point accelerances of vertical vibration were measured for two cases—with and without wheel/rail interactions. In the latter case the wheel/rail interactions were isolated by inserting rubber blocks between the wheels and the rail, so the track was preloaded to the same extent.

Figure 6.20 shows the results from the prediction and measurement. The rail is UIC 60. The parameters in the prediction for the track foundation and for the wheel and contact spring are chosen as follows:

$K_p = 120$ MN/m^2, $\eta_p = 0.25$, $K_b = 150$ MN/m^2, $\eta_b = 1.0$,
$M_s = 162$ kg, $d = 0.63$ m, $M_w = 600$ kg, $K_H = 684$ MN/m

The contact stiffness K_H is chosen smaller than that used in the previous sections because the static contact load comes from the bogie only and thus is smaller. The point accelerance measured is produced by averaging 4 impacts. The coherence

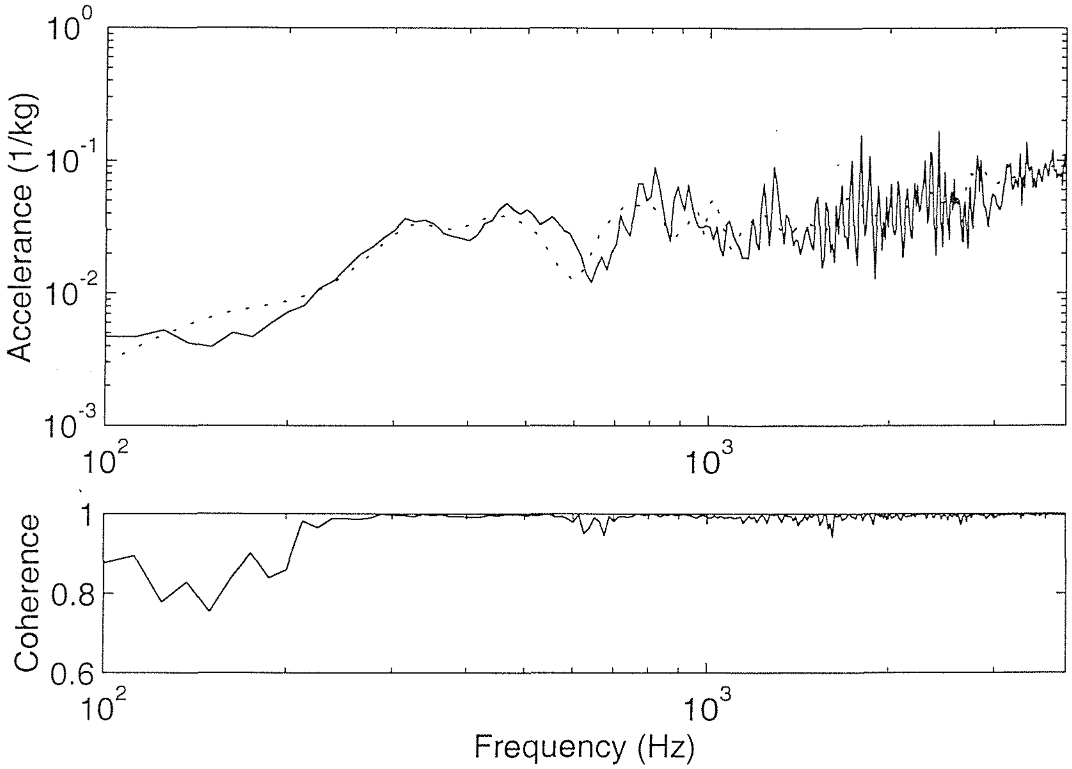

Figure 6.20. Comparison of the point accelerances (amplitude) from prediction and measurement. — from measurement, two wheels interacting with the rail, excitation at mid-span and about 1.9 m away from the first wheel, ····· from prediction.

curve shows good consistency in the measurement results. Good agreement with the prediction can be found from Figure 6.20 over the range 100 – 4000 Hz, although many sharp peaks and troughs occur at high frequencies due to the wave reflections from both ends of the test track, as identified by de France [8].

In order to highlight the effects of the wheel/rail interactions, both measured and predicted point accelerances from both cases with and without wheel/rail interactions are presented in Figure 6.21. The accelerance for the wheel/rail interacted case can be seen to fluctuate from about 400 Hz in both measurements and predictions. The pinned-pinned resonance cancellation can be clearly observed by comparing the two cases. Although the measured pinned-pinned resonance appears in the range 900 – 1000 Hz due to the irregular sleeper spacing as discussed in chapter 5, suppression of these resonance peaks still happens due to the presence of the wheel/rail interactions.

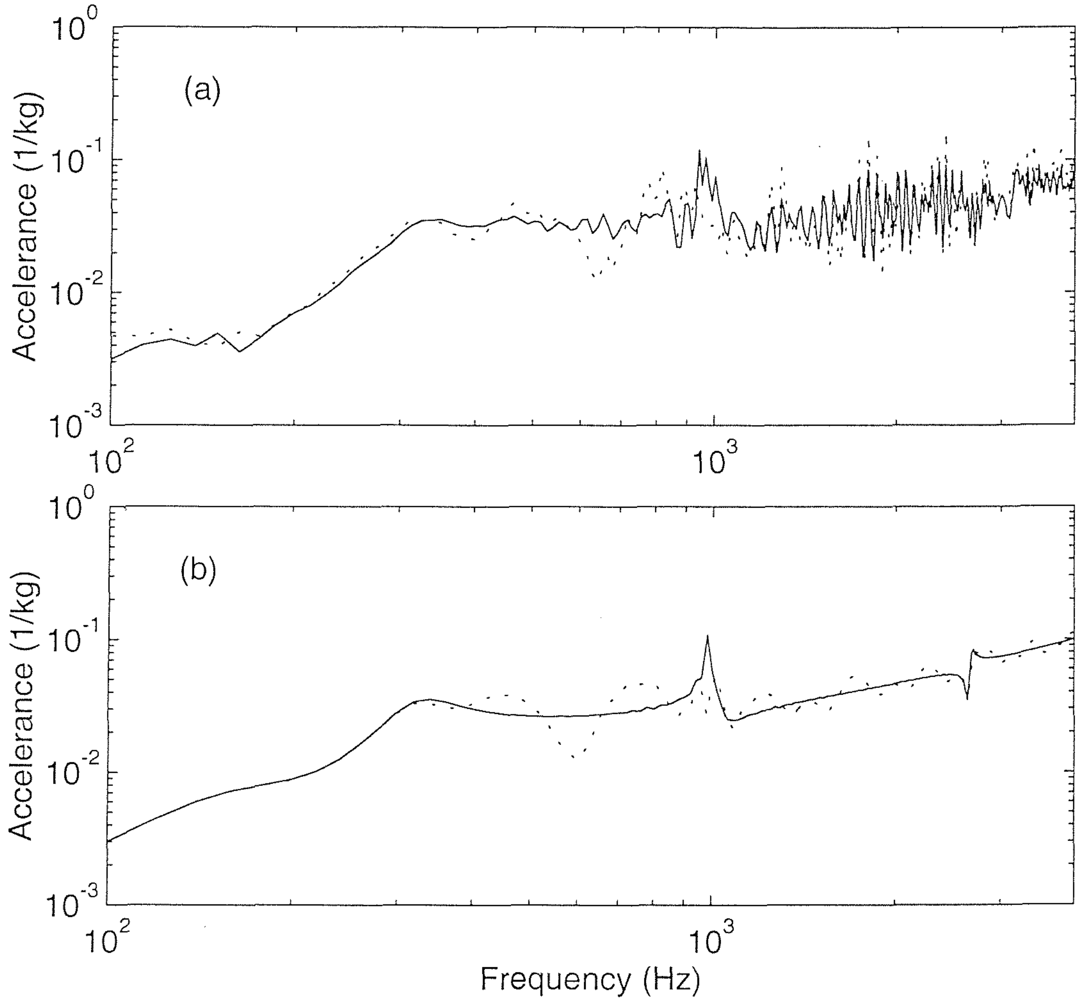

Figure 6.21. Comparison of the measured and predicted point accelerances (amplitude) from the track with and without wheel/rail interactions. (a) from measurements, (b) from predictions. — without wheel/rail interactions, ····· with wheel/rail interactions.

6.5. Conclusions

In this chapter the effects of the multiple wheel/rail interactions on rail vibration have been studied. Firstly, a simple model of a track with only a single additional wheel on the rail has been developed in order to derive the wheel/rail interaction force and the dynamic relationship between the two track models with and without a wheel on it. Then the dynamic properties of the wheel, contact spring and rail without wheel/interaction have been introduced in terms of the receptances. Based on this simple model and a knowledge of the dynamic behaviour of the wheel and rail without a wheel on it, the effects of the wheel/rail interaction on the rail vibration have been analysed from various aspects for both continuously and discretely supported rails. Lastly, two track models with multiple wheels on the rail have been developed for the continuously and discretely supported rails. The effects of the multiple wheel/rail interactions on rail vibration have been investigated using these two models.

The vibration behaviour of the rail with multiple wheels on it is affected by the dynamic properties of both the track and the wheel (including the contact spring). The additional wheel/rail interaction forces are generated according to the wave propagation decay rate in the rail and the point receptance sum of the wheel, contact spring and rail. If the wave propagation decay rate or the point receptance sum is high, the interaction forces will be small. At low frequencies the wheel/rail interaction forces are small because of the high decay rate of the wave propagation so that the point receptance of the rail is virtually unaffected by the presence of additional wheels. At high frequencies the point receptance of the rail with wheels on it fluctuates around that of the rail without a wheel on it because of the low decay rate of the wave propagation. Because of the wave propagation decay the effect of the wheel/rail interaction may be neglected at distances more than 10 m away for the track parameters considered. For the track with one or more wheels on it, the first pinned-pinned resonance is observed to experience cancellation when an excitation acts at mid-span. Moreover, in this case the generated wheel/rail interaction force is expected to exceed the original excitation at a frequency slightly above the first pinned-pinned resonance. These effects have been validated using experiments.

Using the point receptance of the rail with multiple wheels on it and the relative displacement excitation model a more realistic estimate of the wheel/rail interaction force can be achieved. Then the mean square response of the track to each wheel can be added by treating each wheel/rail interaction as an uncorrelated source. Based on this approach, the wheel and rail vibration may be expected to be predicted more accurately, as may the wheel/rail rolling noise. This will be shown in chapter 8.

CHAPTER 7

The Effects of Multiple Wheel Loads Combined with Multiple Wheel/Rail interactions

In this chapter the preloads in the pad and ballast caused by multiple wheel loads are calculated and the preloaded pad and ballast stiffnesses are determined in an extension of the work given in chapter 4. The vibration properties are explored for the track under multiple wheel loads combined with multiple wheel/rail interactions. It is found that the point receptance of the track is reduced and the vibration decay rate is enhanced at low frequencies due to the wheel loads. The effects of the wheel/rail interactions are most significant for frequency range 400 – 2000 Hz. Because of the wheel/rail interactions the vibration decay is enhanced in the regions around the wheels.

7.1. Introduction

When a train runs on the track, the track foundation is loaded by multiple wheels and in the meantime multiple wheel/rail interactions take place due to the roughnesses on the wheel tread and the rail head surface. The effects of the local preload in the track foundation, which is caused by the wheel load due to the train weight, have been studied in chapter 4. It has been shown that the preload increases the pad and ballast stiffness in the loaded region, hence modifying the rail vibration. However, only a single wheel load on the track has been considered which is clearly not the case in practice. If multiple wheel loads are taken into account, the static problem of the load distribution becomes very difficult to solve because the track foundation is essentially non-linear and the superposition principle does not hold. In the last chapter the effects of multiple wheel/rail interactions on the rail vibration are studied without taking account of the preload caused by the wheel loads. To carry out a comprehensive investigation of the vibration behaviour for the track with multiple wheels on the rail, it is clearly desirable to take account of the effects of both the preload in the track foundation caused by the multiple wheel loads and the multiple wheel/rail interactions. The main barrier to doing this is how to calculate the reaction force in the track foundation caused by the multiple wheel loads.

In this chapter a new methodology is developed to calculate the reaction force in the non-linear track foundation due to the multiple wheel loads. Firstly the reaction force in the foundation is calculated using the new methodology. Secondly the preload in the pad and ballast at each support is determined and thus the dynamic stiffness of each element is obtained according to their load-stiffness relationship. Finally a discretely supported Timoshenko beam model is employed for the dynamic behaviour of the track and the receptances and the vibration decay rate for vertical rail vibration are calculated in the frequency range 100 – 5000 Hz with preloaded pad and ballast stiffness and multiple wheel/rail interactions. The influences on the track vibration of both the multiple wheel loads and the multiple wheel/rail interactions are explored by comparing the results from different track models with and without these effects.

Although the effects of the wheel load and additional wheel/rail interaction on track vibration have already been investigated separately in chapters 4 and 6, they are studied again in this chapter by combining these two factors together. More attention is given here to the related practical results than to explanations of these effects.

7.2. Stiffness of track foundation under multiple wheel loads

The load-deflection relations for the railpad and ballast have been found to be non-linear, and thus their stiffness varies with the preload in them. This has been discussed in chapter 4. The preload of the track foundation can be calculated according to the wheel loads due to the train weight, by treating the rail as an infinite beam on an elastic foundation with non-linearity. However, this is not easy because the wheel loads are applied to the rail at multiple points and the superposition principle does not hold here due to the non-linear track foundation. A new method using an alternative linear track foundation to represent the non-linear one is therefore developed in this section.

7.2.1. *Preload in track foundation caused by multiple wheel loads*

In chapter 4 the preload in the track foundation caused by a single wheel load is calculated by simplifying the railway track to an infinite uniform beam supported by a continuous elastic foundation. The differential equation for the rail deflection has the form of

$$EI\frac{d^4u}{dz^4}=-\frac{F(u)}{d} \tag{7.1}$$

where *F(u)* is the reaction force in the foundation of one span as a non-linear function of deflection u and d is the span length. *EI* is the bending stiffness of the beam and z is the distance along the track. *F(u)* is determined by the load-deflection law in Figure 4.4 of chapter 4.

This is a non-linear boundary value problem with the following boundary conditions at an infinite distance from the wheel load as shown in chapter 4:

$$u=0, \quad u'=0 \quad \text{at } z=\pm\infty \tag{7.2, 7.3}$$

where $'$ represents the derivative with respective to z. The solution is obtained in chapter 4 by estimating two parameters $u(0)$ and $u''(0)$ at the wheel load point $z = 0$ to satisfy the boundary conditions in equations (7.2) and (7.3). By symmetry the other two parameters $u'(0)$ and $u'''(0)$ are known. However, the above approach is not appropriate for the case of multiple wheel loads acting on the rail. When this approach is used in the multiple wheel case, many parameters at the wheel load points need to be estimated to satisfy the boundary conditions in equations (7.2) and (7.3) so that the solution searching becomes extremely difficult.

An alternative approach is to use an equivalent linear track foundation to represent the non-linear foundation. It has been found in chapter 4 that if a constant modulus k of a linear elastic foundation is chosen to give the same maximum deflection at the load point as that from the non-linear model, the foundation deflection and reaction force of the linear model are very close to those of the non-linear model, see Figure 4.7 in chapter 4. This is also expected to be valid here for the multiple wheel loads. Unfortunately, of course, the maximum deflection from the non-linear model is not available.

Since the reaction force in the foundation only appears in a local area near the wheel load, the influence of the wheel load on the distant area, for example, more than 3 m away from the load, may be neglected, see Figure 4.6 in chapter 4. Thus for a train of bogied wagons, the preload in the track foundation can be calculated by taking only four wheel loads into account which are from a pair of bogies at the adjacent ends of two wagons. The preload of the foundation at other places along the train can be seen to repeat the same variation periodically according to the wagon length. Figure 7.1 schematically shows a track with four wheel loads on it. By using a linear elastic foundation, the deflection of the rail (or foundation) may be given using the superposition principle [94]:

$$u(z)=\frac{P\beta}{2k}[e^{-\beta|z-a|}(\cos\beta|z-a|+\sin\beta|z-a|)+e^{-\beta|z-a-b|}(\cos\beta|z-a-b|+\sin\beta|z-a-b|)$$
$$+e^{-\beta|z+a|}(\cos\beta|z+a|+\sin\beta|z+a|)+e^{-\beta|z+a+b|}(\cos\beta|z+a+b|+\sin\beta|z+a+b|)] \tag{7.4}$$

where P is the single wheel load, k is the constant modulus of the equivalent elastic foundation and

$$\beta=\sqrt[4]{\frac{k}{4EI}} \tag{7.5}$$

Now the key point is how to choose the modulus k. An optimisation method is used here for determining k by minimising the following objective function y:

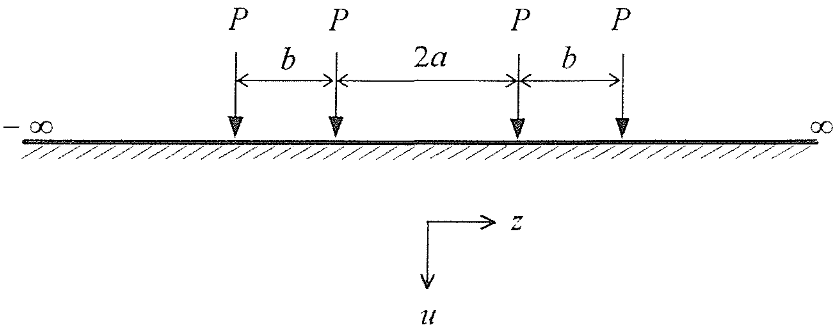

Figure 7.1. Beam with four loads on it on an infinite elastic foundation.

$$y = \int_{-L}^{L} (F_l - F_{nl})^2 dz \qquad (7.6)$$

where F_l is the reaction force in the foundation and is calculated by $F_l = ku$, and u is the foundation deflection and comes from equation (7.4). F_{nl} also is the reaction force but from the non-linear relationship $F(u)$ which is shown in Figure 4.4. Thus F_l represents the result from the linear model, whereas F_{nl} approximately represents the result for the non-linear model although the deflection u for determining F_{nl} is also from equation (7.4). The objective function y is calculated within a reasonable length of the foundation, for example $L = 7$ m. By minimising y the most appropriate modulus k for the equivalent linear foundation can be determined and it is expected that the result from the equivalent linear model will be very close to the result from the non-linear model in terms of the reaction force. When k is found, so is the deflection of the track foundation. The reaction force in the non-linear foundation is represented by F_{nl}. Therefore, the final result is a subtle combination, the foundation deflection is from the equivalent linear model, whereas the reaction force is obtained from using this deflection in the non-linear load-deflection relationship.

Figure 7.2 shows the comparison between the results from the alternative linear foundation and the non-linear foundation for a single wheel load of 75 kN on the

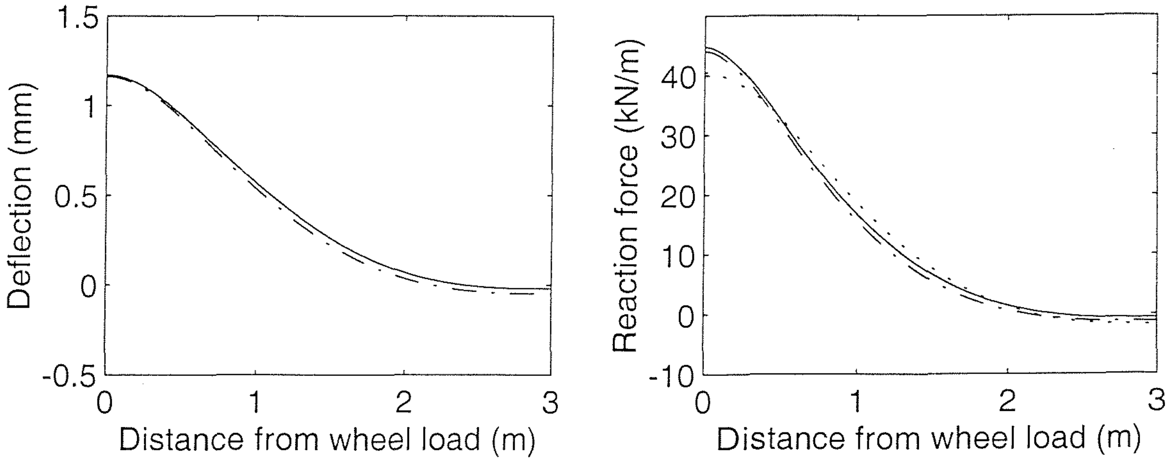

Figure 7.2. Foundation deflection and reaction force under a single wheel load of 75 kN. — numerical results from the non-linear model, -·-·- results from the equivalent linear model and reaction force from the non-linear load-deflection relationship, ······ reaction force from the linear load-deflection relationship.

rail. The non-linear model is calculated using the numerical method developed in chapter 4. The result from the alternative linear model is very close to the result from the non-linear model in terms of both the deflection and the reaction force. However, if the reaction force is calculated by $F_l = ku$, some deviation appears in the loaded area. This shows the benefit of using the non-linear load-deflection relationship.

Figure 7.3 shows the results from the multiple wheel loads. Four wheel loads are applied, each equal to 75 kN. The distances between the wheel loads are $2a = 3.6$ m and $b = 1.8$ m. Because of symmetry the results are calculated and shown for only one half of the foundation. The deflection and reaction force of the foundation can be seen to be very high between the two closer wheels with their peaks near the forcing points. On the other hand, they decrease quite sharply with increasing distance from the load. In the outside area about 2 m away from the loads, the deflection and reaction force become approximately zero. Between the two bogies (close to $x = 0$) they also become close to zero. Thus the foundation preload caused by the wheel load only appears in a limited local area.

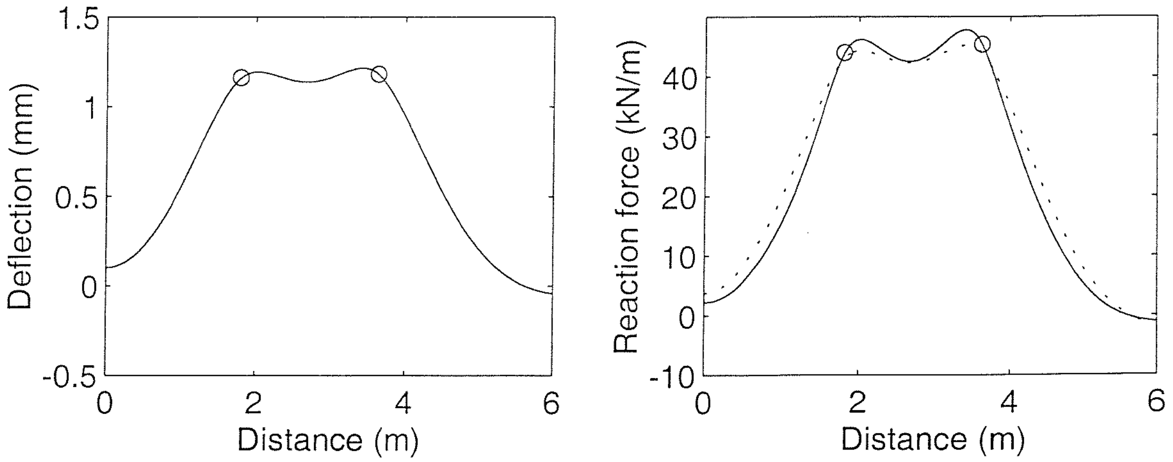

Figure 7.3. Foundation deflection and reaction force under four wheel loads of 75 kN each. — results from the equivalent linear model and reaction force from the non-linear load-deflection relationship, ······ reaction force from the linear load-deflection relationship, o wheel load position.

7.2.2. *Dynamic stiffness of pad and ballast under preload*

When the distribution of the foundation preload is known, the preload in each pad and the ballast under each sleeper can be calculated using the method introduced in chapter 4. Two situations are considered here, the wheel load acting either above a sleeper or at mid-span. The span length d is assumed to be uniform and chosen as $d = 0.6$ m. For the wheel distances considered above, if one wheel is above a sleeper or at mid-span, so is each wheel. This is not essential in the model but is chosen for convenience in presenting the results.

The preloads in the pad and ballast at each support in the area near the wheel loads are shown in Figure 7.4 for the wheel loads either above a sleeper or at mid-span. They are also shown for only one side of the foundation due to symmetry. The

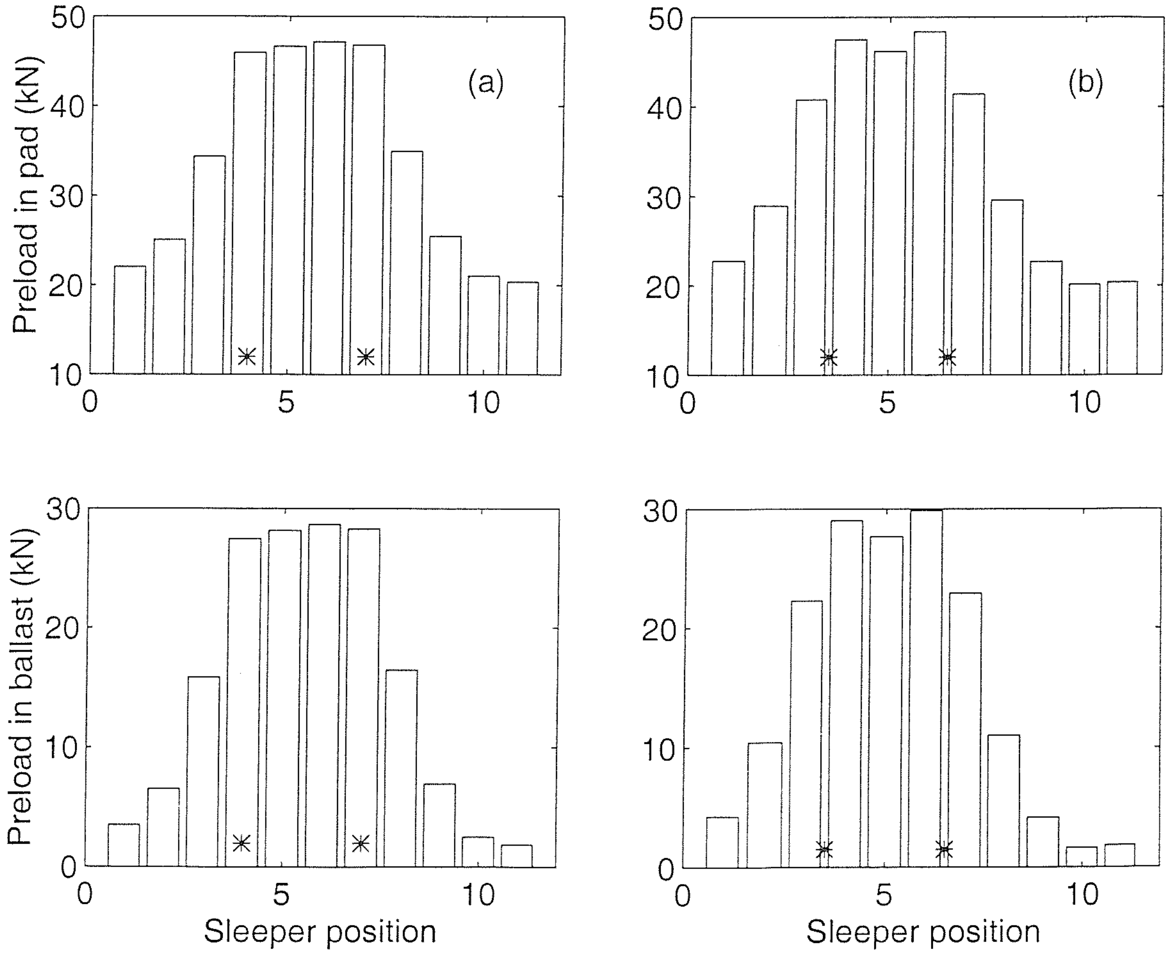

Figure 7.4. Preloads in the pad and ballast caused by four wheel loads of 75 kN each. (a) for loads above a sleeper, (b) for loads at mid-span. * location of the wheel load.

results from both cases are found to be very similar. The preload in each pad includes 20 kN clip load and the rail weight of about 0.36 kN (UIC 60 rail, 60 kg/m). The preload in the ballast for each support includes both the rail weight and the sleeper weight. A monobloc concrete sleeper weighs about 3 kN. Half a sleeper and 0.6 m rail weigh about 1.86 kN. Far from the wheel load the preload in the pad is formed by the clip load and the rail weight and the preload in the ballast only by the rail and sleeper weight.

The preloaded pad and ballast stiffness can be determined from their load-stiffness relationship. As used in chapter 4, the pad static stiffness shown in Figure 4.1 is multiplied by a ratio 3.6 to form the pad dynamic stiffness. The ballast stiffness measured at 200 Hz (see Table 4.2 in chapter 4) is chosen to calculate the ballast dynamic stiffness. Its value which was measured with bibloc sleepers has

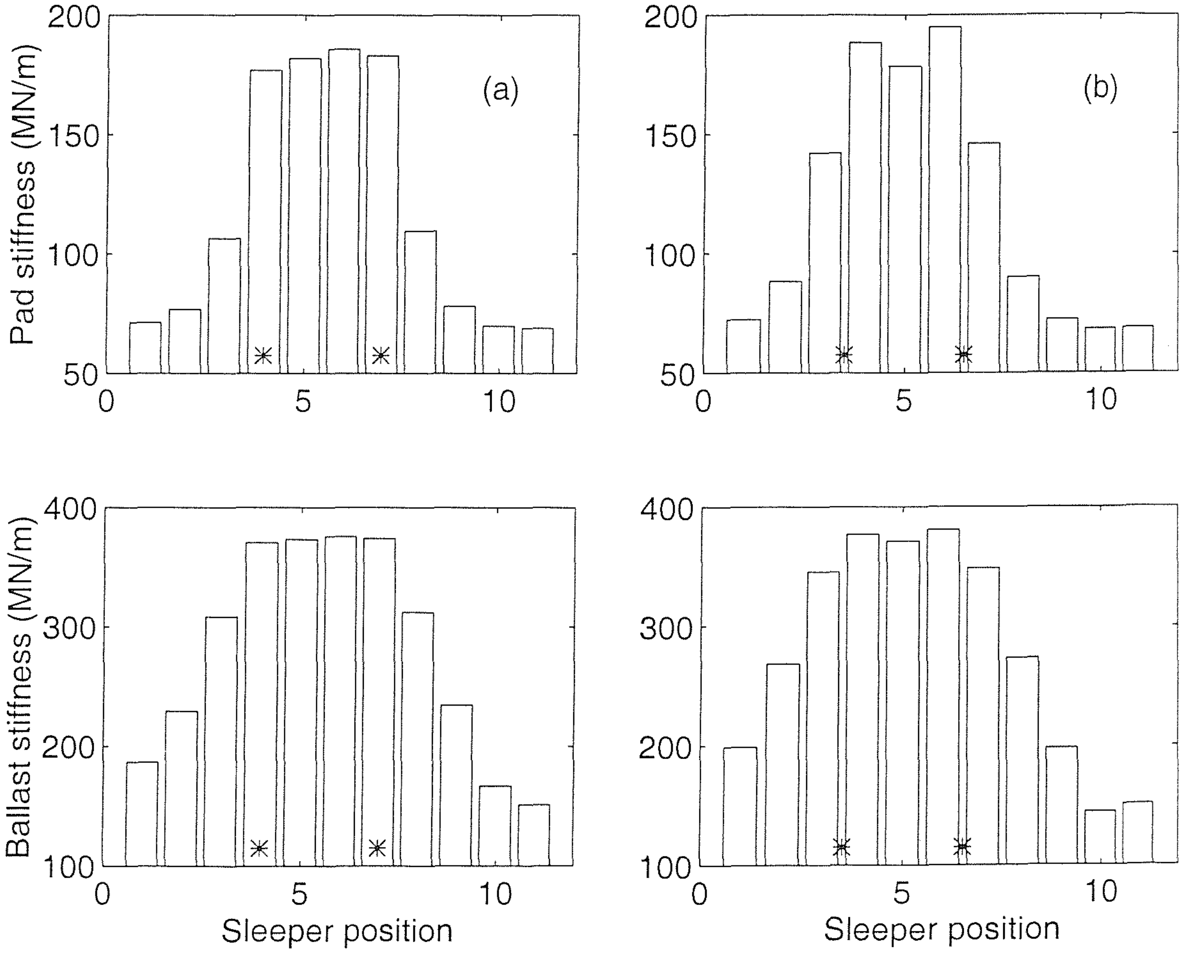

Figure 7.5. Preloaded pad and ballast stiffness, key as for Figure 7.4.

been multiplied by 1.3 to allow for the larger area of ballast in contact with a monobloc sleeper, as treated in chapter 4.

Figure 7.5 shows the pad and ballast dynamic stiffness for the wheel loads above a sleeper and at mid-span. The stiffness variation is similar to the preload variation in Figure 7.4. Between the two closer wheels, the pad and ballast become very stiff due to the large preload in them. Away from the wheel load, they quickly reduce to stable values. These values are the pad stiffness under the clip load and the rail weight and the ballast stiffness under the rail and sleeper weight. The pad and ballast stiffness is affected by the wheel load only at about 10 supports for each bogie because the preload in the foundation is local.

7.3. Modelling of track vibration

As used in chapters 4 and 6, a conventional Timoshenko beam model is employed to represent the rail. The track is modelled with an infinite rail and a finite number of discrete supports. However, since the multiple wheel loads are taken account of, the dynamic stiffness of the pad and ballast is now assigned different values at each support. To include the effects of multiple wheels on the rail, these wheels are treated as additional passive systems attached to the rail, see Figure 6.14. For simplicity the distances between wheels are now chosen as 12.6 m, 1.8 m and 3.6 m which are slightly different from those shown in Figure 6.14. The principles stated in chapter 6 for calculating point and transfer receptances of the track are still valid, and the responses of the rail at the support points and the wheel/rail contact points to a unit force acting at z_{Li} can be written as

$$u(z_m) = -\sum_{\substack{n=1 \\ n \neq Li}}^{M} Z_w u(z_n) \alpha^{RT}(z_m, z_n) - \sum_{n=M+1}^{M+N} Z_{sn} u(z_n) \alpha^{RT}(z_m, z_n) + \alpha^{RT}(z_m, z_{Li})$$

$$m = 1, 2, \cdots, M+N \qquad (7.7)$$

where each term in equation (7.7) has the same meaning as in chapter 6, but the dynamic stiffness for the n-th support is now represented by

$$Z_{sn} = \frac{K_{pn}(K_{bn} - M_s\omega^2)}{K_{pn} + K_{bn} - M_s\omega^2} \qquad n = M+1, M+2, \cdots, M+N \qquad (7.8)$$

where K_{pn} and K_{bn} are the dynamic stiffness of the pad and ballast respectively and related to the preload in them, see Figure 7.5.

After solving equation (7.7), the displacement at any point on the rail can be obtained by substituting $u(z_m)$ into the following equation:

$$u(z) = -\sum_{\substack{n=1 \\ n\neq Li}}^{M} Z_{wn} u(z_n) \alpha^{RT}(z,z_n) - \sum_{n=M+1}^{M+N} Z_{sn} u(z_n) \alpha^{RT}(z,z_n) + \alpha^{RT}(z,z_{Li}) \qquad (7.9)$$

Thus the point receptance at $z = z_{Li}$ and the transfer receptance at z for the rail with multiple wheels on it are given as

$$\alpha_W^R = u(z_{Li}), \quad \alpha_W^{RT}(z) = u(z) \qquad (7.10, 7.11)$$

7.4. Results

7.4.1. *Parameters for the calculations*

The following parameters are used in the numerical calculations for the railway track vibration model:

$E = 2.1\times10^{11}$ N/m^2, $G = 0.77\times10^{11}$ N/m^2, $\rho = 7850$ kg/m^3, $\eta_r = 0.01$,
$A = 7.69\times10^{-3}$ m^2, $I = 30.55\times10^{-6}$ m^4, $\kappa = 0.4$,
$M_s = 150$ kg, $d = 0.6$ m, $\eta_p = 0.25$, $\eta_b = 0.6$

where E is the Young's modulus, G is the shear modulus and ρ is the density. The rail damping is introduced by making E and G complex with the factor $(1+i\eta_r)$, where η_r is the rail loss factor. The geometric properties of the cross-section are characterised by A, the cross-sectional area, I, the area moment of inertia and κ, the shear coefficient. M_s and d are the sleeper mass and the span length respectively. In the loaded area the pad and ballast stiffness K_{pn} and K_{bn} are chosen according to the preload caused by the wheel loads and in the unloaded area they are chosen as constant, see Figure 7.5. The damping of the pad and ballast is also introduced by making K_{pn} and K_{bn} complex with the pad and ballast loss factors η_p and η_b respectively. The ballast loss factor is chosen lower than usual in order to make effects in the response more visible.

The point receptance of the track for vertical vibration is calculated for the excitation acting either at mid-span or above a sleeper in the frequency range 100 –

5000 Hz. The wave propagation decay rate along the rail is examined in the same frequency range. The number of the discrete supports is chosen as $N = 100$. Since the unloaded pad stiffness considered here is much lower than that used in chapter 6, three groups (one group in chapter 6) of the wheel loads and/or wheel/rail interactions are applied in the considered length of the supported rail. In each group there are four wheels with each single wheel load equal to 75 kN.

7.4.2. *General effects of wheel preload and wheel/rail interaction*

Before showing the results of the numerical calculations, it is helpful to review some important features about the effects on the track vibration of the preloaded pad and ballast stiffness and the wheel/rail interactions in order to obtain a better understanding of the results. These features have been observed in chapters 4 and 6 and may be summarised as follows:

1. The point receptance of a railway track at low frequencies is governed by the local supports near the excitation point and is reduced by the stiffened pad and ballast due to the wheel load.
2. The vibration decay at lower frequencies is higher in a loaded area than in an unloaded area because the preloaded pad and ballast are stiffer than when unloaded.
3. The wheel/rail interaction forces (due to the rail vibration rather than the roughnesses) are related to the wave propagation decay rate in the rail and the point receptance sum of the wheel, contact spring and rail. If the wave propagation decay rate or the point receptance sum is high, the interaction forces will be small and vice versa.
4. For a track with one or more additional wheels on it, cancellation of the first pinned-pinned resonance occurs in terms of the point receptance when the excitation acts at mid-span.

7.4.3. *Point receptance*

The point receptances of the track are calculated for the excitation acting at either z_{L1} or z_{L2}. z_{L1} and z_{L2} are chosen to be at mid-span or above a sleeper. Three cases are calculated for comparison, i.e. considering both the wheel/rail interactions and the preloaded foundation, considering the wheel/rail interactions only or considering the preloaded foundation only. Figure 7.6 shows the results for the excitation acting at z_{L1}.

It can be seen that the point receptance of the preloaded track at low frequencies is lower than the unloaded track, and the two low frequency resonances, at which the whole rail bounces on the ballast stiffness and on the pad stiffness, appear at higher frequencies for the preloaded track (approximately 200 and 400 Hz). At high frequencies (above 1200 – 2000 Hz), however, the preload in the foundation caused by the wheel load has no apparent effects on the track vibration in terms of the point receptance.

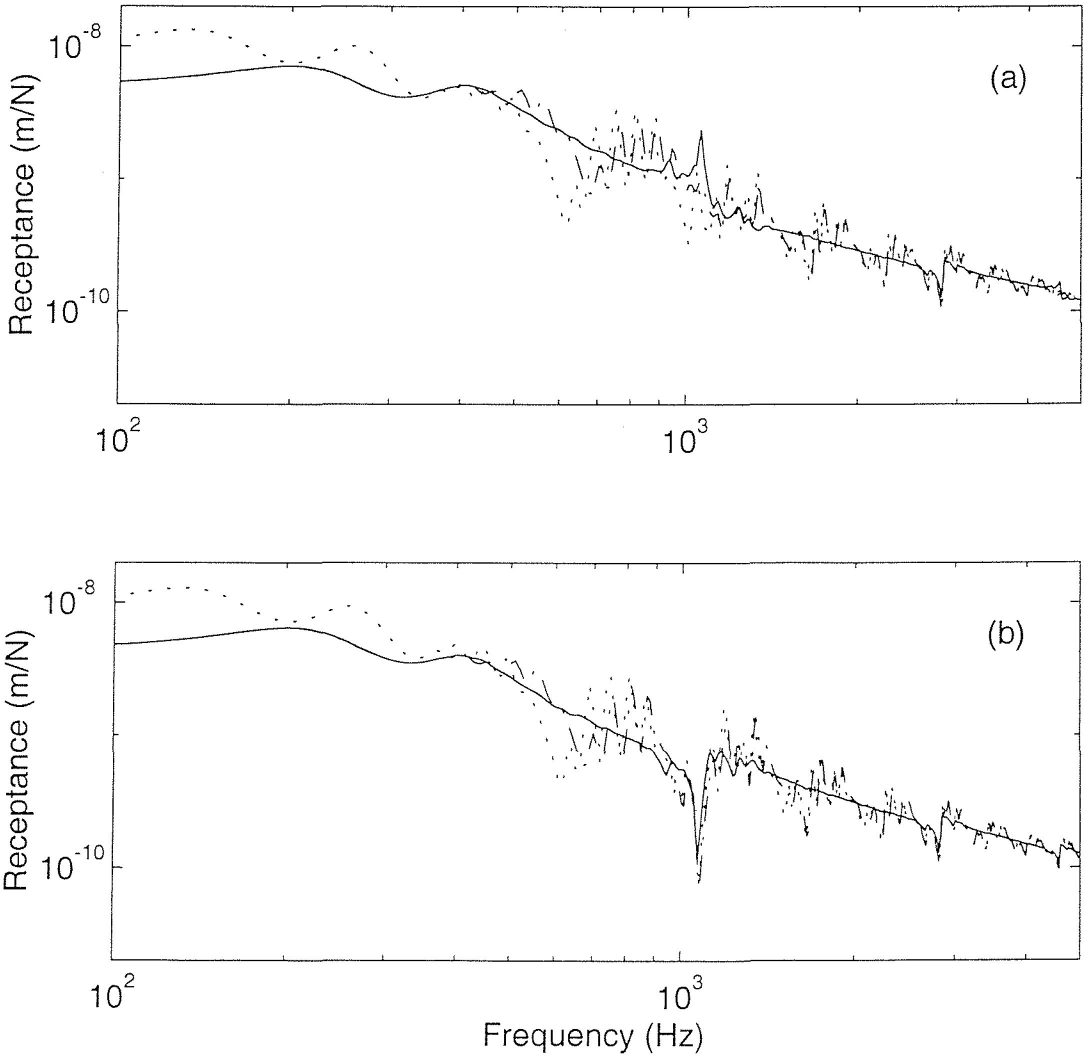

Figure 7.6. Amplitude of the point receptances with excitation at z_{L1} and (a) at mid-span, (b) above a sleeper. — for preloaded foundation only, ---- for both preloaded foundation and wheel/rail interactions, ······ for wheel/rail interactions only.

The effects of the wheel/rail interactions can be seen to be significant mainly at higher frequencies, above about 500 Hz. At low frequencies the point receptance of the track with multiple wheels on the rail is the same as without wheels on the rail. This is because the wave propagation decay rate is high at low frequencies so that the generated wheel/rail interaction force at the wheel positions is weak and the wave reflected by the wheel is also weak and, moreover, it is quickly attenuated before arriving back to the excitation point due to the high decay rate. At higher frequencies the point receptance of the rail with wheel/rail interactions fluctuates around that of the rail without interactions because the wheel/rail interaction forces are greater due to the low decay rate of the wave propagation. For the track with multiple wheels on the rail the first pinned-pinned resonance peak at just above 1000 Hz can be seen to disappear for the excitation acting at mid-span. The detailed analysis concerning the cancellation of the pinned-pinned resonance has been presented in chapter 6. The fluctuation of the point receptance due to the wheel/rail interactions can be seen to be greater around 600 – 1000 Hz. The reason for this is that in this frequency range the point receptance sum of the wheel, contact spring and rail tends to reach its minimum (see chapter 6), whereas the wave propagation decay rate is fairly low (lower for the softer pads considered here than for the pads used in chapter 6), so that the wheel/rail interaction force reaches its maximum. In addition, some sharp ripples of the receptance appear in this frequency range. These ripples are probably caused by the wave reflection from other distant wheel groups. With increasing frequency above 1 kHz, the fluctuation of the point receptance can be seen to decrease gradually.

Figure 7.7 shows the corresponding results for the excitation acting at z_{L2}. In general these results are similar to those for the excitation acting at z_{L1}, but some differences can be observed. Compared with the results for the excitation acting at z_{L1}, the fluctuation of the point receptance at higher frequencies is stronger because the rail at the excitation point can receive the waves reflected by the closer wheels from both sides. Since the wave propagation decay rate is lower for the unloaded track than for the loaded track, the effects of the wheel/rail interactions are greater for the unloaded track in terms of the fluctuation of the point receptance. This is

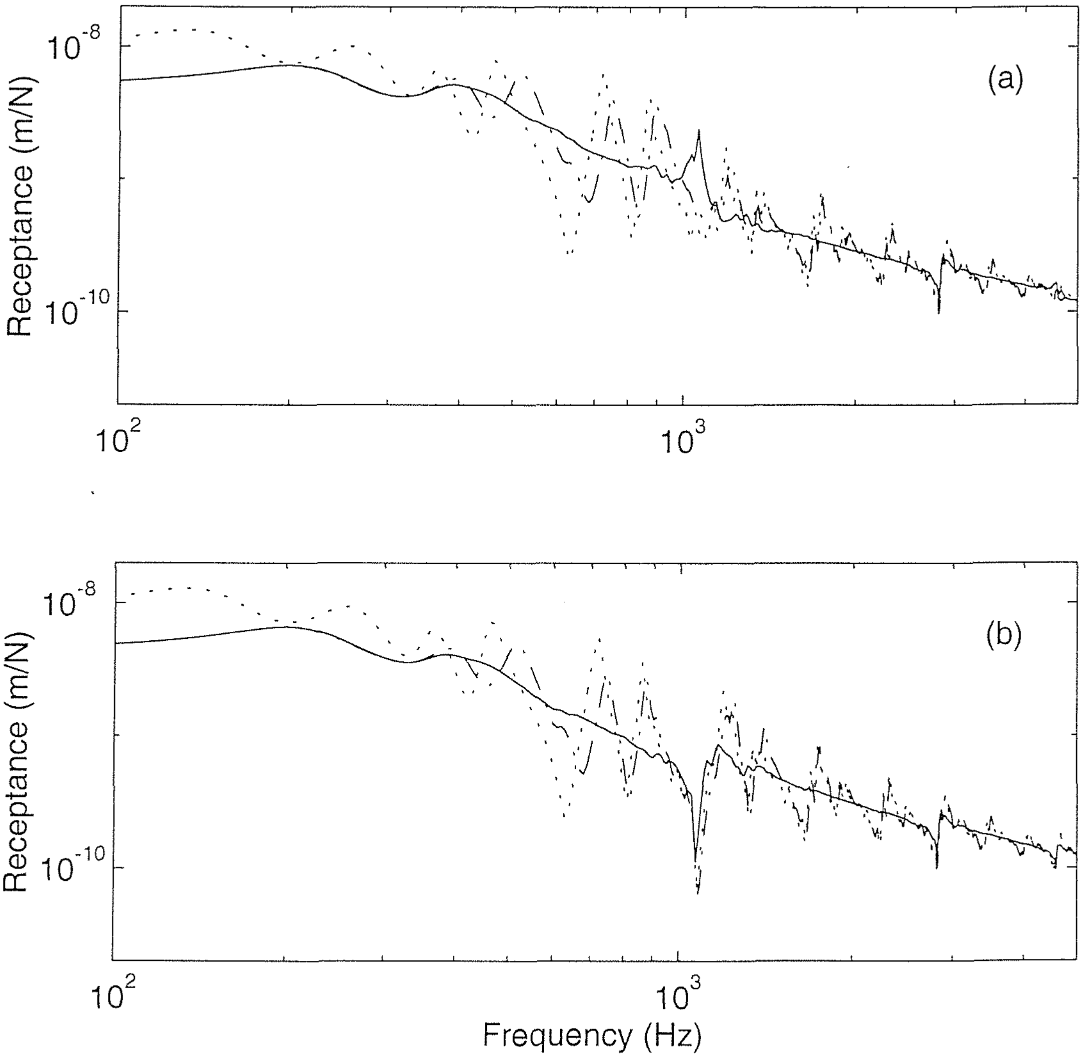

Figure 7.7. Amplitude of the point receptances with excitation at z_{L2} and (a) at mid-span, (b) above a sleeper, Key as for Figure 7.6.

more noticeable in the case of the excitation acting at z_{L2}.

7.4.4. *Transfer receptance and decay rate*

The transfer receptances of the track for vertical vibration are calculated at some frequencies to show some specific features of the vibration transmission along the track. The vibration decay rate in the track is calculated in the frequency range 100 – 5000 Hz from the decay in vibration level over a wagon length from the excitation point divided by the distance (19.8 m). From the decay rate a general view of the vibration decay can be obtained in the considered frequency range, whereas from the transfer receptances along the track detailed information about the vibration transmission can be gained at specific frequencies.

The vibration decay rates along the track are calculated using different track models. These models include the unloaded track with and without wheel/rail interactions and the preloaded track with and without such interactions. Figure 7.8 shows the decay rates to either the left-hand side or to the right-hand side of the

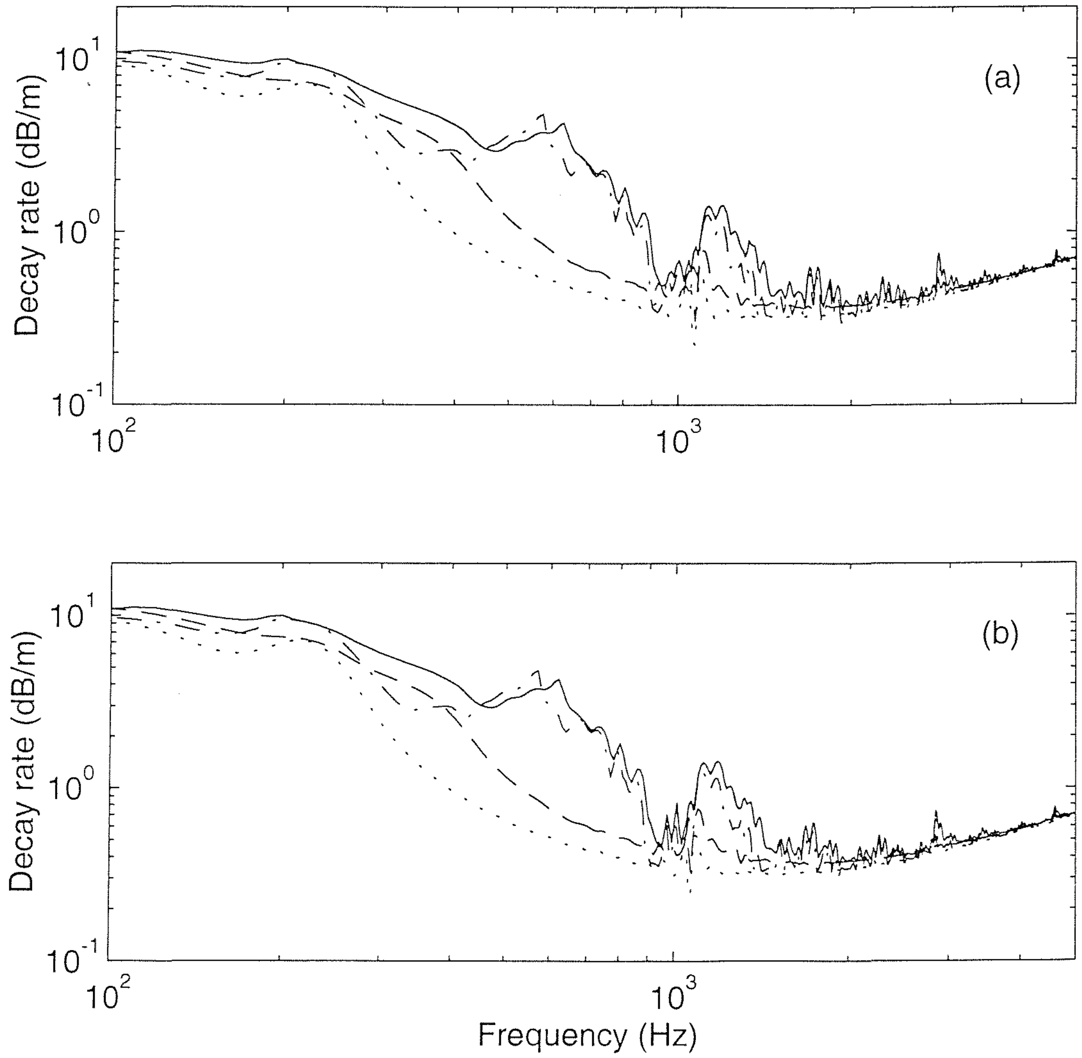

Figure 7.8. Vibration decay rates along the track for different track models with excitation at z_{L2} and above a sleeper. (a) decay to the left-hand side, (b) decay to the right-hand side. — for both preloaded foundation and wheel/rail interactions, – – for preloaded foundation only, -·-·- for wheel/rail interactions only, ······ for unloaded foundation and without wheel/rail interactions.

excitation which acts at z_{L2} and above a sleeper. The decay rates for the case of the excitation acting at z_{L1} are almost the same and thus are not presented. It can be seen from Figure 7.8 that the vibration decay rate is high at low frequencies and low at high frequencies. At low frequencies up to about 200 Hz and high frequencies from about 2 kHz the decay rates for the different track models are very similar. The main differences in decay rate for the different models are between about 300 and 900 Hz and near the first pinned-pinned resonance area above 1 kHz. For the track without wheel/rail interactions the decay rate in the preloaded track is generally higher than in the unloaded track because the stiffness of the preloaded pad and ballast is higher than in the unloaded case. The maximum difference in the decay rate between the preloaded and unloaded tracks may reach about 3 dB/m at about 400 Hz. For the tracks with wheel/rail interactions the vibration decay rates are much higher than for those without such interactions in the frequency range 350 – 850 Hz and around the first pinned-pinned resonance. The largest difference in the decay rate can be seen to be about 6 dB/m for the preloaded track or 8 dB/m for the unloaded track due to the wheel/rail interactions.

The transfer receptances of the track at frequencies 200 Hz, 400 Hz and 1050 Hz are shown in Figures 7.9 – 7.11 respectively. They are calculated at each support point with the excitation at z_{R1} and above a sleeper. For comparison four cases are calculated for the tracks with and without the preloads and with and without the wheel/rail interactions. Compared with the point receptance, variations in the transfer receptance for the track with multiple wheels on it are more complicated because both frequency and spatial position affect the transfer receptance.

At 200 Hz (Figure 7.9) the transfer receptances at the wheel/rail contact points for the track with wheel/rail interactions can be seen to be locally minimum. The reason for this is that at about 200 Hz the receptance of the wheel is approximately equal to the receptance of the wheel/rail contact spring in amplitude but out of phase with it, see Figure 6.6 in chapter 6. Thus the sum of the wheel and contact spring receptances is extremely small so that the rail seems to be pinned by the wheel at the wheel/rail contact point and the transfer receptance there becomes very

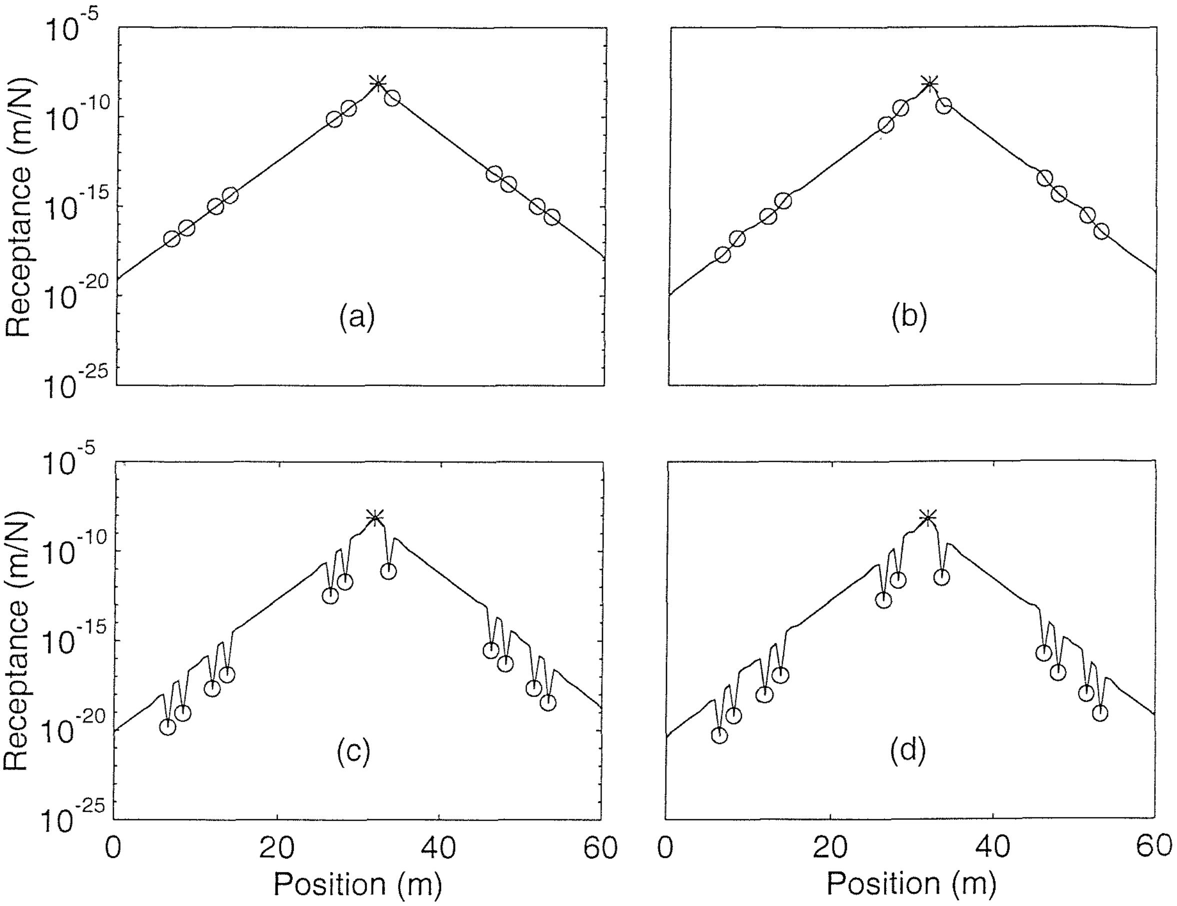

Figure 7.9. Amplitude of transfer receptances at 200 Hz for different models with excitation at z_{R1} and above a sleeper. (a) unloaded foundation and without wheel/rail interactions, (b) preloaded foundation only, (c) wheel/rail interactions only, (d) both preloaded foundation and wheel/rail interactions. * excitation position, o wheel position.

small. Comparing the transfer receptance of the preloaded track at 400 Hz (Figure 7.10) to the unloaded track, the vibration decay is enhanced in the loaded area of the track. What is more, the vibration decay at 400 Hz is also enhanced in the wheel regions by wheel/rail interactions. Furthermore, reflections can be seen to generate standing wave patterns. As a result, the average vibration decay rate over a wagon length for the track with preload and/or wheel/rail interactions is higher than without them, as shown in Figure 7.8. The first pinned-pinned resonance occurs at about 1050 Hz. At this frequency the response varies considerably within a span. Figure 7.11 therefore shows an envelope for this response, the response above sleeper being the minimum and that at mid-span being a maximum. From the transfer

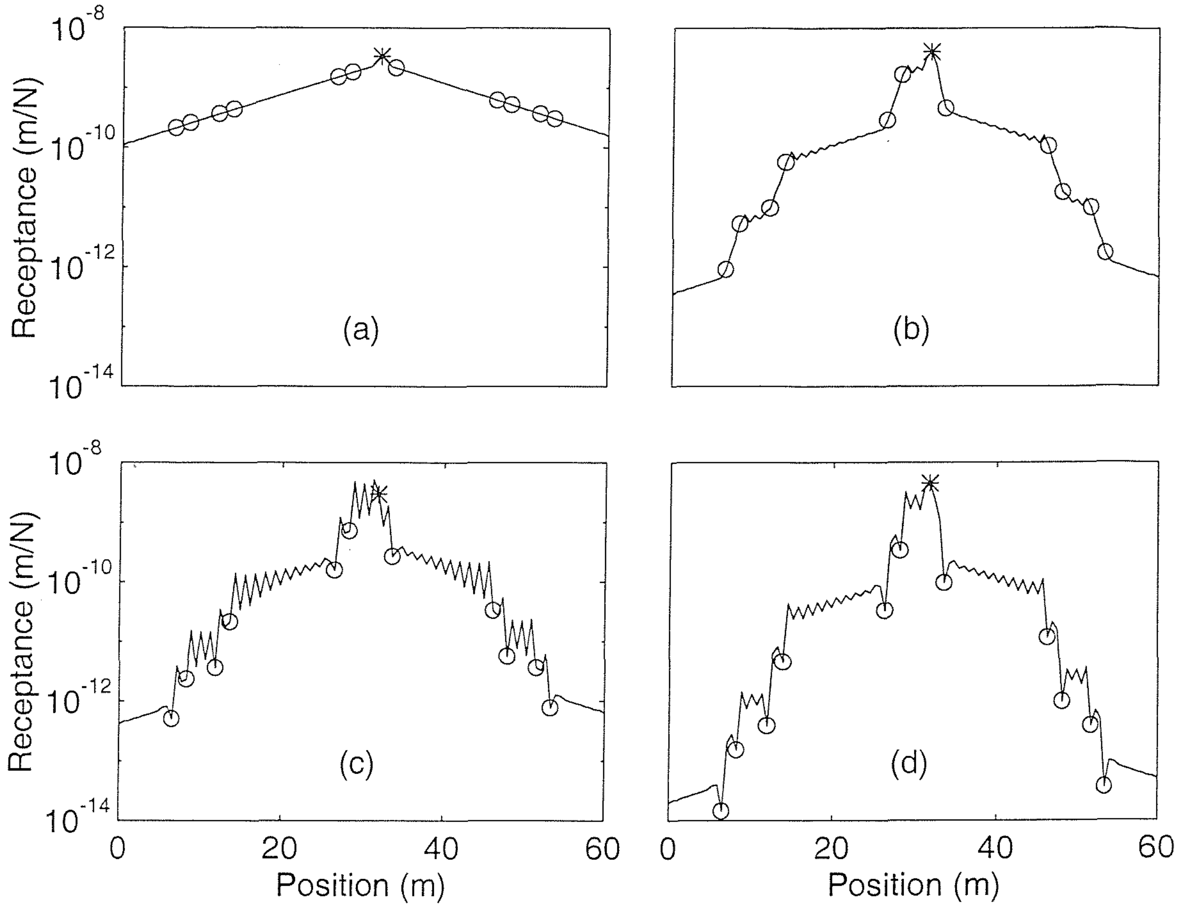

Figure 7.10. Amplitude of transfer receptances at 400 Hz for different models, key as for Figure 7.9.

receptances at this frequency the vibration decay can be seen to increase for the preloaded track or due to the wheel/rail interactions. However, the decay increase is found to happen only in the unloaded area or the area without wheel/rail interaction in terms of the transfer receptances at support positions (solid lines) but in the loaded area or the wheel/rail interaction area in terms of the transfer receptances at mid-spans (dotted lines). In addition, the transfer receptances at the wheel/rail contact points for the track with wheel/rail interactions are locally maximum compared to those at other support positions.

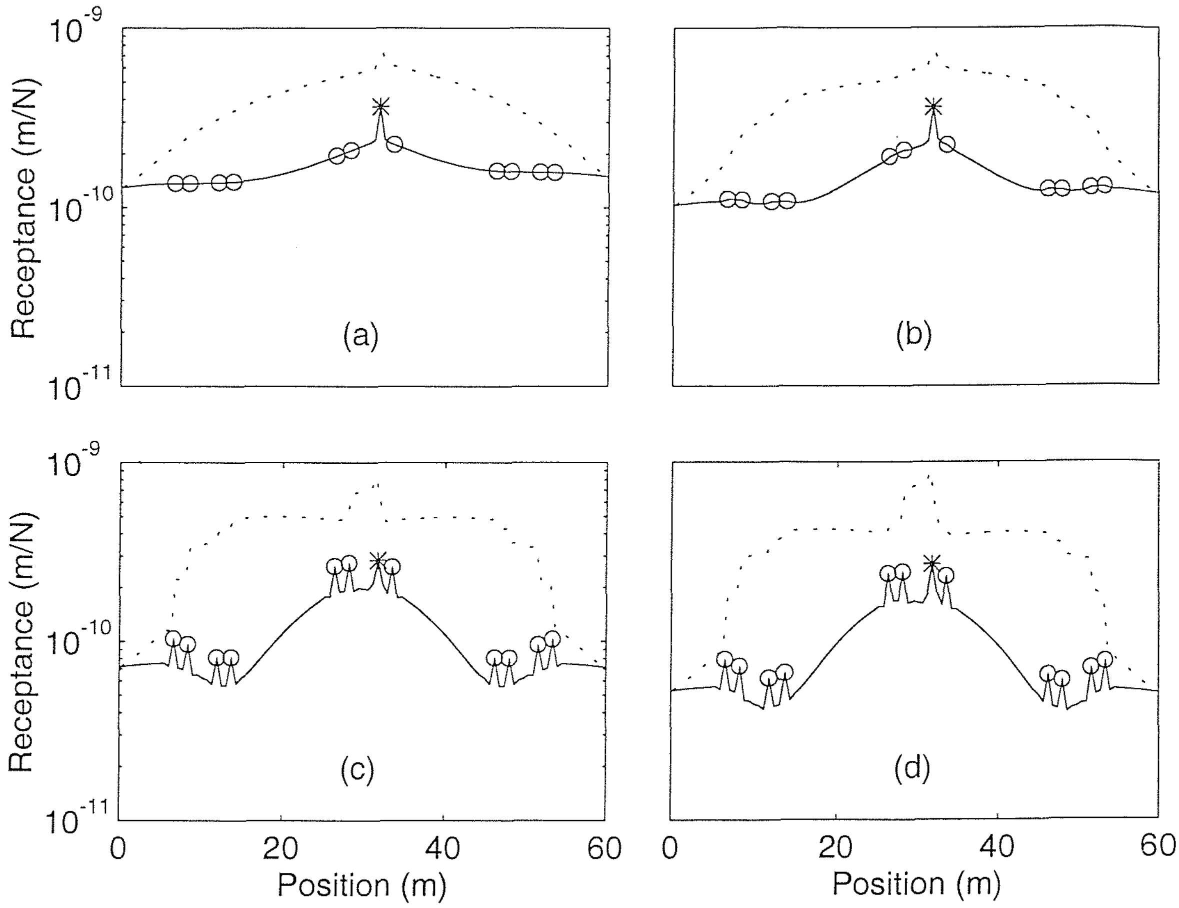

Figure 7.11. Amplitude of transfer receptances at 1050 Hz for different models, key as for Figure 7.9. ······ transfer receptances at mid-span.

7.5. Conclusions

The influences on the track vibration of the preloaded foundation stiffness combined with the wheel/rail interactions have been investigated. The static reaction force in the track foundation caused by the multiple wheel loads has been calculated using an equivalent linear model representing the non-linear model. The pad and ballast stiffness has been determined according to their load-stiffness relationship and the preload in them. A Timoshenko beam model has been employed to represent the infinite rail with the variable stiffness supports and multiple wheel/rail interactions. The point and transfer receptances and the vibration decay rates have been calculated in the frequency range 100 – 5000 Hz for different models. The results from these models have been analysed by comparison.

As concluded in chapter 4, the preload in the track foundation is local and near the wheel loads. At distances more than about 2 m away from the wheels the preload in the foundation due to the train weight can be considered as zero. Thus only a limited number of pads and ballast are preloaded by the wheel loads and become stiffer. Due to the stiffened pad and ballast the point receptance at low frequencies up to about 300 Hz is reduced and the vibration decay rate in the frequency range up to the first pinned-pinned resonance is enhanced. Especially, the wave propagation decay in the loaded area is significantly higher than in the unloaded area in the frequency region 300 – 800 Hz.

The wheel/rail interaction is weak at low frequencies and thus the effects of the wheel/rail interaction are mainly at frequencies 500 – 2000 Hz for the point receptance and from 400 Hz to the first pinned-pinned resonance for the decay rate. Because of the presence of the wave reflections the point receptance of the track with wheels on it fluctuates from about 500 Hz. The fluctuation in the point receptance decreases gradually with increasing frequency from 1 kHz. The first pinned-pinned resonance peak is cancelled due to the wheel/rail interactions when an excitation acts at mid-span, as observed in chapter 6. The vibration decay is enhanced in the wheel/rail interaction areas at frequencies 400 – 800 Hz and around the first pinned-pinned resonance.

CHAPTER 8

Application: Vibration and Noise Prediction of Railway Track for Interaction with a Train

In this chapter the vibration and noise radiation of railway track are predicted based on the ,whole train/track interactions. As an application example of the theoretical models developed in the previous chapters, both the preloaded track foundation stiffness and the multiple wheel/rail interactions are taken account of and a double Timoshenko beam model is used to represent the rail vertical vibration. Results from different track models are compared and the effects of different pad stiffnesses on the track vibration and noise radiation are investigated. It is shown that the influences of the preloads and wave reflections from wheels are significant on the rail receptance and the wheel/rail interaction force, whereas their influences on the overall track vibration level or the noise radiation are limited.

8.1. Introduction

When a train runs along the track, the roughnesses on the wheel tread and the rail surface produce dynamic interaction forces between the wheels and the rail at the frequencies corresponding to the passage speed of the wheel/rail contact over the particular roughness wavelength, so that the track is excited, vibrates and radiates noise. In the meantime the wheels interact with the rail as passive systems attached to the rail, and they also apply static loads to the track due to the train weight. The reaction force of the track foundation to the wheel loads is generally different at different supports. As a result, the foundation stiffness varies at different supports because the track foundation contains components with pronounced non-linear behaviour such as railpads and ballast. As discussed in the previous chapters, both the passive wheel/rail interactions and the varying pad and ballast stiffnesses significantly affect the track vibration.

In this chapter, as an application example of the investigations of various effects in the previous chapters, the railway track vibration is predicted under the consideration of the whole train/track interactions. This means that both the static preloads in the track due to the train weight and the multiple wheel/rail interactions (including both original and generated) along the whole train are taken account of. The vertical track vibration is predicted using the double Timoshenko beam model from chapter 2. The results from different track models and different pad stiffness are compared and analysed. The noise radiation from different models is also predicted in terms of the sound power spectrum and the A-weighted sound power level.

8.2. Interference between vibrations generated by multiple wheels

For the train/track interaction it may be thought that, since the distances between wheels are fixed and each wheel rolls over the same roughness, the multiple wheel/rail interactions ought to be treated as correlated vibration sources with relative phases determined by the wheel separation. Thus the correlation between multiple wheel/rail interactions caused by the roughness should be discussed first.

For simplicity and without losing generality, a two wheel/rail interaction case is analysed here and its result can be readily extended to the multiple wheel/rail interaction case. Figure 8.1 shows two wheels running over the rail roughness $r(z)$. The distance between two wheels is l. The roughness $r(z)$ can be regarded as an ergodic random process with its spectral density $S(k_r)$, where $k_r = 2\pi/\lambda_r$ is the wave

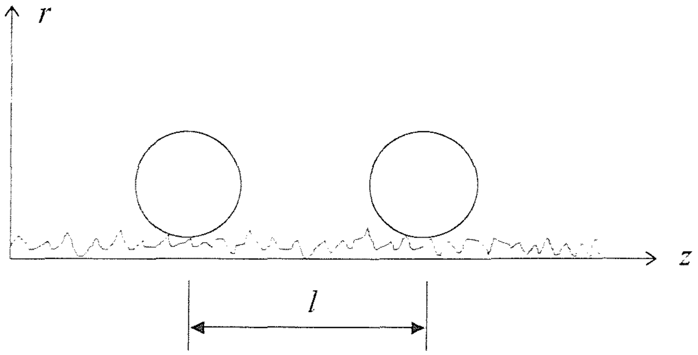

Figure 8.1. Two wheels on a rail roughness.

number of the roughness and λ_r is the roughness wavelength. In practice the rail roughness $r(z)$ can be seen as a broad band process, for example the roughness wavelengths of relevance for rolling noise are typically in the range 5 mm to 0.5 m. At a train speed of 100 km/h (27.8 m/s) they correspond to a frequency range 55 – 5500 Hz, the shorter wavelengths applying to higher frequencies.

Using the autocorrelation function of a random process, the extent of the interference between two wheels running over the rail roughness can be examined by the following correlation coefficient:

$$\rho_l = \frac{R_r(l)}{R_r(0)} \tag{8.1}$$

where $R_r(l)$ is the autocorrelation function and is given as [49]:

$$R_r(l) = \int_{-\infty}^{\infty} S(k_r) e^{ik_r l} dk_r \tag{8.2}$$

For a broad band rail roughness $r(z)$ the correlation coefficient can be written as [49]:

$$\rho_l = \frac{\sin k_{r\max} l}{k_{r\max} l} = \lambda_{r\min} \frac{\sin(2\pi l / \lambda_{r\min})}{2\pi l} \tag{8.3}$$

where k_{rmax} is the greatest roughness wave number considered and corresponds to the shortest roughness wavelength λ_{rmin}. For simplicity equation (8.3) is obtained, on the assumption that the longest roughness wavelength is infinite ($k_{rmin} = 0$).

From equation (8.3) it can be seen that the extent of the interference between two wheels depends on both the wheel separation distance l and the shortest roughness wavelength λ_{rmin} in the roughness spectrum. If the correlation coefficient ρ_l is equal to zero, the two wheel/rail interactions are totally uncorrelated. Most importantly, the wheel separation distances are of the order of 2 m and more, whereas the roughness wavelengths of relevance for rolling noise are in the range 5 mm to 0.5 m, accordingly the correlation coefficient ρ_l is approximately in the region of 0.0005 – 0.05 or even small, the larger value applying to the longer roughness wavelength (lower frequency).

The above argument suggests that the interference effects may be more noticeable at low frequencies, but here the decay rates of waves in the rail are of the order of 10 dB/m, as seen in chapters 4 and 7, so the influence of one wheel/rail interaction at another wheel location will be negligible. In addition the roughness excitation is a combination of wheel and rail roughness. The roughness on each wheel is independent of the others and of the rail roughness. Moreover, each wheel does not follow exactly the same rolling line on the track, so the rail roughness is different, particularly at high frequencies.

For all the above reasons, therefore, the multiple wheel/rail interactions caused by roughnesses during a train running over the track can be treated as uncorrelated vibration sources, so that the mean square response to each wheel can be added. However, the secondary wheel/rail interactions due to the track vibration can not be treated as uncorrelated each other. They are treated as many passive systems attached to the rail when calculating the receptances of the track vibration, as discussed in chapters 6 and 7.

8.3. Track vibration model and relative displacement excitation

A double Timoshenko beam model is employed here to represent the rail vertical vibration. This model has been developed in chapter 2 and schematically shown in Figure 2.5. Figure 8.2 shows schematically a typical train on a discretely supported rail. The track is modelled with an infinite rail and a finite number of discrete supports, as used in the previous chapters. The number of supports should be chosen large enough to guarantee an acceptable approximate solution. The distances between wheels are chosen approximately to represent a bogied container wagon.

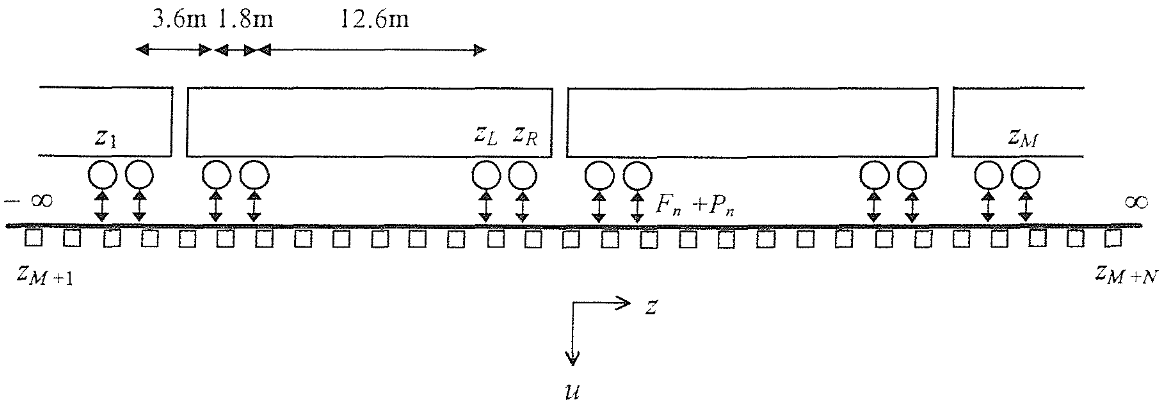

Figure 8.2. Railway track with a train on the rail.

To calculate the response of the rail, both the discrete supports and the wheels are replaced by point forces. The wheel/rail interaction force at the n-th contact point is composed of both the original excitation F_n caused by roughnesses and the generated force P_n caused by incident wave. The responses to the excitation F_j at $z = z_j$ of the rail head and foot, u_{hj} and u_{fj}, at each wheel/rail contact point and each support point can be given using the superposition principle:

$$\begin{aligned} u_{hj}(z_m) = &-\sum_{\substack{n=1\\ n\neq j}}^{M} Z_w u_{hj}(z_n) g_{11}(z_m,z_n) - \sum_{n=M+1}^{M+N} \{[Z_{11n} u_{hj}(z_n) + Z_{13n} u_{fj}(z_n)] g_{11}(z_m,z_n) \\ &+ [Z_{31n} u_{hj}(z_n) + Z_{33n} u_{fj}(z_n)] g_{13}(z_m,z_n)\} + F_j g_{11}(z_m,z_j) \end{aligned} \tag{8.4a}$$

$$\begin{aligned} u_{fj}(z_m) = &-\sum_{\substack{n=1\\ n\neq j}}^{M} Z_w u_{hj}(z_n) g_{31}(z_m,z_n) - \sum_{n=M+1}^{M+N} \{[Z_{11n} u_{hj}(z_n) + Z_{13n} u_{fj}(z_n)] g_{31}(z_m,z_n) \\ &+ [Z_{31n} u_{hj}(z_n) + Z_{33n} u_{fj}(z_n)] g_{33}(z_m,z_n)\} + F_j g_{31}(z_m,z_j) \end{aligned} \tag{8.4b}$$

$$m = 1, 2, \ldots, M+N \quad \text{and} \quad j = 1, 2, \ldots, M$$

where $g_{ij}(z_m, z_n)$ is the Green's function for an unsupported rail and it is defined as the response at z_m of the i-th component of the displacement vector caused by a unit harmonic force at z_n which is the j-th component of the excitation vector. Here subscript 1 represents the head and subscript 3 represents the foot. Z_w is the dynamic stiffness combination of the wheel and contact spring, see equation (6.25) in chapter 6. Z_{ijn} is the dynamic stiffness of the n-th support, see equation (2.37) in chapter 2. Since the track foundation is preloaded by train weight through the wheels and the railpads and the ballast are non-linear, the dynamic stiffness Z_{ijn} is different at each support. Z_{ijn} is calculated using the pad stiffness K_{pn} and ballast stiffness K_{bn} at n-th support, which are determined according to the preload at the support, see Figures 7.4 and 7.5 in chapter 7. M is the number of wheel-rail interactions under consideration, N is the number of the discrete supports. The generated wheel/rail interaction force P_{nj} at $z = z_n$ caused by F_j is given as

$$P_{nj} = -Z_w u_{hj}(z_n) \qquad n = 1, 2, \cdots, M \quad \text{and} \quad n \neq j \tag{8.5}$$

From equations (8.4) the displacements of the rail at each support and wheel/rail contact point can be solved in terms of F_j by taking the sum to the left-hand side, and then inverting the matrix of coefficients of $u_{hj}(z_m)$ and $u_{fj}(z_m)$. It is important to notice that each F_j is independent as discussed in section 8.2. Thus the responses u_{hj}

and u_{fj} to each F_j can be solved separately, and the mean square response to each wheel/rail excitation can be added.

When the displacements at the wheel/rail contact points and the support points are known, the interaction forces or the reaction forces there are also known. Then the response of the rail at any position can be calculated using the superposition principle again.

The original excitation F_j can be determined by the relative displacement (moving roughness) excitation model. For a unit displacement excitation, it is given as

$$F_j = -\frac{1}{\alpha^W + \alpha^C + \alpha^R_{wj}} \qquad j = 1, 2, \cdots, M \tag{8.6}$$

where α^W and α^C are the point receptances of the wheel and contact spring respectively. α^R_{wj} is the point receptance at $z = z_j$ of the rail with multiple wheels on it. It can be obtained by assuming $F_j = 1$ in equation (8.4) and then calculating the response at the forcing point.

The total response of the rail is a superposition of the response caused by each wheel/rail excitation F_j. Since the wheel/rail excitations caused by roughnesses are uncorrelated each other, the mean square response to each F_j can be added to form the total vibration level of the track due to the train/track interaction. For simplicity it may be assumed that the track vibration is similar under each wagon, except in the area close to the ends of a train. Thus only three groups of wheel/rail interactions are taken account of, as shown in Figure 8.2, for calculating the vibration response of the track within one wagon length centred in the central group of wheels. The influences of the wheels further away can be ignored compared with those at nearer locations because of the wave propagation decay.

8.4. Numerical results

The parameters of the wheel and track used for the numerical calculations are shown in Table 8.1. These parameters are chosen from UIC 60 rail and a 920 mm standard freight wheel. For the wheel the simple mass/spring model developed in chapter 6 is used. The track foundation is initially assumed to consist of soft rail

Table 8.1

Parameters of wheel and track

Young's modulus of rail, N/m^2	E	2.1×10^{11}
Shear modulus of rail, N/m^2	G	0.77×10^{11}
Density of rail, kg/m^3	ρ	7850
Loss factor of rail	η_r	0.01
Head area of rail, m^2	A_h	7.09×10^{-3}
Head area moment of inertia, m^4	I_h	30.4×10^{-6}
Shear coefficient of head	κ_h	0.45
Foot area of rail, m^2	A_f	0.6×10^{-3}
Foot area moment of inertia, m^4	I_f	0.118×10^{-6}
Shear coefficient of foot	κ_f	0.85
Head/foot connect spring, N/m^2	k_f	5.33×10^{9}
Wheel mass (all unsprung mass), kg	M_w	600
Modal spring of wheel, N/m	K_M	4.39×10^{9}
Wheel/rail contact spring, N/m	K_H	1.14×10^{9}
Pad stiffness, N/m	K_{pn}	see Figure 7.5
Pad loss factor	η_p	0.25
Sleeper mass (half), kg	M_s	150
Distance between sleepers, m	d	0.6
Ballast stiffness, N/m	K_{bn}	see Figure 7.5
Ballast loss factor	η_b	1

pads and concrete monobloc sleepers. Each single wheel load due to the train weight is equal to 75 kN. The number of the wheels on the rail is chosen as $M = 12$ (four wheels for each group) and the number of the discrete supports is chosen as $N = 120$ for the wheels at mid-span and $N = 121$ for the wheels above a sleeper.

8.4.1. *Comparison of different rail models*

Four different models are used for numerical simulations. These are the tracks with or without wheel static preloads and with or without wheel/rail interactions. The results from the different track models are presented in terms of the point receptance, the point receptance sum of the wheel, contact spring and rail, the wheel/rail excitation force and the spatially integrated squared velocity of the rail: the sum of $|v|^2 dz$ over a wagon length, where dz is the length of a short piece of rail and v is the vibration velocity of this piece of rail. Similarly for the sleepers the sum of $|v|^2$ on the sleepers over a wagon length is calculated. The sleeper velocity at each support is calculated according to the corresponding rail velocities of the head and foot at that support and the resilient coupling between the rail and sleeper (refer to Figure 2.5 and equation (2.18b) in chapter 2). Although some results are similar to those in the previous chapters, they are presented here to give a complete application example.

Figure 8.3 shows the point receptances of the different models. The excitation is at mid-span and situated at $z = z_R$, see Figure 8.2. At low frequencies the point

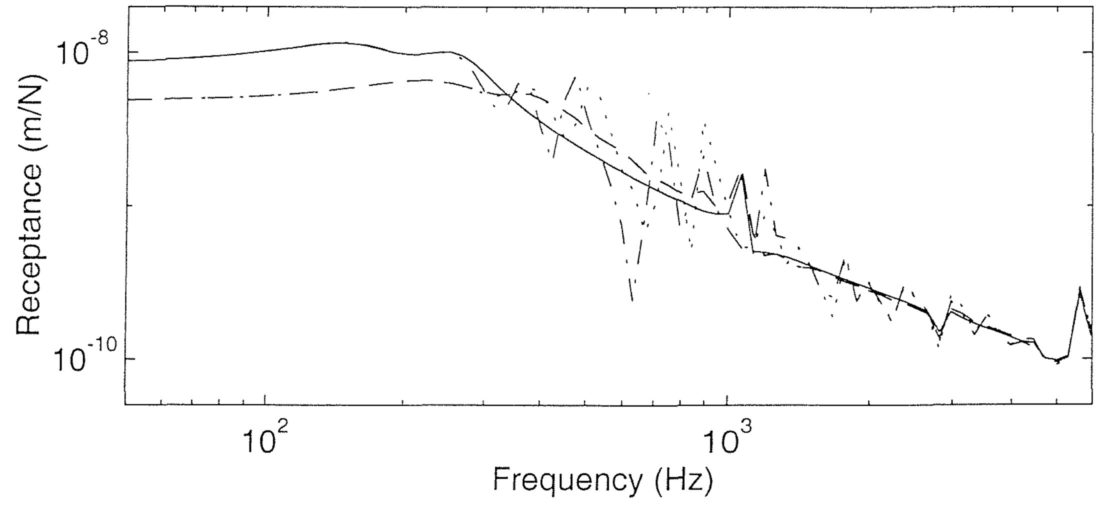

Figure 8.3. Point receptance amplitude of different track models with excitation at z_R and at mid-span. — without preloads and wheel/rail interactions, – – for preloaded foundation only, -·-·- for wheel/rail interactions only, ····· for both preloaded foundation and wheel/rail interactions.

receptance can be seen to be the same for the cases with and without wheel/rail interactions because the high decay rate of the track vibration at low frequencies leads to weak wheel/rail interactions. On the other hand, the point receptance of the loaded track is lower than that of the unloaded track because at low frequencies it is determined only by a few supports near the excitation and the stiffness of the supports there is much higher compared to those in the unloaded area. From about 300 Hz for the unloaded track and from about 400 Hz for the loaded track, the point receptances of the tracks with wheel/rail interactions fluctuate around those without such interactions. The fluctuation is very strong in the frequency region 400 – 1200 Hz, and it is larger for the unloaded track than for the loaded track because of the lower vibration decay rate of the former. The pinned-pinned resonance peak above 1000 Hz is cancelled for the cases with the wheel/rail interactions. At high frequencies, however, the fluctuation in the point receptance becomes weak and the point receptance is not affected by the preloads. The peak at about 5500 Hz is due to the cut-on of the foot flapping.

Figure 8.4(a) shows the point receptance sum at z_R (at mid-span) of the wheel, wheel/rail contact spring and rail for the track with both preloads and wheel/rail interactions. This sum is important because it determines the original excitation force to the wheel and the rail through equation (8.6). From Figure 8.4(a) it can be seen that below 150 Hz the point receptance sum is determined by the wheel and rail receptances which are out of phase. At middle frequencies the point receptance sum is approximately equal to the rail receptance, whereas at high frequencies it is equal to the receptance of the contact spring as both the wheel receptance and the rail receptance are small compared to the contact spring. Figure 8.4(b) shows the results from the different models. The point receptance sum can be seen to be higher for the unloaded track than for the loaded track in the low frequency region. In the high frequency region above 1300 Hz, however, they are the same for all cases and equal to the receptance of the contact spring.

Figure 8.5 shows the wheel/rail interaction forces due to 1 μm relative displacement (moving roughness) excitation at each frequency applied at z_R (at mid-span) for the different models. As the wheel/rail interaction force is the inverse

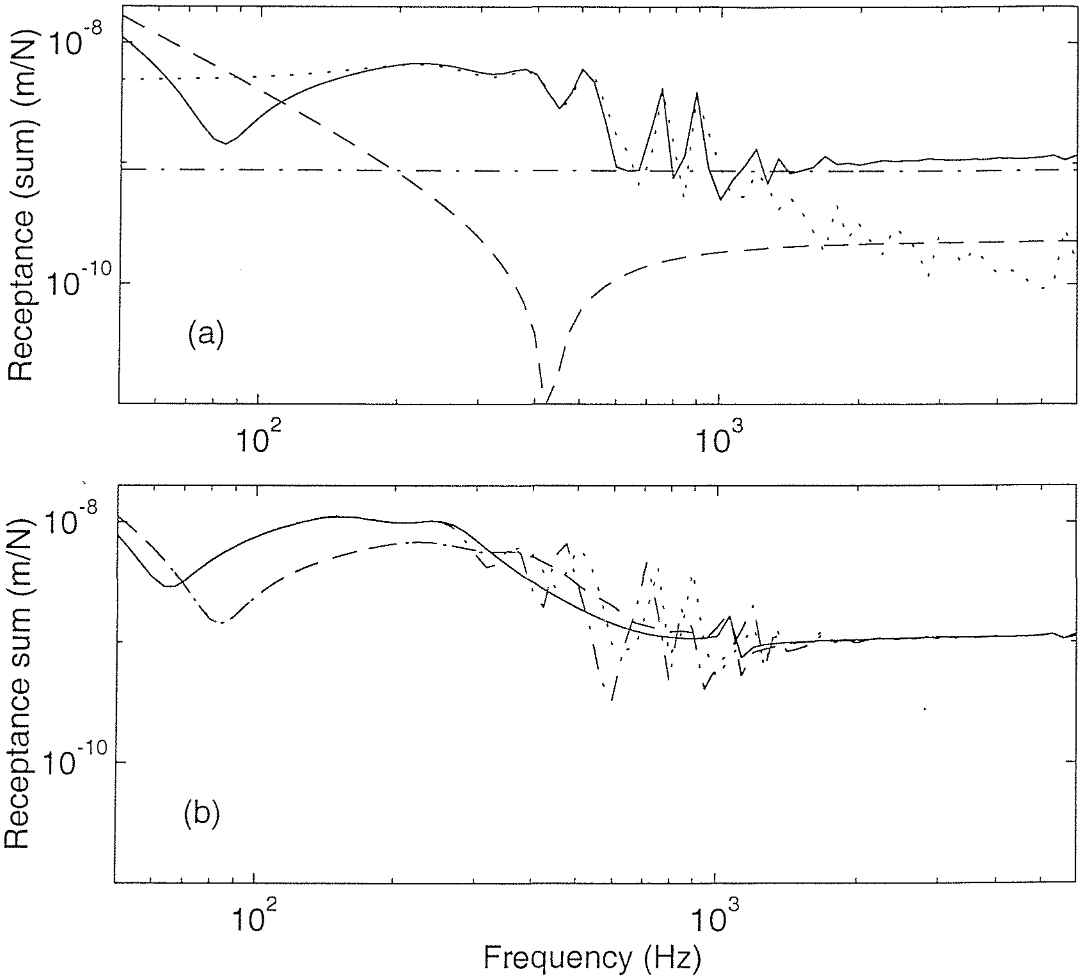

Figure 8.4. Point receptance sum (amplitude) at z_R (at mid-span) of wheel, wheel/rail contact spring and rail. (a) — point receptance sum, – – wheel receptance, -·-·- contact spring receptance, ····· rail receptance. (b) — point receptance sum for the track without preloads and wheel/rail interactions, – – for preloaded foundation only, -·-·- for wheel/rail interactions only, ····· for both preloaded foundation and wheel/rail interactions.

of the point receptance sum, the peaks in Figure 8.4 become the troughs here and the troughs become the peaks. Therefore, the interaction force at low frequencies is much larger for the loaded track than for the unloaded track. At middle frequencies it fluctuates strongly due to the presence of the wave reflections from other wheels. At high frequencies the interaction forces are the same for each model.

Figure 8.6 shows the vibration level of the rail and sleepers from the different models in terms of the sum of $|v|^2dz$ or $|v|^2$ on the sleepers over a wagon length due to 1 μm relative displacement excitation at each wheel/rail contact position. Here dz

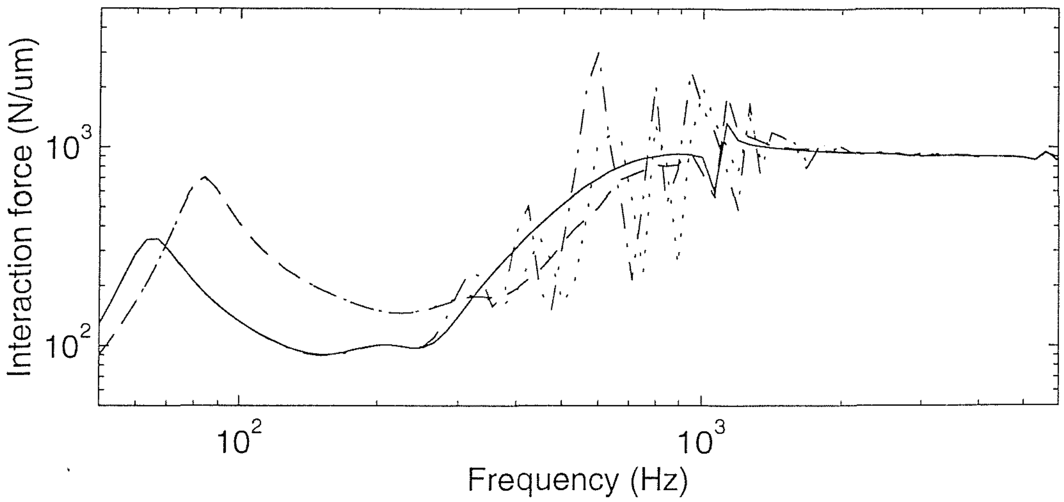

Figure 8.5. Wheel/rail interaction force (amplitude) due to 1 μm relative displacement excitation, key as for Figure 8.3.

is chosen equal to a quarter span length. The $|v|^2dz$ sum or $|v|^2$ sum is directly related to the sound power radiated from the rail and sleepers. It can be seen from Figure 8.6 that the vibration level of the rail is low at low frequencies and high at high frequencies, whereas for sleepers it is high at low frequencies and low at high frequencies. Because of the foot flapping the $|v|^2dz$ sum of the rail foot goes up above 3 kHz, whereas it is comes down for the rail head. In general, the rail vibration level is slightly lower for the loaded track than for the unloaded track. The sleeper vibration level from about 300 Hz, in contrast, is higher for the loaded track than for the unloaded track. This is because at high frequencies the force transmitted to the sleepers at the loaded area is larger due to the stiffened pads. The fluctuation in the vibration level caused by wave reflections from other wheels is much smaller compared with that in the point receptance or the wheel/rail excitation force. The reason for this is fairly interesting: the fluctuations in the rail vibration receptance and in the wheel/rail excitation force are in the opposite directions. As a result, a higher receptance of the track corresponds to a lower wheel/rail excitation force and a higher vibration response of the track. These effects tend to cancel each other to certain extent. Thus the influences of the wave reflections from other wheels are limited in terms of the $|v|^2dz$ sum or $|v|^2$ sum of the rail and sleepers.

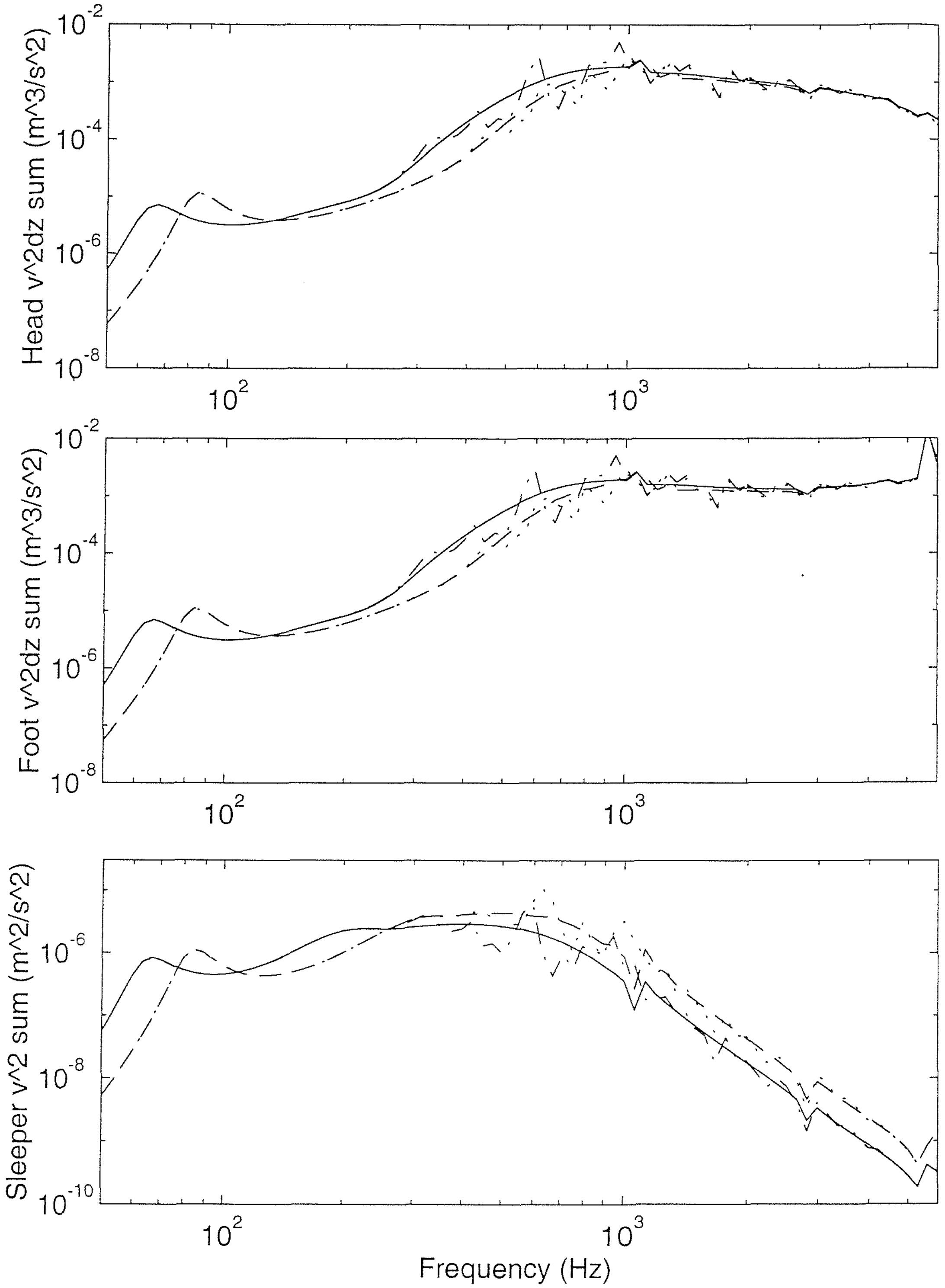

Figure 8.6. $|v|^2 dz$ sum of the rail head and foot and $|v|^2$ sum of sleepers over a wagon length due to 1 μm relative displacement excitation at each wheel/rail contact position (all wheels at mid-span), key as for Figure 8.3.

8.4.2. *Comparison with continuously supported rail model*

Using a continuous track model the mathematical treatment becomes much simpler, compared with the discretely supported rail model, and the time for numerical calculations can be dramatically reduced. However, the pinned-pinned resonance can not be observed using a continuous model. In addition only a uniform foundation is possible in the continuous model instead of the preloaded pad and ballast stiffness which is assigned different values at each support. The former is not a problem when the wheel/rail interactions are present because the response in the

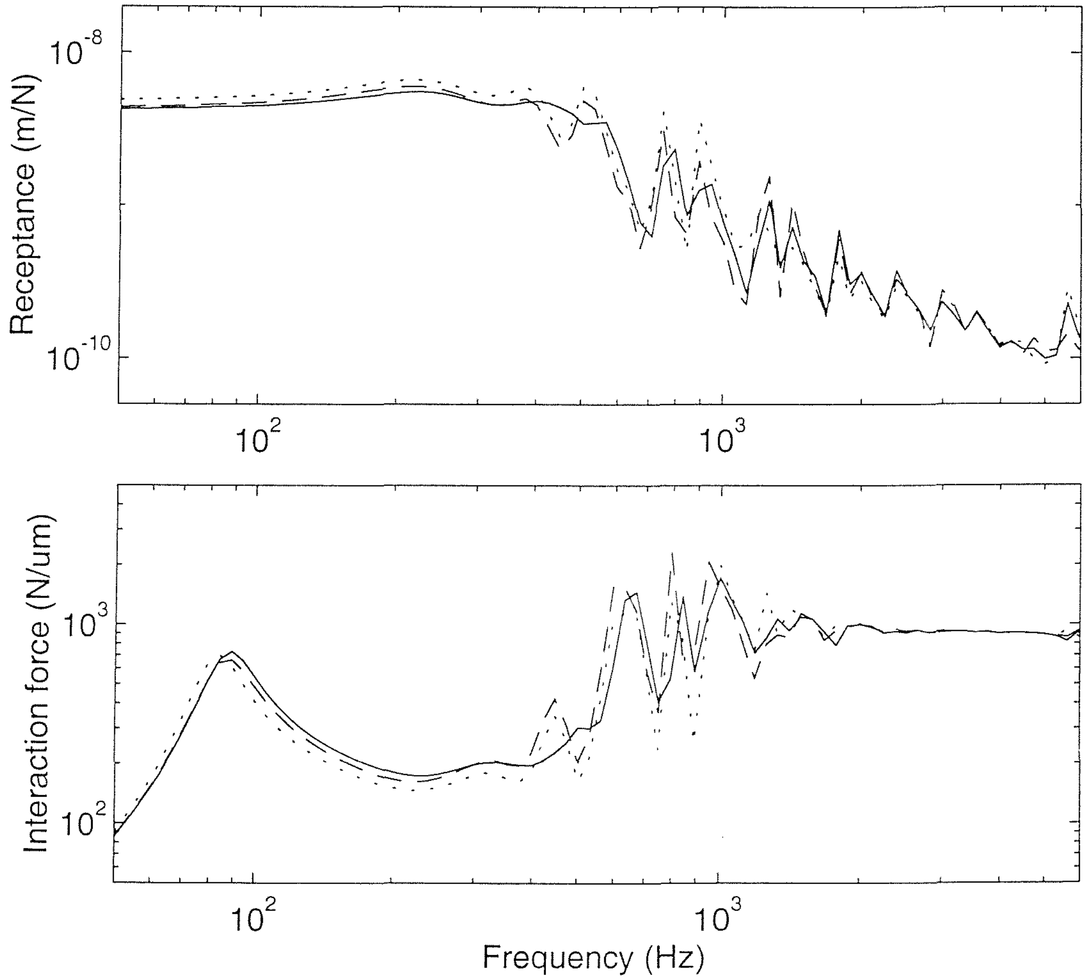

Figure 8.7. Result comparison of different track models with both preloaded foundation and wheel/rail interactions in terms of point receptance and wheel/rail interaction force. — for the continuous model, – – for the discrete model with wheels above sleeper, ····· for the discrete model with wheels at mid-span.

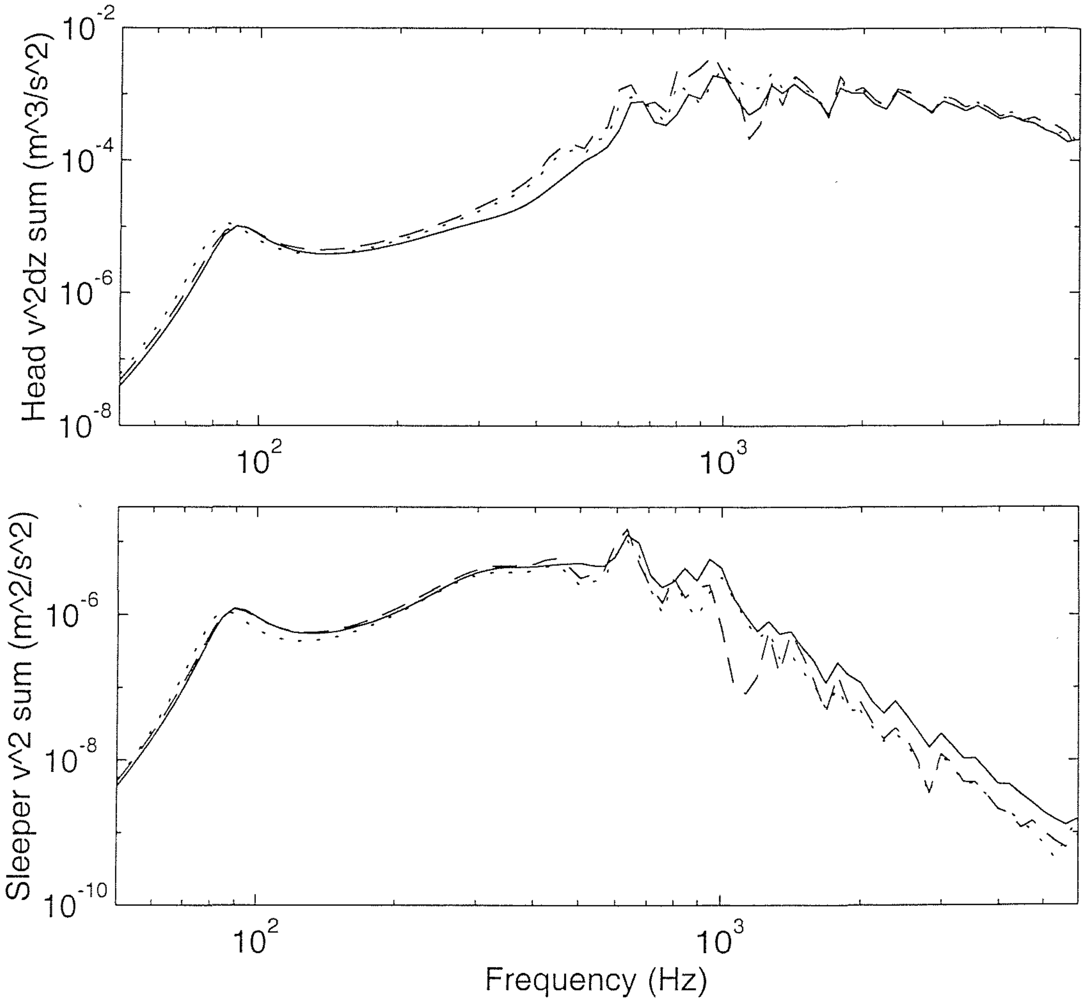

Figure 8.8. Vibration level of the rail head and sleepers due to 1 μm relative displacement excitation from different track models, key as for Figure 8.7.

pinned-pinned resonance peak is now cancelled. In order to calculate for the loaded track, the foundation stiffness for the continuous model is chosen in accordance with the support at which the largest stiffness occurs due to the preload.

Figures 8.7 and 8.8 show the results of the point receptance, wheel/rail interaction force and the vibration level of the rail head and sleepers from the continuous model and the discrete model with excitations at mid-span and above sleeper. Both the preloaded foundation stiffness and the wheel/rail interactions are taken account of in all these models. The point receptance and the wheel/rail interaction force from the continuous model are quite consistent with those from the discrete model. However, the vibration level of the rail head is under-predicted and that of the sleepers is over-predicted. These are due to the uniformly high foundation stiffness used in the continuous model. Nevertheless, the continuous track model is still acceptable as an approximation of the discrete model.

8.4.3. *The effects of different pad stiffness*

The stiffness of the rail pad, inserted between the rail and the sleeper, is a critical parameter in determining the track vibration and thus the noise radiated from the track. Theoretical studies have shown that a stiff pad couples the rail to the sleeper, leading to a reduction in the radiation of sound from the rail whilst increasing the sleeper noise [96]. Conversely a soft pad leads to a low sleeper noise component but a greater rail noise. The studies in [96] are based on using a uniform value of the pad and ballast stiffness along the track. Such studies have been extended in chapters 4 and 7 under the consideration of the non-linear stiffness behaviour of the pad.

Here the influence of the pad stiffness on the track vibration is investigated by taking account of both multiple wheel preloads and multiple wheel/rail interactions. Three types of railpad are considered: soft, medium and stiff. The soft pad stiffness has been used throughout the previous calculations in this chapter. Figure 8.9 shows the static load-stiffness curves for these three pads [99]. The maximum preloads in the pads (including 20 kN from the clips) are similar for the three pad cases and

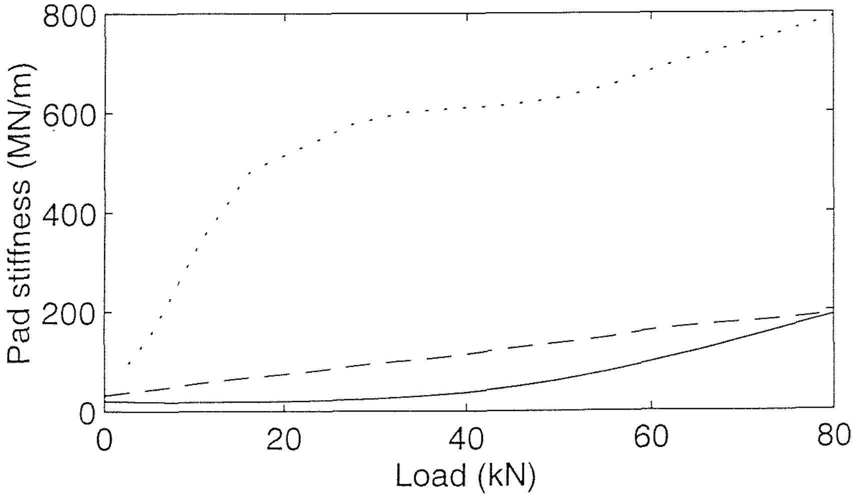

Figure 8.9. Static pad stiffness variations with loads [99]. — for the soft pad, – – for the medium pad, ····· for the stiff pad.

around 50 kN if each wheel load is equal to 75 kN. The ratio of the dynamic stiffness to the static stiffness is chosen as 3.6 for the soft and medium pads and 2.3 for the stiff pad [99]. In terms of the maximum dynamic stiffness in the loaded area, the medium pad is about 2.5 times as stiff as the soft pad, and the stiff pad is about 3 times as stiff as the medium pad.

Figure 8.10 shows the point receptance and the average vibration decay rate for an unloaded track without wheels on it. Three types of railpad are used for the track and their stiffnesses are chosen as $K_p = 68.8$ MN/m for the soft pad, $K_p = 270$ MN/m for the medium pad and $K_p = 1191$ MN/m for the stiff pad. It can be seen that using stiffer pad leads to a lower receptance and a higher vibration decay rate.

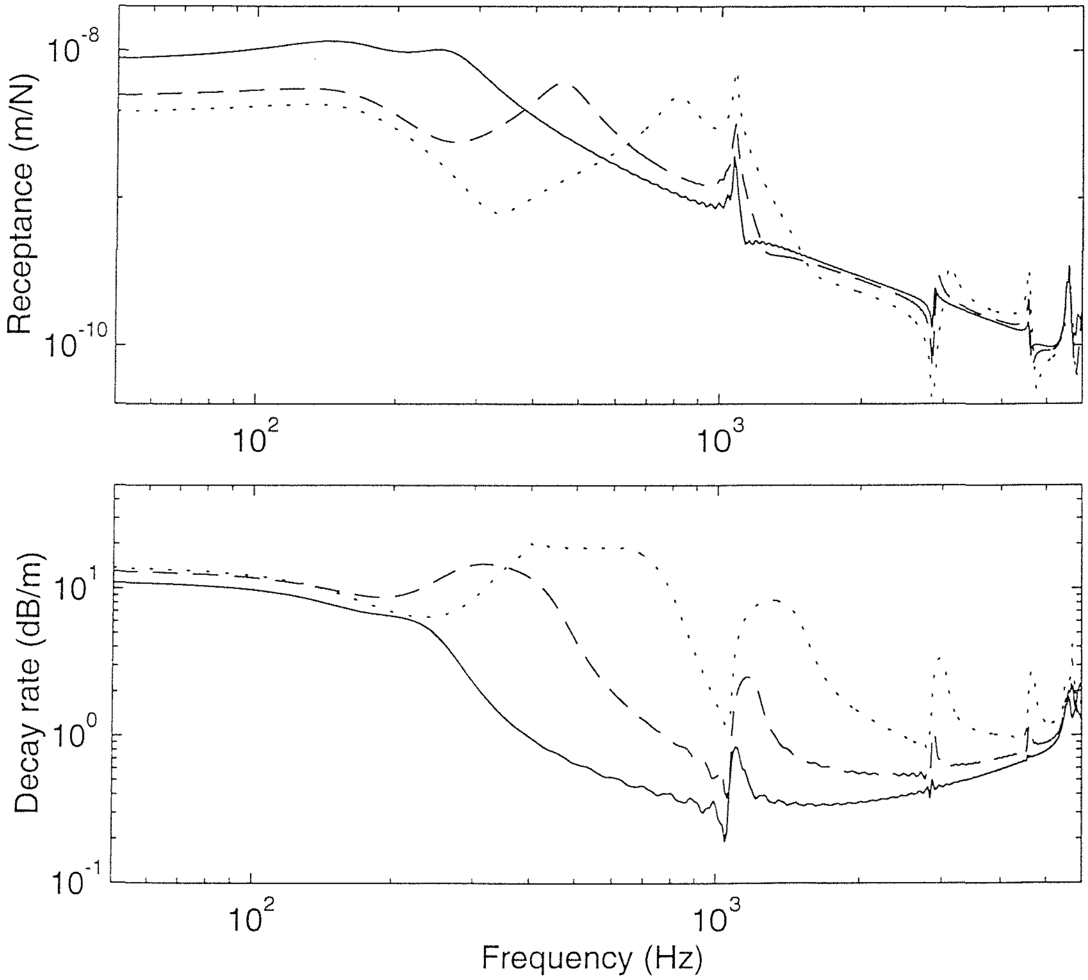

Figure 8.10. Receptance amplitude and vibration decay rate of an unloaded track without wheels on it. — for the track using soft pads, – – for the track using medium pads, ····· for the track using stiff pads.

Figures 8.11 and 8.12 show a comparison of the results from the tracks with the three types of pad stiffness in terms of the point receptance, wheel/rail interaction force and the vibration level with multiple wheels present. The point receptance can be seen to be lower for the stiff pad at low frequencies. The resonance of the whole rail bouncing on the pad stiffness appears at a higher frequency for the stiff pad. At high frequencies, however, the point receptance is less affected by the pad stiffness. The influence of the wave reflection from other wheels becomes weaker and weaker

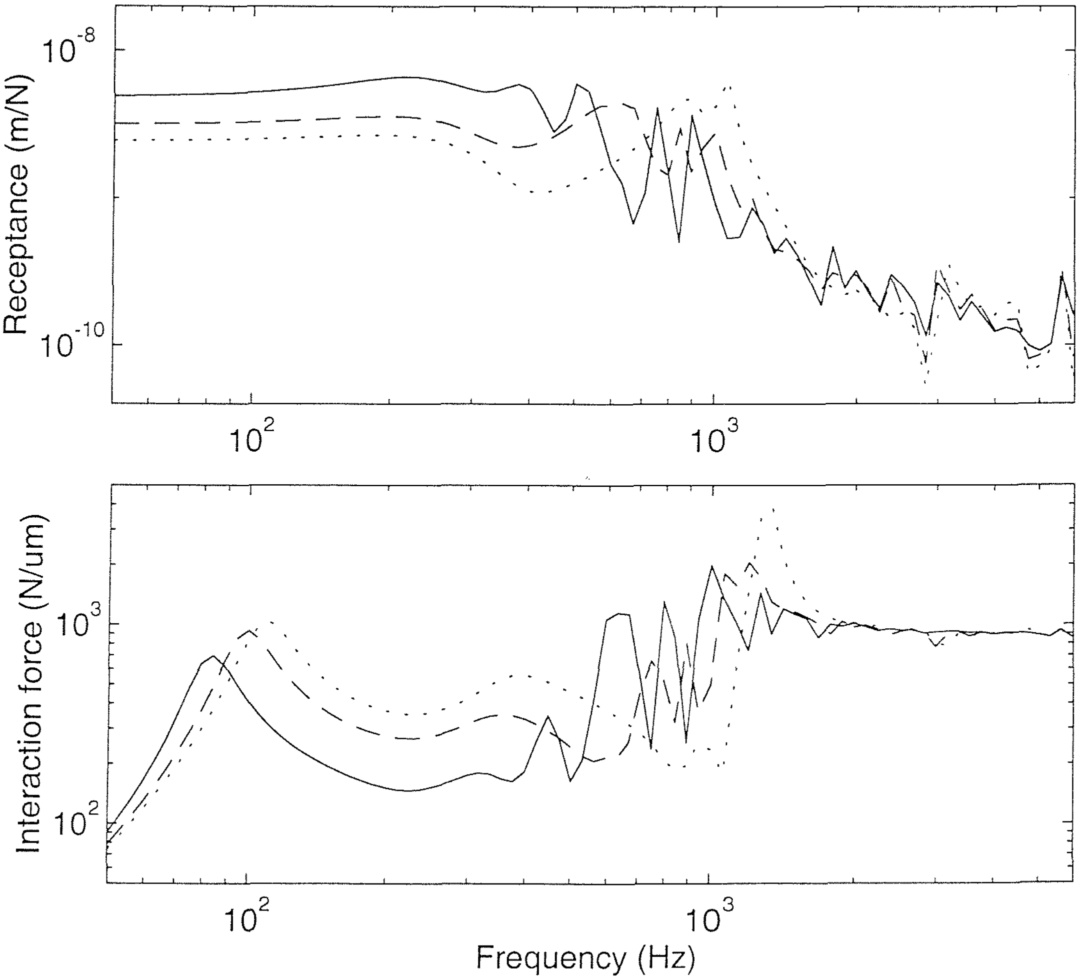

Figure 8.11. Result comparison from different pad stiffness for the track with both preloaded foundation and wheel/rail interactions in terms of point receptance and wheel/rail interaction force due to 1 μm relative displacement excitation, all wheels at mid-span. — from the soft pad, – – from the medium pad, ····· from the stiff pad.

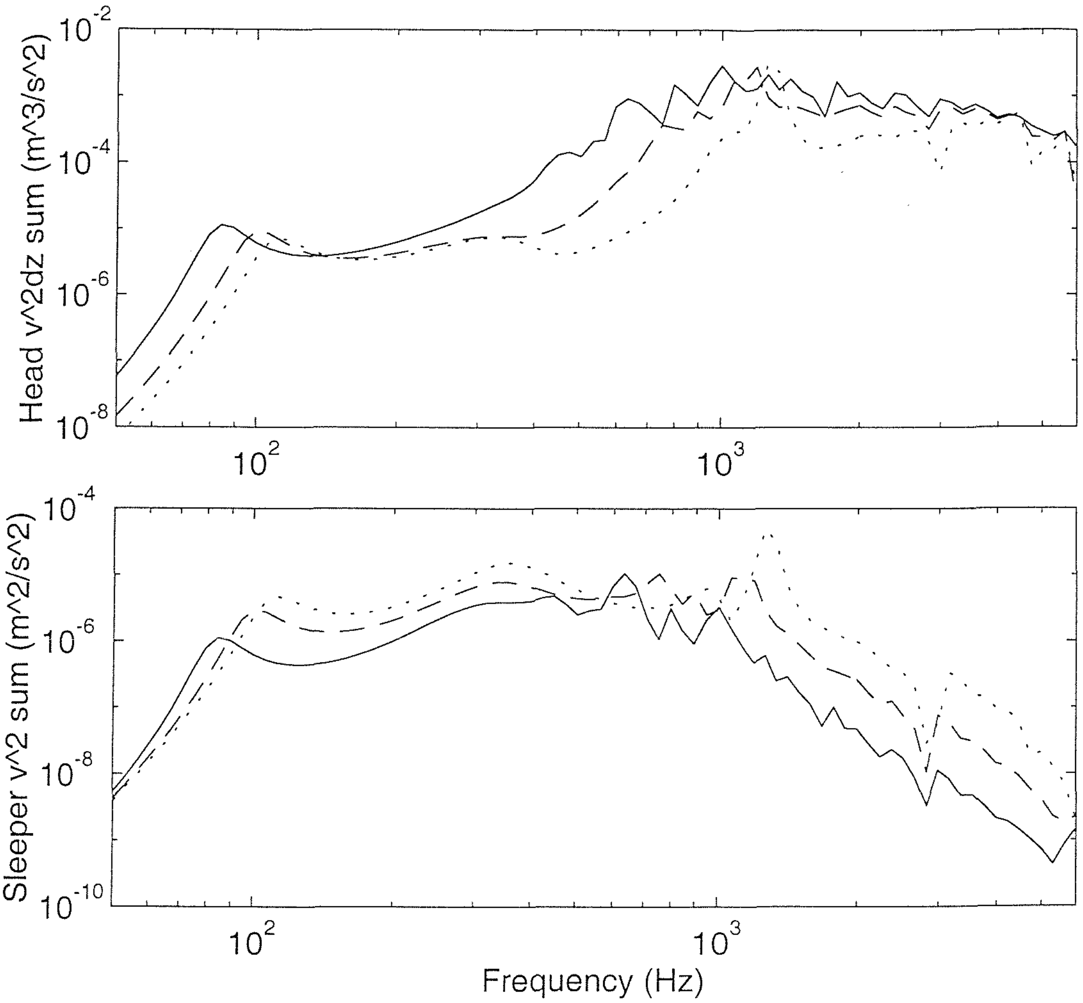

Figure 8.12. Vibration level of the rail head and sleepers due to 1 μm relative displacement excitation for the track with different pad stiffness, key as for Figure 8.11.

with incresing pad stiffness because of the wave propagation decay becoming greater and greater (see Figure 8.10). The wheel/rail interaction force in the frequency region 100 – 500 Hz is larger for the stiff pad because of the lower point receptance. At high frequencies, however, the interaction forces are almost the same for all cases. The vibration level of the rail is higher for the rail with the soft pad. There are different reasons to explain this in different frequency regions. In the frequency region about 50 – 80 Hz, the wheel/rail excitation force and receptance are larger for the soft pad. In the frequency region about 200 – 600 Hz, the receptance is higher and the vibration decay is low for the soft pad (see Figure 8.10) although the wheel/rail excitation force is smaller. In the frequency region about 600

– 1000 Hz, the excitation force is larger and the vibration decay is low for the soft pad. At high frequencies the stiff pad introduces more damping which leads to more reduction in the vibration level for the track with the stiff pad although the wheel/rail excitation forces are similar for all pads. On the other hand, the vibration level of the sleepers is higher for the stiff pad and lower for the soft pad, especially at frequencies above 1 kHz, because the forces transmitted to the sleepers are larger through the stiff pads.

8.4.4. *Radiated noise*

The sound power levels produced by the rail and sleeper radiation are calculated by combining the predicted vibration level spectra of the rail and sleepers with radiation efficiencies in one-third octave bands. The vibration level is determined according to the track responses to a unit relative displacement excitation at each wheel/rail contact point combined with a standard roughness spectrum from cast-iron block tread braked wheel and smooth rail. The roughness spectrum is shown in Figure 8.13. For simplicity lateral rail vibration is not considered although it is also important, especially for the track with stiff pads.

The radiation from the rail and sleepers are calculated using the models from TWINS [84]. In TWINS a series of equivalent acoustic sources located inside the rail are used to replace the vibrating rail for calculating the rail radiation. They are source triples, each consisting of a monopole and two dipoles (directed along two

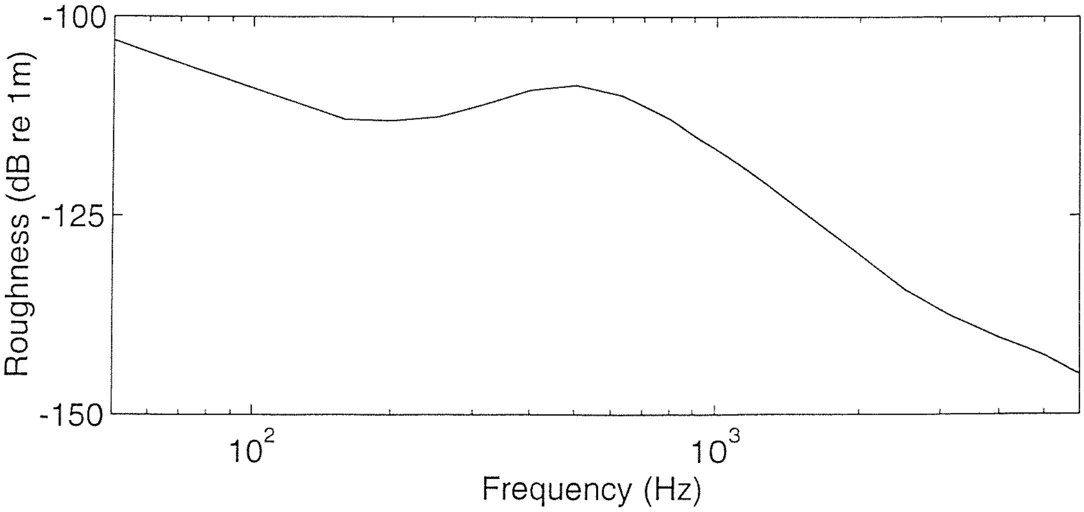

Figure 8.13. Assumed roughness spectrum.

axes of the rail cross-section respectively), and fill the rail cross-section. Along the rail axis each of these sources is actually a line source. These equivalent sources are chosen, for each frequency, by minimising the difference between the produced and original surface intensities in a least square sense. This approach was originally developed by Heckl and Petit [29, 58].

The sleeper radiation is calculated using a baffled rectangular piston model from TWINS. Each sleeper is considered to radiate separately. The power radiated by the sleepers of a length of track, L, with sleeper spacing d and sleeper dimensions $b \times l$ is given by

$$W_S = \frac{\rho c b l L \overline{\tilde{v}^2}}{d} \frac{1}{1+(f_{cs}/f)^2} \tag{8.7}$$

where ρ is the density of the air, c is the sound speed in the air, $\overline{\tilde{v}^2}$ is the spatially averaged mean square of the sleeper velocity (r.m.s.) over the length L and f_{cs} is the critical frequency

$$f_{cs} = \frac{c}{\sqrt{2\pi b l}} \tag{8.8}$$

At low frequencies, where multiple sleepers are within half an acoustic wavelength, they are treated as a single monopole source, thus modifying the radiation efficiency [84].

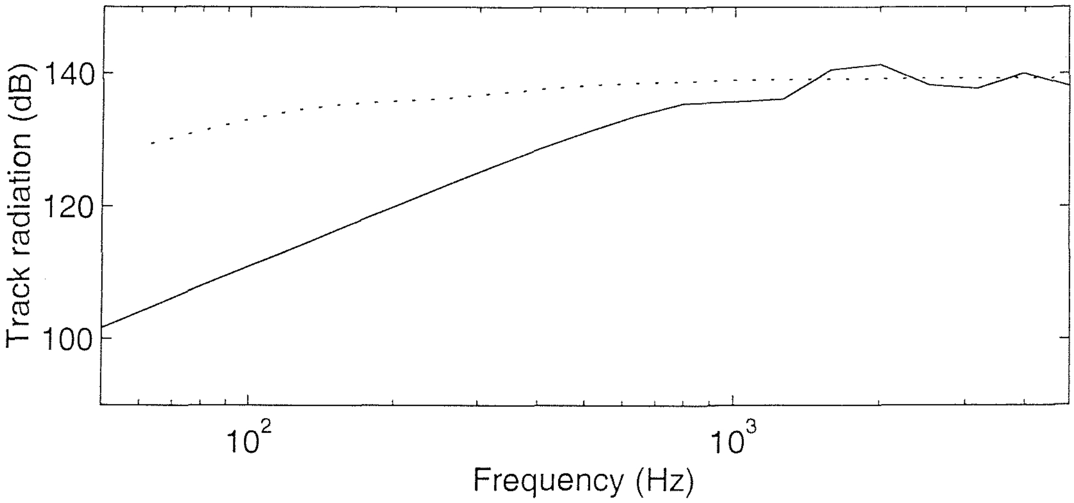

Figure 8.14. Radiated sound power (dB re 10^{-12} W) from rail and sleepers per metre of track for 1 m/s peak velocity amplitude. — from UIC 60 rail, ····· from sleepers.

Figure 8.14 (from [84]) shows the radiated sound power spectrum per metre from UIC 60 rail cross-section model. The rail radiation is from vertical vibration with a peak amplitude of 1 m/s. The radiated sound power from sleepers per metre of track (half) for 1 m/s peak velocity amplitude is also shown in Figure 8.14. The sleeper is concrete monobloc with b = 0.2 m, l = 1.25 m and d = 0.6 m. The rail radiation efficiency can be seen to increase with increasing frequency. At high frequencies, it can be expected to approach 1. Compared with the rail radiation, the sleeper radiation is near constant in the whole frequency range 50 – 5000 Hz.

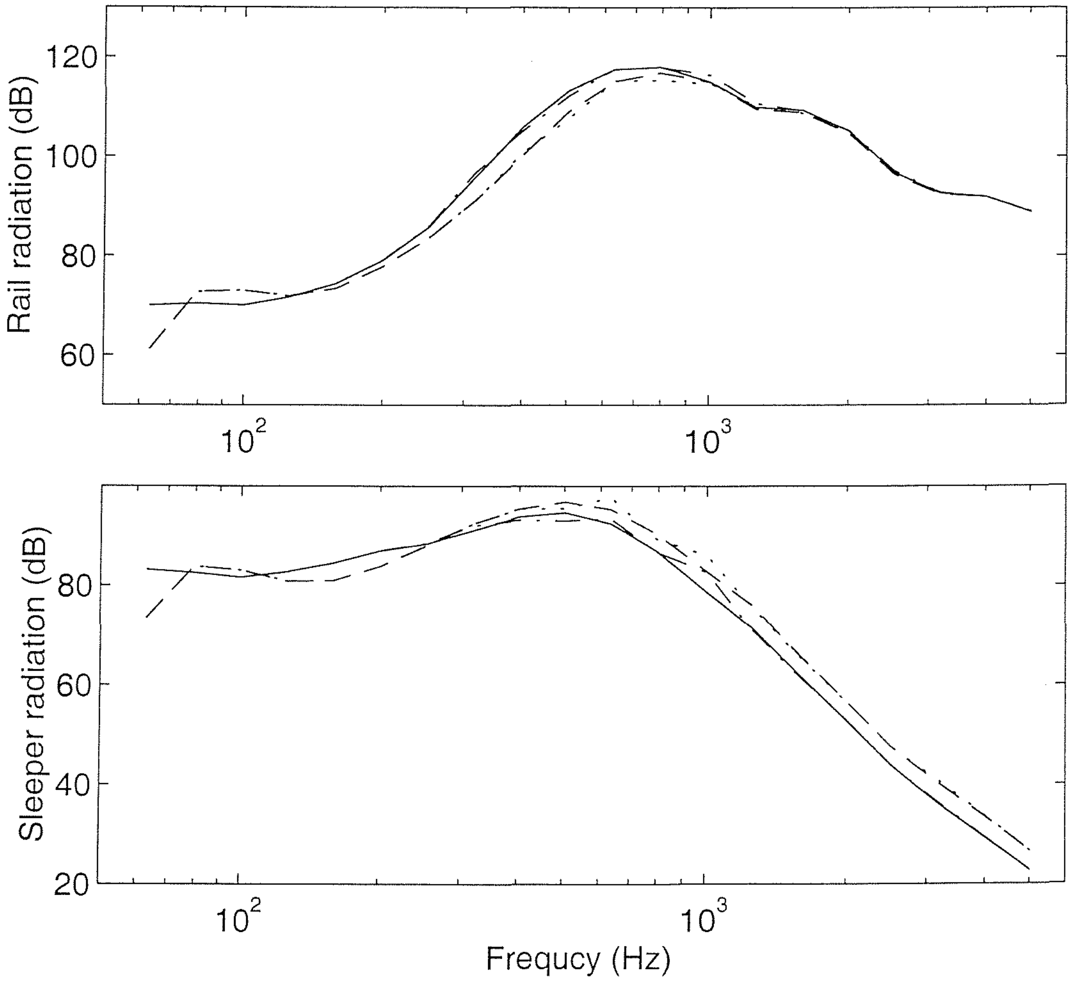

Figure 8.15. Radiated sound power (dB re 10^{-12} W) from rail and sleepers over a wagon length due to the roughness shown in Figure 8.13 at each wheel/rail contact position (all wheels at mid-span). — without preloads and wheel/rail interactions, – – for preloaded foundation only, -·-·- for wheel/rail interactions only, ····· for both preloaded foundation and wheel/rail interactions.

Combining the data shown in Figure 8.14, with the $|v|^2 dz$ sum and $|v|^2$ sum due to 1 μm roughness for the rail and sleeper respectively, and the roughness spectrum in Figure 8.13, the radiated sound power from the rail and sleepers over a wagon length can be obtained.

Figure 8.15 shows the radiated sound power spectra from the rail and sleepers over a wagon length in one-third octave bands for four different models with the soft railpads and with all the wheels being at mid-span. The rail radiation is very low at low frequencies compared with that at high frequencies because of the low radiation efficiencies, whereas the sleeper radiation at low frequencies has a high level since the sleeper vibration level is high here and the radiation efficiencies are not low. It can be observed therefore that the low frequency noise of a track is mainly from sleepers and the high frequency noise is dominated by the rail. The rail radiation is slightly higher for the unloaded track than for the loaded track, whereas the sleeper radiation shows an inverse change. The effects of the passive wheel/rail interactions are hardly recognised after averaging the narrow band spectrum in one-third octave bands.

The A-weighted sound power levels from four different track models with the soft, medium and stiff rail pads are listed in Table 2. It can be seen from Table 2 that the effects of the non-linear pad and ballast stiffness and the wave reflections from other wheels are limited in terms of the noise radiation. When the wheel load increases from 75 kN to 125 kN, the reduction in the rail radiation and the increase in the sleeper radiation due to the preloads become noticeable in the soft pad case. This is because the pad stiffness at the supports close to the wheel loads increases dramatically, being about six times as high as those at the unloaded area (refer to Table 4.6 in chapter 4). The rail noise is under-predicted using the continuously supported model, especially for the track with stiff pads and for the loaded track. This is because the foundation stiffness of the continuously supported track is uniform and chosen in accordance with the largest stiffness in the loaded track. The reduction in the rail radiation and the increase in the sleeper radiation due to the use of stiff pads can clearly be observed by comparing the three cases of the soft, medium and stiff pad stiffness.

Table 8.2

A-weighted sound power levels from four track models, dB re 10^{-12} *W. The first number is for the rail and the number in brackets is for the sleeper. Track type: I - without preloads and wheel/rail interactions, II - preloads only, III - wheel/rail interactions only, IV - with both preloads and wheel/rail interactions. Excitation position: A - above sleeper, B - at mid-span, C - for continuously supported model. * for the case of each static wheel load equal to 125 kN (otherwise 75 kN).*

Pad stiffness	Excitation position	Track type			
		I	II	III	IV
Soft	A	120.0 (93.3)	118.9 (96.3)	120.9 (93.1)	119.4 (96.9)
			*117.0 (99.0)		*116.9 (98.9)
	B	119.9 (93.0)	118.8 (95.4)	120.2 (93.0)	118.4 (96.1)
	C	119.7 (93.3)	117.0 (97.3)	120.1 (93.3)	117.0 (97.4)
Medium	A	116.7 (98.5)	115.4 (99.6)	117.0 (98.6)	115.5 (99.7)
			*114.6 (100.2)		*114.6 (100.3)
	B	117.9 (97.5)	115.8 (97.7)	116.7 (97.5)	115.2 (98.0)
	C	115.4 (97.8)	112.5 (98.8)	115.4 (97.9)	112.5 (98.9)
Stiff	A	111.5 (102.9)	110.5 (102.5)	111.5 (102.9)	110.5 (102.5)
			*109.9 (102.7)		*109.9 (102.7)
	B	113.0 (99.1)	112.1 (98.9)	112.4 (99.0)	111.9 (98.9)
	C	107.6 (100.8)	106.2 (100.1)	107.6 (100.8)	106.3 (100.1)

8.5. Conclusions

Based on the whole train/track interactions, the vibration and the radiation of the railway track are predicted using different models considering the preloaded foundation stiffness and wave reflections from other wheels. Comparisons are carried out between the continuous model and the discrete model of the track. Also the effects of different pad stiffness on the track vibration and noise radiation are studied.

The influences of the preloads and wave reflections from wheels are significant on the rail vibration receptance and the wheel/rail interaction force. Under the preloads the track foundation is locally stiffened, leading to a low point receptance and a high wheel/rail interaction force at low frequencies. The wave reflections from wheels are most noticeable for the track with soft pads, leading to significant fluctuations in the rail vibration receptance and the wheel/rail interaction force in the middle frequency region and a cancellation of the pinned-pinned resonance peak. However, the influences of the preloads and wave reflections on the track vibration level and the noise radiation are limited, except for the track with soft pads. Including multiple wheels affects the noise levels by up to 1 dB(A), while the preload can reduce levels by up to 3 dB(A) for the strongly progressive soft pad studied. Using a stiff pad leads to a reduction in the radiation from the rail whilst increasing the sleeper noise. Conversely a soft pad leads to a low sleeper noise component but a greater rail noise.

CHAPTER 9

Summary and Conclusions

9.1. Background

Railway track vibration, caused by roughnesses on the wheel tread and rail head surface, is a significant source of noise in a fairy broad frequency range 50 – 5000 Hz. Although a lot of research work on railway track dynamics has been carried out over many years, some problems in this area still remained to be solved, for example, the non-linear behaviour of the railpad and ballast and its effect on track vibration, multiple wheel/rail interactions and their consequences in the rail vibration and noise generation. On the other hand new problems arise as some unknown or neglected characteristics of railway track have been found. For example, the ballast stiffness is found to be irregular along the track and so is the sleeper spacing, and therefore, the effect of these irregularities on track vibration needed to be studied. In addition, models used to represent rail dynamics needed to be improved so that the rail vibration can be calculated more effectively, especially for the lateral vibration of a rail with discrete supports. In fact the lateral vibration behaviour of a discretely supported rail had yet to be well investigated due to a lack of appropriate models.

The above stated problems form the original motivation of the work in this thesis. These problems have been studied in the foregoing chapters and many detailed conclusions have been drawn in the corresponding chapters. Even so, it is useful to summarise briefly the more important among them.

9.2. Simplified models for rail vibration at high frequencies

The cross-sectional deformation of a rail is significant in high frequency vibration. The most important deformation types include flapping of the rail foot, bending and torsion of the rail head and foot and bending of the web. Simple beam models of the whole rail can not represent these cross-sectional deformations and thus are not appropriate to investigate the high frequency vibration of a rail. FE or FE-like models are inconvenient for calculating responses of the rail to an external excitation, especially when the discrete supports of the rail are taken into account.

Simplified multiple beam models for high frequency rail vibration have been developed in this thesis. As the vertical and lateral vibration behaviour of a rail are effectively uncoupled from each other, a double Timoshenko beam model is developed for vertical vibration and an interconnected beam model for lateral vibration. The new models can effectively represent rail cross-sectional deformations at high frequencies. Comparisons with FE models have shown good agreement in terms of frequency-wavenumber dispersion relations. Good agreement with measurement data has also been reached in terms of point receptances and vibration decay rates along the rail.

In vertical vibration, the rail foot flapping occurs at high frequencies which leads to the foot response being considerably larger than that of the head, for example up to a factor 10 at about 5600 Hz. Compared to the vertical vibration, the lateral vibration of a rail is more complicated. Many peaks or troughs in the receptance appear in the frequency region from about 400 Hz to 3000 Hz. Among them are three pinned-pinned resonances corresponding to the bending wave, torsional wave and web bending wave, so that for the lateral vibration the pinned-pinned effects are more complicated than for vertical vibration due to the presence of multiple waves. The decay of the lateral vibration with distance also has complicated behaviour due to the presence of multiple waves.

In order to obtain reliable predictions for the rail vibration, the characteristic data for the simplified multiple beam models should be chosen carefully. Some key data may be determined according to the cut-on frequencies of the corresponding cross-sectional deformations. To check these data, the dispersion relation for each wave from a simplified model needs to be compared to that from a corresponding FE model. To guarantee a satisfactory prediction of the rail response, the former should be as close as possible to the latter.

9.3. The effects of multiple wheel static loads

The resilient components in the track foundation such as the pad and ballast have pronounced non-linearity and thus their stiffness depends on the preload in them. When a train runs on the track, the track foundation is loaded by multiple wheels and the preload in the foundation increases the pad and ballast stiffness in the loaded regions, hence modifying the rail vibration.

As the dynamic displacements are small, the track vibration can be represented by a linear model with stiffnesses that are chosen according to the quasi-static load in the foundation. The preload in the track foundation due to a train's weight is local and near the wheel loads. At distances more than about 2 m away from the wheels the preload in the foundation can be considered as zero. Thus only a limited number of pads and ballast are preloaded by the wheel loads. The preloaded pads and ballast become stiffer and thus affect the railway vertical vibration behaviour to some extent. In general their stiffnesses in the loaded area are different at each support. Due to the stiffened pad and ballast the point receptance of track vibration is reduced at low frequencies and the vibration decay rate in the frequency range up to the first pinned-pinned resonance is enhanced. Especially, the wave propagation decay in the loaded area is significantly higher than in the unloaded area. For high frequency vibration above the first pinned-pinned resonance, the effects of the wheel static loads can be ignored.

9.4. Influences of irregularities in the ballast stiffness and sleeper spacing

The sleeper spacing of a track is found not to be constant. In fact it varies in a certain region. The ballast stiffness also varies between different support positions because the contact state between the sleeper and ballast is affected by many uncertain factors. It would be better to take the sleeper spacing and ballast stiffness as random variables and to study track vibration from a statistical point of view.

Owing to the variations in the sleeper spacing and ballast stiffness, the point receptance and the vibration decay rate are distributed in a certain area instead of having a fixed value. The random ballast stiffness mainly affects the low frequency vibration of the track, whereas the random sleeper spacing affects the track vibration in a wide frequency region up to above the first pinned-pinned resonance. Due to the random sleeper spacing the pinned-pinned resonance phenomenon is much less sharp than in the uniform sleeper spacing case and in some cases is completely suppressed. For a railway track with stiffer pads, its dynamic behaviour is more significantly affected by the random sleeper spacing, compared with the track with softer pads. In terms of railway rolling noise, the randomness of the track foundation leads to only small effects and no significant increase or decrease in the track noise.

9.5. Passive multiple wheel/rail interactions

When a train runs on the track, multiple wheel/rail interactions take place. There are two types of interactions. One is a source of excitation due to the roughnesses on the wheel tread and the rail head surface. The other is passive and generated by the rail vibration. The latter leads to wave reflections from the wheels and thus the track vibration is affected by these wheels on the rail.

It is found that the passive wheel/rail interactions are generated in accordance with the wave propagation decay rate in the rail. At low frequencies the wheel/rail interaction forces are small because of the high decay rate of the wave propagation so that the point receptance of the rail is virtually unaffected by the presence of additional wheels. At middle and high frequencies the point receptance of the rail with wheels on it fluctuates around that of the rail without wheels on it because of the low decay rate of the wave propagation. When an excitation acts at mid-span, the first pinned-pinned resonance peak experiences cancellation due to the wave reflections from other wheels. The vibration decay is enhanced in the wheel/rail interaction area at middle frequencies and around the first pinned-pinned resonance.

9.6. Receptances, wheel/rail excitation and noise radiation

The original wheel/rail interaction forces can be calculated using the relative displacement excitation model. In this model the point receptance from a loaded track with multiple wheel/rail interactions should be used. The wheel/rail excitation force is related to the roughness spectrum and the point receptance sum of the wheel, contact spring and rail. At low frequencies the point receptance sum is determined by the wheel and rail receptances. In the middle frequency region up to the first pinned-pinned resonance it is approximately equal to the rail receptance, whereas at high frequencies it is equal to the receptance of the contact spring. As the wheel/rail excitation force is inversely proportional to the point receptance sum, it fluctuates strongly in the middle frequency region due to the presence of the wave reflections from other wheels, with a low receptance of the rail corresponding to a high excitation force and vice versa.

Considering the train/track interaction, each wheel/rail excitation can be treated as incoherent since the roughness is a broad band random process in terms of its wavelength and the wheel separation distances are much larger than the roughness wavelength. Thus the mean square response of the track to each wheel can be added to form the whole response to the train/track interaction.

Although the influences of the preloads and wave reflections from wheels are significant on the rail vibration receptance and the wheel/rail interaction force, their influences on noise radiation from the track are limited. This is because the variations in the rail vibration receptance and in the wheel/rail excitation are opposite. As a result, a higher receptance of the track corresponds to a lower wheel/rail excitation and a higher vibration response of the track. Their effects cancel each other to a large extent. In addition the fluctuation and the narrow band peaks (or troughs) in track response are more or less smoothed after averaging them into one-third octave bands.

Using a stiff pad leads to a reduction in the radiation from the rail whilst increasing the sleeper noise. Conversely a soft pad leads to a low sleeper noise component but a greater rail noise.

9.7. Suggestions for further work

Further experimental investigation into the variation in sleeper spacing, ballast stiffness and possibly pad stiffness need to be carried out so that their actual statistical distributions can be established. Since the realistic track has these stochastic parameters, strictly speaking, the track dynamic response and noise radiation should be predicted in terms of the mean values and deviations, taking account of wheel static loads and multiple wheel/rail interactions. However, some extremely complicated problems will arise, for example, the calculation of the preload in the track foundation caused by the train weight under the consideration of random sleeper spacing and ballast stiffness. How to deal with it is a big challenge.

As the pinned-pinned resonance is cancelled or suppressed in practice due to the wave reflections from other wheels or due to the random sleeper spacing, the continuously supported rail model can be used to take advantage of its simpler formulation. However, only a uniform foundation is allowed in the continuous track model, whereas the track foundation has different stiffness in the loaded regions. In order to calculate the point receptance, the foundation stiffness for the continuous model should be chosen to be equal to the largest stiffness, but unfortunately, this leads to vibration levels of the rail and sleepers that are under-predicted and over-predicted respectively. Thus how to properly use the continuously supported track model requires a further study. A possible approach is to modify the decay rates to allow for the partial nature of the loading.

The effects on lateral track vibration of random sleeper spacing and ballast stiffness, multiple wheel static loads and multiple wheel/rail interactions also need to be studied. Similar approaches to those used in this thesis for vertical vibration can be used for lateral vibration.

The linear theory of the wheel/rail interaction should be checked to make sure in what range of roughnesses it is valid in terms of track vibration and noise radiation. This is because of non-linearity in the vertical contact spring between the wheel and rail and in the lateral creep terms. When rails are corrugated or at discontinuities such as rail joints or wheel flats, the non-linearity ought to be included in the wheel/rail interaction model. Here the wheel and track can be considered as linear systems, but coupled by a non-linear contact element. Non-linearity in the track support may also need to be included.

For a preliminary study the track dynamics may be represented by an equivalent single degree of freedom system for each frequency with its parameters being chosen in accordance with the point receptance and vibration energy of the track. Using a series of such SDOF models for the track and a simplified wheel model (also an SDOF model), which are coupled by the non-linear contact spring, the wheel/rail interaction can be determined at each frequency for a high-level roughness excitation, and thus the effects of the non-linear contact can be examined at each frequency considered.

Detailed investigation of the effects on track vibration of various factors found in practice allows for the use of simpler track models with confidence. For example, in terms of rolling noise prediction, a simple track model such as one ignoring additional wheels on the rail can be used to avoid the complex of multiple wheel/rail interactions, because the influences of the wave reflections from other wheels are limited. Also a continuously supported rail model can be used to represent track dynamics instead of a discretely supported rail model as the pinned-pinned resonance is suppressed in practice due to the waves reflected from other wheels and the random sleeper spacing. On the other hand, however, use of the new models developed in the thesis is essential for studying particular effects, for example to calculate the wheel/rail interaction forces, which is important for the generation of rail corrugations, the track model with multiple wheels on the rail should be used.

As a consequent application, the theoretical models developed in this thesis, such as the multiple Timoshenko beam models, the preloaded track and multiple wheel/rail interaction models, can be included in TWINS to improve the currently used models. Ultimately the work described here will find its use in the design and assessment of noise reduction technology applied to the track, such as damping devices, new rail sections, modified rail pads and new track forms.

APPENDIX A

The Effects of the Pad Rotational Stiffness on the Rail Vertical Vibration

A1. Equations of motion for a Timoshenko beam with moment excitation

Since the rail vibration at high frequencies is less affected by the track foundation, the effects of the pad rotational stiffness on the rail vertical vibration are investigated here only up to 1500 Hz. Thus a simple Timoshenko beam is used to represent the rail dynamic behaviour. Assuming that the external excitations are both an oscillating force and an oscillating moment applied at $z = 0$ and specified by $Fe^{i\omega t}\delta(z)$ and $Me^{i\omega t}\delta(z)$ respectively, the equations of motion of an infinite and unsupported Timoshenko beam can be written as follows:

$$\rho A\ddot{u} + GA\kappa(\Phi' - u'') = Fe^{i\omega t}\delta(z) \tag{A1}$$

$$\rho I\ddot{\Phi} + GA\kappa(\Phi - u') - EI\Phi'' = Me^{i\omega t}\delta(z) \tag{A2}$$

where u represents the transverse (vertical) motion of the beam, Φ represents the rotation of the beam cross-section and $'$ indicates the derivative with respect to z. E is the Young's modulus, G is the shear modulus and ρ is the density. The geometric properties of each cross-section are characterised by A, the cross-sectional area, I, the area moment of inertia and κ, the shear coefficient.

The responses to either the force or the moment or both at any position of the unsupported beam can be easily obtained by changing equations (A1) and (A2) into the state space form and then applying the Laplace transform and contour integration, as used in chapter 2.

A2. Discretely supported track model considering pad rotational stiffness

In Figure A1 the track is modelled by an infinite uniform Timoshenko beam with a finite number of supports which are composed of railpads, sleepers and

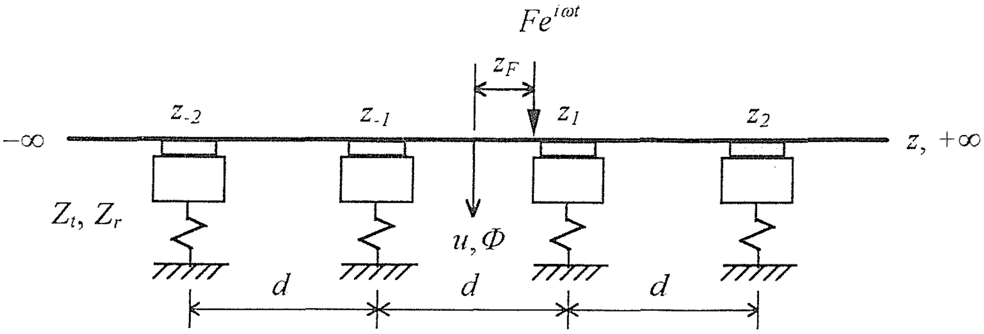

Figure A1. Discretely supported track model.

ballast. As both excitation and response are harmonic, the track supports can be characterised by their dynamic stiffness, Z_t and Z_r. Z_t and Z_r represent translational and rotational dynamic stiffnesses of the supports respectively, and can be given as

$$Z_t = \frac{K_p(1+i\eta_p)\left[K_b(1+i\eta_b) - M_s\omega^2\right]}{K_p(1+i\eta_p) + K_b(1+i\eta_b) - M_s\omega^2} \tag{A3}$$

$$Z_r = \frac{b^2 K_p(1+i\eta_p)}{12} \tag{A4}$$

where K_p and η_p are the pad stiffness and loss factor, K_b and η_b are the ballast stiffness and loss factor, M_s is the sleeper mass and b is the length of the railpad. The rotational stiffness of the supports Z_r is actually produced due to the pad dimension in the rail axis. For simplicity the rotational inertia of the sleeper is chosen as infinite.

A3. Track responses to an external harmonic force

The dynamic excitation imposed by the rolling wheel is represented by a stationary harmonic force $Fe^{i\omega t}$, where $i = \sqrt{-1}$ and ω is the angular frequency of the harmonic excitation. The rail responses to the harmonic force, including the flexural displacement $u(z)$ and the slope $u'(z)$, can be calculated using the Green's function and the superposition principle:

$$u(z) = -\sum_{\substack{n=-N \\ n\neq 0}}^{N} \{Z_t u(z_n) g_{11}(z,z_n) + Z_r u'(z_n) g_{12}(z,z_n)\} + F g_{11}(z,z_F) \tag{A5}$$

$$u'(z) = -\sum_{\substack{n=-N \\ n\neq 0}}^{N} \{Z_t u(z_n) g_{31}(z,z_n) + Z_r u'(z_n) g_{32}(z,z_n)\} + F g_{31}(z,z_F) \tag{A6}$$

where Green's function $g_{ij}(z, z_n)$ is defined as the response at z of the unsupported rail to a unit harmonic force/moment applied at z_n. Subscript 1 corresponds to the flexural displacement u or the force, subscript 2 corresponds to the rotation Φ of the rail cross-section or the moment and subscript 3 corresponds to the rail slope u'. $g_{ij}(z, z_n)$ can be determined by solving equations (A1) and (A2).

Using a similar approach to that used in chapter 2, the rail point and cross receptances to an external force can be obtained, which are the responses $u(z)$ and $u'(z)$ at the forcing point $z = z_F$ due to a unit harmonic force.

A4. Effects of the pad rotational stiffness on rail vertical vibration

The following parameters are chosen for the track model in the numerical calculations:

$E = 2.1\times10^{11}$ N/m^2,	$G = 0.77\times10^{11}$ N/m^2,	ρ = 7850 kg/m^3
$A = 7.69\times10^{-3}$ m^2,	$I = 30.55\times10^{-6}$ m^4,	$\kappa = 0.4$
K_p = 70 MN/m,	K_b = 150 MN/m,	M_s = 162 kg
$\eta_p = 0.25$,	$\eta_b = 1.0$	b = 0.15 m

The pad stiffness which is chosen K_P = 70 MN/m corresponds to an unloaded soft railpad. For comparison K_p = 270 and 1200 MN/m are also chosen to represent medium and hard railpads respectively in calculations.

Figure A2 shows the point receptance and the cross receptance (the rail slope) for the discretely supported rail with excitation acting at mid-span. The span length d is chosen equal to 0.6 m. The results are shown for three cases—the soft, medium and hard pad stiffness. The solid and dotted lines represent the track supports with and without considering the pad rotational stiffness respectively. It can been seen from Figure A2 that the effects of the pad rotational stiffness on the rail vertical vibration are very limited. This is because the pad rotational stiffness is much smaller compared to the rail bending stiffness EI so that it can be totally omitted for the rail vertical vibration. However, the pad rotational stiffness significantly affects the rail lateral vibration, see chapter 3.

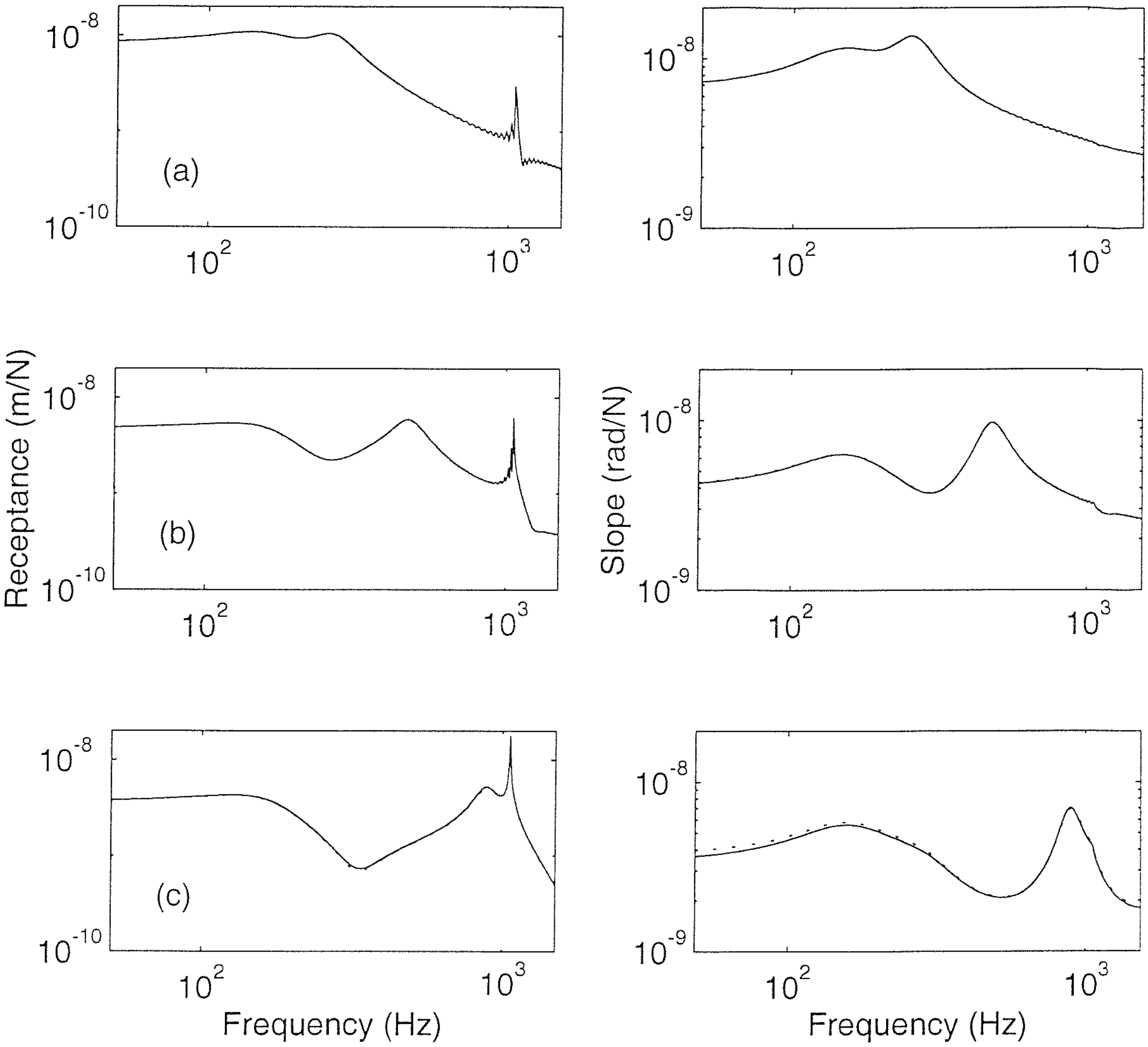

Figure A2. Vertical vibration receptances of the discretely supported rail with and without considering pad rotational stiffness. (a) K_p = 70 MN/m, (b) K_p = 270 MN/m, (c) K_p = 1200 MN/m. — with pad rotational stiffness, ····· without pad rotational stiffness.

APPENDIX B

Equations of Motion for Multiple Beam Model and the Green's Function Calculation

B1. Equations of motion for multiple beam model

In chapter 3 a rail is divided into three parts in the multiple beam model for lateral vibration: the head and the foot are represented by two infinite Timoshenko beams and the web is replaced by numerous beams along the rail which connect the head and foot. The mass and stiffness matrices of the web (pre unit length) $\mathbf{M}_w$ and $\mathbf{K}_w$ are given by [59]

$$\mathbf{M}_w = \begin{bmatrix} m_{11} & 0 & m_{13} & m_{14} & 0 & m_{16} \\ 0 & 0 & 0 & 0 & 0 & 0 \\ m_{31} & 0 & m_{33} & m_{34} & 0 & m_{36} \\ m_{41} & 0 & m_{43} & m_{44} & 0 & m_{46} \\ 0 & 0 & 0 & 0 & 0 & 0 \\ m_{61} & 0 & m_{63} & m_{64} & 0 & m_{66} \end{bmatrix} = \frac{\rho A_w}{420} \begin{bmatrix} 156 & 0 & -22h_w & 54 & 0 & 13h_w \\ 0 & 0 & 0 & 0 & 0 & 0 \\ -22h_w & 0 & 4h_w^2 & -13h_w & 0 & -3h_w^2 \\ 54 & 0 & -13h_w & 156 & 0 & 22h_w \\ 0 & 0 & 0 & 0 & 0 & 0 \\ 13h_w & 0 & -3h_w^2 & 22h_w & 0 & 4h_w^2 \end{bmatrix} \tag{B1}$$

$$\mathbf{K}_w = \begin{bmatrix} k_{11} & 0 & k_{13} & k_{14} & 0 & k_{16} \\ 0 & 0 & 0 & 0 & 0 & 0 \\ k_{31} & 0 & k_{33} & k_{34} & 0 & k_{36} \\ k_{41} & 0 & k_{43} & k_{44} & 0 & k_{46} \\ 0 & 0 & 0 & 0 & 0 & 0 \\ k_{61} & 0 & k_{63} & k_{64} & 0 & k_{66} \end{bmatrix} = \frac{EI_w}{h_w^3} \begin{bmatrix} 12 & 0 & -6h_w & -12 & 0 & -6h_w \\ 0 & 0 & 0 & 0 & 0 & 0 \\ -6h_w & 0 & 4h_w^2 & 6h_w & 0 & 2h_w^2 \\ -12 & 0 & 6h_w & 12 & 0 & 6h_w \\ 0 & 0 & 0 & 0 & 0 & 0 \\ -6h_w & 0 & 2h_w^2 & 6h_w & 0 & 4h_w^2 \end{bmatrix} \tag{B2}$$

where I_w is the web area moment of inertia per unit length about the rail axis.

Rewrite $\mathbf{M}_w$ and $\mathbf{K}_w$ as follows:

$$\mathbf{M}_w = \begin{bmatrix} M_1 & 0 & M_3 & M_4 & 0 & M_6 \end{bmatrix} \tag{B3}$$

$$\mathbf{K}_w = \begin{bmatrix} K_1 & 0 & K_3 & K_4 & 0 & K_6 \end{bmatrix} \tag{B4}$$

where subscript i represents the i-th column of $\mathbf{M}_w$ or $\mathbf{K}_w$. Substituting V_h, M_h, V_f and M_f from equation (3.3) into equations (3.1) and (3.2), then combine them to give

$$\begin{aligned}\mathbf{M}_{hf}\ddot{\mathbf{q}} - \mathbf{D}\mathbf{q}'' - \mathbf{G}\mathbf{q}' + \mathbf{K}_s\mathbf{q} = {} & -M_1(\ddot{v}_h - \frac{h_h\ddot{\theta}_h}{2}) - M_3\ddot{\theta}_h - M_4(\ddot{v}_f + \frac{h_f\ddot{\theta}_f}{2}) - M_6\ddot{\theta}_f \\ & -K_1(v_h - \frac{h_h\theta_h}{2}) - K_3\theta_h - K_4(v_f + \frac{h_f\theta_f}{2}) - K_6\theta_f \\ & +\begin{pmatrix} 0 & 0 & V_h\dfrac{h_h}{2} & 0 & 0 & -V_f\dfrac{h_f}{2}\end{pmatrix}^{\mathrm{T}}\end{aligned} \tag{B5}$$

where

$$\mathbf{M}_{hf} = \begin{bmatrix} \rho A_h &&&&& \\ & \rho I_h &&&& \\ && \rho I_{ph} &&& \\ &&& \rho A_f && \\ &&&& \rho I_f & \\ &&&&& \rho I_{pf} \end{bmatrix} \tag{B6}$$

$$\mathbf{D} = \begin{bmatrix} GA_h\kappa_h &&&&& \\ & EI_h &&&& \\ && GJ_h &&& \\ &&& GA_f\kappa_f && \\ &&&& EI_f & \\ &&&&& GJ_f \end{bmatrix} \tag{B7}$$

$$\mathbf{G} = \begin{bmatrix} 0 & -GA_h\kappa_h &&&& \\ GA_h\kappa_h & 0 &&&& \\ && 0 &&& \\ &&& 0 & -GA_f\kappa_f & \\ &&& GA_f\kappa_f & 0 & \\ &&&&& 0 \end{bmatrix} \tag{B8}$$

$$\mathbf{K}_s = \begin{bmatrix} 0 &&&&& \\ & GA_h\kappa_h &&&& \\ && 0 &&& \\ &&& 0 && \\ &&&& GA_f\kappa_f & \\ &&&&& 0 \end{bmatrix} \tag{B9}$$

$$\mathbf{q}=\begin{pmatrix} v_h & \psi_h & \theta_h & v_f & \psi_f & \theta_f \end{pmatrix}^{\mathrm{T}} \tag{B10}$$

$$\begin{aligned} V_h &= m_{11}(\ddot{v}_h - \frac{h_h\ddot{\theta}_h}{2}) + m_{13}\ddot{\theta}_h + m_{14}(\ddot{v}_f + \frac{h_f\ddot{\theta}_f}{2}) + m_{16}\ddot{\theta}_f \\ &+ k_{11}(v_h - \frac{h_h\theta_h}{2}) + k_{13}\theta_h + k_{14}(v_f + \frac{h_f\theta_f}{2}) + k_{16}\theta_f \end{aligned} \tag{B11}$$

$$\begin{aligned} V_f &= m_{41}(\ddot{v}_h - \frac{h_h\ddot{\theta}_h}{2}) + m_{43}\ddot{\theta}_h + m_{44}(\ddot{v}_f + \frac{h_f\ddot{\theta}_f}{2}) + m_{46}\ddot{\theta}_f \\ &+ k_{61}(v_h - \frac{h_h\theta_h}{2}) + k_{63}\theta_h + k_{64}(v_f + \frac{h_f\theta_f}{2}) + k_{66}\theta_f \end{aligned} \tag{B12}$$

Equation (B5) can be further simplified to

$$\mathbf{M}\ddot{\mathbf{q}} - \mathbf{D}\mathbf{q}'' - \mathbf{G}\mathbf{q}' + \mathbf{K}_R\mathbf{q} = \mathbf{0} \tag{B13}$$

where

$$\begin{aligned} \mathbf{M} = \mathbf{M}_{hf} + \mathbf{M}_w &+ \begin{bmatrix} 0 & 0 & -M_1\frac{h_h}{2} & 0 & 0 & M_4\frac{h_f}{2} \end{bmatrix} \\ &- \begin{bmatrix} 0 & 0 & 0 & 0 & 0 & 0 \\ 0 & 0 & 0 & 0 & 0 & 0 \\ m_{11}\frac{h_h}{2} & 0 & (m_{13} - m_{11}\frac{h_h}{2})\frac{h_h}{2} & m_{14}\frac{h_h}{2} & 0 & (m_{16} + m_{14}\frac{h_f}{2})\frac{h_h}{2} \\ 0 & 0 & 0 & 0 & 0 & 0 \\ 0 & 0 & 0 & 0 & 0 & 0 \\ -m_{41}\frac{h_f}{2} & 0 & -(m_{43} - m_{41}\frac{h_h}{2})\frac{h_f}{2} & -m_{44}\frac{h_f}{2} & 0 & -(m_{46} + m_{44}\frac{h_f}{2})\frac{h_f}{2} \end{bmatrix} \end{aligned} \tag{B14}$$

$$\begin{aligned} \mathbf{K}_R = \mathbf{K}_s + \mathbf{K}_w &+ \begin{bmatrix} 0 & 0 & -K_1\frac{h_h}{2} & 0 & 0 & K_4\frac{h_f}{2} \end{bmatrix} \\ &- \begin{bmatrix} 0 & 0 & 0 & 0 & 0 & 0 \\ 0 & 0 & 0 & 0 & 0 & 0 \\ k_{11}\frac{h_h}{2} & 0 & (k_{13} - k_{11}\frac{h_h}{2})\frac{h_h}{2} & k_{14}\frac{h_h}{2} & 0 & (k_{16} + k_{14}\frac{h_f}{2})\frac{h_h}{2} \\ 0 & 0 & 0 & 0 & 0 & 0 \\ 0 & 0 & 0 & 0 & 0 & 0 \\ -k_{41}\frac{h_f}{2} & 0 & -(k_{43} - k_{41}\frac{h_h}{2})\frac{h_f}{2} & -k_{44}\frac{h_f}{2} & 0 & -(k_{46} + k_{44}\frac{h_f}{2})\frac{h_f}{2} \end{bmatrix} \end{aligned} \tag{B15}$$

B2. The Green's function calculation

Considering an infinitely long free rail subjected to a unit harmonic excitation $\mathrm{F}_j e^{i\omega t}$ acting at the point $z = 0$, the equation of motion can be given as follows:

$$-\mathbf{D}\mathbf{q}_j'' - \mathbf{G}\mathbf{q}_j' - (\omega^2\mathbf{M} - \mathbf{K}_R)\mathbf{q}_j = \mathbf{F}_j\delta(z) \tag{B16}$$

Here $\mathbf{F}_j$ is composed only by the j-th component (unit moment) when $j = 3$ or 6, but as pointed out before, when $j = 1$ or 4 the unit force acts at the top of the rail head or at the bottom of the rail foot respectively. Thus $\mathbf{F}_1$ and $\mathbf{F}_4$ are given as follows:

$$\mathbf{F}_1 = \begin{bmatrix} 1 & 0 & \dfrac{h_h}{2} & 0 & 0 & 0 \end{bmatrix}^{\mathrm{T}} \tag{B17}$$

$$\mathbf{F}_4 = \begin{bmatrix} 0 & 0 & 0 & 1 & 0 & -\dfrac{h_f}{2} \end{bmatrix}^{\mathrm{T}} \tag{B18}$$

Equation (B16) can be written in the state space form

$$\mathbf{X}_j' = \mathbf{A}\mathbf{X}_j + \mathbf{P}_j\delta(z) \tag{B19}$$

where

$$\mathbf{X}_j = \begin{bmatrix} \mathbf{q}_j(z) \\ \mathbf{q}_j'(z) \end{bmatrix} \tag{B20}$$

$$\mathbf{A} = \begin{bmatrix} \mathbf{0} & \mathbf{I} \\ -\mathbf{D}^{-1}(\omega^2\mathbf{M} - \mathbf{K}_R) & -\mathbf{D}^{-1}\mathbf{G} \end{bmatrix} \tag{B21}$$

$$\mathbf{P}_j = [\ \mathbf{0}\ \ -\mathbf{D}^{-1}\mathbf{F}_j]^{\mathrm{T}} \tag{B22}$$

$$\begin{aligned} \mathbf{q}_j(z) &= \begin{bmatrix} q_{1j} & q_{2j} & q_{3j} & q_{4j} & q_{5j} & q_{6j} \end{bmatrix}^{\mathrm{T}} \\ &= \begin{bmatrix} v_{hj} & \psi_{hj} & \theta_{hj} & v_{fj} & \psi_{fj} & \theta_{fj} \end{bmatrix}^{\mathrm{T}} \end{aligned} \tag{B23}$$

Taking the Laplace transform of Eq. (B19) gives

$$(s\mathbf{I} - \mathbf{A})\mathbf{X}_j(s) = \mathbf{P}_j \tag{B24}$$

The Laplace transform of the rail head/foot displacement/rotation caused by the unit harmonic force/moment has the form of

$$Q_{ij}(s) = \frac{\Delta_{ij}(s)}{\Delta(s)} \qquad i = 1, 3, 4, 6 \tag{B25}$$

where, $\Delta(s)$ is the determinant of matrix $s\mathbf{I} - \mathbf{A}$ and $\Delta_{ij}(s)$ is the determinant of the matrix which is obtained from $s\mathbf{I} - \mathbf{A}$ by replacing its i-th column by $\mathbf{P}_j$. The Green's function $g_{ij}(z,z')$ is found by performing the Laplace inverse transform using contour integration:

$$g_{ij}(z,z')=\frac{1}{2\pi i}\int_{\gamma-i\infty}^{\gamma+i\infty}Q_{ij}(s)e^{s(z-z')}ds=\sum_{\substack{k\text{ with }\mathrm{Re}(s_k)<0\text{ or}\\ \mathrm{Im}(s_k)<0\text{ if }\mathrm{Re}(s_k)=0}}\mathrm{Res}[\mathrm{Q}_{ij}(s_k)e^{s_k|z-z'|}] \tag{B26}$$

where the residues at the poles s_k are given by

$$\mathrm{Res}[\mathrm{Q}_{ij}(s_k)e^{s_k|z-z'|}]=\frac{\Delta_{ij}(s_k)}{\Delta'(s_k)}e^{s_k|z-z'|} \tag{B27}$$

APPENDIX C

Comparison of the Wave Dispersion Relations in a Rail from Different FE Models and Multiple Beam Model

C1. Comparison of simplified and original cross-section of UIC 60 rail

The simplified version of UIC 60 rail cross-section is shown in Figure 3.4 and its beam-plate FE model is shown in Figure 3.5. In order to check the correctness of this simplified version, a 3-D FE model with the original cross-section of UIC 60 rail is employed and the results from both FE models are compared in terms of the wave dispersion relation. The cross-section of the 3-D FE model is shown in Figure C1. A one metre long rail section is considered for calculations with symmetry or antisymmetry boundary conditions applied at its ends to simulate the waves in an infinite rail. Calculations are carried out using ANSYS with linear brick elements—'solid 45'. Results from both models are shown in Figure C2 in terms of wave dispersion relation.

From Figure C2 the main deviations between the two models can be seen to appear in wave I at high frequencies and in the cut-on frequency of wave IV. The higher frequency of wave IV cut-on for the original rail indicates that the original

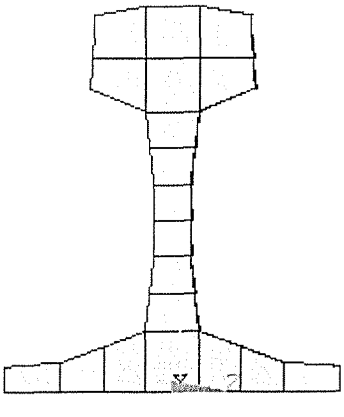

Figure C1. Cross-section of the 3-D FE model of original UIC 60 rail.

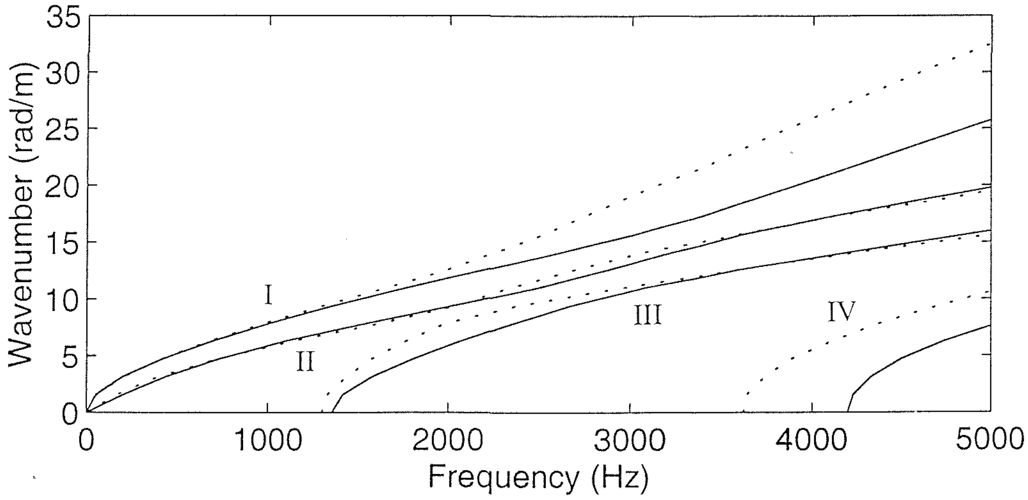

Figure C2. Dispersion relation of waves in a free rail for lateral vibration. — from the 3-D FE rail model with original cross-section shown in Figure C1, ······ from the beam-plate FE model shown in Figure 3.5.

rail has a higher web bending stiffness. The lower wavenumber of wave I in the original rail at high frequencies implies that the foot torsional stiffness of the original rail is much greater than that of the simplified rail because the deformation related to the wave I is dominated by foot torsion at high frequencies, see Figure C3. These deviations appear because the tapered transitions between the web and head and between the web and foot of an actual rail have not been well represented in the simplified rail cross-section.

C2. Results from multiple beam model with improved parameters

In order to reduce the deviations some parameters of the multiple beam model should be further tuned based on the parameters from the simplified rail cross-section. For example, I_w , the web area moment of inertia per unit length about the rail axis and h_w, the height of the web, combine to determine the web bending stiffness. The adjusted parameters now are chosen as follows

$h_w = 0.095$ m $\qquad J_h = 1.240\times10^{-6}$ m^4 $\qquad J_f = 0.806\times10^{-6}$ m^4

The web area moment of inertia remains unchanged but without increasing by ten percent (in chapter 3 I_w is increased by ten percent). The above values for the

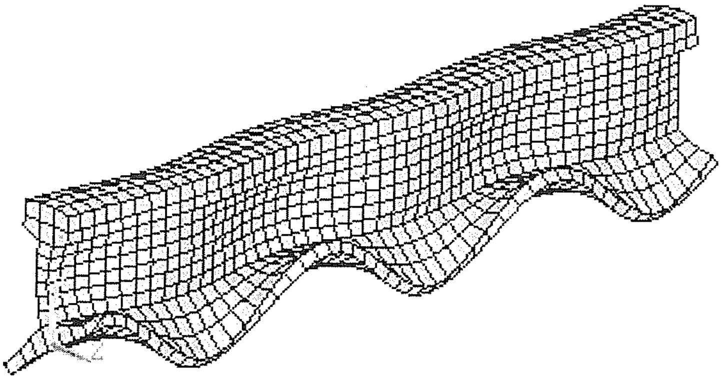

Figure C3. Deformation of a rail at 3381 Hz, which is characterised with wave I.

torsional moments of the head and foot, J_h and J_f, are the actually used parameters in calculations, whereas in chapter 3 the torsional moment of the web inertia should be added to J_h and J_f, see section 3.2.4. Reducing the web height leads to increase the web bending stiffness and thus to increase the cut-on frequencies of wave III and wave IV (web bending). In accordance with decrease of the web height, the distances between the head centre and web and between the foot centre and web, which are represented by $h_h/2$ and $h_f/2$ in equations (3.1) and (3.2), are increased from 19.5 mm to 24 mm and from 8.75 mm to 14 mm respectively. This is also required in practice due to the tapered transitions between the web and head and

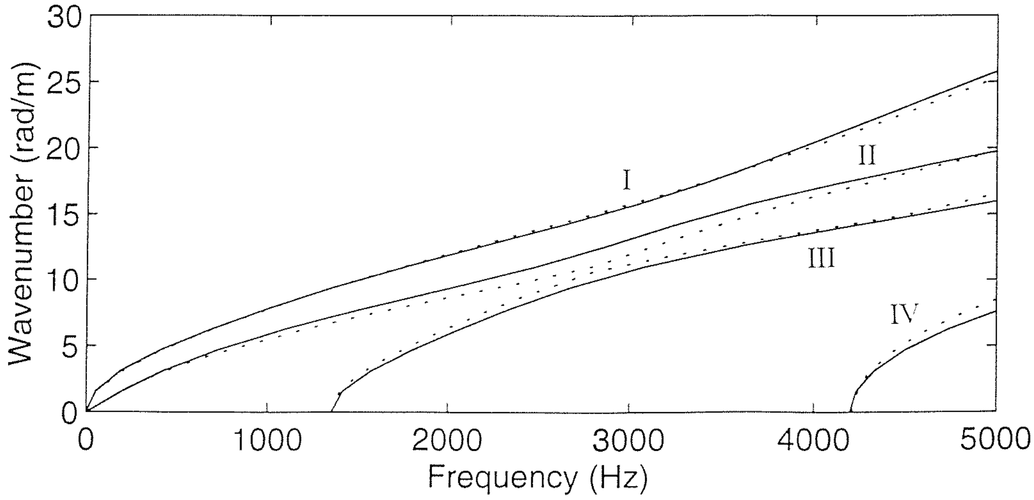

Figure C4. Dispersion relation of waves in a free rail for lateral vibration. — from the 3-D FE rail model, ······ from the beam-plate FE model with improved parameters.

Table C1

Cross-sectional parameters used in the multiple beam model for UIC 60 rail

Parameters	A_h	I_h	I_{ph}	J_h
Simplified version	2.847×10^{-3} m^2	1.264×10^{-6} m^4	1.625×10^{-6} m^4	1.033×10^{-6} m^4
Tuned version	2.847×10^{-3} m^2	1.264×10^{-6} m^4	1.625×10^{-6} m^4	1.240×10^{-6} m^4
Parameters	A_f	I_f	I_{pf}	J_f
Simplified version	2.625×10^{-3} m^2	4.921×10^{-6} m^4	4.988×10^{-6} m^4	0.403×10^{-6} m^4
Tuned version	2.625×10^{-3} m^2	4.921×10^{-6} m^4	4.988×10^{-6} m^4	0.806×10^{-6} m^4
Parameters	A_w	I_w	h_w	$h_h/2$, $h_f/2$
Simplified version	2.166×10^{-3} m^2	0.630×10^{-6} m^4	0.114 m	19.5, 8.75 mm
Tuned version	2.166×10^{-3} m^2	0.572×10^{-6} m^4	0.095 m	24, 14 mm

between the web and foot. Increasing these distances leads to decrease wave III cut-on frequency and to increase wave IV cut-on frequency. Compared with the parameters used by the multiple beam model in chapter 3, the whole torsional moment of the head J_h increases by 20 % and the whole torsional moment of the head J_f is doubled. This leads to reduce the wavenumber of wave I at high frequencies. For comparison these two sets of cross-sectional parameters for the multiple beam model are listed in Table C1.

Figure C4 shows the results from both the 3-D FE model with the original cross-section and the multiple beam model with the improved parameters for UIC 60 rail in terms of the frequency-wavenumber relation. It can be seen from Figure C4 that a very good agreement has been reached between the FE model and the multiple beam model after the parameters of the beam model are tuned.

APPENDIX D

Approximations to Static Ballast Stiffness Measured by Igeland and Oscarsson

In the model presented in the chapters 4 and 7, it has been assumed that the relationship between the reaction force, F and the displacement, u of ballast has the form:

$$F = b u^{3/2} \tag{D1}$$

This has been based on very small amount of dynamic measurements from [11]. In [28] Igeland and Oscarsson give the results of more comprehensive measurements of the static stiffness of ballast, performed at a site known as Goose Hill in Sweden. The monobloc concrete sleepers were disconnected from the rail and a load was applied to both the railseats of one sleeper. The deflection of the sleeper end was measured against a fixed datum. The results are reproduced in Figure D1(a) in which the load given is applied at each railseat. Surprisingly large differences in the sleeper end deflection were found between adjacent sleepers.

Before comparing these results with those from [11], it should be noted that the latter results are based on single block with base size 0.84 m × 0.28 m. In the results from [28] the sleeper is three times longer (2.5 m) so that the overall stiffness can be expected to be greater. What is of interest here, however, is whether an expression of the form assumed in equation (D1) is also appropriate to the data from [28]. Fitting an expression of this form to the results from [28] gives a good fit for sleeper S5, but a poor fit for the other sleepers. Sleepers S2 and S4 appear to be more closely represented by a higher power, u^2 and $u^{5/2}$ respectively.

However, it may be noted that sleepers S2 and S4 exhibit a significant initial deflection for only a small load, following which the results for all three sleepers appear to have a similar slope. This suggests that a more appropriate model may be one of the form:

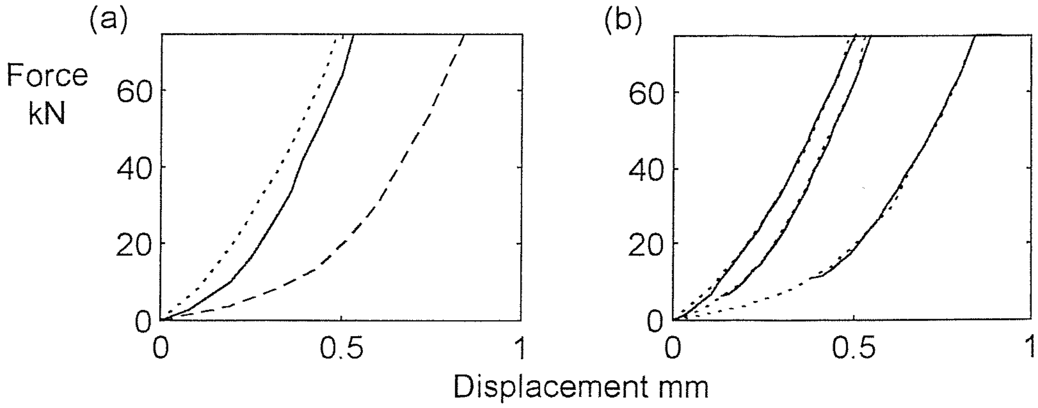

Figure D1. Load applied to concrete monoblock sleeper at each rail seat versus deflection at sleeper end. (a) Measured from [28]; —— sleeper 2; – – – sleeper 4; ······· sleeper 5. (b) —— approximations based on equation (D2), ······· measurements from (a).

$$F = F_0 + b(u - u_0)^{3/2} \quad \text{for } u > u_0 \qquad \text{(D2)}$$

Results for such a model are given in Figure D1(b). They can be seen to be a good approximation to the measured results for appropriate choice of u_0 and F_0. The slope parameter b, is found to be in the range 6.4×10^9 to 8.3×10^9 Nm$^{-3/2}$ for all three sleepers. This means that the variations found between the stiffnesses of the adjacent sleepers are likely to be due not to the material behaviour of the ballast or ground, but to the initial 'slack' in the ballast under each sleeper. These values of b correspond roughly to the 50 Hz dynamic stiffness values given in Table 4.2.

The measured data from [28] therefore appear to give reasonable support to the use of a stiffness law such as equation (D1). Significant variations are found, not in the stiffness law itself, but in the initial part of the load-deflection curve.

APPENDIX E

Measurements of the Effects on the Rail Vibration of Multiple Wheels on the Track

E1. Purpose of the measurements

The objective of the measurements is to validate the prediction of the effects of multiple wheel/rail interactions on the rail vibration. In addition it is possible to explore these effects through the measurements by comparing the results from the situations with and without wheel/rail interactions.

E2. Test track for the measurements

The measurements have been carried out on a test track which was built for the University of Southampton at Chilworth, Southampton. It is a 36 m long, full scale

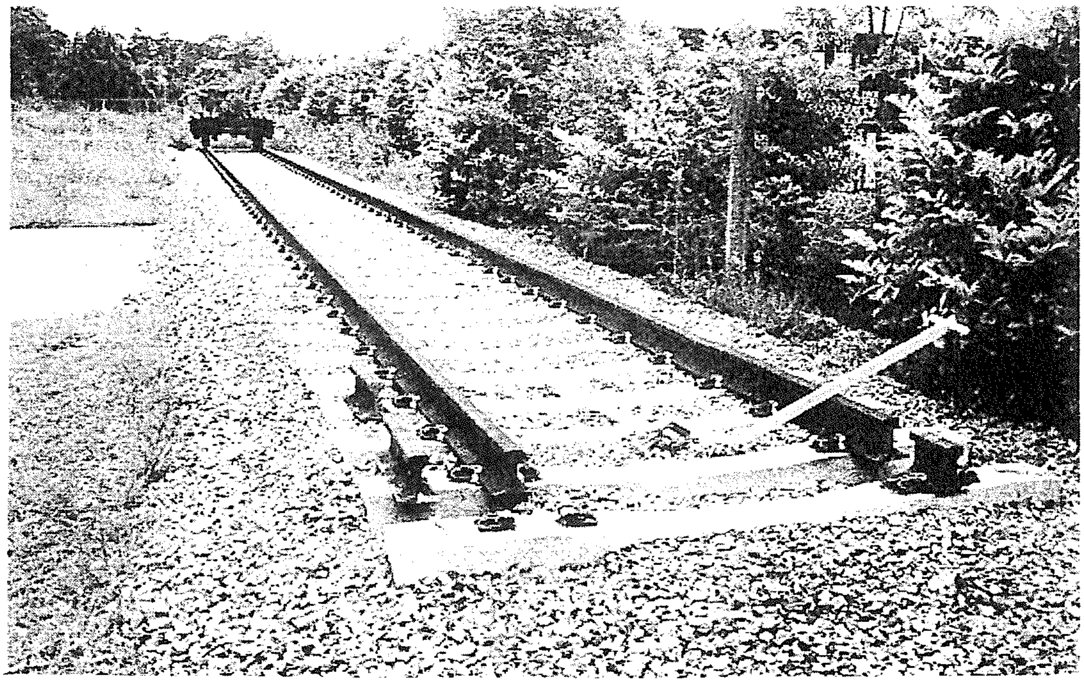

Figure E1. The test track at Chilworth, Southampton.

main line type track. An overall view of the test track is shown in Figure E1. The test track has the following characteristics:

(1) Rails: UIC 60;
(2) Rail fasteners: Pandrol fastclips;
(3) Railpads: Pandrol studded rubber railpads;
(4) Sleepers: concrete monobloc;
(5) Ballast: 30 cm thick under sleepers, compacted with a vibra-tamper.

As the test track is only 36 m long, the high frequency response of the rail includes waves reflected from the free ends of the track. The reflected waves lead to many peaks and troughs appearing at high frequencies in the response spectrum. This can be observed in the measurement results.

E3. Equipment for the measurements

The following items have been used in the measurements:

(1) Instrumented hammer: B&K 8202
    fitted with force gauge B&K 8200, sensitivity 3.89 pC/N
    sensitivity at output of the hammer 0.91 pC/N
(2) Accelerometers: B&K 4384
    sensitivity 1 ± 1% pC/N
    frequency range 0.1 Hz ~ 12.6 kHz
(3) Charge amplifiers: B&K 2635
    sensitivity 0.1 mV ~ 10 V/pC
    frequency range 0.1 Hz ~ 200 kHz
(4) Signal analyser: Diagnostic Instruments 2200
    2 channels real-time analyser

E4. Measurement arrangement

The measurement layout is shown schematically in Figure E2. Two wheel/rail interactions are generated through a bogie standing on the rail, which is placed approximately at the middle of the test track. As the bogie weighs about 50 kN, the track is lightly preloaded. To decoupled the wheel/rail interactions and to keep the

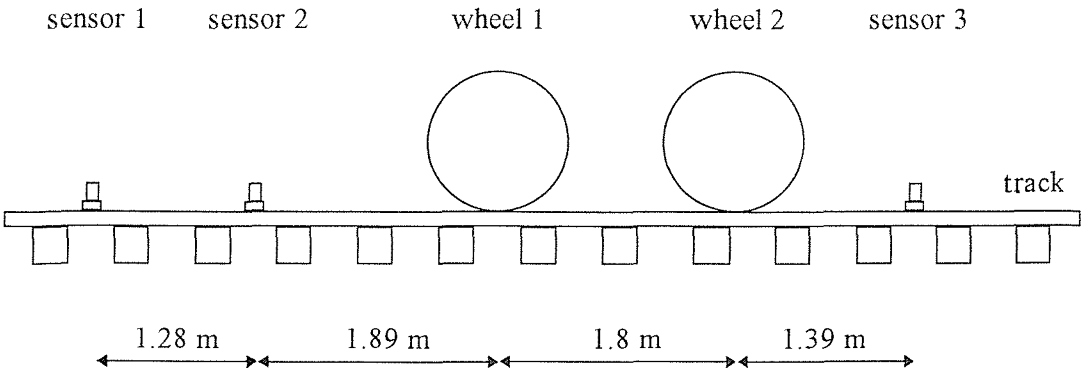

Figure E2. Measurement layout with a bogie (two wheels) on the track.

track preload unchanged when measuring the rail vibration without wheel/rail interactions, rubber blocks are inserted between the wheels and the rail. Point and transfer accelerances are measured for the cases with and without wheel/rail interactions. The point accelerance is measured with sensors 1 and 2 and the transfer accelerance is measured with sensor 3. All these sensors are placed at mid-span. The distance between two wheels is 1.8 m. Since the span lengths of the test track are irregular, most of them being around 0.63 m (see chapter 5), only wheel 1, which is closest to the excitation, is placed at mid-span and wheel 2 is at about one third of a span from the nearest sleeper. An instrumented hammer is used to produce impact excitation. The excitation point is chosen to be very close to sensor 1 or 2. The responses measured are produced by averaging 4 impacts.

E5. Results

Figure E3 shows the point accelerances at sensors 1 and 2. The coherence curves show good consistency in the measurement data. For comparison the predictions from a discretely supported track model are also shown in Figure E3. The parameters of the model can be found in chapter 6. Good agreement with the predictions can be seen from Figure E3 over the range 100 – 4000 Hz, although many sharp peaks and troughs occur in the measurements at high frequencies due to the wave reflections from both ends of the test track.

In order to observe the effects of the wheel/rail interactions, the measured point accelerances from the cases with and without wheel/rail interactions are compared

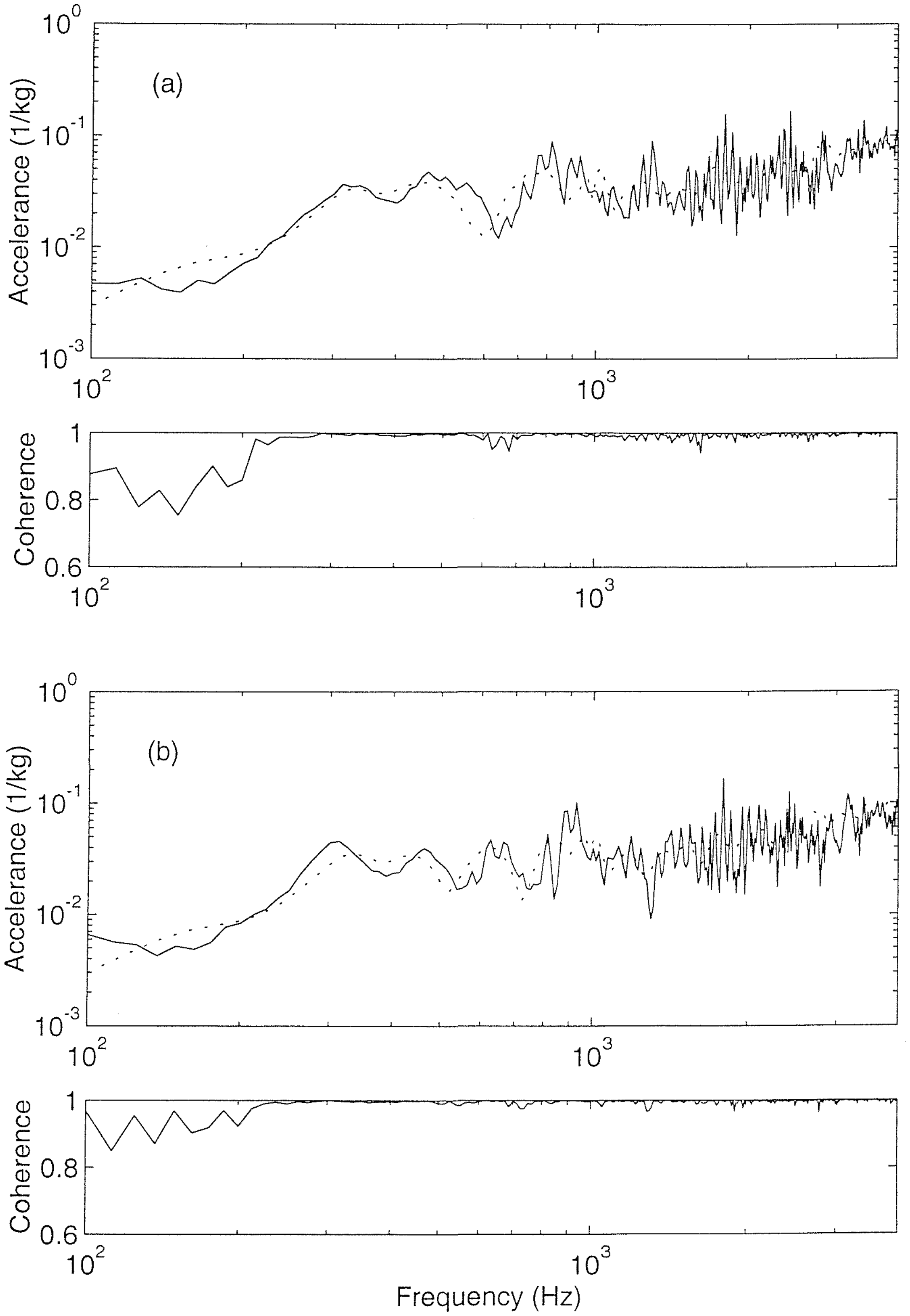

Figure E3. Comparison of the point accelerances (amplitude) from measurements and predictions. (a) excitation at sensor 1 (see Figure E2), (b) excitation at sensor 2. — from measurements, ····· from predictions.

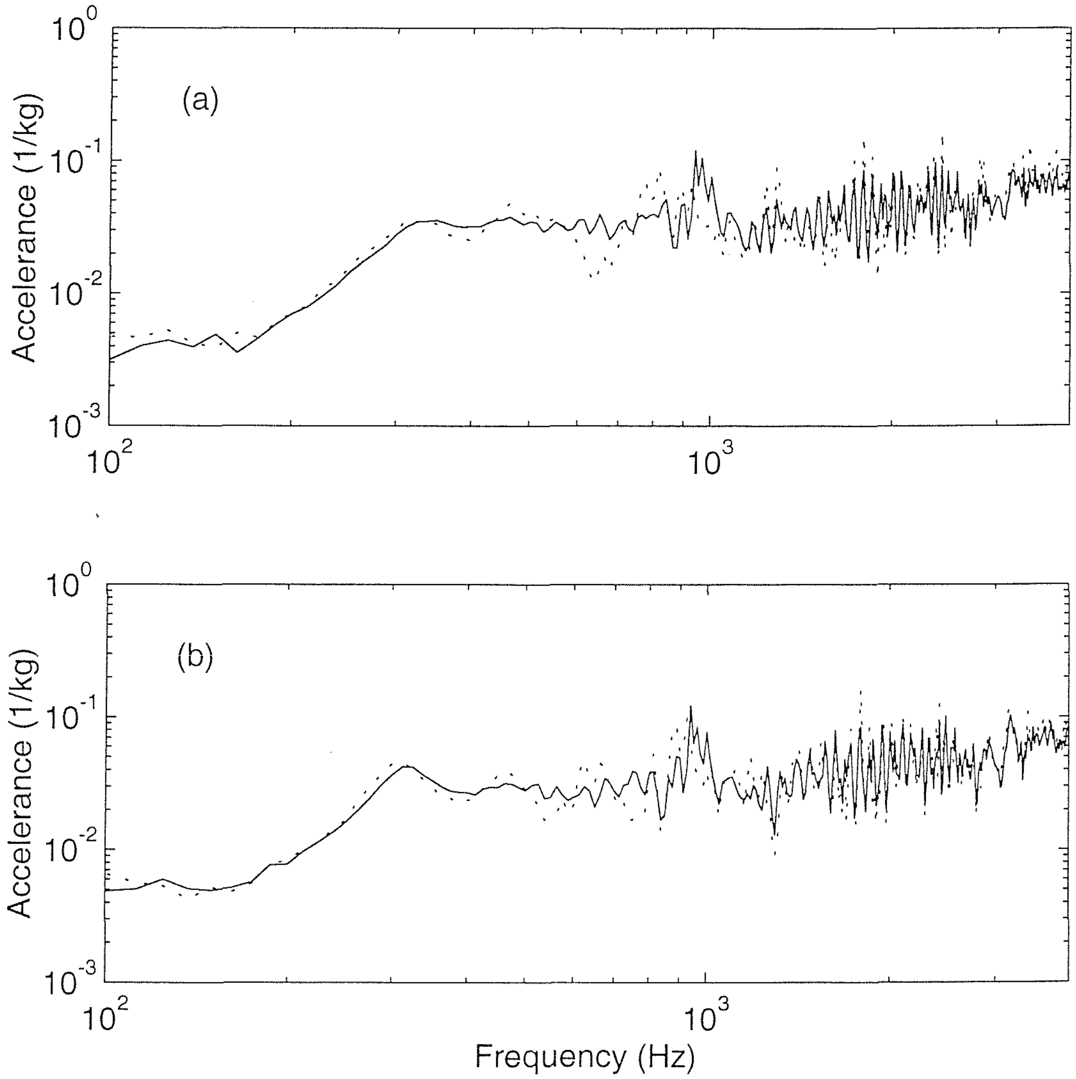

Figure E4. Comparison of the measured point accelerances (amplitude) from the track with and without wheel/rail interactions. (a) excitation at sensor 1, (b) excitation at sensor 2. — without wheel/rail interactions, ····· with wheel/rail interactions.

in Figure E4. The accelerance for the wheel/rail interaction case can be seen to fluctuate relative to the result without interactions from about 400 Hz. The pinned-pinned resonance cancellation can be clearly observed by comparing the two cases. Although the pinned-pinned resonance appears in the range 900 – 1000 Hz due to the irregular sleeper spacing as discussed in chapter 5, suppression of these resonance peaks still happens due to the presence of the wheel/rail interactions.

The transfer accelerances are shown in Figure E5 for the excitation at sensors 1 and 2 and they are compared with the predictions. The measurement data are poor at low frequencies. This is probably because the transfer accelerance should

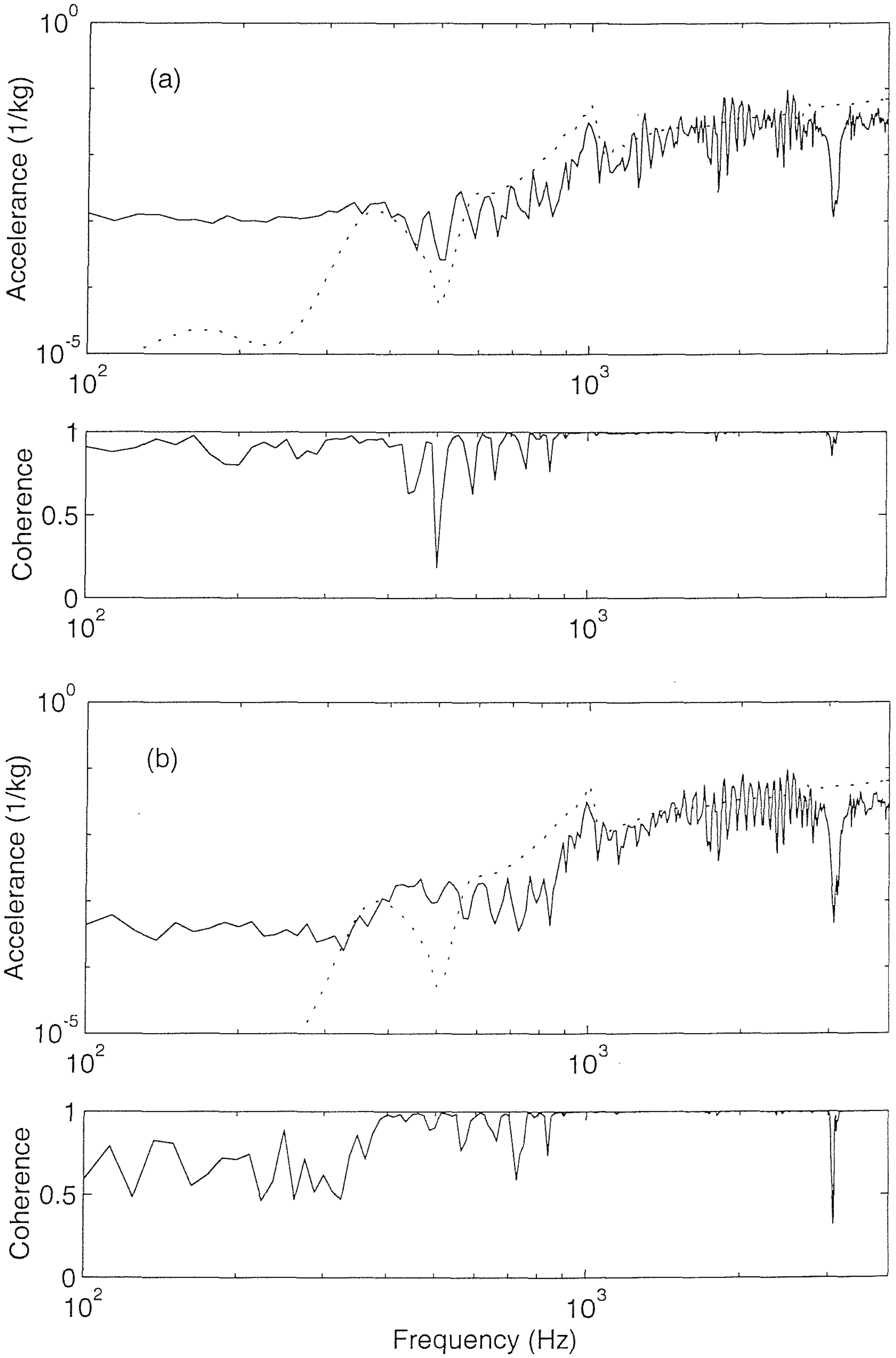

Figure E5. Comparison of the transfer accelerances (amplitude) at sensor 3 from measurements and predictions. (a) excitation at sensor 1, (b) excitation at sensor 2. — from measurements, ····· from predictions.

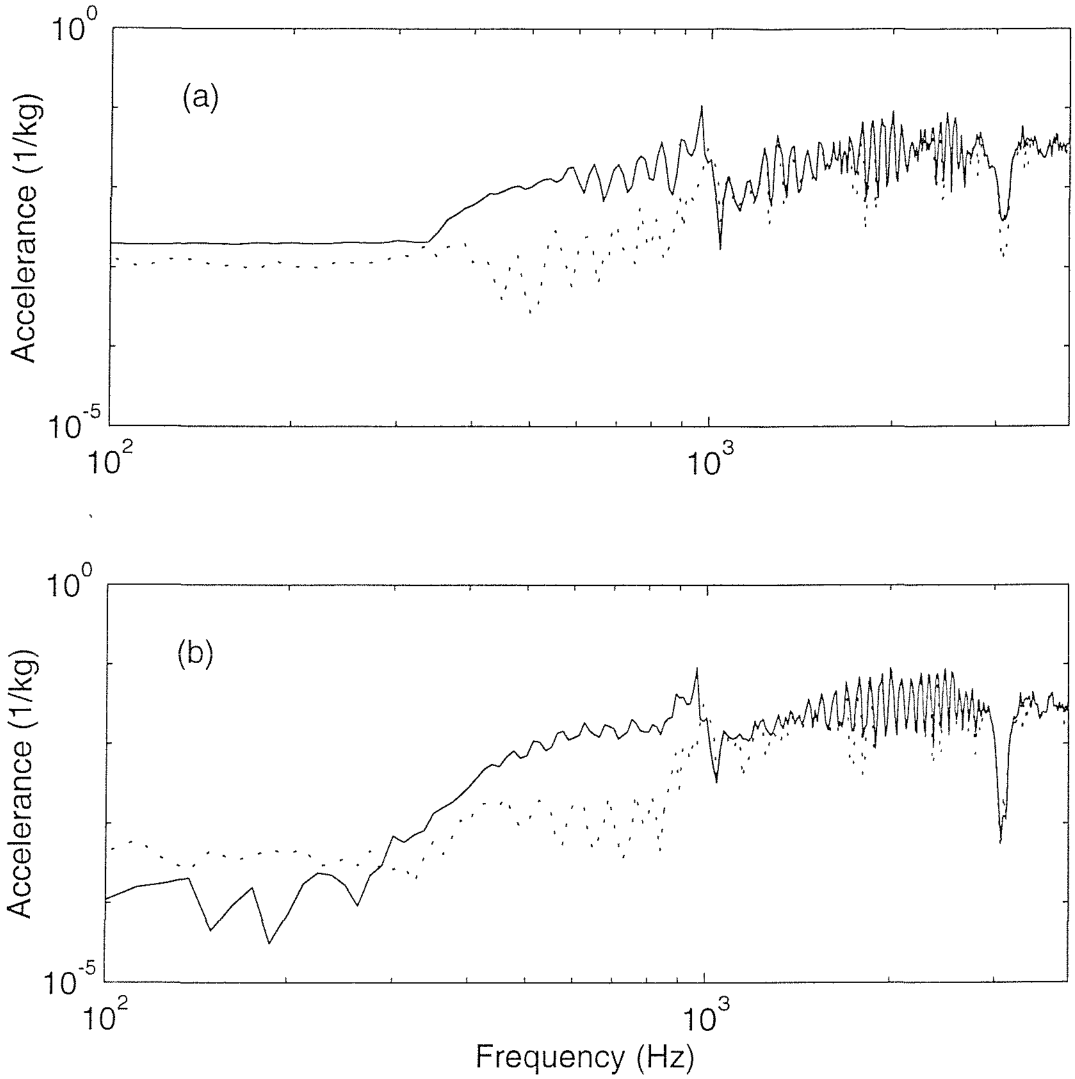

Figure E6. Comparison of the measured transfer accelerances (amplitude) at sensor 3 from the track with and without wheel/rail interactions. (a) excitation at sensor 1, (b) excitation at sensor 2. — without wheel/rail interactions, ····· with wheel/rail interactions.

experience a wide dynamic range of more than 80 dB in the frequency region 100 – 4000 Hz but the signal/noise ratio is limited for the measurement equipment chain. Nevertheless quite good agreement can be found between the measurements and predictions at high frequencies.

Figure E6 shows a comparison of the transfer accelerances measured from both case with and without the wheel/rail interactions. Although the data are poor at low frequencies, an important point can be observed from Figure E6: the vibration decay for the case with the wheel/rail interactions is much higher than that for the case without such interactions in the frequency range 450 – 950 Hz, whereas at high frequencies they are similar for both cases, as predicted in chapter 7. Sharp dips can be seen at about 3 kHz in the measured transfer accelerances. This might be due to the second pinned-pinned resonance, which should appear around 3 kHz and at which a dip should occur in terms of accelerance or receptance (see Figure 6.3 in chapter 6). The dip is sharp in the transfer receptance probably as the wave propagation decay is relatively high near the pinned-pinned resonances.

References

1. Bogacz, R., Krzyzynski, T. and Popp, K. 1989 On the generalization of Mathews' problem of the vibration of a beam on elastic foundation. ZAMM **69**, 243-252.
2. Burden, R. L. and Faires, J. D. 1993 Numerical Analysis. 5th edn, International Thompson, Boston.
3. Chonan, S. 1978 Moving harmonic load on an elastically supported Timoshenko beam. ZAMM **58**, 9-15.
4. Clark, R. A., Dean, P. A., Elkins, J. A. and Newton, S. G. 1982 An investigation into dynamic effects of railway vehicles running on corrugated rails. Journal Mechanical Engineering Science **24**, 65-76.
5. Commission of the European Communities 1996 European Commission Green Paper: Future Noise Policy. COMMA (96) 540 final, ChB-CO-96-548-EN-C, Brussels.
6. Dahlberg, T. and Nielsen, J. 1991 Dynamic behaviour of free-free and in-situ concrete railway sleepers. Report F138, Division of Solid Mechanics, Chalmers University of Technology, Gothenburg.
7. Dalenbring, M. 1995 A study of the effect of track parameter changes on vertical rail vibration. TRITA-FKT Report 9506, Dept. of Vehicle Engineering, Royal Institute of Technology, Stockholm.
8. de France, G. 1998 Railway track: Effect of rail support stiffness on vibration and noise. MSc Dissertation, ISVR, University of Southampton.
9. Duffy, D. G. 1990 The response of an infinite railroad track to a moving, vibrating mass. ASME Journal of Applied Mechanics **57**, 66-73.

10. Fenander, Å. 1997 Frequency dependent stiffness and damping of railpads. Proc. Instn. Mech. Engrs. Part F **211**, 51-62.
11. Ferguson, N. S. 1988 The vibration of rolling discs. PhD Thesis, University of Southampton.
12. Frémion, N., Goudard, J. P. and Vincent, N. 1996 Improvement of ballast and sleeper description in TWINS – step 1: experimental characterisation of ballast properties. VIBRATEC report ref. 072.028a.
13. Frýba, L, 1972 Vibration of solids and structures under moving loads. Noordhoff International Publishing, Groningen.
14. Frýba, L, 1988 Dynamics of rail and track. ILR-Bericht 58, 9-38.
15. Gavric, L. 1995 Computation of propagating waves in free rail using a finite element technique. Journal of Sound and Vibration **185**, 531-543.
16. Grassie, S. L., Gregory, R.W., Harrison, D. and Johnson, K. L. 1982 The dynamic response of railway track to high frequency vertical excitation. Journal Mechanical Engineering Science **24**, 77-90.
17. Grassie, S. L., Gregory, R.W. and Johnson, K. L. 1982 The dynamic response of railway track to high frequency lateral excitation. Journal Mechanical Engineering Science **24**, 91-95.
18. Grassie, S. L., Gregory, R.W. and Johnson, K. L. 1982 The dynamic response of railway track to high frequency longitudinal excitation. Journal Mechanical Engineering Science **24**, 97-102.
19. Grassie, S. L., Gregory, R.W. and Johnson, K. L. 1982 The behaviour of railway wheelsets and track at high frequencies of excitation. Journal Mechanical Engineering Science **24**, 103-111.
20. Grassie, S. L. and Cox, S. J. 1984 The dynamic response of railway track with flexible sleepers to high frequency vertical excitation. Proc. Instn. Mech. Engrs **198D**, 117-124.
21. Grassie, S. L. and Cox, S. J. 1984 The dynamic response of railway track with unsupported sleepers. Proc. Instn. Mech. Engrs **199D**, 123-135.
22. Grassie, S. L. 1989 Resilient railpads: their dynamic behaviour in the laboratory and on the track. Proc. Instn. Mech. Engrs. **203**F, 25-32.

23. Grassie, S. L. 1991 A contribution to dynamic design of railway track. Proc. 12th IAVSD Symposium, Lyon, 195-209.

24. Grassie, S. L. 1995 Dynamic modelling of concrete railway sleepers. Journal of Sound and Vibration **187**, 799-813.

25. Gry, L. 1996 Dynamic modelling of railway track based on wave propagation. Journal of Sound and Vibration **195**, 477-505.

26. Heckl, M. A. 1991 Acoustic behaviour of a periodically supported Timoshenko beam. Report to the ORE Committee C163.

27. Heckl, M. A. 1992 Anregung von gekoppelten Wellen auf einem Timoshenko-Balken mit äquidistanten Stutzstellen. Proceedings of DAGA 92, 1033-1036.

28. Heckl, M. A. 1995 Railway noise – Can random sleeper spacing help? Acustica **81**, 559-564.

29. Heckl, M. and Petit, M-F. 1991 Radiation from rails and sleepers. Theory and model experiments. Report of Institut für Technische Akustik, TU Berlin.

30. Igeland, A. and Oscarsson, J. 1996 Modelling of railway track for computer simulation of dynamic train/track interaction. Report F193, Division of Solid Mechanics, Chlmers University of Technology, Gothenburg.

31. Igeland, A. 1996 Railhead corrugation growth explained by dynamic interaction between track and bogie wheelsets. Proc. Instn. Mech. Engrs. Part F **210**, 11-20.

32. Ilias, H. and Knothe, K. 1992 Ein diskret-kontinuierliches Gleismodell unter dem Einfluß schnell bewegter, harmonisch schwankener Wanderlasten. Fortschritt-Berichte VDI, Reihe 12, Nr. 177.

33. Janssens, M. H. A. and Thompson, D. J. 1996 Improvement of ballast and sleeper description in TWINS. step 2: development and implementation of theoretical models. TNO report TPD-HAG-RPT-960108, TNO Institute of Applied Physics, Delft.

34. Jezequel, L. 1981 Response of periodic systems to a moving load. J. Appl. Mech. **48**, 613-618.

35. Kalker, J. J. 1979 Survey of wheel-rail rolling contact theory. Vehicle System Dynamics **8**, 317-358.

36. Kalker, J. J. 1990 Three dimensional elastic bodies in rolling contact. Kluwer, Dordrecht.
37. Kanamori, T. 1980 A few experiments on elasticity of rubber pad. JNR, Railway Technical Reviews, Quarterly Reports **21**(4).
38. Kisilowski, J., Strzyzakowski, Z. and Sowinski, B. 1988 Application of discrete-continuous model system in investigating dynamics of wheel-track system vertical vibration. ZAMM **68**, T70-T71.
39. Knothe, K. and Gross-Thebing, A. 1986 Derivation of frequency dependent creep coefficients based on an elastic half-space model. Vehicle System Dynamics **15**, 133-153.
40. Knothe, KL. and Grassie, S. L. 1993 Modelling of railway track and vehicle/track interaction at high frequencies. Vehicle System Dynamics **22**, 209-262.
41. Knothe, KL., Strzyzakowski, Z. and Willner, K. 1994 Rail vibrations in the high frequency range. Journal of Sound and Vibration **169**, 111-123.
42. Kurze, U. J. 1997 Refined calculations or improved understanding of rail vibrations? Acustica **83**, 506-515.
43. Mead, D. J. 1970 Free wave propagation in periodically supported infinite beams. Journal of Sound and Vibration **11**, 187-197.
44. Mead, D. J. 1973 A general theory of harmonic wave propagation in linear periodic systems with multiple coupling. Journal of Sound and Vibration **27**, 235-260.
45. Mead, D. J. 1986 A new method of analyzing wave propagation in periodic structures; application to periodic Timoshenko beams and stiffened plates. Journal of Sound and Vibration **104**, 9-27.
46. Meinke, P., Hehenberger, W., Perger, K. and Gruber, J. 1979 Track dynamics at high vehicle speed. Proc. 6th IAVSD Symposium, Berlin, 290-300.
47. Munjal, M. L. and Heckl, M. 1982 Vibration of a periodic rail-sleeper system excited by an oscillatory, stationary, transverse point force. Journal of Sound and Vibration **81**, 491-100.

48. Müller, S., Krzyzynski, T. and Ilias, H. 1995 Comparison of semi-analytical methods of analysing periodical structures under moving load. Vehicle System Dynamics Supplement **24**, 325-339.

49. Newland, D. E. 1984 An introduction to Random vibrations and Spectral Analysis. 2nd edn, Longman, London.

50. Nielsen, J. 1990 Eigenfrequencies and eigenmodes of beam on elastic foundation. Report F128, Division of Solid Mechanics, Chalmers University of Technology, Gothenburg.

51. Nielsen, J. 1994 Dynamic interaction between wheel and track - a parametric search towards an optimal design of rail structures. Vehicle System Dynamics, **23**, 115-132.

52. Nordborg, A. 1998 Vertical rail vibration: pointforce excitation. Acustica **84**, 280-288.

53. Nordborg, A. 1998 Vertical rail vibration: parametric excitation. Acustica **84**, 289-300.

54. Nordborg, A. 1998 Parametrically excited rail/wheel vibration due to track-support irregularities. Acustica **84**, 854-859.

55. Oertli, J. and Wassmer, D. 1996 Rail noise control in Switzerland: legislation, environment, politics and finances. Journal of sound and vibration **193**, 403-406.

56. O. R. E. 1987 Wheel/rail contact noise—further comparative analysis of noise vibration and roughness data. Office for Research and Experiment of the International Union of Railways. Question C163 Railway Noise. Report No. 8.

57. Patil, S. P. 1987 Natural frequencies of a railroad track. J. Appl. Mech. **54**, 299-304.

58. Petit, M-F., Heckl, M., Bergemann, J. and Baae, J. 1992 Berechnung des Abstrahlmaβes von Eisenbahnschienen anhand der Multipolsynthese. proceedings DAGA, 997-1000.

59. Petyt, M. 1990 Introduction to finite element vibration analysis. Cambridge University Press, Cambridge.

60. Remington, P. J. 1976 Wheel/rail noise, part I: characterization of the wheel/rail dynamic system. Journal of sound and vibration **46**, 359-380.

61. Remington, P. J. 1976 Wheel/rail noise, part IV: rolling noise. Journal of sound and vibration **46**, 419-436.
62. Remington, P. J. 1987 Wheel/rail rolling noise I: theoretical analysis. J. Acoust. Soc. Am. **81**, 1805-1823.
63. Remington, P. J. 1987 Wheel/rail rolling noise II: validation of the theory. J. Acoust. Soc. Am. **81**, 1824-1832.
64. Ripke, B. and Knothe, K. 1991 Die unendlich lange Schiene auf diskreten Schwellen bei harmonischer Einzellasterregung. Fortschritt-Berichte VDI, Reihe 11, Nr. 155.
65. Ripke, B. 1995 Hochfrequente Gleismodellierung und Simulation der Fahrzeug-Gleis-Dynamik unter Verwendung einer nichtlienearen Kontaktmechanik. Fortschritt-Berichte VDI, Reihe 12, Nr. 249.
66. Sato, Y. 1977 Study on high frequency vibrations in track operated with high-speed trains. JNR, Railway Technical Reviews, Quarterly Reports **18**, 109-114.
67. Sato, Y., Odaka, T. and Takai, H. 1987 Theoretical analysis on vibration of ballasted track. Railway Technical Research Report No. 1347.
68. Scholl, W. 1982 Schwingungsuntersuchung an Eisenbahnschienen. Acustica **52**, 10-14.
69. Scholl, W. 1984 Two theoretical models for wave propagation in rails. Proceedings of the Second International Conference on Recent Advances in Structural Dynamics, Southampton Vol. II, 699-707.
70. Scholl, W. 1987 Darstellungen des Körperschalls in Platten durch Übertragungsmatrizen und Anwendung auf die Berechnung der Schwingungsformen von Eisenbahnschienen. Fortschritt-Berichte VDI, Reihe 11, Nr. 93.
71. Sibaei, Z. 1992 Vertikale Gleisdynamik beim Abrollen eines Radsatzes - Behandlung im Frequenzbereich. Fortschritt-Berichte VDI, Reihe 11, Nr. 165.
72. Smith, C. C. and Wormley, D. N. 1975 Response of continuous periodically supported guideway beams to travelling vehicle loads. ASME Journal of Dynamics Systems, Measurement, and Control **97**, 21-29.

73. Strzyzakowski, Z., and Ziemanski, L. 1991 On the application of the finite strips method to dynamical analysis of vehicle-track systems. ZAMM **71**, 221-224.
74. Tassilly, E. and Vincent, N. 1991 A linear model for the corrugation of rails. Journal of Sound and Vibration **150**, 25-45.
75. The Mathworks Inc. 1993 Matlab Reference Guide. The Mathworks Inc.
76. Thompson, D. J. 1990 Wheel-rail noise: theoretical modelling of the generation of vibrations. PhD Thesis, ISVR, University of Southampton.
77. Thompson, D. J. 1993 Wheel-rail noise generation, part I: introduction and interaction model. Journal of Sound and Vibration **161**, 387-400.
78. Thompson, D. J. 1993 Wheel-rail noise generation, part II: wheel vibration. Journal of Sound and Vibration **161**, 401-419.
79. Thompson, D. J. 1993 Wheel-rail noise generation, part III: rail vibration. Journal of Sound and Vibration **161**, 421-446.
80. Thompson, D. J. 1993 Wheel-rail noise generation, part IV: contact zone and results. Journal of Sound and Vibration **161**, 447-466.
81. Thompson, D. J. 1993 Wheel-rail noise generation, part V: inclusion of wheel rotation. Journal of Sound and Vibration **161**, 467-482.
82. Thompson, D. J. 1997 Experimental analysis of wave propagation in railway tracks. Journal of Sound and Vibration **203**, 867-888.
83. Thompson, D. J. 1998 Reducing railway rolling noise at source. Noise and Vibration World wide, May, 15-19.
84. Thompson, D. J. and Janssens, M. H. A 1994 TWINS: Track-wheel interaction noise software. Theoretical manual, version 2.2. TNO report TPD-HAG-RPT-93-0214, TNO Institute of Applied Physics, Delft.
85. Thompson, D. J. and Vincent, N. 1995 Track dynamic behaviour at high frequencies. Part 1: Theoretical models and laboratory measurements. Vehicle System Dynamics Supplement **24**, 86-99.
86. Thompson, D. J., Hemsworth, B. and Vincent, N. 1996 Experimental validation of the TWINS prediction program for rolling noise, part 1: description of the model and method. Journal of Sound and Vibration **193**, 123-135.

87. Thompson, D. J., Fodiman, P. and Mahé, H. 1996 Experimental validation of the TWINS prediction program for rolling noise, part 2: results. Journal of Sound and Vibration **193**, 137-147.
88. Thompson, D. J. and Verheij, J. W. 1997 The dynamic behaviour of rail fasteners at high frequencies. Applied Acoustics **52**, 1-17.
89. Thompson, D. J., van Vliet, W. J. and Verheij, J. W. 1998 Developments of the indirect method for measuring the high frequency dynamic stiffness of resilient elements. Journal of Sound and Vibration **213**, 169-188.
90. Thompson, D. J. and Jones, C. J. C. 1998 Reducing railway noise. Engineering Technology, June/July, 10-13.
91. Timoshenko, S. 1915 Strengths of rails. Transactions of the Institute of Ways of Communication, St. Petersburg, Russia.
92. Timoshenko, S. 1926 Method of analysis of statical and dynamical stresses in rail. Proc. Second Int. Congress for Appl. Mech., Zürich, 407-418.
93. Timoshenko, S. and Langer, F. B. 1932 Stresses in railroad track. J. Appl. Mech. **54**, 277-302
94. Timoshenko, S. 1958 Strength of Materials, Part II Advanced Theory and Problems. 3rd edn, Van Nostrand Reinhold, New York.
95. Vincent, N. and Thompson, D. J. 1995 Track dynamic behaviour at high frequencies. Part 2: Experimental results and comparisons with theory. Vehicle System Dynamics Supplement **24**, 100-114.
96. Vincent, N., Bouvet, P., Thompson, D. J and Gautier, P. E. 1996 Theoretical optimization of track components to reduce rolling noise. Journal of Sound and Vibration, **193**, 161-171.
97. Winkler, E. 1867 Die Lehre von der Elastizität und Festigkeit. Verlag H. Dominikus, Prague.
98. Winkler, E. 1875 Der Eisenbahnoberbau. 3rd edn, Verlag H. Dominikus, Prague.
99. Bouvet, P. and Vincent, N. 1998 Laboratory characterization of rail pad dynamic properties. Vibratec Report 450.004.RA.05.A.
100. Nafeh, A. and Mook, D. 1979 Nonlinear Oscillations. John Wiley, New York.